Viscoplastic displacement flows in narrow channels

Thèse

Ali Eslami

Doctorat en génie chimique
Philosophiæ doctor (Ph. D.)

Québec, Canada

Viscoplastic displacement flows in narrow channels

Thèse

Ali Eslami

Sous la direction de:

Seyed Mohammad Taghavi, directeur de recherche

Résumé

Les écoulements à déplacement se produisent fréquemment dans les applications naturelles et industrielles. Bien que les déplacements Newtoniens aient été pris en considération dans une grande variété d'études théoriques et expérimentales dans les dernières décennies, un nombre considérable de fluides pratiques présentent des caractéristiques viscoplastiques, rendant la prévision du comportement des écoulements plus difficile. Les écoulement de déplacement viscoplastiques sont généralement contrôlés par un équilibre entre diverses forces, y compris la force visqueuse, la force de flottabilité, la force d'inertie, contrainte d'écoulement, etc., en plus de caractéristiques miscibles et non miscibles. Une compétition entre ces forces peut conduire à des comportements imprévisibles et exotiques de déplacement. Permettant une compréhension approfondie de ces écoulements, dans cette thèse de doctorat nous avons étudié l'écoulement à déplacement d'un fluide viscoplastique par un fluide Newtonien dans une géométrie simple, c.-à-d. un canal étroit et confiné.

Dans la première partie de cette thèse (chapitres 1 à 3), nous étudions expérimentalement les écoulements à déplacement non-miscibles d'un fluide viscoplastique par un fluide Newtonien. En particulier, nous analysons le mouvement d'air dans un gel de Carbopol, dans une cellule de Hele-Shaw de section rectangulaire. Cette géométrie est composée de deux plaques parallèles rigides. Nous étudions les résultats en termes d'efficacité de déplacement et de morphologie des modèles d'écoulement. Nous démontrons que les comportements complexes du gel Carbopol, c.-à-d. les fortes propriétés viscoplastiques et les faibles propriétés viscoélastiques, affectent les caractéristiques d'écoulement de déplacement. Ensuite, nous étendons cette étude au déplacement d'un gel de Carbopol par une huile de silicone afin de considérer les effets de la mouillabilité sur l'écoulement. Nous observons qu'une combinaison de comportements viscoplastiques et de mouillabilité exerce un impact significatif sur les modèles d'écoulement à déplacement, pour lesquels quatre régimes d'écoulement différents sont identifiés : un régime capillaire, un régime de contrainte d'écoulement, un régime visqueux et un régime élasto-inertiel. Enfin, nous étudions les impacts du rapport d'aspect de la section transversale de la cellule sur les caractéristiques de déplacement viscoplastique.

Dans la deuxième partie de cette thèse (chapitres 4 à 5), nous étudions numériquement les écoulements à déplacement miscibles d'un fluide viscoplastique par un fluide Newtonien dans un long canal plan 2D. Pour un déplacement «heavy-light», l'analyse des modèles d'écoulement en fonction de divers paramètres sans dimension nous permet d'identifier trois régimes d'écoulement distincts : déplacements «center-type»/«slump- type», «back flow»/«no-back flow» et déplacement «stable/instable». Nous décrivons les effets du rapport de viscosité des fluides, de la flottabilité, de la contrainte d'écoulement et de l'inclinaison du canal sur les régimes d'écoulement susmentionnés.

Abstract

Displacement flows frequently occur in natural and industrial applications. Although Newtonian displacements have been considered in a wide range of theoretical and experimental studies in the recent decades, a considerable number of practical fluids exhibit viscoplastic features, making it hard to predict the flow behaviors. Viscoplastic displacement flows are generally controlled by a balance between a variety of forces, including viscous, buoyant, inertial, yield stress, etc., in addition to miscible and immiscible features. A competition between these forces may lead to exotic, unpredictable displacement flow behaviors. To provide a deep understanding of these flows, in this Ph.D. thesis we investigate the displacement flow of a viscoplastic fluid by a Newtonian fluid in a simple flow geometry, i.e., a narrow confined channel.

In the first part of this thesis (*Chapter*s 1-3), we experimentally study immiscible displacement flows of a viscoplastic fluid by a Newtonian fluid. In particular, we analyze the invasion of air into a Carbopol gel in a rectangular cross-section Hele-Shaw cell. This flow geometry is composed of two rigid parallel plates with a small gap. We study the results in terms of the displacement efficiency and morphology of the flow patterns. We demonstrate that the complex behaviors of the Carbopol gel, i.e., strong viscoplastic properties and weak viscoelastic properties, affect the displacement flow features. We then extend this study to the displacement of a Carbopol gel by silicon oil in order to consider the effects of wettability on the flow. We observe that a combination of viscoplastic behaviors and wettability exerts a significant impact on the displacement flow patterns, for which four different flow regimes are identified: a *capillary* regime, a *yield stress* regime, a *viscous* regime and an *elasto-inertial* regime. Finally, we investigate the impacts of the cell cross-section aspect ratio on viscoplastic displacement flow features.

In the second part of this thesis (*Chapter*s 4-5), we numerically study miscible displacement flows of a viscoplastic fluid by a Newtonian fluid in a long 2D plane channel. For a heavy-light displacement, analyzing the displacement flow patterns as a function of various dimensionless parameters allows us to identify three distinct flow regimes: *center/slump*-type, *back/no-back*-flow and *stable/unstable* displacements. We describe the effects of the viscosity ratio of fluids, buoyancy, yield stress and channel inclination on the aforementioned flow regimes.

Table of contents

List of tables

List of figures

“Dedicated to my wonderful parents and my beautiful and intelligent wife”

Acknowledgement

I would like to convey my gratitude and appreciation to all people who have made this dissertation possible. My deepest gratitude goes first and foremost to my supervisor, Professor Seyed Mohammad Taghavi, for giving me the opportunity to undertake this Ph.D. for his patience, continuous support, encouragement and immense knowledge. As his first student, it definitely was an honor for me to be a part of his research group. During my Ph.D., his guidance and mentoring helped me to significantly improve my skills and in learning the fundamentals of conducting scientific research.

I would like to thank Professor Denis Rodrigue for useful discussions and his invaluable comments about the rheology. I am deeply grateful to Professor Ian Frigaard for his generous support and helpful guidance particularly in the simulation part.

I acknowledge all the people at Laval University, especially Jérôme Nöel, Jean-Nicolas Ouellet and Yann Giroux for their outstanding help in the fabrication and modification of different experimental setups. I appreciate Dr. Roozbeh Molllaabbasi and Mr. Sooran Noroozi for their thoughtful remarks that helped me to improve my thesis considerably.

I would like to thank the Discovery Grant of the Natural Sciences and Engineering Research Council (NSERC) and Canada Foundation for Innovation for the financial supports. I am also indebted to Calcul Quebec and Compute Canada for the HPC platform which have made CFD simulation tests possible.

I would like to thank Prof. Kamran Alba and Prof. Ali Roustaei for their guidance in the simulation part at the early stage of this research. My sincere gratefulness to all my friends, an inspiring group of people especially Amin Amiri, Shan Lyu, Hossein Hasanzadeh, Soheil Akbari, Mahdi Izadi and Hossein Rahmani.

I would like to acknowledge the support of my brothers, Mohammad and Reza for their endless love and support during the time of this study. Moreover, I would like to acknowledge my kind parents, who stood by me and supported all my ideas and dreams, for strongly encouraging me to pursue my Ph.D. I love you dearly.

Finally, I would like to express my gratitude to my beautiful, intelligent, beloved wife, Elnaz, who with her helps, supports and kindness, encouragement, and constant love have always sustained me throughout my life journey. I am forever thankful to have you in my life.

Foreword

This thesis is composed of five chapters and presented as articles in the insertion form. Three chapters of this thesis have been already published (*Chapter*s 1, 2, and 4). *Chapter* 5 is conditionally accepted by a journal. *Chapter* 3 is in preparation for a journal submission. The introduction and conclusion sections are originally written by Ali Eslami and they have never been published before. This project is supervised by Prof. Seyed Mohammad Taghavi. The articles are listed below:

Chapter 1: **A. Eslami**, S.M. Taghavi. "Viscous fingering regimes in elasto-visco-plastic fluids". Journal of Non-Newtonian Fluid Mechanics 243, 79-94 (2017).

Chapter 2: **A. Eslami**, S.M. Taghavi. "Viscous fingering of yield stress fluids: The effects of wettability". Journal of Non-Newtonian Fluid Mechanics 264, (2019) 25–47.

Chapter 3: **A. Eslami**, S.M. Taghavi. "Controlling branched fingering patterns in viscous fingering of yield stress fluids". Under preparation for submission as a Letter for a journal.

Chapter 4: **A. Eslami**, I.A. Frigaard and S.M. Taghavi. "Viscoplastic fluid displacement flows in horizontal channels: Numerical simulations". Journal of Non-Newtonian Fluid Mechanics 249, 79-96 (2017).

Chapter 5: **A. Eslami**, R. Mollaabbasi, A.Roustaei, S.M. Taghavi. "Pressure-driven displacement flows of yield stress fluids: Viscosity ratio effects". Canadian Journal of Chemical Engineering (https://doi.org/10.1002/cjce.23597).

Moreover, fruitful collaboration occurred during the research for this thesis, and their results are presented as articles:

(1) A. Amiri, **A. Eslami**, R. Mollaabbasi, F. Larachi, S.M. Taghavi. "Removal of a yield stress fluid by a heavier Newtonian fluid in a vertical pipe". Journal of Non-Newtonian Fluid Mechanics 268, (2019) 81–100.

(2) J. Greener, M. Parvinzadeh Gashti, **A. Eslami**, M.P. Zarabadi, S.M. Taghavi. "A microfluidic method and custom model for continuous, non-intrusive biofilm viscosity measurements under different nutrient conditions". Biomicrofluidics 10 (6), 064107 (2016).

Besides, some of the extracted results were presented in the following refereed conference proceedings:

(1) **A. Eslami**, S.M. Taghavi. "Removal of yield stress fluids from rectangular channels". 8th Viscoplastic Fluids: from Theory to Application (VPF8), Cambridge, London, United Kingdom, September 16-20, 2019.

(2) **A. Eslami**, R. Mollaabbasi, S.M. Taghavi. "Effects of viscosity ratio and channel inclination on displacement of viscoplastic fluids: Numerical and analytical approaches". 29th Interamerican Congress of Chemical Engineering Incorporating the 68th Canadian Chemical Engineering Conference (CSCHE), Toronto, Canada, October 28-31, 2018.

(3) **A. Eslami**, S.M. Taghavi. "Effects of wetting on the viscous fingering of non-Newtonian fluids". 29th Interamerican Congress of Chemical Engineering Incorporating the 68th Canadian Chemical Engineering Conference (CSCHE), Toronto, Canada, October 28-31, 2018.

(4) **A. Eslami**, R. Mollaabbasi, S.M. Taghavi. "Effects of a channel inclination on displacements of viscoplastic fluids". Canadian Society for Mechanical Engineers (CSME) International Congress, Toronto, Canada, May 27-30, 2018.

(5) **A. Eslami**, A. Shevelly, N. Podduturi, K. Alba, I. Frigaard, S.M. Taghavi. "Buoyant displacement flows of viscoplastic fluids in horizontal channels". 23rd Annual Conference of the CFD Society of Canada (CFDSC), Waterloo, Canada, June 7-10, 2015.

(6) A. Shevelly, N. Podduturi, **A. Eslami**, S.M. Taghavi, K. Alba. "High density difference buoyant displacement flows in an inclined 2D channel". 23rd Annual Conference of the CFD Society of Canada (CFDSC), Waterloo, Canada, June 7-10, 2015.

(7) **A. Eslami**, K. Alba, I. Frigaard, S.M. Taghavi. "Numerical simulation of a displacement flow of a viscoplastic fluid'. 25th Canadian Congress of Applied Mechanics (CANCAM) London, Ontario, Canada, May 31 - June 4, 2015.

Introduction

Displacement flows through confined geometries are one of the most fascinating interfacial flows, from both practical and physical points of view. These flows are observed in numerous industrial applications such as removal of drilling mud by cement slurry in oil and gas well completion processes, cleaning of paraffin of waxy crude oil from pipelines, cleaning of food processing equipment, biofilm removal and cleaning of processing machinery, etc. The fluids involved in the aforementioned fluid flow systems can have various properties, e.g., different viscosities, densities, rheology behaviours; also, they appear in various flow geometries, including channels, pipes, annuli, ducts, etc. In many displacement processes, the removal of a gel material (i.e., typically viscoplastic) from interior geometries (e.g., pipes and channels) is of interest. This Ph.D. thesis studies the displacement of viscoplastic fluids in confined narrow channels.

The outline of this Ph.D. thesis is as follows. The relevant literature, the problem statement, the objectives and the general methodology are explained in the *Introduction* section. *Chapter* 1 experimentally looks into the effects of the complex rheology on the displacement fluids in narrow channels. *Chapter* 2 is closely related to *Chapter* 1 by considering impacts of wettability on viscoplastic displacement flows. The influences of the flow geometry on viscoplastic displacements are discussed experimentally in *Chapter* 3. In *Chapter* 4, the displacement of a viscoplastic fluid by a Newtonian fluid in a 2D channel is investigated numerically. *Chapter* 5 numerically presents the impacts of a viscosity ratio on displacement flows in a 2D channel. The thesis is wrapped up in the *Conclusion* section by highlighting the novel contributions of the thesis and the future perspectives.

I. Newtonian displacement flows

Even the displacement of simple fluids, i.e., Newtonian fluids, includes a considerable number of phenomena and forces. Expectedly, this number increases for viscoplastic displacement systems. Therefore, before moving onto analyzing viscoplastic displacements, it is useful to initially analyze Newtonian displacement flows, as carried out in this section.

One of the proper examples of displacement flows is an oil recovery process, in which water or gas is injected into a reservoir to displace oil and drive it towards the production well. During this displacement process, some fingers are formed at the interface of the fluids. Development of these fingers leads to a decrease in the sweep efficiency, i.e., the oil recovery efficiency. These fingers occur due to a fluid flow instability and they are formed when a less viscous fluid displaces a more viscous fluid. Therefore, they are called the *viscous fingering* instability. Since such fingers have a significant role on the efficiency of the displacement/removal of the displaced fluid, our focus in this section is mainly on various parameters which affect the viscous fingering features.

The viscous fingering phenomenon generally refers to the evolution of instabilities that take place during the displacement of fluids through a traditional Hele-Shaw cell or a porous medium, when a less viscous fluid pushes a more viscous one. This instability is noticed as a representative of interfacial pattern formations, for which the interface between the fluids becomes unstable and consequently a variety of finger-like interfacial patterns are formed. The Hele-Shaw cell is a suitable simple setup to analyze the interfacial instabilities which can provide significant insights into the fundamental aspects of flow pattern morphologies (78; 41). The Hele-Shaw cell is usually made of two parallel flat plates with a small gap thickness. There exists two very common types of Hele-Shaw cells, i.e., the rectangular cross-section cell and the radial cell (see Table I).

Ref.	**Cell type**	**Gap thickness (m)**	**Displacing fluid**	**Displaced fluid**
(34)	Rectangular	0.001	Air	Silicone oil
(10)	Radial	0.000254	Water	Glycerol
(7)	Rectangular	0.002	Polyacrylamide	Silicone oil
(1)	Rectangular	0.0005	Air or silicone oil	Oil or water
(19)	Rectangular	0.00075 – 0.00143	Air	Polystyrene and oil
(18)	Rectangular	0.000254 – 0.00143	Air	Silicone oil
(33)	Rectangular	0.003	Water	Sodium dodecyl sulphate
(44)	Rectangular	0.0005 – 0.002	Air	PPG silica suspension
(60)	Rectangular	0.00025 – 0.00075	Air	Polymer gel
(60)	Radial	0.00025	Air	Polymer gel
(8)	Radial	0.0003	Kerosene	Glycerin
(57)	Rectangular	0.000125 – 0.001	Air	Polymer gel or foam
(45)	Rectangular	0.0005	Air	HPMC polymer
(97)	Rectangular	0.0015 – 0.0046	Nitrogen gas	Paraffin oil
(52)	Radial	0.0003	Water	Clay
(17)	Radial	0.000075	Oil or water	Glycerin
(21)	Rectangular	0.001	Nitrogen gas	Paraffin oil
(81)	Rectangular	0.00079	Air	Silicone oil

Table I – The characteristics of Hele-Shaw cell and type of fluids in the literature.

The viscous fingering instability has been initially studied by Hill *et al.* (40) in a vertical rectangular Hele-Shaw cell. The fluids involved in their experimental studies had different viscosities and densities, for which both the gravity force and the viscosity contrast result in the formation of the interfacial instabilities. They observed three different flow configurations based on the interface between two fluids: an inherently stable, an inherently unstable and finally a stable flow. These flow configurations are influenced by the velocity value. In 1958, Saffman and Taylor (77), experimentally and theoretically, studied the immiscible displacements of a viscous fluid (glycerin or oil) by another fluid (air, water) in a horizontal rectangular Hele-Shaw cell wherein the two fluids were immiscible. They found that the interface between the fluids is unstable and accordingly the fingering pattern is formed. They also proposed that the flow of two fluids in the Hele-Shaw cell is two-dimensional and the interface between two fluids is a line. They assumed that the pressure of the displacing fluid, air, is uniform and the viscous fluid flow follows Darcy's law (as explained below) and the nonlinearities of the system arise from the boundary conditions of the interface. They mentioned that when the surface tension value is zero, the interface is unstable for a wide range of velocities (9). Chuoke *et al.* (20) extended the work of Hill *et al.* (40) by considering the surface tension and indicated that the instability can occur for all the velocities larger than a critical velocity. They succeeded to decompose the perturbed interface into fundamental Fourier perturbation modes. Note that as Saffman and Taylor were one of the first researchers who experimentally and theoretically studied the viscous fingering instability, the term *Saffman-Taylor* instability is also frequently used to describe the phenomena explained.

As mentioned above, the investigation of the viscous fingering instability has initially focused on the immiscible Newtonian fluid flows in the uniform rectangular Hele-Shaw cells. However, due to its large number of industrial applications, analyzing the viscous fingering instability has been extended to include various conditions, e.g., non-Newtonian fluids, miscible fluids, radial Hele-Shaw cells, etc. The aforementioned parameters have remarkable impacts on the flow patterns, which we will explain in the following sections in more detail. For instance, Fig. I shows three examples of viscous fingering instability patterns at different conditions.

I.1 Darcy's Law

For Newtonian flows in confined geometries, the relation between the average velocity (i.e., averaged over the gap thickness) and the applied pressure gradient can be explained by the Hele-Shaw flow theory (41). Here, the gap thickness between the solid walls is very small. In the case of Newtonian fluids, the fluid motion in the Hele-Shaw cell (quasi-two-dimensional cell) is described by Darcy's law, which relates the two-dimensional averaged velocity across

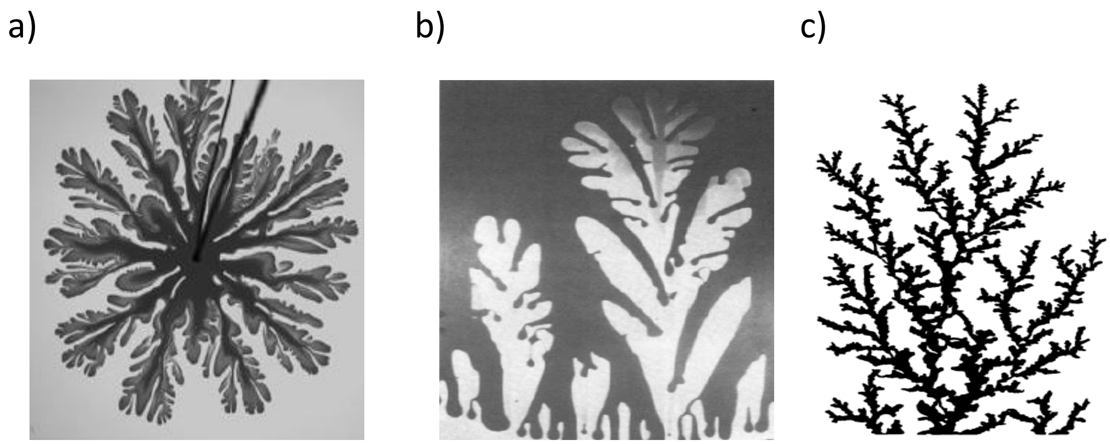

FIGURE I – Various viscous fingering patterns in Hele-Shaw cells. (a) Miscible Newtonian fluid in a radial geometry (10). (b) Immiscible Newtonian fluid in a vertical cell (62). (c) Miscible non-Newtonian fluid in a horizontal rectangular cell (88).

the gap $\hat{v}$ [1] to the local pressure $\hat{p}$:

$$\hat{v} = -\frac{\hat{b}^2}{12\hat{\mu}}\nabla\hat{p}, \tag{1}$$

where $\hat{b}$ and $\hat{\mu}$ are the gap thickness and shear viscosity, respectively. The other governing equation is:

$$\nabla.\hat{v} = 0. \tag{2}$$

Since the two fluids are incompressible, the pressure field satisfies Laplace's equation:

$$\nabla^2\hat{p} = 0. \tag{3}$$

The Young-Laplace equation can be employed to consider the pressure jump across the interface:

$$\Delta\hat{p} = \hat{\sigma}\left(1/\hat{R}_1 + 1/\hat{R}_2\right), \tag{4}$$

where $\hat{\sigma}$, $\hat{R}_1$ and $\hat{R}_2$ denote the surface tension, the radius of the interface curvature in the direction perpendicular to the parallel plates and in the plane of motion, respectively. In addition, Mclean and Saffman (63) showed that by considering $1/\hat{R}_1 \approx 2/\hat{b}$, the pressure drop at the finger interface turns into:

$$\Delta\hat{p} = \frac{\hat{\sigma}}{\hat{R}_2} + \frac{2\hat{\sigma}}{\hat{b}}\cos\theta, \tag{5}$$

where θ is the contact angle of the meniscus. As the gap thickness of the cell $(\hat{b})$ is much smaller than the cell width $(\hat{W})$, the larger radius of curvature $(\hat{R}_2)$ has a negligible impact on the flow (9; 92). Therefore, the pressure jump over the interface can be simplified to $\Delta\hat{p} = 2\hat{\sigma}/\hat{b}$.

1. In this thesis, we adopt the convention of denoting dimensional quantities with the ˆ symbol and dimensionless quantities without ˆ symbol.

Several studies have been carried out on the applicability of Darcy's law for various flow features in Newtonian fluids by considering the inertial effects (36; 76), the wall wetting film thickness (67) and the interface shape (81). For example, Park and Homsy (67) derived an expression for the Young-Laplace equation, for the pressure drop across the interface, in which the impact of a wetting film thickness was taken into account. They proposed that when the displaced fluid wets the cell, the pressure drop depends also on the local capillary number ($Ca = \frac{\hat{\mu}\hat{U}}{\hat{\sigma}}$). This equation can be expressed as:

$$\Delta\hat{p} = \frac{2\hat{\sigma}}{\hat{b}}(1 + 3.8Ca^{2/3}) + \frac{\hat{\sigma}}{\hat{R}_2}(\frac{\pi}{4} + O(Ca^{2/3})). \tag{6}$$

I.2 Displacement efficiency and finger width

The fluid displacement efficiency is one of the most important parameters with regard to displacement applications. The fluid displacement efficiency or sweep recovery is defined as the fractional surface (or volume) of the displaced fluid pushed by the displacing fluid. The efficiency of such displacement depends on many flow parameters, including the physical properties of the fluids, the injection velocity, the geometry condition, etc. For analyzing the sweep recovery in the Saffman-Taylor instability, the finger width ($\hat{w}$) or the relative finger width ($\lambda = \hat{w}/\hat{W}$) has been used. The finger width value is changed by various conditions. For example, Saffman and Taylor (77) have shown that $\hat{w}$ is inversely proportional to the displacing finger tip velocity ($\hat{U}$). Furthermore, they and other researchers have demonstrated that the relative finger width (λ) reaches a plateau value of ~ 1/2 at higher velocities (41; 46; 77).

The capillary number ($Ca = \frac{\hat{\mu}\hat{U}}{\hat{\sigma}}$), representing the viscous force to the capillary force, is an important dimensionless parameter affecting the width of a displacing finger. The finger width is a result of the competition between viscous forces and capillary forces in a way that the viscous forces narrow the finger, while capillary forces enhance the finger width (12; 58). In the Newtonian viscous fingering instability, using $1/B$ as a control parameter results in the collapse of all finger widths onto the same universal curve (87; 77; 9). $1/B$ is expressed as a function of the capillary number and the aspect ratio of the cell:

$$1/B = Ca\delta^2, \tag{7}$$

where $\delta = \hat{W}/\hat{b}$ is the aspect ratio of the Hele-Shaw cell.

It has been shown that all the relative finger width versus $1/B$ for different aspect ratios and viscosities collapse onto a master curve and λ monotonically decreases by $Ca\delta^2$. Nevertheless, Moore *et al.* (66) showed that, for larger aspect ratios, λ displays a maximum as the capillary number is decreased. Also, unlike the previous studies, they indicated that the data points do not fall into the master curve when $\delta \geq 250$.

Recently, de Lozar *et al.* (23) experimentally studied the effects of the aspect ratio on the finger width for non-negligible gravitational effects. In their experiments air was injected into rectangular cells filled by silicon oil. The aspect ratio of the cell varied from 1 (square cross-section channel) to 15 (rectangular cross-section channel). They plotted the relative finger width λ versus the control parameter $1/B$ for different aspect ratios. They showed that when the effect of buoyancy is not negligible, all λ fall on the mater curve for larger aspect ratios. However, their results reveal that the relative finger widths for non-negligible gravitational effects cannot collapse onto a single curve when the aspect ratio is small ($\delta \leq 6$).

I.3 Inertia effect

In the past several decades, a vast majority of the experimental and theoretical studies of the Saffman-Taylor instability in the Hele-Shaw cell have assumed that the inertia effects are negligible; therefore they have assumed that only the balance between the capillary force and the viscous force (quantified by Ca) in the Newtonian fluids controls the finger width value. The Reynolds number ($Re = \frac{\hat{\rho}\hat{U}\hat{b}}{\hat{\mu}}$) is one of the suitable dimensionless numbers to consider the inertia effect in this type of flow, representing the ratio of inertial forces to viscous forces. In the definition of the Reynolds number, $\hat{\mu}$ and $\hat{\rho}$ are the viscosity and the density of the displaced fluid, respectively.

A few attempts have been made in order to show the influences of the inertia on the viscous fingering instability. Gondret and Rabaud (36) and Ruyer (76) have modified Darcy's law by considering the inertia effects for Newtonian fluids. He and Belmonte (39) showed that the inertia effect has a tendency to stabilize the interface. They mentioned that even a relatively small inertia may contribute to stabilize the interface and suppressing disturbances. Additionally, a small value of inertia does not make a dramatic modification on the Saffman-Taylor instability; however, no clear conclusion could be obtained at large inertial effects (39).

Chevalier *et al.* (18) experimentally studied the effect of inertia on the finger width in the Hele-Shaw cell. They demonstrated that the inertia force in immiscible Newtonian displacement flows leads to widening the fingers. They indicated that the effect of inertia on the Saffman-Taylor instability becomes important for higher values of Re where the viscosity of the displaced fluid is low and the gap thickness of the Hele-Shaw cell is high. In addition, they showed that for higher values of the Reynolds numbers the experimental finger width data-points cannot be rescaled using the classical control parameter ($1/B$). Recently, the work of Chevalier *et al.* (18) has been extended to non-Newtonian fluids by considering high imposed velocities, demonstrating that inertia has a significant impact on the finger width (31; 32).

I.4 Miscibility (mixing) and immiscibility (surface tension)

When both the displacing and displaced fluids are immiscible ($\hat{\sigma} > 0$), the viscosity and concentration remain constant in each phase and therefore, a pressure jump at the interface should be considered. However, there is no sharp interface between two fluids when they are miscible ($\hat{\sigma} = 0$) and accordingly the diffusion and mixing between two fluids are important in the miscible case (91). The dimensionless Péclet number ($Pe = \frac{\hat{U}\hat{b}}{\hat{D}}$) is an appropriate parameter in this case, where $\hat{D}$ is the diffusion coefficient. Pe can be used to evaluate the effects of advective transport and molecular diffusion on the displacement efficiency. Diffusion between two fluids becomes important when the Péclet number is small, while at large Péclet number, the degree of molecular diffusive transport compared to advective transport is very small. In other words, larger values of Pe imply that the displacing and displaced fluids do not have enough time to mix over the time scale of interest. Petitjeans and Maxworthy (71) showed that at larger Peclet numbers ($Pe > 1000$) a sharp interface between the two fluids is formed. This makes it possible to draw a comparison between immiscible and miscible fluids in a tube geometry. It means that for $Pe \to \infty$, the flow tends to the immiscible limit at $\hat{\sigma} = 0$. Therefore, although the miscible flow is fundamentally different from an immiscible one, the miscible flow at large Pe may resemble an immiscible flow at $Ca \to \infty$ (83).

The displacement flow patterns for both miscible and immiscible fluids have been compared by Chen (16), for flows in radial Hele-Shaw cells at the same flow rate. Fig. IIa, b and c illustrate the flow patterns of miscible viscous fingering wherein glycerin is displaced by water. As can be seen, at different flow rates, there is not much difference in the morphology of fingers. However, the flow rate has a notable impact on the immiscible fingering pattern (Fig. IId, e and f), where oil displaces glycerin. As seen, by increasing the flow rate the fingers become narrow at smaller flow rates and also at larger flow rates, a side branching pattern is formed.

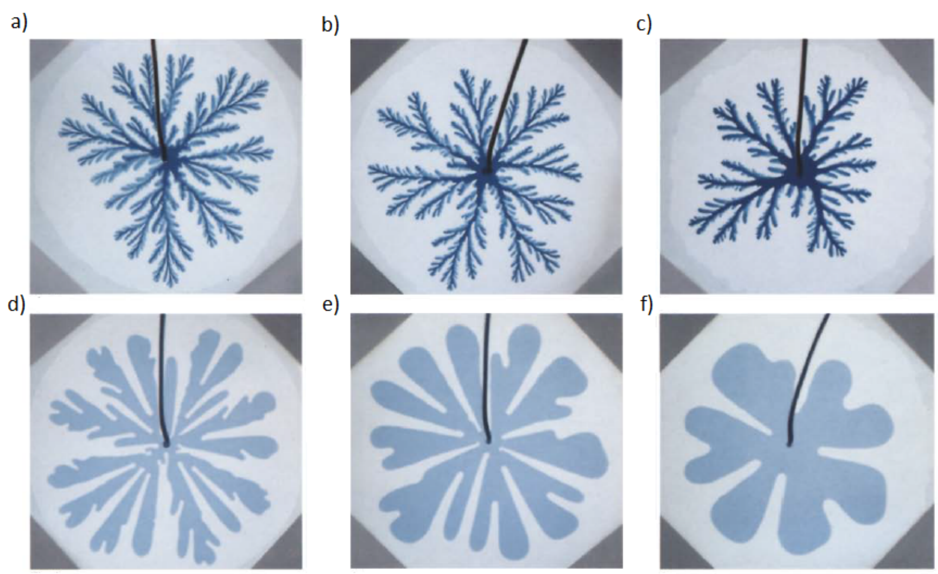

FIGURE II – Miscible viscous fingering when dyed water displaces glycerin in a Hele-Shaw cell. (a) $q = 0.002$ ml/s, (b) $q = 0.00054$ ml/s and (c) $q = 0.00014$ ml/s. Immiscible viscous fingering when dyed oil displaces glycerin in a Hele-Shaw cell. (d) $q = 0.002$ ml/s, (e) $q = 0.00054$ ml/s and (f) $q = 0.00014$ ml/s (16).

Chen *et al.* (15) have studied numerically the miscible displacement flow in tubes. They mentioned that both Pe and a viscous Atwood number ($At_\mu = \frac{\hat{\mu}_2 - \hat{\mu}_1}{\hat{\mu}_2 + \hat{\mu}_1}$) control the displacement flow features such as the concentration profiles of the fluids. In the definition of the viscous Atwood number, $\hat{\mu}_2$ and $\hat{\mu}_1$ denote the viscosity of displaced and displacing fluids, respectively. Their findings have been confirmed by Lajeunesse *et al.* (50; 51), experimentally and theoretically. They demonstrated that, at high Pe, the finger shape and also the concentration profile during miscible displacement flows depend on the viscosity ratio. They indicated that when the viscosity ratio is smaller than a critical value, the shape of the interface between the fluids resembles a symmetric tongue across the gap. However, when the viscosity ratio is larger than the critical value ($\frac{\hat{\mu}_2}{\hat{\mu}_1} > 1.5$), a different finger pattern is formed.

I.5 Residual wetting layers

One of the crucial aspects associated to displacements is the formation of residual layers or wetting films of the displaced fluid on the solid surfaces. Generally, during the displacement of a high viscous wetting fluid by a less viscous non-wetting fluid, the advancing finger leaves behind a wetting film of the displaced fluid on the solid wall of the flow geometry. Fig. III shows that the interface between the displacing fluid (fluid 1) and the displaced fluid (fluid 2) is a meniscus in a three-dimensional plane. As seen, there exist residual wetting layers in both the lower and upper walls of the cell.

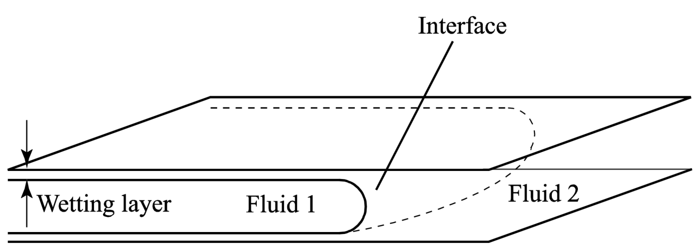

Figure III – Schematic view of the propagation of a single finger in a Hele-Shaw cell which produces a film behind the finger (84).

The thickness of the wetting film has been the subject of many studies. For example, Bretherton (14) theoretically determined the film residual behind a flat interface for a Newtonian fluid flowing in capillary tubes. He found that the film is uniform and thin, and also is a function of $Ca^{2/3}$. The film thickness ($\hat{t}$) can be calculated from equation (8) based on the Bretherton's law, which is also confirmed experimentally by Taylor (85) for small capillary numbers ($Ca < 0.001$):

$$\frac{\hat{t}}{\hat{R}} = 1.34(Ca)^{\frac{2}{3}}, \tag{8}$$

where $\hat{R}$ denotes the radius of the tube. However, the film thickness in the Hele-Shaw cell may not be uniform as a result of the normal velocity variation along the interface (67; 82); consequently, the finger moves in the cell with a non-uniform gap thickness. Tabeling *et al.* (81; 82) experimentally measured the film thickness for the displacement of silicon oil by air in a uniform Hele-Shaw cell. They indicated that the film thickness value influences the finger width particularly at higher velocities (for more information on film/biofilm formation in micro cells see (4; 37; 38)).

Aussillous and Quéré (6) have extend the Bretherton's theory to a wider range of capillary numbers (Ca up to 2) by considering the wetting film thickness in defining the curvature at the displacing finger front:

$$\frac{\hat{t}}{\hat{R}} = \frac{1.34Ca^{2/3}}{1 + 3.35Ca^{2/3}}. \tag{9}$$

There are several studies of displacement of miscible and immiscible fluids in various flow geometries which draw our attention to the thickness of the residual wetting layers and the fact that the finger width is controlled by the film thickness left at the walls during the displacement. For example, for immiscible flows, Magnini *et al.* (59) and Atasi *et al.* (5) have examined the impacts of buoyancy on the film thickness through a vertical and horizontal long circular cross-section tubes, respectively. de Lozar *et al.* (23) and de Lozar *et al.* (24) have studied the effects of the capillary number and the tube aspect ratio on the residual layer on the displacement of viscous fluid by air through rectangular cross-section tubes experimentally and theoretically. Petitjeans and Maxworthy (71) measured the amount of residual layers on the solid walls during the displacement of miscible fluids in both vertical and horizontal tubes as a function of At_μ and Pe. Their results displayed that the amount of residual layers is enhanced by increasing At_μ. Kuang*et al.* (49) experimentally showed that, at larger values of Pe, the fractional volume of the more viscous fluid left on the solid walls is constant and only depends on the viscous Atwood number.

I.6 Flow geometry and control of instability

In the literature of displacement flows, there are several studies where the influences of geometrical perturbations on the viscous fingering instability flows have been investigated, for instance by adding a thin wire inside the Hele-Shaw cell (99; 75), grooving in the top/bottom solid walls of the channel (75) and also adding a gradient to the gap of a cell (97).

Zhao *et al.* (97) have experimentally investigated the effects of a linear variation of the gap thickness on the viscous fingering instability in a non-uniform Hele-Shaw cell (tapered cell). They have shown that the finger morphology is affected by the gap gradient (b') in a way that the single finger becomes stable/unstable according to the sign of the gap gradient. At a given condition, when $b' < 0$ the finger has sharper tip while for $b' > 0$ the finger exhibits a flattened tip. However, for $b' = 0$ the displacing finger tip splitting occurs. Dias and Miranda (25) have theoretically studied the impacts of a small gap gradient on the stability of the interface; they have mentioned that tapered the Hele-Shaw cell is a simple geometric way to control the development of interfacial fingering instabilities.

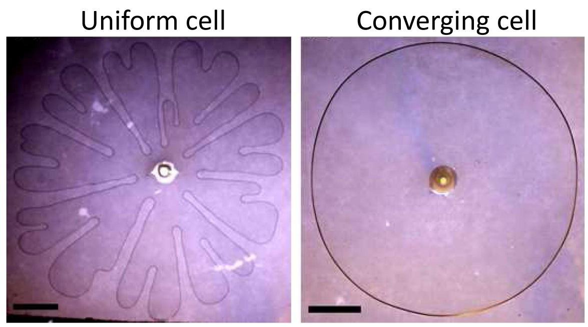

FIGURE IV – Experimental snapshots of viscous fingering: (a) Uniform cell and (b) Converging cell (84).

The effect of the depth gradients on the onset of interfacial instabilities for fluid displacements in the rectangular cross-section cell was conducted by Al-Housseiny *et al.* (1). In order to control of the interfacial instabilities, they employed the tapered geometries. They demonstrated that the variable vertical radius of the Young-Laplace equation leads to changes in the dispersion relation and consequently the interface between the fluids can be stable below/above a critical capillary number based on the sign of the gap gradient. They mentioned that for capillary numbers lower than the critical value the negative depth gradient removes the fingering and thus the interface between the fluids becomes stable, while for higher values of the critical capillary number the interface is unstable.

Recently, Bongrand and Tsai (11) experimentally studied the effects of a radial depth gradient in the radial Hele-Shaw cell for the the viscous fingering instability. They observed that when a less viscous fluid moves a more viscous fluid in a converging radial cell, unlike the traditional homogeneous passages, the interface can be stabilized (see Fig. IV).

I.7 Wettability

It has been shown that the wetting properties of the flow geometry can vary remarkably depending on the type of solid surfaces and fluids (96). Wettability describes the fluids' affinity to the solid surface. Due to complex interactions of fluid-solid surfaces (liquid-confining walls), much of the literature on displacement flows has focused on the rheology of fluids and conditions of the flow. However, the impacts of wettability on displacements have not been well understood. In fact, the majority of the Saffman-Taylor instability studies have considered non-wetting flows where the displaced fluid preferentially wets the cell.

The wettability can stabilize the displacement flow, in particular, at very low imposed velocity. Trojer *et al.* (86) experimentally showed the stabilizing effects of wettability at lower capillary numbers in granular media. They found that wettability delays the development of instabilities to higher values of the capillary number. Jung *et al.* (43) demonstrated that the interface between two fluids (immiscible flows) remains smooth and stable when the displacing fluid wets the medium. Furthermore, Stokes *et al.* (79) mentioned that when the displacing fluid preferentially wets the solid surfaces, the finger width is larger than when the displaced fluid wets the medium.

It is necessary to emphasize that in the literature of multiphase flows in porous media, the wetting and non-wetting displacing fluids are referred to as imbibition and drainage regimes, respectively. In other words, the drainage (imbibition) refers to the case where the advancing fluid wets the solid surface less (more) than the displaced fluid (96; 79).

To wrap up this section, let us classify the parameters affecting displacement in the Saffman-Taylor instability in two main groups. The first group includes the parameters that are related to the flow, i.e., gap thickness, aspect ratio and flow velocity. The second group has direct relations with physico-chemical nature of the fluids, i.e., interfacial tension, wettability and rheological behaviours (for example viscosity of the fluids). We have so far reviewed the effects of most of the aforementioned parameters, except rheological behaviours, on displacement flows. Non-Newtonian fluid behaviours and also their rheological impacts on the displacement flows are the subject of the following sections.

A reader already familiar with non-Newtonian rheology can skip the next section.

II. Non-Newtonian fluids

The rheological behaviours of non-Newtonian fluids are different from Newtonian fluids. In Newtonian fluids, the relation between the shear stress and the shear rate is linear while this relation in non-Newtonian fluids is more complicated. The rheological behaviours of non-Newtonian fluids affect the fluid displacement efficiency and the displacement morphology. In order to better understand non-Newtonian fluid displacement flows, analyzing the rheological behaviours of these fluids can be useful.

II.1 Viscosity

The viscosity of a fluid is known as the fluid resistance against the flow, caused by molecular motions which lead to an internal friction. In other words, viscosity is the physical property that characterizes the flow resistance of simple fluids. Newton's viscosity law displays the relationship between the shear stress and the shear rate of a fluid as a constant, for a given temperature. However, the viscosity of non-Newtonian fluids can be a function of the shear rate and time. Although non-Newtonian fluids are grouped into various categories, here, only viscoplastic and viscoelastic fluids are briefly explained.

II.2 Viscoplastic fluids

Viscoplastic fluids exhibit a yield stress. Below a critical shear stress, a viscoplastic fluid shows solid-like characteristics. However, the fluid starts to flow as soon as the shear stress exceeds the critical stress called the yield stress. In other words, the flow curve does not pass through the origin. Therefore, the general equation for the flow curve for viscoplastic fluids can be written as $\hat{\tau} = \hat{\tau}_Y + f(\hat{\dot{\gamma}})$, where $\hat{\tau}_Y$ is the yield stress and $f(\hat{\dot{\gamma}})$ is a function of the shear rate. Rheological behaviors of viscoplastic fluids can be modeled using constitutive equations. There exist several constitutive relations to describe the rheological behaviors of viscoplastic fluids. Here, we introduce the three common ones.

Bingham Model

One of the simplest viscoplastic models is the Bingham model expressed as:

$$\hat{\dot{\gamma}} = 0 \quad \Leftrightarrow \quad \hat{\tau} \leqslant \hat{\tau}_Y, \tag{10}$$

$$\hat{\tau} = \left(\frac{\hat{\tau}_Y}{\hat{\dot{\gamma}}} + \hat{\mu}\right)\hat{\dot{\gamma}} \quad \Leftrightarrow \quad \hat{\tau} > \hat{\tau}_Y. \tag{11}$$

Herschel-Bulkley Model

The Herschel-Bulkley model extends the simple power-law model to include a yield stress as follows:

$$\hat{\dot{\gamma}} = 0 \quad \Leftrightarrow \quad \hat{\tau} \leqslant \hat{\tau}_Y, \tag{12}$$

$$\hat{\tau} = \left(\hat{\kappa}\hat{\dot{\gamma}}^{n-1} + \frac{\hat{\tau}_Y}{\hat{\dot{\gamma}}}\right)\hat{\dot{\gamma}} \quad \Leftrightarrow \quad \hat{\tau} > \hat{\tau}_Y, \tag{13}$$

where n is the power-law index and $\hat{\kappa}$ is the consistency index.

Casson Model

The Casson model describes the flow of yield-stress fluids and can be expressed as follows:

$$\hat{\dot{\gamma}} = 0 \quad \Leftrightarrow \quad \hat{\tau} \leqslant \hat{\tau}_Y, \tag{14}$$

$$\hat{\tau} = \left(\sqrt{\hat{\kappa}} + \sqrt{\frac{\hat{\tau}_Y}{\hat{\dot{\gamma}}}}\right)^2 \hat{\dot{\gamma}} \quad \Leftrightarrow \quad \hat{\tau} > \hat{\tau}_Y. \tag{15}$$

The Casson model can exhibit behaviors of yield and shear-thinning non-Newtonian fluids.

II.3 Viscoelastic fluid

Viscoelasticity is a feature of materials showing both viscous and elastic behaviours. Elasticity can be defined as the tendency of solid materials to return to their original shape after removing the external force. The elastic and viscous behaviours of materials can be defined based on the Hooke's law and Newton's law, respectively. The ideally elastic behaviour follows Hooke's law: $\hat{\tau} = \hat{G}\hat{\gamma}$, where $\hat{G}$ and $\hat{\gamma}$ denote the shear modulus and the shear strain, respectively. The value of the shear modulus of ideally elastic materials is independent of the value and duration of the applied shear load. Moreover, it is known that internal stresses are functions of the shear rate and the shear strain for a purely viscous material and a purely elastic material, respectively. However, for viscoelastic materials, internal stresses are functions of deformation (shear strain, shear rate). There are several models, such as the Maxwell model, which can provide a description for the behaviour of viscoelastic materials.

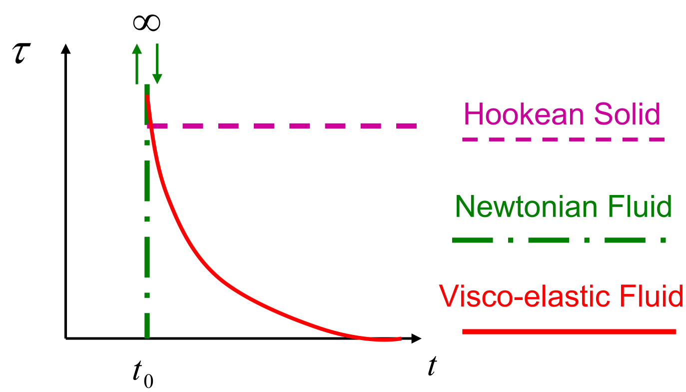

FIGURE V – Response to stress relaxation test where a shear strain is suddenly applied on materials (42).

The Maxwell model is constructed by the combination of linear conventional mechanical elements which represent purely viscous and purely elastic properties (64). Fig. V demonstrates the response to a stress relaxation test where a shear strain is suddenly applied on the samples. As seen, for a Newtonian fluid (i.e., purely viscous fluid) the relaxation time of stress is zero. For a Hookean solid sample (i.e., purely elastic material) the relaxation time is infinity. For a Maxwell fluid, the initial stress response is purely elastic then is exponentially decreased with time till reaches a plateau value (42). Note that the linear Maxwell model is valid for smaller values of the applied deformation.

III. Non-Newtonian displacement flows

In subsection II, we explained Newtonian displacement flow features (focusing on the viscous fingering instability) and their characteristics. However, the majority of practical fluids exhibit non-Newtonian behaviours. Examples include drilling fluids, fresh concretes, detergents, cosmetics, sauces, etc. Due to complex rheological behaviours, the displacement flows in general, and the viscous fingering problem in particular, are not well understood for non-Newtonian fluids (61). In this section, we focus on the effects of non-Newtonian behaviours on the viscous fingering problem.

This section aims to provide a better understanding about the influences of non-Newtonian rheological behaviours, i.e., yield stress, shear-thinning and viscoelastic behaviours on the pattern formation and the finger width. Nevertheless, before going into details, it is worth looking at general impacts of considering a non-Newtonian fluid as the displaced fluid in place of a Newtonian fluid. For instance, Fig. VI shows that the flow patterns in Newtonian and non-Newtonian flows are formed in completely different morphologies.

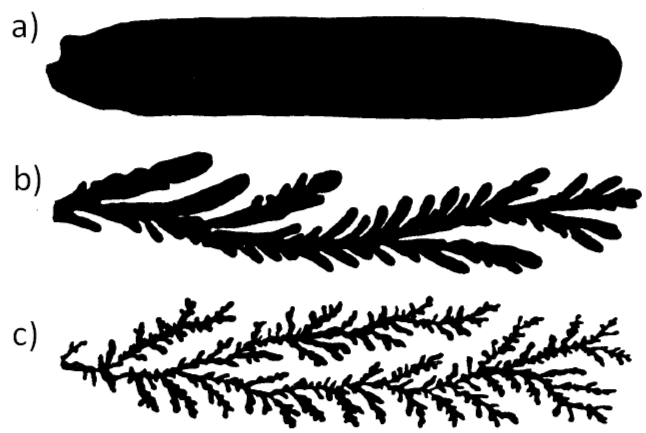

FIGURE VI – Viscous fingering pattern in a Hele-Shaw cell. (a) Newtonian fluid at low velocity. (b) Newtonian fluid at high velocity. (c) Non-Newtonian fluid at low velocity (90).

III.1 Viscous fingering of yield-stress fluids

The yield stress affects the stability of the interface and accordingly the pattern formation and the finger width are changed. Since there is a non-linear relation between the pressure gradient and the velocity for these fluids, the yield stress effect should be taken into account in Darcy's law for viscoplastic fluids (94). Note that the initial investigation into instability of the interface for the displacement of viscoplastic fluids in porous media has been done by Pascal (69; 68; 70) which provide an insight about the complex nature of these flows.

In an experimental study of the viscous fingering instability in the Hele-Shaw cell using a commercial hair gel, Lindner *et al.* (57) have been first to specify the yield stress regime during the displacement of viscoplastic fluids by air. They have backed up their interesting experimental results with their theoretical results from an earlier paper (22). Lindner *et al.* (57) have found two different flow patterns for yield stress fluids. In the first regime, at low velocity, the finger tip-splitting occurs (Fig. VIIa) which means that there is more than one finger in the cell. However, at high velocities, there is one finger in the middle of the cell (Fig. VIIb).

The variation of the finger width versus the velocity for the regimes discussed is shown in Fig. VIIc. In the first regime (tip-splitting pattern), the mean finger width is independent of the finger velocity whereas, in the second regime, the finger width depends on the finger velocity (one finger pattern). Maleki *et al.* (60) have also observed three different flow patterns during yield stress displacement flows in both circular and rectangular Hele-Shaw cells.

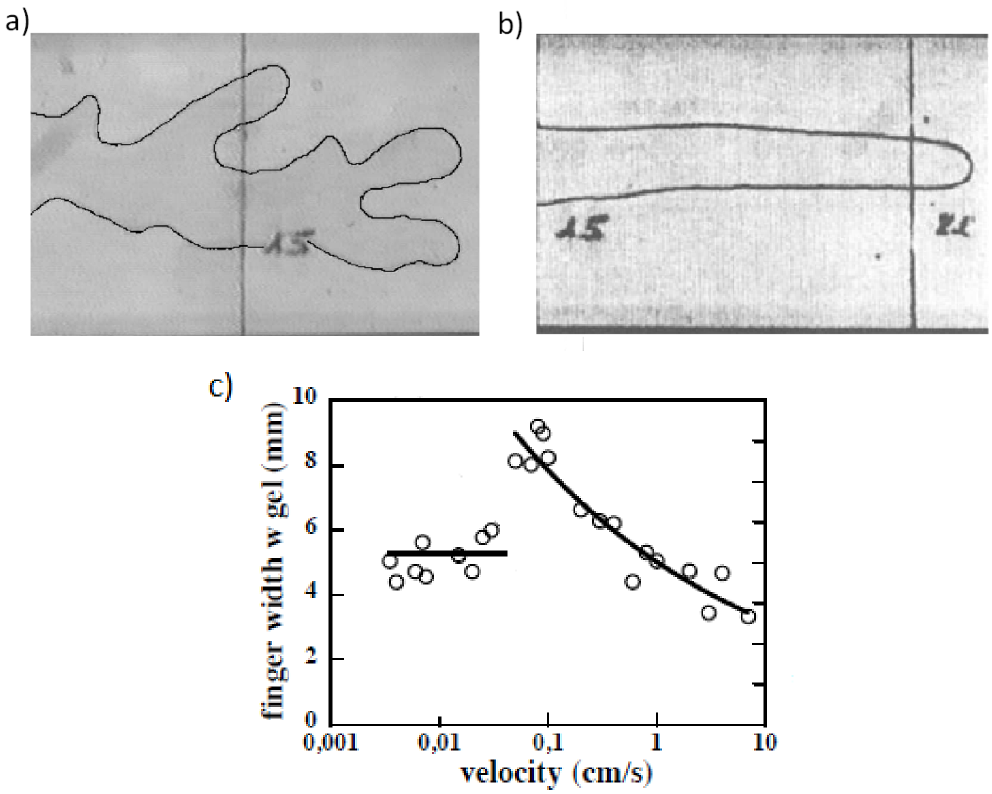

FIGURE VII – Experimental snapshots of the viscous fingers: (a) low velocities and (b) high velocity. (c) The variation of finger width versus finger velocity for yield stress fluid (57; 58).

Residual layers

As already mentioned for Newtonian fluids, during displacement flows, the displaced fluid wets the walls and the displacing one leaves behind a residual thin film of the displaced fluid on the walls. The thickness of this film notably affects the flow and it is a function of the capillary number whereas the thickness of the residual layers for viscoplastic fluids is a function of the capillary and Bingham numbers (31).

Poslinski *et al.* (74) experimentally studied the displacement of a viscoplastic fluid by air in a horizontal tube and found that the film thickness is much larger compared to that in Newtonian fluids and it can increase up to 0.35 of the tube radius at high air flow rates. Eslami *et al.* (31) demonstrated that the mean residual layer thickness in viscoplastic fluid flows is larger than their Newtonian counterparts. In addition, it has been shown that the residual layer thickness for viscoplastic fluid depends on the tube geometry, finger shape and fluid properties (26). Allouche *et al.* (2) have quantified the layer film thickness in viscoplastic fluids for a 2D channel flow using combined theoretical and computational approaches. Freitas *et al.* (35) have also shown that the yield stress value has a remarkable impact on the displacement flow patterns and the residual layer thickness, decreasing the thickness by an increment in the yield stress value.

III.2 Viscous fingering of shear-thinning fluids

It is generally accepted that most of the non-Newtonian fluids exhibit more than one non-Newtonian feature. For examples, several polymer solutions demonstrate both shear-thinning behaviours and normal stress effects, which can affect the finger width in the viscous fingering instability (13); gel materials exhibit yield stress, shear-thinning and elastic effects (not always) which affect the viscous fingering instability (60). There are some studies mainly focusing on the shear-thinning effects for the viscous fingering instability (47; 48; 56; 73) wherein the relation between the viscosity and shear rate affects the flow considerably. In shear-thinning fluids the viscosity has a power-law dependency on the shear rate ($\hat{\tau} = \hat{\kappa}\hat{\dot{\gamma}}^n$).

For Xanthan solutions, as a good example of shear-thinning fluids, the viscosity decreases with an increment in the shear rate. Moreover, there is a direct relation between the viscosity and the concentration of Xanthan (56). For immiscible displacement flows (air-Xanthan solution), at a given velocity, Lindner *et al.* (56) indicated that the relative finger width decreases by increasing the Xanthan concentration and also by decreasing power-law index.

Darcy's law for shear-thinning fluids can be adapted by replacing the constant viscosity with a shear dependent viscosity ($\hat{\mu}\left(\hat{\dot{\gamma}}\right)$), which results in a modified Darcy's law (47; 48; 88; 73):

$$\hat{v} = -\frac{\hat{b}^2}{12\hat{\mu}(\hat{\dot{\gamma}})}\nabla\hat{p}. \tag{16}$$

It is worth noting that this substitution is only valid when the fluids exhibit very weakly shear-thinning effects ($n > 0.65$) (56).

Li *et al.* (53) studied miscible displacements of Alcoflood polymers (shear-thinning) by water in a rectangular Hele-Shaw cell. They observed two different flow patterns for weak and strong shear-thinning behaviours. Fig. VIIIa shows the displacement of a weakly shear-thinning solution ($n = 0.82$) by water at three flow rates. As can be seen, the fingers split into smaller ones and they become thinner at lower flow rates, while at high flow rates the tip-splitting is suppressed (see Fig. VIII a3). Nevertheless, for strongly shear-thinning solutions, the finger morphologies are fundamentally different and the fingers start to exhibit a side-branching pattern (Fig. VIIIb). Furthermore, for the latter case, the fingers are broad respect to weakly shear-thinning.

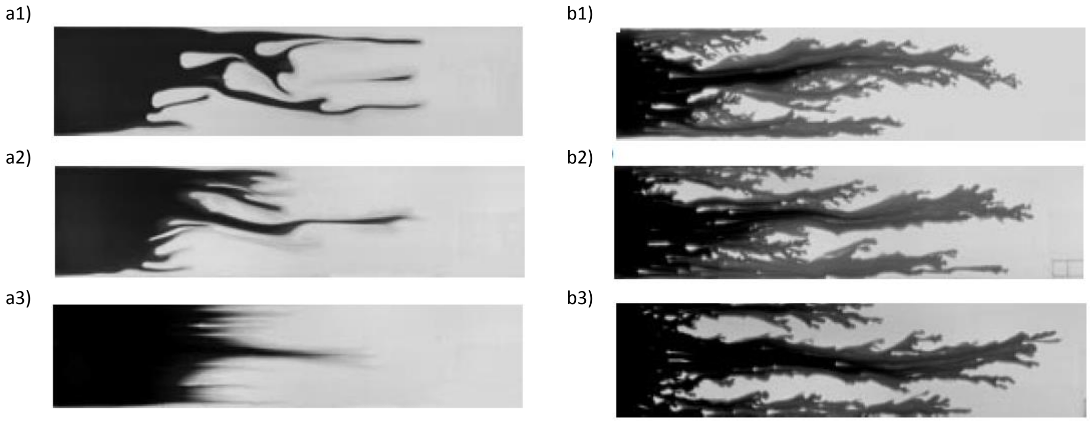

FIGURE VIII – Displacement of Alcoflood solutions by water for weakly shear-thinning n = 0.85 with injection rate of (a1) 0.431 ml/min, (a2) 2.168 ml/min and (a3) 10.790 ml/min. Displacement of Alcoflood solutions by water at flow rate rate 2.168 ml/min for strongly shear-thinning (b1) n = 0.59, (b2) n = 0.57 and (b3) n = 0.49 (53).

III.3 Viscous fingering of viscoelastic fluids

As mentioned earlier, the rheology of fluids affect the displacement flow features. In this subsection, these features are described for viscoelastic fluids. Van Damme *et al.* (89) investigated miscible displacements of clay paste (viscoelastic fluid) by water in a rectangular Hele-Shaw cell. They indicated that the elastic modulus ($\hat{G}'$) is a main parameter to control the fingering features. They showed that for viscoelastic displacement flows, by increasing the gap thickness the finger width is increased and also the finger tip-splitting is decreased. They found that the following expression can predict the finger width as a function of the elastic modulus and the gap thickness:

$$\hat{l} = \frac{\hat{b}\hat{P}^{0.5}}{12\hat{G}'^{0.5}}, \tag{17}$$

where $\hat{P}$ is the injection pressure and $\hat{l}$ denotes the finger width prediction.

Zhao and Maher (98) studied the morphology of viscoelastic fingering patterns in radial Hele-Shaw cells. In their experiment, the effects of four independent parameters on the pattern formation were investigated, including the gap thickness, the flow rate, the concentration of the displaced fluid and the molecular weight of polymers. Fig. IX illustrates some typical patterns that were formed in displacements of a viscoelastic polymer solution by water. At higher flow rates, the fingers are smoother and straighter whereas they become more branched and ramified at lower flow rates. As seen, the number of fingers for the higher molecular weight is lesser than the number of fingers for the lower molecular weight. Changing the gap thickness

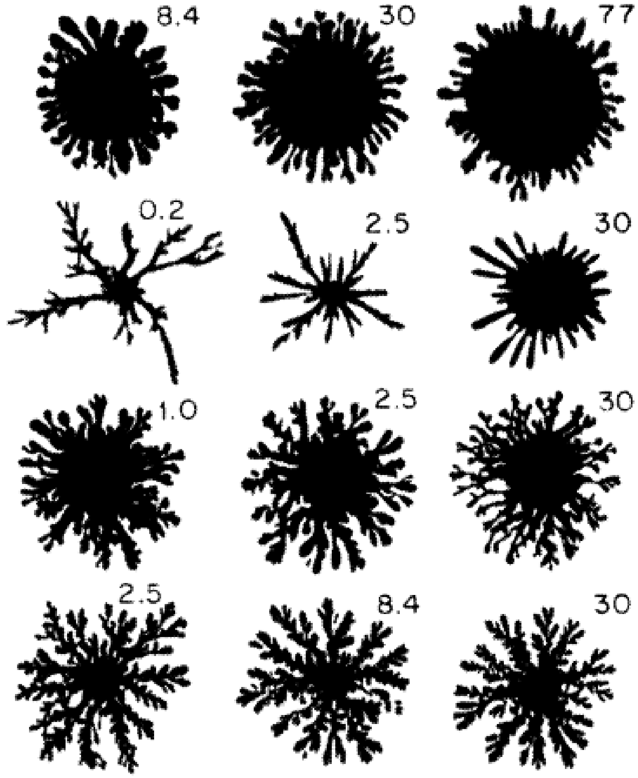

FIGURE IX – Example of typical patterns for viscoelastic fluids. For each row, the injection rate increases from low value on the left to high value on the right. The first two rows are for the high molecular weight (concentrations are 0.3 wt% and 0.8 wt%, respectively). The last two rows are for the low molecular weight (concentrations are 5 wt% and 10 wt%, respectively). $\hat{b}$ = 0.4 mm for all cases except for the first row where $\hat{b}$ = 0.8 mm. The numbers in the graph indicate the injection rates in (ml/min) (98).

does not have a significant impact on the pattern morphology. In the fourth row of the graph, where the molecular weight is low and the concentration is high, by increasing the flow rate the pattern morphology does not change.

IV. Computational Fluid Dynamics (CFD) simulation

We have so far previously reviewed the experimental approach used to study displacement flows. This section discusses numerical simulations of displacement flows using CFD approaches. There are several advantages in using CFD methods instead of experimental approaches. Some of these advantages are:

- Reducing consumed time and cost.
- Studying the flow properties without disturbing the flow.

— Investigating the effect of one parameter without the interference of the others.
— Observing the flow properties for inaccessible locations in the experiment.
— Setting the flow parameters in CFD simulations is much easier than in experiments.
— Possibility of studying the effects of several parameters simultaneously.

The relevant fluid mechanics equations can be summarized as the mass and momentum conservation equations. The conservation of mass equation is:

$$\frac{\partial \hat{\rho}}{\partial \hat{t}} + \nabla.\left(\hat{\rho}\hat{\bar{v}}\right) = 0. \tag{18}$$

The conservation of momentum equation is:

$$\frac{\partial}{\partial \hat{t}}(\hat{\rho}\hat{\bar{v}}) + \nabla.\left(\hat{\rho}\hat{\bar{v}}\hat{\bar{v}}\right) = -\nabla\hat{p} + \nabla.(\hat{\bar{\bar{\tau}}}) + \hat{\rho}\hat{\bar{g}} + \hat{\bar{\bar{F}}}, \tag{19}$$

where $\hat{\rho}$, $\hat{p}$, $\hat{\bar{\bar{\tau}}}$, $\hat{\bar{v}}$, $\hat{\bar{g}}$, $\hat{t}$ and $\hat{\bar{\bar{F}}}$ are the density, the pressure, the deviatoric stress tensor, the flow velocity vector, the gravity acceleration vector, time and source terms due to external forces, respectively. Note that, the horizontal bar marks represent the vector quantities.

One of the methods to solve these equations is to simplify the equations using approximations and dimensional analysis. Another method is to consider numerical solutions of the equations, known as CFD simulations. The strategy of CFD is converting the continuous problem domain to a discrete domain. There are various methods of discretization. The most famous discretization techniques are: Finite Difference, Finite Volume and Finite Elements methods. In these methods, a system of differential equations which involves a very large number of repetitive calculations is solved on computer systems.

IV.1 Miscible displacement flows

Wielage and Frigaard (93) studied the displacement of a simple yield stress fluid (Bingham fluid) by a Newtonian fluid in a 2D rectangular channel. They investigated the effect of the Reynolds number and the Bingham number on the residual wall layer thickness at large Pe. The equations of motion (the Navier-Stokes and the continuity) coupled with the concentration-diffusion equation were used as follow (in dimensionless form):

$$\begin{aligned} &\mathrm{Re}\left[\frac{\partial}{\partial t}u + (u.\nabla)u\right] = -\nabla p + \nabla.\tau, \\ &\nabla.u = 0, \\ &\frac{\partial}{\partial t}c + u.\nabla c = 0, \end{aligned} \tag{20}$$

where c, u, p and τ denote the concentration, velocity, pressure and the deviatoric stress, respectively. In their simulations the two fluids had the same density. For the displaced fluid the Bingham fluid model was used. They showed that, at a given Bingham number, by increasing the Reynolds number the thickness of residual wall layers is decreased. However, at low Reynolds number (e.g., $Re = 0.1$), residual layer thicknesses collapse onto a single curve.

Swain *et al.* (80) studied displacements of viscoplastic fluids by Newtonian fluids in a 2D channel. The displaced fluids exhibited yield stress and shear-thinning/shear-thickening effects. They investigated the influences of the yield stress and the power-law index on concentration contours. They mentioned that, at a given conditions, the width of the displacing fluid is enhanced by increasing the Bingham number. Moreover, they found that when the displaced fluid exhibits shear-thinning effects ($n = 0.7$), the interfacial instability becomes vigorous due to the presence of a competition between the yield stress effect and the shear-thinning effect. For $n = 1.3$, i.e., shear-thickening, the yield stress effect and the power-law index strengthen each other to diminish the shear stress in the flow region. They also mentioned that when a denser viscoplastic fluid (more viscous fluid) is displaced by a lighter Newtonian fluid (less viscous fluid) the flow can be destabilized via a Rayleigh–Taylor or a Kelvin–Helmholtz type instability. Eslami *et al.* (28) investigated a heavy-light displacement of viscoplastic fluids. They showed that the Bingham number, a densimetric Froude number ($\frac{\hat{V}_0}{\sqrt{At\hat{g}\hat{D}}}$) and the Reynolds number have significant impacts on both the flow pattern and the thickness of residual layers. They observed the appearance of Kelvin–Helmholtz-like instabilities close to the interface of fluids is due to the density contrast.

Yuan and Azaiez (95) numerically investigated the effects of inertia on Newtonian miscible displacements in a Hele-Shaw cell. The concentration fields for different modified Reynolds number ($Re^* = \frac{1}{12\delta}Re$) are shown in Fig. X, where δ is the aspect ratio of the Hele-Shaw cell. As can be seen, by increasing Re^* the structure and the number of fingers are not modified, implying that the inertia effect cannot suppress the viscous fingering instability.

We end this subsection by reminding the reader that, relevant to this Ph.D. thesis, readers may consult other references (2; 80; 28; 65; 83; 3; 30; 29) for further details on the computational aspects in viscoplastic flows involving interfacial patterns for miscible fluids.

IV.2 Immiscible displacement flows

The effect of the yield stress on the viscous fingering phenomenon for immiscible fluids have been numerically studied by Ebrahimi *et al.* (27). They have shown the finger pattern is dramatically affected by the yield stress value. The impacts of the Bingham number on the finger patterns for two different surface tension parameters are illustrated in Fig. XI, for which the Bingham number is defined as: $Bn = (\frac{\hat{\tau}_Y\hat{W}}{\hat{\mu}\hat{U}})$ and the surface tension parameter is defined as $\Gamma = 1/12Ca\delta^2$. As seen, by increasing the Bingham number at a given surface tension parame-

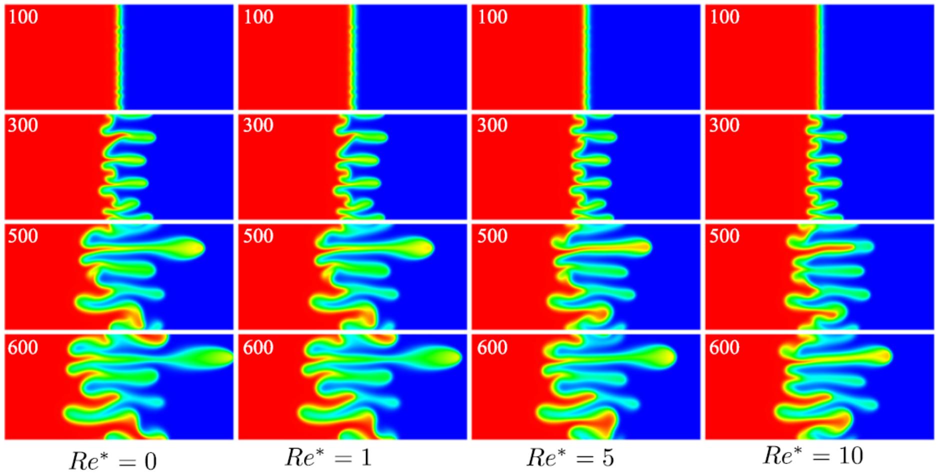

Figure X – Concentration fields for different Re^* (95).

ter, side-branching patterns start to form. Also, by decreasing the surface tension parameter, tip-splitting occurs instead of side-branching. Increasing the Bingham number leads to enhance the viscosity difference between the displacing and displaced fluid; consequently, tip-splitting is augmented.

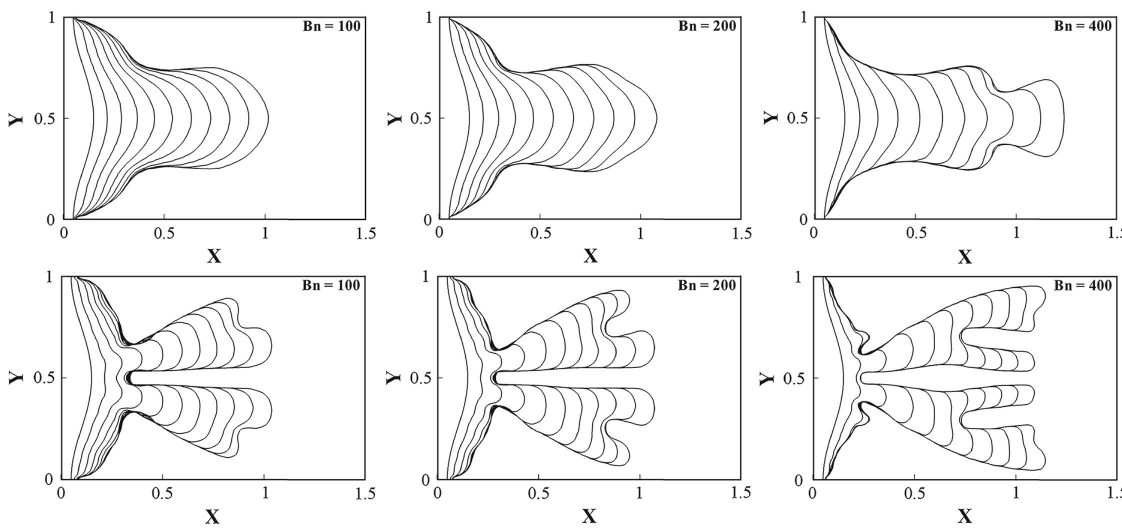

Figure XI – The effect of the Bingham number on the shape of the finger shape at $\Gamma = 0.002$ (upper row) and at $\Gamma = 0.0004$ (lower row) (27).

Liang (55) numerically investigated the impact of the surface tension value on the pattern formation during the displacement of water by air in a Hele-Shaw cell. They showed that by increasing the surface tension, the patterns change from fractal structures to smooth boundary fingers. Fig. XII presents the results for the pattern formation as a function of the surface tension ($1/B$). At high surface tension, the finger tip exists at the center of the Hele-Shaw cell and the finger is slightly asymmetric. Then, by increasing $1/B$, the finger tip approaches the side of the cell. By further increasing $1/B$, the finger tip splitting is changed. At the smallest values of the surface tension (largest $1/B$) highly branched and dendritic patterns are formed.

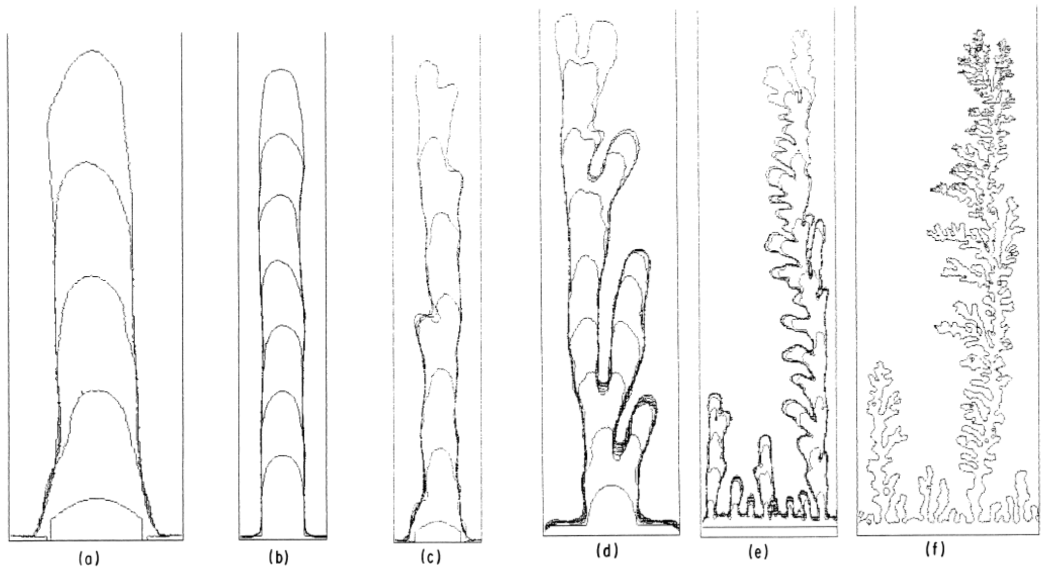

FIGURE XII – The different pattern formations as a function of surface tension. (a) $1/B$ = 35, (b) $1/B$ = 46, (c) $1/B$ = 104, (d) $1/B$ = 208, (e) $1/B$ = 2083 and (f) $1/B$ = 16666 (55).

V. Research objectives

Based on the literature review conducted, it is fair to say that Newtonian displacement flows of two fluids have been properly understood, particularly in terms of the viscous fingering instability. However, despite a few developments in analyzing the basic mechanisms in viscoplastic displacement flows, they have not been well understood. This is mainly due to the complex rheology of these fluids, and the presence of a large number of parameters that control the viscoplastic displacement flow dynamics. To address this large gap in the literature and provide a fundamental understanding of these flows, this Ph.D. thesis considers the displacement of a viscoplastic fluid by a Newtonian fluid, using experimental and numerical approaches. The specific objective is to provide reliable answers to the following critical questions:

• What is the effect of the complex rheology on the viscous fingering instability when the fluid simultaneously exhibits many competing non-Newtonian features, including yield stress, shear-thinning and weakly-elastic behaviours?

• How is viscous fingering affected by wettability? How can the combination of wettability and viscoplastic behaviours affect the displacement flow?

• Can the flow geometry affect the viscoplastic displacement flow? What is the impact of the aspect ratio on the displacement efficiency?

• How does an interplay between buoyancy and inertia affect the flow patterns? What is the impact of the yield stress on interfacial instabilities?

• What are the effects of the viscosity ratio and the flow geometry inclination on the removal of viscoplastic fluids in a displacement flow?

In order to address the aforementioned questions, we have performed the following activities:

— We have considered the viscous fingering instability for viscoplastic fluids through a Hele-Shaw cell, over a wide range of flow parameters. We have developed experiments in which a less viscous fluid (i.e., air) displaced a more viscous fluid (i.e., Carbopol gel, a common laboratory fluid). The gel used exhibited yield stress, shear-thinning as well as elastic behaviors. We have analyzed the effects of this complex rheology on the viscous fingering instability. *Chapter* 1 presents the findings of this work.

— We have experimentally investigated wetting viscoplastic displacements in a Hele-Shaw cell where a less viscous wetting fluid (i.e., silicone oil) displaced a more viscous non-wetting fluid (i.e., Carbopol gel). To quantify the effects of wettability on viscoplastic displacements, we have considered a case in which, unlike traditional studies, the displacing fluid wetted the Hele-Shaw cell walls. The results of this study are presented in *Chapter* 2.

— In order to examine the impacts of the flow geometry aspect ratio on viscoplastic displacement flows, we have experimentally studied a two-phase interfacial flow in a channel with a wide range of aspect ratios. In our experiments, air pushed a Carbopol gel (i.e., a yield stress fluid) in a long, uniform horizontal channel of various rectangular cross-sections. *Chapter* 3 reports the findings of this work.

— We have numerically studied miscible displacement flows of yield stress fluids by Newtonian fluids, along a 2D horizontal plane channel, in which a heavy fluid pushed a light fluid. In order to investigate the impacts of yield stress, inertia and buoyancy on viscoplastic displacement flow features, our simulations have covered a wide range of the most relevant dimensionless groups (e.g., the Reynolds, Froude and Bingham numbers). The results of this study are presented in *Chapter* 4.

— In order to investigate the effects of the viscosity ratio and the flow geometry inclination on the removal of viscoplastic fluids, we have numerically studied miscible viscoplastic displacement flows along a near-horizontal 2D plane channel, where a Newtonian fluid displaced a Bingham fluid. Our simulations have covered a wide range of Bingham numbers, viscosity ratios, and also a specific range of channel inclinations. *Chapter* 5 explains the findings of this work.

A final note may be that, considering recent attempts to control Newtonian displacement flows using various techniques (1; 11; 54; 72), controlling viscoplastic displacements may also become possible when a clear understanding of these flows becomes available. By delivering a substantial amount of high quality experimental and computational data to address the knowledge gap in the literature of viscoplastic displacement flows, this Ph.D. thesis may be a step in that direction.

I Bibliographie

[1] T.T. Al-Housseiny, P.A. Tsai, and H.A. Stone. Control of interfacial instabilities using flow geometry. *Nat. Phys.*, 8(10) :747–750, 2012.

[2] M. Allouche, I. Frigaard, and G. Sona. Static wall layers in the displacement of two visco-plastic fluids in a plane channel. *J. Fluid Mech.*, 424(1) :243–277, 2000.

[3] A. Amiri, A. Eslami, R. Mollaabbasi, F. Larachi, and S. M. Taghavi. Removal of a yield stress fluid by a heavier Newtonian fluid in a vertical pipe. *J. non-Newt. Fluid Mech.*, 268 :81–100, 2019.

[4] F. Asayesh, M. Zarabadi, and J. Greener. A new look at bubbles during biofilm inoculation reveals pronounced effects on growth and patterning. *Biomicrofluidics*, 11(6) :064109, 2017.

[5] O. Atasi, S. Khodaparast, B. Scheid, and H.A. Stone. Effect of buoyancy on the motion of long bubbles in horizontal tubes. *Phys. Rev. Fluids*, 2(9) :094304, 2017.

[6] P. Aussillous and D. Quéré. Quick deposition of a fluid on the wall of a tube. *Phys. Fluids*, 12(10) :2367–2371, 2000.

[7] J. Avendano, N. Pannacci, B. Herzhaft, P. Gateau, and P. Coussot. Enhanced displacement of a liquid pushed by a viscoelastic fluid. *J. Coll. Inter. Sci.*, 410 :172–180, 2013.

[8] A.G. Banpurkar, A.V. Limaye, and S.B. Ogale. Occurrence of coexisting dendrite morphologies : Immiscible fluid displacement in an anisotropic radial Hele-Shaw cell under a high flow rate regime. *Phys. Rev. E*, 61(5) :5507, 2000.

[9] D. Bensimon, L.P. Kadanoff, S. Liang, B.I. Shraiman, and C. Tang. Viscous flows in two dimensions. *Rev. Mod. Phys.*, 58(4) :977, 1986.

[10] I. Bischofberger, R. Ramachandran, and N.R. Fingering versus stability in the limit of zero interfacial tension. *Nat. Commun.*, 5, 2014.

[11] G. Bongrand and P.A. Tsai. Manipulation of viscous fingering in a radially tapered cell geometry. *Phys. Rev. E.*, 97(6) :061101, 2018.

[12] D. Bonn, H. Kellay, M.B. Amar, and J. Meunier. Viscous finger widening with surfactants and polymers. *Phys. Rev. Lett.*, 75(11) :21–32, 1995.

[13] D. Bonn and J. Meunier. Viscoelastic free-boundary problems : non-Newtonian viscosity vs normal stress effects. *Phys. Rev. Lett.*, 79(14) :2662, 1997.

[14] F.P. Bretherton. The motion of long bubbles in tubes. *J. Fluid Mech.*, 10(2) :166–188, 1961.

[15] C.Y. Chen and E. Meiburg. Miscible displacements in capillary tubes. part 2. numerical simulations. *J. Fluid Mech.*, 326 :57–90, 1996.

[16] J.D. Chen. Radial viscous fingering patterns in Hele-Shaw cells. *Exp. Fluids*, 5(6) :363–371, 1987.

[17] J.D. Chen. Growth of radial viscous fingers in aHele-Shaw cell. *J. Fluid Mech.*, 201 :223–242, 1989.

[18] C. Chevalier, M.B. Amar, D. Bonn, and A. Lindner. Inertial effects on Saffman–Taylor viscous fingering. *J. Fluid Mech.*, 552 :83–97, 2006.

[19] C. Chevalier, A. Lindner, M. Leroux, and E. Clément. Morphodynamics during air injection into a confined granular suspension. *J. non-Newt. Fluid Mech.*, 158(1) :63–72, 2009.

[20] R.L. Chuoke, P. Van Meurs, and C. van der Poel. The instability of slow, immiscible, viscous liquid-liquid displacements in permeable media. *Trans. AIME*, 216 :188–194, 1959.

[21] Y. Couder, N. Gerard, and M. Rabaud. Narrow fingers in the Saffman–Taylor instability. *Phys. Rev. A*, 34(6) :5175, 1986.

[22] P. Coussot. Saffman–Taylor instability in yield-stress fluids. *J. Fluid Mech.*, 380 :363–376, 1999.

[23] A. de Lozar, A.L. Hazel, and A. Juel. Scaling properties of coating flows in rectangular channels. *Phys. Rev. Lett.*, 99(23) :234501, 2007.

[24] A. De Lozar, A. Juel, and A.L. Hazel. The steady propagation of an air finger into a rectangular tube. *J. Fluid Mech.*, 614 :173–195, 2008.

[25] E. O. Dias and J.A. Miranda. Taper-induced control of viscous fingering in variable-gap Hele-Shaw cell. *Phys. Rev. E*, 87(5) :053015, 2013.

[26] Y. Dimakopoulos and J. Tsamopoulos. Transient displacement of a viscoplastic material by air in straight and suddenly constricted tubes. *J. non-Newt. Fluid Mech.*, 112(1) :43–75, 2003.

[27] B. Ebrahimi, P. Mostaghimi, H. Gholamian, and K. Sadeghy. Viscous fingering in yield stress fluids : a numerical study. *J. Eng. Math.*, pages 1–16, 2015.

[28] A. Eslami, I.A. Frigaard, and S.M. Taghavi. Viscoplastic fluid displacement flows in horizontal channels : Numerical simulations. *J. non-Newt. Fluid Mech.*, 249 :79–96, 2017.

[29] A. Eslami, R. Mollaabbasi, A. Roustaei, and S. M. Taghavi. Pressure-driven displacement flows of yield stress fluids : viscosity ratio effects. *Can. J. Chem. Eng.*, 1–14, 2019, https ://doi.org/10.1002/cjce.23597.

[30] A. Eslami, R. Mollaabbasi, and S. M. Taghavi. Effects of a channel inclination on displacements of viscoplastic fluids. CSME-SCGM, 2018, http ://dx.doi.org/10.25071/10315/35277.

[31] A. Eslami and S.M. Taghavi. Viscous fingering regimes in elasto-visco-plastic fluids. *J. non-Newt. Fluid Mech.*, 243 :79–94, 2017.

[32] A. Eslami and S.M. Taghavi. Viscous fingering of yield stress fluids : The effects of wettability. *J. non-Newt. Fluid Mech.*, 264 :25–47, 2019.

[33] J. Fernandez, R. Krechetnikov, and G.M. Homsy. Experimental study of a surfactant-driven fingering phenomenon in a Hele-Shaw cell. *J. Fluid Mech.*, 527 :197–216, 2005.

[34] A. Franco-Gómez, A.B. Thompson, A.L. Hazel, and A. Juel. Sensitivity of saffman–taylor fingers to channel-depth perturbations. *J. Fluid Mech.*, 794 :343–68, 2016.

[35] J. F. Freitas, E. J. Soares, and R. L. Thompson. Viscoplastic-viscoplastic displacement in a plane channel with interfacial tension effects. *Chem. Eng. Sci.*, 91 :54–64, 2013.

[36] P. Gondret and M. Rabaud. Shear instability of two-fluid parallel flow in a Hele–Shaw cell. *Phys. Fluids*, 9(11) :3267–3274, 1997.

[37] J. Greener. On the nature of "skeletal" biofilm patterns,"hidden" heterogeneity and the role of bubbles to reveal them. *NPJ biofilms and microbiomes*, 5(1) :12, 2019.

[38] J. Greener, M. Parvinzadeh Gashti, A. Eslami, M. P. Zarabadi, and S. M. Taghavi. A microfluidic method and custom model for continuous, non-intrusive biofilm viscosity measurements under different nutrient conditions. *Biomicrofluidics*, 10(6) :064107, 2016.

[39] A. He and A. Belmonte. Inertial effects on viscous fingering in the complex plane. *J. Fluid Mech.*, 668 :436–445, 2011.

[40] S. Hill et al. Channeling in packed columns. *Chem. Eng. Sci.*, 1(6) :247–253, 1952.

[41] G.M. Homsy. Viscous fingering in porous media. *Annu. Rev. Fluid Mech.*, 19(1) :271–311, 1987.

[42] S. Hormozi. *Multi-layer flows with yield stress fluids.* PhD thesis, University of British Columbia, 2011.

[43] M. Jung, M. Brinkmann, R. Seemann, T. Hiller, and S. de La Lama, M.S.and Herminghaus. Wettability controls slow immiscible displacement through local interfacial instabilities. *Phys. Rev. Fluids*, 1(7) :074202, 2016.

[44] N. Kagei, D. Kanie, and M. Kawaguchi. Viscous fingering in shear thickening silica suspensions. *Phys. Fluids*, 17(5) :054103, 2005.

[45] M. Kawaguchi, A. Shibata, K.i Shimomoto, and T. Kato. Effect of geometry and anisotropy of a Hele-Shaw cell on viscous fingering of polymer solutions. *Phys. Rev. E*, 58(1) :785, 1998.

[46] D.A. Kessler, J. Koplik, and H. Levine. Pattern selection in fingered growth phenomena. *Adv. Phys.*, 37(3) :255–339, 1988.

[47] L. Kondic, P. Palffy-Muhoray, and M.J. Shelley. Models of non-Newtonian Hele-Shaw flow. *Phys. Rev. E*, 54(5) :R4536, 1996.

[48] L. Kondic, M.J. Shelley, and P. Palffy-Muhoray. Non-Newtonian Hele-Shaw flow and the Saffman–Taylor instability. *Phys. Rev. Lett.*, 80(7) :1433, 1998.

[49] J. Kuang, T. Maxworthy, and P. Petitjeans. Miscible displacements between silicone oils in capillary tubes. *Eur. J. Mech. B/Fluids*, 22(3) :271–277, 2003.

[50] E. Lajeunesse, J. Martin, N. Rakotomalala, and D. Salin. 3D instability of miscible displacements in a Hele-Shaw cell. *Phys. Rev. Lett.*, 79(26) :5254, 1997.

[51] E. Lajeunesse, J. Martin, N. Rakotomalala, D. Salin, and Y.C. Yortsos. Miscible displacement in a Hele-Shaw cell at high rates. *J. Fluid Mech.*, 398 :299–319, 1999.

[52] E. Lemaire, P. Levitz, G. Daccord, and H. Van Damme. From viscous fingering to viscoelastic fracturing in colloidal fluids. *Phys. Rev. Lett.*, 67(15) :2009, 1991.

[53] H. Li, B. Maini, and J. Azaiez. Experimental and numerical analysis of the viscous fingering instability of Shear-Thinning fluids. *Can. J. Chem. Eng.*, 84(1) :52–62, 2006.

[54] S. Li, J.S. Lowengrub, J. Fontana, and P. Palffy-Muhoray. Control of viscous fingering patterns in a radial Hele-Shaw cell. *Phys. Rev. Lett.*, 102(17) :174501, 2009.

[55] S. Liang. Random-walk simulations of flow in Hele-Shaw cells. *Phys. Rev. A*, 33(4) :2663, 1986.

[56] A. Lindner, D. Bonn, and J. Meunier. Viscous fingering in a shear-thinning fluid. *Phys. Fluids*, 12(2) :256–261, 2000.

[57] A. Lindner, P. Coussot, and D. Bonn. Viscous fingering in a yield stress fluid. *Phys. Rev. Lett.*, 85(2) :314, 2000.

[58] A. Lindner, P. Coussot, and D. Bonn. Viscous fingering in a gel. In *Branching in Nature*, pages 433–438. Springer, 2001.

[59] M. Magnini, S. Khodaparast, O.K. Matar, H.A. Stone, and J.R. Thome. Dynamics of long gas bubbles rising in a vertical tube in a cocurrent liquid flow. *Phys. Rev. Fluids*, 4(2) :023601, 2019.

[60] N. Maleki-Jirsaraei, A. Lindner, S. Rouhani, and D. Bonn. Saffman–Taylor instability in yield stress fluids. *J. Phys. Condens. Matter*, 17(14) :S1219, 2005.

[61] S. Malhotra and M.M. Sharma. Impact of fluid elasticity on miscible viscous fingering. *Chem. Eng. Sci.*, 117 :125–135, 2014.

[62] T. Maxworthy. The nonlinear growth of a gravitationally unstable interface in a Hele-Shaw cell. *J. Fluid Mech.*, 177 :207–232, 1987.

[63] J.W. McLean and P.G. Saffman. The effect of surface tension on the shape of fingers in a Hele-Shaw cell. *J. Fluid Mech.*, 102 :455–469, 1981.

[64] T.G. Mezger. *The rheology handbook : for users of rotational and oscillatory rheometers*. Vincentz Network GmbH & Co KG, 2006.

[65] R. Mollaabbasi and S.M. Taghavi. Buoyant displacement flows in slightly non-uniform channels. *J. Fluid Mech.*, 795 :876–913, 2016.

[66] M.G. Moore, A. Juel, J.M. Burgess, W.D. McCormick, and H.L. Swinney. Fluctuations in viscous fingering. *Phys. Rev. E.*, 65(3) :030601, 2002.

[67] C.W. Park and G.M. Homsy. Two-phase displacement in Hele-Shaw cells : theory. *J. Fluid Mech.*, 139 :291–308, 1984.

[68] H. Pascal. Dynamics of moving interface in porous media for power law fluids with yield stress. *Int. J. Eng. Sci.*, 22(5) :577–590, 1984.

[69] H. Pascal. Rheological behaviour effect of non-Newtonian fluids on dynamic of moving interface in porous media. *Int. J. Eng. Sci.*, 22(3) :227–241, 1984.

[70] H. Pascal. Rheological effects of non-Newtonian behavior of displacing fluids on stability of a moving interface in radial oil displacement mechanism in porous media. *Int. J. Eng. Sci.*, 24(9) :1465–1476, 1986.

[71] P. Petitjeans and T. Maxworthy. Miscible displacements in capillary tubes. part 1. experiments. *J. Fluid Mech.*, 326 :37–56, 1996.

[72] D. Pihler-Puzovic, P. Illien, M. Heil, and A. Juel. Suppression of complex fingerlike patterns at the interface between air and a viscous fluid by elastic membranes. *Phys. Rev. Lett.*, 108(6) :074502, 2012.

[73] E.C. Poire and M.B. Amar. Finger behavior of a shear thinning fluid in a Hele-Shaw cell. *Phys. Rev. Lett.*, 81(10) :2048, 1998.

[74] A.J. Poslinski, P.R. Oehler, and V.K. Stokes. Isothermal gas-assisted displacement of viscoplastic liquids in tubes. *Polym. Eng. Sci.*, 35(11) :877–892, 1995.

[75] M. Rabaud, Y. Couder, and N. Gerard. Dynamics and stability of anomalous Saffman–Taylor fingers. *Phys. Rev. A*, 37(3) :935, 1988.

[76] C. Ruyer-Quil. Inertial corrections to the darcy law in a Hele–Shaw cell. *C R Acad Sci IIb Mec*, 329(5) :337–342, 2001.

[77] P.G. Saffman and G. Taylor. The penetration of a fluid into a porous medium or Hele-Shaw cell containing a more viscous liquid. In *Proc. R. Soc. A.*, 245, 312–329, 1958.

[78] H. S. H Shaw. *Investigation of the nature of surface resistance of water and of stream-line motion under certain experimental conditions.* Inst. NA, 1898.

[79] J.P. Stokes, D.A. Weitz, J.P. Gollub, A. Dougherty, M.O. Robbins, P.M. Chaikin, and H.M. Lindsay. Interfacial stability of immiscible displacement in a porous medium. *Phys. Rev. Lett.*, 57(14) :1718, 1986.

[80] P. A. P. Swain, G. Karapetsas, O.K. Matar, and K.C. Sahu. Numerical simulation of pressure-driven displacement of a viscoplastic material by a Newtonian fluid using the lattice Boltzmann method. *Eur. J. Mech. B-Fluid*, 49 :197–207, 2015.

[81] P. Tabeling and A. Libchaber. Film draining and the Saffman–Taylor problem. *Phys. Rev. A*, 33(1) :794, 1986.

[82] P. Tabeling, G. Zocchi, and A. Libchaber. An experimental study of the Saffman-Taylor instability. In *Physicochemical Hydrodynamics*, pages 515–525. Springer, 1988.

[83] S. M. Taghavi. A two-layer model for buoyant displacement flows in a channel with wall slip. *J. Fluid Mech.*, 852 :602–640, 2018.

[84] H. Tani and A. Tani. Effect of the wetting layer on the fingering pattern in a hele–shaw cell. *J. Phys. Soc. Jpn.*, 83(3) :034401, 2014.

[85] G.I. Taylor. Deposition of a viscous fluid on the wall of a tube. *J. Fluid Mech.*, 10(02) :161–165, 1961.

[86] M. Trojer, M.L. Szulczewski, and R. Juanes. Stabilizing fluid-fluid displacements in porous media through wettability alteration. *Phys. Rev. Applied*, 3(5): 054008, 2015.

[87] G. Tryggvason and H. Aref. Numerical experiments on Hele-Shaw flow with a sharp interface. *J. Fluid Mech.*, 136 :1–30, 1983.

[88] H. Van Damme, E. Alsac, C. Laroche, and L. Gatineau. On the respective roles of low surface tension and non-Newtonian rheological properties in fractal fingering. *Europhys. Lett.*, 5(1) :25, 1988.

[89] H. Van Damme, C. Laroche, L. Gatineau, and P. Levitz. Viscoelastic effects in fingering between miscible fluids. *J. Phys.*, 48(7) :1121–1133, 1987.

[90] H. Van Damme, E. Lemaire, Y. Ould, M. Abdelhaye, A. Mourchid, and P. Levitz. Pattern formation in particulate complex fluids : A guided tour. In *Non-linearity and breakdown in soft condensed matter*, pages 134–150. Springer, 1994.

[91] E. Walling, R. Mollaabbasi, and S.M. Taghavi. Buoyant miscible displacement flows in a nonuniform Hele-Shaw cell. *Phys. Rev. Fluids*, 3(3) :034003, 2018.

[92] S. J. Weinstein, E.B. Dussan, and L.H. Ungar. A theoretical study of two-phase flow through a narrow gap with a moving contact line : Viscous fingering in a Hele-Shaw cell. *J. Fluid Mech.*, 221 :53–76, 1990.

[93] K. Wielage-Burchard and I. A. Frigaard. Static wall layers in plane channel displacement flows. *J. non-Newt. Fluid Mech*, 166(5) :245–261, 2011.

[94] S.D.R. Wilson. The taylor-saffman problem for a non-Newtonian liquid. *J. Fluid Mech.*, 220 :413–425, 1990.

[95] Q. Yuan and J. Azaiez. Inertial effects of miscible viscous fingering in a Hele-Shaw cells. *Fluid Dynam. Res.*, 47(1) :015506, 2014.

[96] B. Zhao, C.W. MacMinn, and R. Juanes. Wettability control on multiphase flow in patterned microfluidics. *Proceedings of the National Academy of Sciences*, 113(37) :10251–10256, 2016.

[97] H. Zhao, J. Casademunt, C. Yeung, and J.V. Maher. Perturbing Hele-Shaw flow with a small gap gradient. *Phys. Rev. A*, 45(4) :2455, 1992.

[98] H. Zhao and J.V. Maher. Viscoelastic effects in patterns between miscible liquids. *Phys. Rev. E*, 45(12) :R8328, 1992.

[99] G. Zocchi, B.E. Shaw, A. Libchaber, and L.P. Kadanoff. Finger narrowing under local perturbations in the Saffman–Taylor problem. *Phys. Rev. A*, 36(4) :1894, 1987.

Chapitre 1

Viscous fingering regimes in elasto-visco-plastic fluids

1.1 Résumé

Nous étudions expérimentalement l'instabilité de Saffman-Taylor le mouvement de l'air dans un fluide non-Newtonien (solution de Carbopol) dans une cellule de Hele-Shaw rectangulaire. En plus des caractéristiques visqueuses, le fluide non-Newtonien utilisé présente la contrainte d'écoulement, la rhéofluidification ainsi que les comportements élastiques. Les principaux paramètres sans dimension qui gère les divers régimes de écoulements sont le nombre de Bingham (Bn), le nombre capillaire (Ca), le nombre de Weber (We), le nombre de Weissenberg (Wi), le rapport d'aspect du canal ($\delta \gg 1$), et l'indice en loi de puissance de la rhéofluidification (n). Trois régimes d'écoulement principaux sont observés, à savoir un régime de contrainte d'écoulement, un régime visqueux et un régime d'élasto-inertie. Nous présentons une description détaillée de chaque régime et quantifions leurs limites de transition par rapport aux groupes sans dimension. Certains des aspects de écoulements secondaire, par exemple l'épaisseur de la couche de paroi résiduelle et un régime de structure en réseau, ont également été étudiés.

1.2 Abstract

We experimentally study the Saffman-Taylor instability of air invasion into a non-Newtonian fluid (i.e., Carbopol solution) in a rectangular Hele-Shaw cell. In addition to viscous features, the non-Newtonian fluid used exhibits yield stress, shear-thinning as well as elastic behaviors. The key dimensionless parameters that govern the various flow regimes are the Bingham number (Bn), the capillary number (Ca), the Weber number (We), the Weissenberg number (Wi), the channel aspect ratio ($\delta \gg 1$), and the shear-thinning power-law index (n). Three main flow regimes are observed, i.e., a *yield stress* regime, a *viscous* regime and an *elasto-inertial* regime. We present a detailed description for each regime and quantify their transition boundaries

versus dimensionless groups. Some of the secondary flow aspects, e.g., the wall residual layer thickness and a *network structure* regime, have been also studied.

1.3 Introduction

Displacement flows are often vulnerable to interfacial instabilities in a variety of physical, chemical, biological, geophysical, and engineering systems. Of particular interest has been the *viscous fingering* instability or the *Saffman-Taylor* instability (72), which occurs when a less-viscous fluid displaces a more-viscous one, and refers to the appearance of finger-like interfacial patterns (85; 49; 30). This interesting phenomenon is regarded as a representative of interfacial pattern formation and it has been studied numerously, from various perspectives, since it also frequently occurs in nature and industrial applications, such as sugar refining (28), carbon sequestration (15), enhanced oil recovery (60), oil well cementing (7), printing devices (77), chromatographic separations (70), coating (29), adhesives (57), and growth of bacterial colonies (5).

Viscous fingering in a traditional Hele-Shaw cell (30; 49), made of two parallel flat plates with a small gap, has received much attention as a suitable framework to analyze interfacial instabilities in narrow confined passages, e.g., in porous media (30). In the case of Newtonian fluids, the fluid motion in the Hele-Shaw cell is described by Darcy's law, which relates the two-dimensional averaged velocity across the gap $\hat{V}$ [1] to the local pressure $\hat{p}$. Darcy's law is valid for laminar flows through porous media in the limit of low Reynolds number, *Re* (see (30; 27)). The other governing equation of the system is the mass conservation. These two equations are

$$\hat{v} = -\frac{\hat{b}^2}{12\hat{\mu}}\nabla\hat{p}, \tag{1.1}$$

$$\nabla.\hat{v} = 0, \tag{1.2}$$

where $\hat{b}$ and $\hat{\mu}$ denote the gap thickness and shear viscosity, respectively. Due to incompressibility, the pressure field satisfies Laplace's equation, $\nabla^2\hat{p} = 0$. In order to determine the pressure jump across the interface, the Young-Laplace equation is used, i.e., $\Delta\hat{p} = \hat{\sigma}\left(1/\hat{R}_1 + 1/\hat{R}_2\right)$, where $\hat{\sigma}$ denotes the surface tension, and $\hat{R}_1$ and $\hat{R}_2$ are the interface curvature radius in the direction perpendicular to the parallel plates and that in the plane of motion, respectively. Since the gap thickness of the Hele-Shaw cell ($\hat{b}$) is small, it can be assumed that $1/\hat{R}_1 \approx 2/\hat{b}$, and that the larger radius of curvature, $\hat{R}_2$, has a negligible effect (82; 6). Thus, the pressure jump over the interface is simplified to $\Delta\hat{p} \approx 2\hat{\sigma}/\hat{b}$.

1. In this paper we adopt the convention of denoting dimensional quantities with the ˆ symbol and dimensionless quantities without.

Although various flow features, e.g., the wall wetting film thickness (61), the interface shape (75) and inertial effects (71; 27), may require modifications to Darcy's law, this relation has been generally found suitable for Newtonian fluids. In particular, the shape and the width of the advancing finger ($\hat{w}$) can be obtained. For example, Saffman and Taylor (72) have shown in their classical work that $\hat{w}$ is inversely proportional to the finger tip velocity ($\hat{U}$). They and other researchers have also shown that the relative finger width ($\lambda = \hat{w}/\hat{W}$) reaches a limiting value of ~ 1/2 at high finger tip velocities (30; 34; 72). Despite many efforts, the applicability of Darcy's law to realistic non-Newtonian fluids has been more limited compared to Newtonian fluids (41; 65).

The Saffman-Taylor instability problem for non-Newtonian fluids is not very well defined (47) due to complex rheological behaviors exhibited by these fluids. The effects of several key non-Newtonian properties have been investigated, such as yield stress (43; 46; 17; 62), shear-thinning (83; 25; 9), shear-thickening (25; 55; 9) and elastic behaviors (47; 31). A new, diverse class of problems have been discovered (17; 24; 58), e.g., snowflake-like patterns (11) and branched, fractal, or fracture-like structures (59; 39; 32). In particular, it has been found that shear-thinning effects induce dendritic patterns (with side branching) or crack-like patterns (with angular branches and sharp tips) (37; 3). Shear-thickening features may widen or narrow the finger width (33). Viscoplastic properties have been found to strikingly modify Newtonian morphological patterns. For theses fluids, Lindner *et al.* (43) have discovered the existence of a yield stress regime (with ramified structures) and a viscous regime (with a single finger) at small and moderate velocities. Maleki *et al.* (46) have also observed a side-branching regime at larger velocities. Numerical simulations of Ebrahimi *et al.* (21) confirmed some of the observed behaviors for these fluids. Finally, a fluid's thixotropy drastically affects the finger shape, leading to chaotic behaviors at longer times (22).

In general, in the displacement of a more viscous, wetting fluid by a less viscous, non-wetting fluid, the advancing finger leaves behind a wetting film of the displaced fluid on the wall of the flow geometry, the thickness of which has been the subject of many studies. For example, Bretherton (10) theoretically studied the film residual behind a flat interface for a Newtonian fluid flowing in a tube, at small capillary numbers, and found that the film is uniform and thin. For Newtonian fluids in the Hele-Shaw cell, the maximum film thickness is a function of $Ca^{2/3}$(75; 76), also reported by Bretherton (10) for the tube geometry. However, the film thickness in the Hele-Shaw cell may not be uniform as a result of the normal velocity variation along the interface (61; 76). Poslinski *et al.* (66) experimentally studied the displacement of a viscoplastic fluid by air in a horizontal tube and found that the film thickness is much larger compared to Newtonian fluids and it can increase up to 0.35 of the tube radius at high air flow rates. The film thickness for viscoplastic fluid depends on the tube geometry, finger shape and fluid properties, as numerically observed by (20). Through a combined theoretical and computational study, Allouche *et al.* (2) quantified the residual wall layer film thickness for viscoplastic for a 2D channel flow. Freitas *et al.* (26) have also shown that the yield stress value has a significant effect on the flow patterns and layer thickness, e.g., the film thickness decreases by an increase in the yield stress.

Although, as discussed, there are numerous studies in the literature addressing viscous finger of non-Newtonian fluids, there is hardly a clear picture of all the leading order flow regimes, especially versus the dimensionless parameters that govern the flow. This is due the fact that the complex rheology makes it hard to study the flow in generality as there is a wide range of parameters that control the flow (for example see Tables 1.1 & 1.2 showing the definitions & ranges of several dimensional/dimensionless parameters used in our study). Almost certainly, some of the non-Newtonian features are known in separate contexts, but our understanding is limited when they are present at the same time or compete with one another, which is the case in most non-Newtonian fluids. In addition, it is now accepted that many laboratory fluids, previously believed to be "ideal" in a sense that they only present a single non-Newtonian characteristic, in fact exhibit many competing non-Newtonian features simultaneously. A good example may be a Carbopol solution, which is shear-thinning, viscoplastic, weakly viscoelastic, although with no significant thixotropy (13; 68; 63; 38). In the light of the limitations of the literature mentioned, some of the key contributions of our study can be summarized as follows. (i) We characterize the regimes of viscous fingering for a common laboratory fluid, i.e., Carbopol solution, exhibiting an interesting range of complex rheology. (ii) Through conducting a large number of experiments (~ 600), we are able to describe the flow regimes versus the dimensionless groups and delineate leading order boundaries between them. An effort has been devoted to find the best combination of the key dimensionless numbers to appropriately and clearly explain each regime and their corresponding transitions. (iii) While shedding further light on the previously-discovered regimes for viscoplastic fluids (e.g., (43; 46)), i.e., the yield stress and viscous regimes, we also find for the first time an elasto-inertial flow regime, which corresponds to simultaneous presence of inertial and elastic effects, at high shear-rates. (iv) We provide an in-depth look into some of the secondary, interesting features of the flow, e.g., the wall residual film thickness and a network structure regime inside the finger domain. (v) Finally, there is a trend in recent studies to control the viscous fingering phenomena, for Newtonian fluids, through using various methods, e.g., non-uniformity of the geometry (1) (see also (54)), imposed flow rate variation (40), and elastic wall boundaries (64). The extensions of these fascinating methods to control viscous finger for non-Newtonian fluids may only become possible when a clear, general picture of viscous fingering in non-Newtonian fluids becomes available. The current work may be a step in that direction.

The outline of the paper is as follows. In section 1.4, the experimental setup, procedures, and fluid characterizations are discussed. Section 1.5 covers throughly the main flow regimes as well as some secondary flow behaviors. The paper concludes with a brief summary.

Parameter	Name	SI Unit	Range or Value
$\hat{W}$	Channel width	m	6.8×10^{-2}
$\hat{w}$	Finger width	m	$(5.6 - 23.2) \times 10^{-3}$
$\hat{b}$	Gap thickness	m	9×10^{-4} & 1.5×10^{-3}
$\hat{L}$	Channel length	m	2.6×10^{-1}
$\hat{V}$	Mean imposed flow velocity (flow rate divided by channel cross section)	m/s	$(0 - 307) \times 10^{-3}$
$\hat{U}$	Finger tip velocity	m/s	$(0 - 1705) \times 10^{-3}$
$\hat{\rho}$	Carbopol density	kg/m^3	$\sim 9.985 \times 10^{2}$
$\hat{C}$	Carbopol concentration	% (wt/wt)	$(1 - 1.5) \times 10^{-3}$
$\hat{\mu}$	Carbopol viscosity	Pa.s	$(5.2 - 793) \times 10^{-1}$
$\hat{\sigma}$	Surface tension	N/m	$\sim 6.6 \times 10^{-2}$
$\hat{\sigma}_{eff}$	Effective surface tension	N/m	$\sim (6.6 - 7.05) \times 10^{-2}$
$\hat{\tau}_Y$	Yield stress	Pa	$5.5 - 13.7$
$\hat{N}_1$	First normal stress difference	Pa	$0 - 168.1$
$\hat{\Lambda}$	Relaxation time	s	$\sim (0.4 - 134) \times 10^{-3}$
$\hat{t}_{ave}$	Wall residual layers average thickness	m	$(2.9 - 14.4) \times 10^{-5}$
$\hat{n}_d$	Number of cavities in the network structure regime	-	$(4.8 - 25.9) \times 10^{1}$
$\hat{d}_{ave}$	Mean characteristic diameter of cavities in the network structure regime	m	$(4.7 - 83) \times 10^{-4}$

TABLE 1.1 – The ranges and values of the dimensional parameters in our work. The reported viscosity values correspond to the shear rates between 0.12 and 518 (1/s).

Parameter	Name	Definition	Range or value
Bn	Bingham number	$\frac{\hat{\tau}_y}{\kappa(\hat{V}/\hat{b})^n}$	$(3 - 19) \times 10^{-1}$
Bn^*	Modified Bingham number	$\frac{Bn}{1+Bn}$	$(2 - 7.3) \times 10^{-1}$
Ca	Capillary number	$\frac{\hat{\mu}\hat{U}}{\hat{\sigma}_{eff}}$	$(9 - 146.5) \times 10^{-1}$
Ca^*	Modified capillary number	$\frac{Ca\ \delta^{1+n}}{1+We^*/We^*_c}$	$(5.9 - 120.5) \times 10^{-1}$
Re	Reynolds number	$\frac{\hat{\rho}\hat{U}\hat{b}}{\hat{\mu}}$	$(2.7 - 81000) \times 10^{-7}$
t	Relative film thickness	$\frac{\hat{t}_{ave}}{\hat{b}}$	$(34 - 96) \times 10^{-3}$
We	Weber number	$\frac{\hat{\rho}\hat{U}^2\hat{b}}{\hat{\sigma}_{eff}}$	$(6.5 - 789200) \times 10^{-5}$
We^*	Modified Weber number	$We\ \delta^{1+n}$	$(2 - 126200) \times 10^{-2}$
Wi	Weissenberg number	$\frac{\hat{\Lambda}\hat{U}}{\hat{b}}$	$(1.24 - 574) \times 10^{-2}$
δ	Aspect ratio	$\frac{\hat{W}}{\hat{b}}$	45.3 & 75.5
λ	Relative finger width	$\frac{\hat{w}}{\hat{W}}$	$(8 - 34) \times 10^{-2}$

TABLE 1.2 – The ranges and values of the dimensionless parameters in our work.

1.4 Experimental descriptions

Our experiments study was performed in a traditional, rectangular Hele-Shaw cell formed by two closely-spaced, smooth plexiglas plates. The channel dimensions and the flow parameters are given in Table 1.1. The plates of the cell were 1/2 inch thick to prevent bending. The plates were separated by a thin Nitrile Butadiene Rubber (NBR) spacer. The gap thickness was set using level screws distributed along both sides of the cell. This thickness was also controlled with digital caliper and a digital level meter. Rubber and level screws were used to prevent any fluid loss and control the gap thickness. A schematic of the experimental cell is shown in Fig. 1.1. The cell was initially filled with the displaced fluid, which was a Carbopol solution (Carbomer 940, Making Cosmetics Co.). Then, from the inlet of the cell, the displacing fluid (air) was injected. Light Emitting Diode (LED) stripes along with light diffuser panels were used to adjust the light. Light absorption calibrations were performed in a usual fashion. The advancing fingers and the accompanied complex patterns were recorded using a high-speed digital camera (Basler A2040-90um) coupled to computer for direct image acquisition and treatment. In addition, an ultra-high-speed camera (FASTCAM UX100) was occasionally used for extremely large flow velocities. The images were post-processed using MATLAB, ImageJ and the camera software. The inlet mean imposed velocity was determined by an Alicat mass flow controller with a resolution of 0.0001 (lit/min).

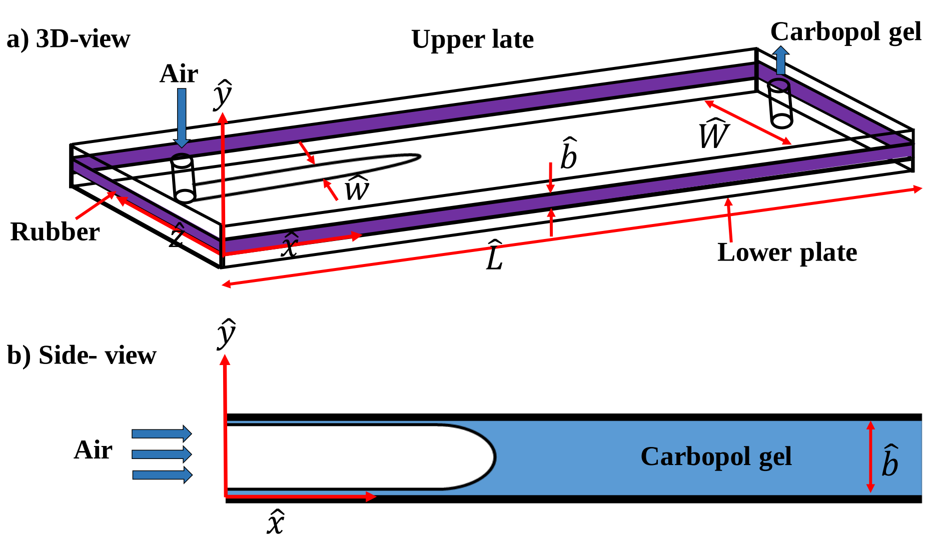

FIGURE 1.1 – Schematic view of the experimental set-up (i.e., a rectangular Hele-Shaw cell). (a) A 3D-view of the geometry and the flow. (b) Side view.

1.4.1 Fluid preparation and characterization

Carbopol is widely used as a thickener in cosmetic and pharmaceutical products (68; 38; 35) and as a gelling agent in systems where clarity is needed. The Carbopol rheology is mainly controlled by the concentration and pH of the solution. Carbopol is initially mixed with water to create an acidic solution, which is then neutralized with a base agent at intermediate pH (e.g., NaOH). At small concentrations, the density of the neutralized transparent solution is close to that of water.

For visualization purposes, the Carbopol gel used in our experiments was dyed with a small amount of black ink for visualization purposes. Three different Carbopol solutions were used for the experiments, for which the composition is shown in Table 1.3. The conventional abbreviations introduced in the table for different Carbopol concentrations will be used throughout the rest of the paper. The rheological measurements for Carbopol solutions (termed low, medium and high concentrations) were performed using an AR-G2 TA Instrument digital controlled shear stress-shear rate rheometer. A cone-and-plate geometry was used, with 60 (mm) cone and plate diameter, 2.04° cone angle and 56 (μm) gap at the cone tip. Identical loading procedures were implemented in all tests.

Neglecting elastic effects and concentrating on viscoplastic properties, the Herschel-Bulkley model is an appropriate rheological model that describes the shear behavior of Carbopol gel:

$$\hat{\tau} = \hat{\tau}_Y + \hat{\kappa}\hat{\dot{\gamma}}^n, \tag{1.3}$$

which also includes the simpler Bingham, power-law and Newtonian models. The Herschel-Bulkley model is defined by three parameters : a fluid consistency index ($\hat{\kappa}$), a yield stress ($\hat{\tau}_Y$), and a power-law index (n). The Herschel-Bulkley viscosity ($\hat{\mu}$), which depends on the Carbopol concentration and the shear rate ($\hat{U}/\hat{b}$), is calculated as (see Fig. 1.2a):

$$\hat{\mu} = \hat{\tau}_y \left(\frac{\hat{b}}{\hat{U}}\right) + \hat{K}\left(\frac{\hat{U}}{\hat{b}}\right)^{n-1}. \tag{1.4}$$

Figure 1.2a shows that $\hat{U}/\hat{b}$ affects the viscosity significantly, where the viscosity of Carbopol strongly decreases with the shear rate. Examples of rheometer flow curves of different Carbopol solutions (along with the fitted Herschel-Bulkley model data) are given in Fig. 1.2b. The yield stress value is enhanced by increasing the Carbopol concentration.

In order to gain insight about the elastic properties of our Carbopol gels, oscillatory frequency sweep tests (with the angular frequency $\hat{\omega}$) were conducted to quantify the relation between the elastic and viscous properties of the experimental samples. The values of the storage modulus, $\hat{G}'(Pa)$, and that of the loss modulus, $\hat{G}''(Pa)$, depend on the Carbopol concentration of each sample. The storage and loss moduli represent elastic and viscous characteristics, respectively. Complex modulus can be calculated by $\hat{G}^* = \sqrt{\hat{G}'^2 + \hat{G}''^2}$. The loss factor, $\tan\epsilon$, is the ratio of viscous to elastic portion of the viscoelastic deformation, defined as $\tan\epsilon = \frac{\hat{G}''}{\hat{G}'}$. Figure 1.2c displays the variation of storage and loss moduli for different Carbopol gels. The values of both moduli increase with increments in the frequency. It can be also seen that by increasing

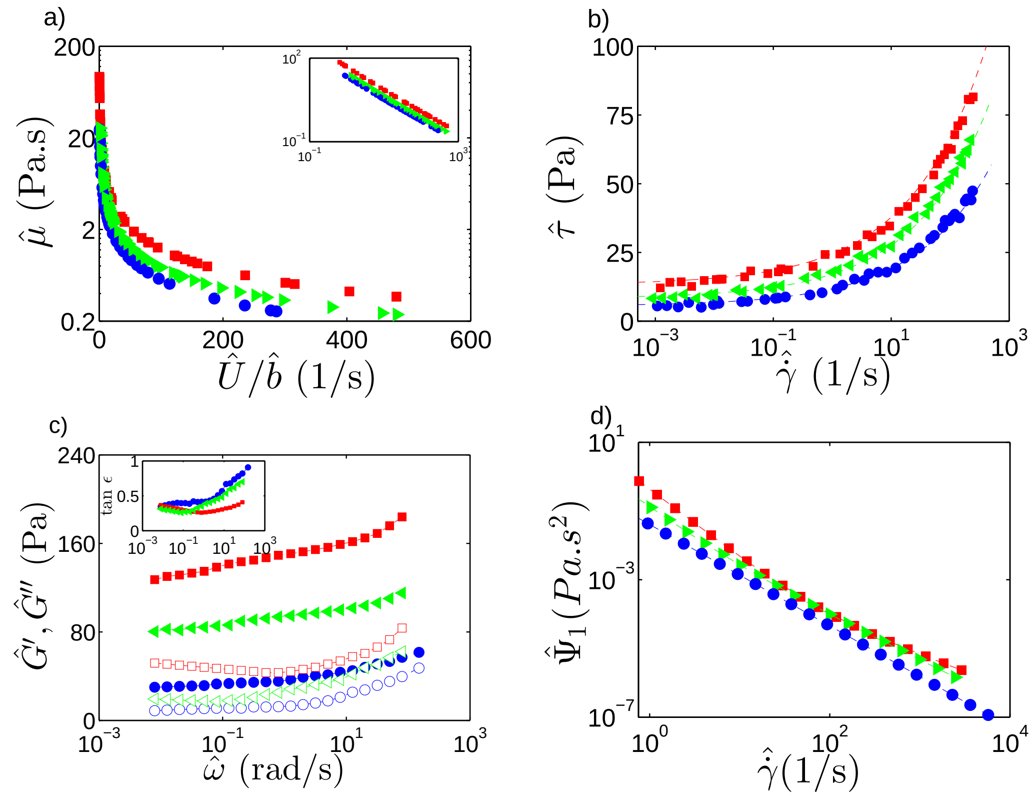

FIGURE 1.2 – Various rheology results for experiments with LCC (●), MCC (▶) and HCC (■). (a) Viscosity ($\hat{\mu}$) as a function of the shear rate ($\hat{U}/\hat{b}$) based on equation (1.4). The inset shows the same data as in the main graph but with a logarithmic scale. (b) Flow curves of the shear stress $\hat{\tau}$ versus the shear rate $\dot{\hat{\gamma}}$. The dashed lines correspond to the Herschel-Bulkley model parameters fitted to data. (c) The storage modulus (filled symbols) and the loss modulus (hollow symbols) as a function of frequency ($\hat{\omega}$). The inset shows the loss factor versus frequency. (d) The first normal stress coefficient ($\hat{\Psi}_1$) as a function of the shear rate.

the Carbopol concentration, the ratio of the storage modulus to the loss modulus is generally enhanced. The inset of Fig. 1.2c shows that the loss factor varies in the range of $0.3 \leq \tan\delta \leq 0.9$. Since the loss factor is smaller than unity, the elastic effects are important. Our Carbopol gels are generally comparable in their elastic behavior as well as loss factor with the values reported in the literature (18; 35).

The Weissenberg number is the appropriate dimensionless number to quantify viscoelastic behaviors under flow, defined as the ratio of the relaxation time ($\hat{\Lambda}$) to the timescale of flow ($\hat{b}/\hat{U}$). To find the Weissenberg number of our Carbopol gels, the following steps were taken. First, the first normal stress difference (N_1), as the evidence of elastic effects, was calculated using the Lodge-Meissner relation (which is frequently employed) (52):

$$\hat{N}_1 = \gamma.\hat{\tau}, \tag{1.5}$$

where γ and $\hat{\tau}$ are the shear strain and the shear stress, respectively. The former was calculated

Carbopol solution	Carbopol % (wt/wt)	NaOH % (wt/wt)	$\hat{\tau}_Y$ (Pa)	$\hat{\kappa}$ (Pa.s^n)	n
Low Carbopol concentration (LCC)	0.10	0.029	5.5	5.7	0.32
Medium Carbopol concentration (MCC)	0.12	0.035	8.3	7.6	0.31
High Carbopol concentration (HCC)	0.15	0.043	13.7	11.8	0.35

TABLE 1.3 – Carbopol composition and determined parameters from rheological measurements, assuming the Herschel-Bulkley model.

through amplitude sweep tests. It is accepted that the comparison between the calculated N_1 from the Lodge-Meissner relation and the values directly measured by a rheometer is satisfactory ((52) and references therein). In the second step, the normal stress coefficient was found through its definition, i.e., $\hat{\Psi}_1 = \hat{N}_1/\hat{\dot{\gamma}}^2$. Finally, $\hat{\Lambda}$ was determined by (19; 87)

$$\hat{\Lambda} = \frac{\hat{\Psi}_1(\frac{\hat{U}}{\hat{b}})}{2\hat{\mu}(\frac{\hat{U}}{\hat{b}})}. \tag{1.6}$$

Figure 1.2d illustrates the first normal stress coefficient ($\hat{\Psi}_1$) as a function of the shear rate ($\hat{\dot{\gamma}}$) for different Carbopol concentrations, showing that $\hat{\Psi}_1$ becomes trivial at larger shear rates and it increases with an increase in the Carbopol concentration.

We end this characterization section by reminding that the air-Carbopol surface tension value used for analyzing our experimental results is slightly lower than that of air-water, i.e., $\hat{\sigma}$ = 0.066 (N/m), taken from the literature (8). Through developing a Wilhelmy technique, Boujlel and Coussot (8) have shown that the surface tension variation versus low concentrations of Carbopol is nearly negligible, which is the case in our experiments.

1.5 Results and discussions

In this section, we present and discuss our main findings for a wide range of experimental parameters studied. In a typical experiment, the cell is already full of Carbopol solution while a constant pressure gradient is applied to the system. Due to the large viscosity difference between air and Carbopol, the air penetrates into the gel, forming various interesting patterns, which we will discuss below. Examining experimental results consists of two separate analyzes: first, analyzing the morphological behaviors based on experimental images and, second, quantifying the finger width and the finger tip velocity. The last two parameters remain almost constant throughout each experiment, except for close to the channel ends.

1.5.1 Main flow behavior

Let us begin with explaining the main flow regimes in our experiments and their qualitative features. In a sequence of increasing the mean imposed displacement velocity, $\hat{V}$, while the rest of the flow parameters are fixed, we observe that the flow morphology changes significantly. For example, Fig. 1.3a presents three different regimes with distinct patterns observed in a typical experimental set. These flows regimes, also presented as videos in supplementary materials, can be explained as follows:

— At low $\hat{V}$, a *yield stress* regime is observed, which consists of many fingers (top image). In fact the process initially starts with a finger, for which the tip quickly splits and asymmetric fingers are formed. The destabilization and splitting continues and more fingers are progressively created. Therefore, the displacement flow eventually exhibits a ramified structure with many fingers.

— At larger $\hat{V}$, the flow behavior changes; here, a *viscous* regime with a single, narrow finger is found (middle image). The shape of this single finger is very similar to that of classical viscous fingers in Newtonian displacement flows (44; 81). In this regime, the tip splitting is suppressed. The formed finger is approximately symmetric and it is placed more or less in the middle of the channel.

— At much larger $\hat{V}$, the flow presents an *elasto-inertial* regime. In this pattern, there is usually an asymmetric finger in middle of the channel while there are secondary instabilities at the finger sides, leading to a side-branching structure (bottom image). While the main finger does not present tip splitting, highly branched finger sides are eventually formed. These branches may have different lengths and angles. It may be worth noting the relevant literature of viscoelastic displacement flows where a variety of side branching morphologies, depending on the fluid type and the imposed velocity, are observed (49).

Although, these observations were described versus the mean imposed velocity $\hat{V}$, they can be equally presented versus the finger tip velocity ($\hat{U}$), since these two velocities are proportional. The finger tip velocity is however preferred as velocity scale to define the capillary number.

Figure. 1.3d plots the variation of the finger width, $\hat{w}$, versus the finger tip velocity, $\hat{U}$. It should be noted that in some cases the local finger width varies along the channel so that the average finger width has been used to calculate all the dimensional and dimensionless parameters throughout this work. However, the variation of the local finger width with time is negligible. The three different flow regimes, which were explained in Fig. 1.3a, are marked by different symbols on this graph. At low $\hat{U}$, where the yield stress regime is found, the finger width remains nearly constant as $\hat{U}$ increases. At larger $\hat{U}$, the finger width changes its behavior as it starts to continuously decrease with $\hat{U}$. At very large $\hat{U}$, the flow transitions to the elasto-inertial regime, where the variation of $\hat{w}$ is not monotonic. For example, at

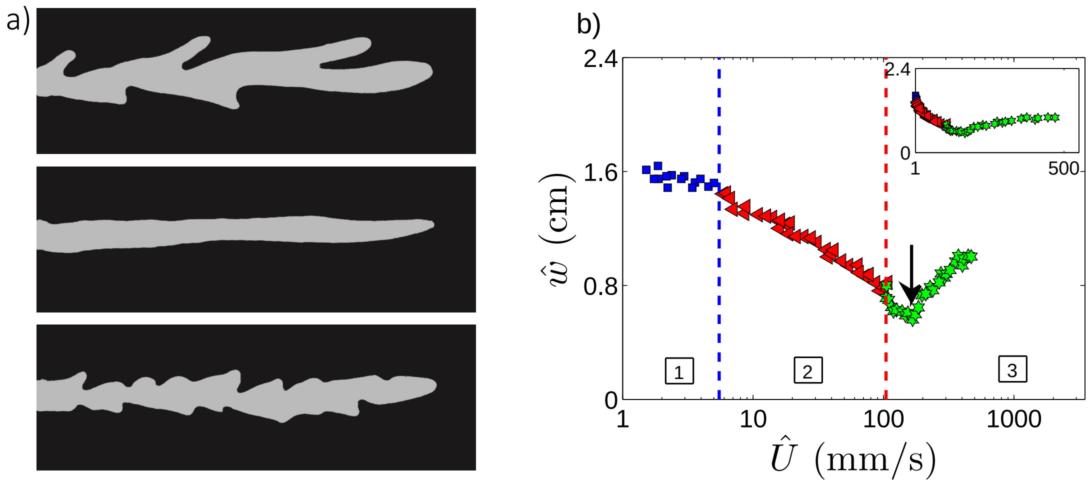

FIGURE 1.3 – Experimental results of the displacement of an MCC gel by air in a Hele-Shaw cell geometry with $\hat{b}$ = 0.9 (mm). (a) Experimental images of the displacement flow. The air flows from left to right. Effects of increasing the mean imposed velocity ($\hat{V}$) on the finger patterns can be seen. The mean imposed velocities are $\hat{V}$ = 0.58, 6.3, 31.4 (mm/s) and the finger tip velocities are $\hat{U}$ = 2.4, 30.2, 147.5 (mm/s), from top to bottom. The field of view for each of these snapshots is 4.7×21.3 (cm^2). (b) Variation of the finger width, $\hat{w}$, versus the finger tip velocity, $\hat{U}$. Three different flow regimes are marked by ■ (yield stress regime), ▸ (viscous regime), and ★ (elasto-inertial regime). The arrow indicates the transition point where inertial effects start to become important. The inset shows the same data as in the main graph but with a linear scale.

the transition point to this regime, although the flow morphology changes, the finger width initially continues to decrease. However, at larger velocities, $\hat{w}$ suddenly starts to increase and it finally reaches almost a plateau at extremely large $\hat{U}$ (visible in the inset). The change in the morphology may be attributed to elastic effects, while the non-monotonic behaviors of $\hat{w}$ implies the appearance of inertial effects. It will be argued later, in more details, that inertial effects are responsible for the increase in the finger width.

Figure 1.4 shows variation of the finger width versus the finger tip velocity, for different Carbopol concentrations and channel thicknesses. Although the value of $\hat{w}$ is affected by both of these parameters, a general common behavior can be recognized for all experiments: $\hat{w}$ is nearly independent of velocity at very small $\hat{U}$, decreases at medium $\hat{U}$, suddenly starts to increase at large $\hat{U}$ and finally reaches almost a plateau at very large $\hat{U}$.

1.5.2 Yield stress regime

In an interesting experimental study using gels and foams, Lindner *et al.* (43; 44) were first to quantify the yield stress regime of viscoplastic fluids. They backed up their experimental results with their theoretical predictions from an earlier paper (17). Although our experimental gel is different, our results in this regime show very good agreement with the findings of Lindner *et*

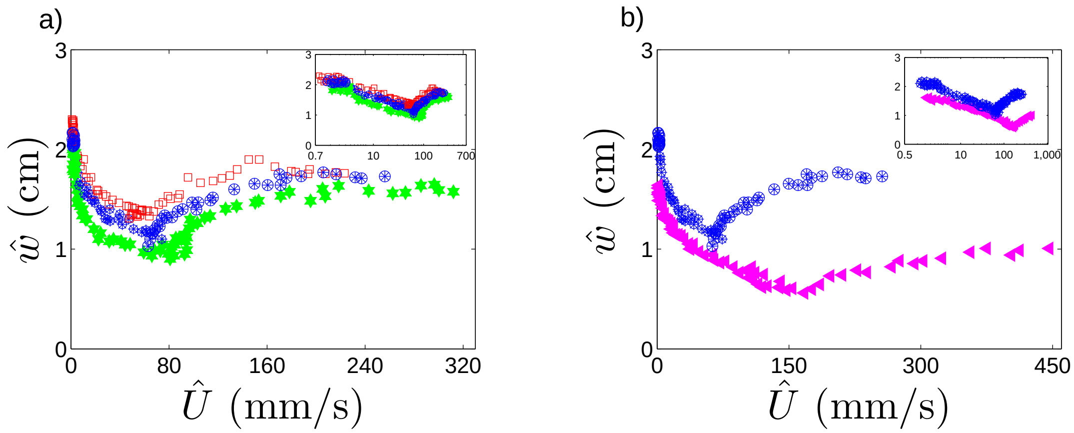

FIGURE 1.4 – Variation of the finger width versus the finger tip velocity: (a) The results are shown for three Carbopol concentrations and a fixed channel thickness ($\hat{b}$ = 1.5 (mm)). The data correspond to experiments with LCC (□), MCC (⊛) and HCC (★). (b) The results for two different channel thicknesses and a fixed MCC. The data correspond to experiments with $\hat{b}$ = 1.5 (mm) (⊛) and $\hat{b}$ = 0.9 (mm) (◂). The insets are the same as the main graph but with a semi-log x-axis, where the three regimes are more visible.

al. (43); see also (46). Although, Van dam *et al.* (81) have observed tip-splitting and ramified structure for the shear-thinning fluid at very low velocities, we believe that, similar to the work of Lindner *et al.* (43), the patterns observed in our experiments at low velocities are due to yield stress rather than shear-thinning effects. Figure 1.5 shows the finger width versus the finger tip velocity. As can be seen, there is not much noise in our experimental results, unlike those of Lindner *et al.* (43). This figure shows that the finger width is independent of the finger tip velocity (or the mean imposed flow velocity) in the yield stress regime, for a large number of experimental data presented. The reason is that, for small $\hat{U}$, the yield stress is predominant so that the displaced fluid is not yielded everywhere and therefore the each air finger does not sense the presence of the channel walls or other fingers (see (43)). The appearance of the ramified structure can be attributed to this feature since the finger can frequently split without feeling the surroundings.

Based on Darcy's law, there is a linear relation between pressure gradient and velocity for Newtonian fluids in the Hele-Shaw cell. For these fluids, Chouki *et al.* (14) have demonstrated through linear stability analyzes that the wavelength of maximum growth ($\hat{\lambda}_m$) is governed by the ratio of capillary to viscous stresses expressed as $\hat{\lambda}_m \propto \sqrt{\frac{\hat{\sigma}\hat{b}^2}{\hat{\mu}\hat{U}}}$, in which the viscous stress has been approximated by $\frac{\hat{\mu}\hat{U}}{\hat{b}}$. However, the relation between pressure gradient and velocity for yield stress fluids is non-linear and instability may occur even at vanishing velocities (17). Thus, as the stress approaches the yield stress at low shear rates, we may simply replace the viscous stress in the relation for λ_m by the yield stress to find $\hat{\lambda}_m \propto \sqrt{\frac{\hat{\sigma}\hat{b}}{\hat{\tau}_y}}$ (46). More rigorously, Coussot (17) has analytically proved that this relation is appropriate. Assuming that the finger

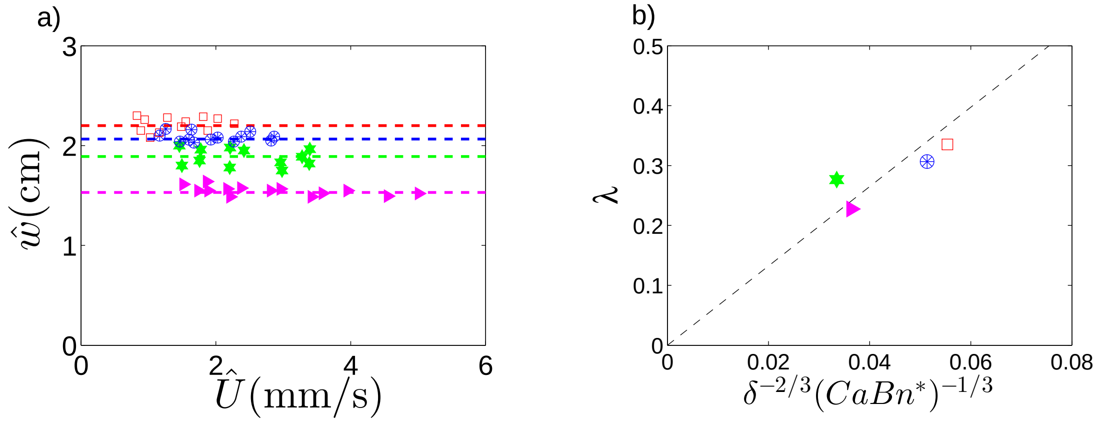

FIGURE 1.5 – Results for the yield stress regime with the following experimental parameters: $\hat{b}$ = 1.5 (mm) & LCC (□), $\hat{b}$ = 1.5 (mm) & MCC (⊛), $\hat{b}$ = 1.5 (mm) & HCC (★), and $\hat{b}$ = 0.9 (mm) & MCC (▸). (a) Variation of the finger width versus the finger tip velocity. The horizontal dashed lines show the mean values of $\hat{w}$ for all $\hat{U}$ in this regime. These mean values are used for plotting the subfigure on the right. (b) The dimensionless mean value of finger width ($\lambda = \hat{w}/\hat{W}$) as a function of $\delta^{-2/3}\left(CaBn^*\right)^{-1/3}$.

width after destabilization corresponds to the maximum growth wavelength, we can show that the dimensionless finger width in the yield stress regime satisfies $\lambda \propto \delta^{-2/3}(CaBn^*)^{-1/3}$, where Bn^* is the modified Bingham number (78) defined as $Bn^* = \frac{\hat{\tau}_y}{\hat{\tau}_y+\kappa(\hat{V}/\hat{b})^n} = \frac{Bn}{1+Bn}$. Figure 1.5b shows the dimensionless mean value of the finger width λ as a function of $\delta^{-2/3}(CaBn^*)^{-1/3}$, showing a nearly-linear relation, which is in good agreement with previous theoretical (17) and experimental observations for other types viscoplastic fluids (43; 46).

1.5.3 Viscous regime

We showed earlier that at higher velocities, the displacement of Carbopol by air transitions from the yield stress regime to the viscous regime. Two features are associated to the viscous regime in our viscoplastic displacements. First, morphologically, a thin finger advances in the middle of the channel. Second, the finger width decreases as the mean imposed flow velocity or the finger tip velocity increases. Let us look further into the variation of the finger width in this regime.

Figure 1.6a presents the variation of the dimensional finger width ($\hat{w}$) as a function of the finger tip velocity ($\hat{U}$) for various experimental parameters. All of the experimental data show a continuous decrease in $\hat{w}$ in the viscous regime. In this regime, viscous forces balance surface tension forces. The latter increase as the velocities increase. Figure 1.6a interestingly shows that for a given $\hat{U}$, the width of finger decreases by increasing the concentration of Carbopol, which is perhaps due to the overall increase in the viscosity of the Carbopol solution. In addition, this subfigure shows that for a constant Carbopol concentration, increasing the channel thickness

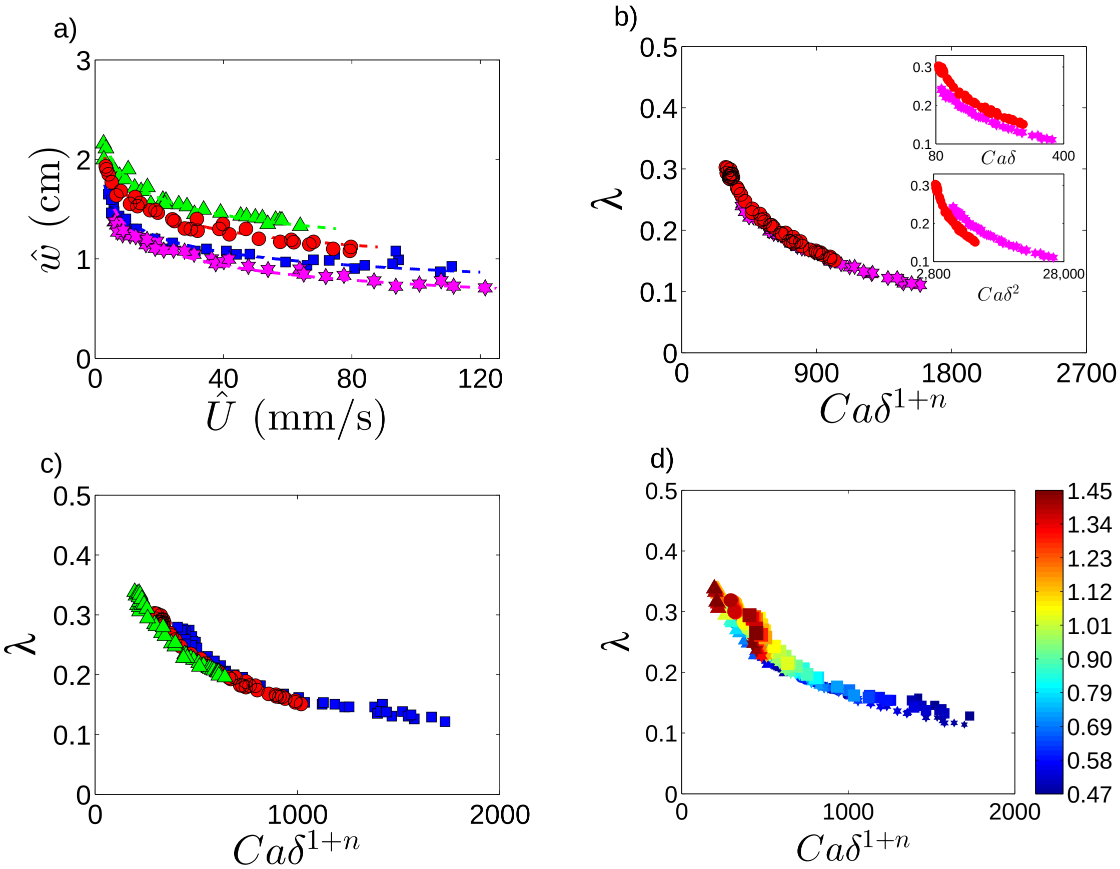

FIGURE 1.6 – Finger width versus various parameters for $\hat{b}$ = 1.5 (mm) & LCC (▲), $\hat{b}$ = 1.5 (mm) & MCC (•), $\hat{b}$ = 1.5 (mm) & HCC (■), and $\hat{b}$ = 0.9 (mm) & MCC (★). (a) $\hat{w}$ versus $\hat{U}$. The dashed lines are fitted curves as eye guides. (b) λ versus $Ca\ \delta^{1+n}$, showing the collapse of two data sets (different channel thicknesses) onto a single curve. In the top & bottom insets, the exponents of δ are 1 and 2, respectively. (c) λ as a function $Ca\ \delta^{1+n}$, showing the collapse of 4 data sets (different Carpool concentrations) onto a single curve. (d) Values of the Bingham number Bn (indicated by size and by the color in the color bars), plotted against λ and $Ca\ \delta^{1+n}$ for all the data sets.

widens the displacement flow finger.

It is known that for Newtonian fluids, $Ca\ \delta^2$ is the appropriate dimensionless group which enables the collapse of all finger widths onto a master curve (30; 50; 75; 80). This dimensionless group has been also used for weakly shear-thinning fluids with modified Darcy's law in which viscosity $\hat{\mu}$ is substituted by shear dependent viscosity $\hat{\mu}\left(\hat{\dot{\gamma}}\right)$ (41; 36; 65; 80; 3). Lindner *et al.* (41) showed that this substitution is only valid when the fluids are very weakly shear-thinning ($n > 0.65$). This becomes relevant to our work since the power-law index in the Herschel-Bulkley model (n) for our gel is less than 0.4 so that our fluids are not weakly shear-thinning. Lindner *et al.* (43) suggested $Ca\ \delta$ as a suitable dimensionless group for viscoplastic fluids with significant shear-thinning effects. Figure 1.6b plots λ versus $Ca\ \delta^{1+n}$ while the insets are versus $Ca\ \delta^2$ and $Ca\ \delta$. We observe from the insets that neither $Ca\ \delta^2$ nor $Ca\ \delta$ enables a perfect collapse of the data. Instead, as the results of the main figure suggest, $Ca\ \delta^{1+n}$ works nearly perfectly as the control parameter for our experiments. The exponent of the aspect ratio that we propose $(1+n)$ shows that the dependency on the aspect ratio is weaker compared to Newtonian fluids, which may be attributed to 3D effects (43). The exponent seems valid for our moderately shear-thinning viscoplastic fluids while it is also consistent with previous finding for Newtonian fluids ($n = 1$) as well as strongly shear-thinning fluids ($n \ll 1$). Although our results seem reasonable, the mechanism behind the modification of the dimensionless group is not crystal clear. In addition to 3D effects, the literature also suggests that the deviation from Darcy's law for strongly shear-thinning fluids may be due to slip layers formation for these fluids in the flow (36; 37). These layers in polymeric liquids originate from velocity gradient at the solid-liquid interface at high shear rates (53; 36; 48).

Figure. 1.6c shows a reasonable collapse of λ versus $Ca\ \delta^{1+n}$, for various Carbopol concentrations. Figure 1.6d plots a neat collapse of data for all sets of experiments in the viscous regime. The values of the Bingham number are superposed as color bars onto this figure, showing the true nature of viscous domination: the data points clearly have different Bn but they nevertheless collapse onto the same master curve. Generally, it is clear from this subfigure that the capillary and Bingham numbers have opposite effects on the dimensionless finger width, λ: by increasing Ca the finger width decreases but by increasing Bn generally (not always) the finger width increases.

1.5.4 Transition between viscous and yield stress regimes

One would like to ideally distinguish different flow regimes versus the dimensionless groups that govern the flow. It is *a priori* expected that Ca must be an important parameter to govern the transition between the viscous and yield stress regimes. In addition, a suitable dimensionless number to consider yield stress effects is the Bingham number. To find the appropriate dimensionless group governing the transition, various combination of the dimensionless forms were examined. Figure 1.7a shows the variation of λ versus $Ca\ \delta^{1+n}/Bn$ for the yield stress and the viscous regimes. For different experimental parameters, it can be seen that λ is initially independent of $Ca\ \delta^{1+n}/Bn$ whereas it decreases versus $Ca\ \delta^{1+n}/Bn$ after a transition point, which takes place at $Ca\ \delta^{1+n}/Bn \approx 550$, on average. Figure 1.7b shows the experimental data points that belong to different flow regimes in the plane of $Ca\ \delta^{1+n}$ and Bn. The yield stress, viscous and elasto-inertial regimes are marked by different symbols. An oblique dashed line is superposed on this figure and it has a slope of $Ca\ \delta^{1+n}/Bn = 550$ (based on the findings of Fig. 1.7a), which can interestingly separate the yield stress and viscous regimes. The special form of the transition dimensionless group, i.e., $Ca\ \delta^{1+n}/Bn$, may be justified by reminding that the transition between the yield stress and viscous regimes occurs at a critical point where the ratio of viscous to surface tension stresses (Ca) significantly exceeds that of yield to viscous stresses (Bn).

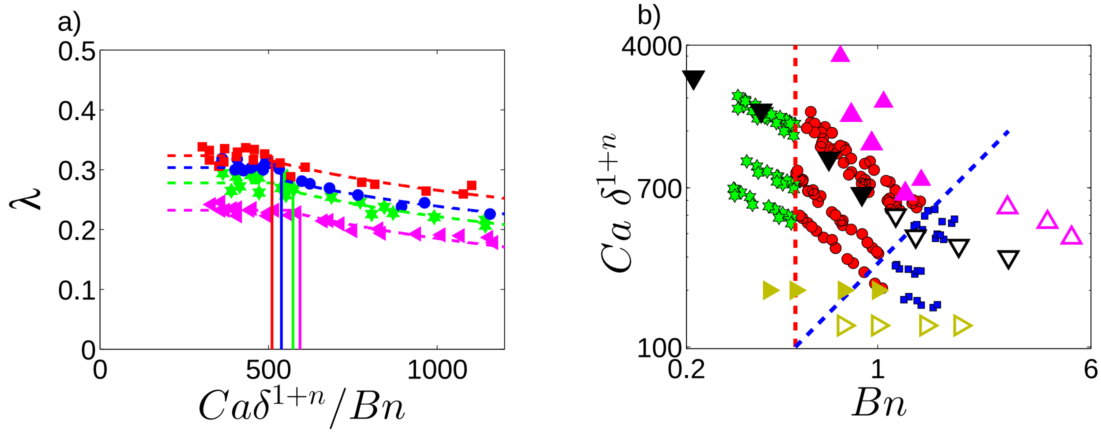

FIGURE 1.7 – (a) λ as a function of $Ca\ \delta^{1+n}/Bn$. The dashed lines are fitted curves as eye guides. The vertical solid lines indicate the transition points at which λ starts to decrease, for each experimental sequence of increasing velocity (on average $Ca\ \delta^{1+n}/Bn \approx 550$). The data correspond to the experiments with $\hat{b}$ = 1.5 (mm) & LCC (■), $\hat{b}$ = 1.5 (mm) & MCC (•), $\hat{b}$ = 1.5 (mm) & HCC (★), and $\hat{b}$ = 0.9 (mm) & MCC (◂). (b) Different flow regimes observed in the plane of $Ca\ \delta^{1+n}$ and Bn. The symbols correspond to the yield stress regime (■), the viscous regime (•), and the elasto-inertial regime (★). The oblique dashed line indicates the transition between the yield stress and viscous regimes ($Ca\ \delta^{1+n}/Bn$ = 550). The vertical dashed line at Bn = 0.5 separates the data corresponding to the viscous and elasto-inertial regimes. The yield stress and viscous regime data points from the literature are also superposed. The symbols correspond to the yield stress regime (hollow symbols) and the viscous regime (filled symbols). The data are from (43) (▼,▽), (21) (▸,▷) and (46) (▲,△).

To test accuracy of $Ca\ \delta^{1+n}/Bn \approx 550$ to delineate the transition between the yield stress and viscous regimes, several data points from different experimental and numerical studies available in the literature (43; 46; 21) are also superposed on Fig. 1.7b. This figure shows that proposed relation is more or less in good agreement with the previous findings from diverse studies.

In Fig. 1.7b, the data points corresponding to the viscous and elasto-inertial regimes are also segregated, on the two sides of the vertical dashed line at $Bn \approx 0.5$. This implies that the transition to elasto-inertial regime occurs when the yield stress effects, captured by the Bingham number, are negligible ($Bn < 0.5$). However, we have already shown that small Bn flows for our Carpobol solutions correspond to large Wi flows (see Fig. 1.2d). In fact, as will be shown in the following section, although Fig. 1.7b shows the smallness of the relative yield stress effects in the elasto-inertial regime, the critical transition between the viscous and elasto-inertial regimes is in fact govern by Wi not Bn.

1.5.5 Elasto-inertial regime

By increasing the mean imposed flow velocity, we transition from the viscous regime to the elasto-inertial regime. By "elasto-inertial" regime, we mean a regime where both elastic and inertial effects are present. Morphologically, in this regime, there usually exists a single finger in more or less the middle of channel while the sides of the finger present branches or wavy-like interfacial patterns. This is attributed to elastic effects (creating non-zero first normal stress difference). In terms of the finger width in this regime, $\hat{w}$ initially continues to decrease with $\hat{U}$ but suddenly starts to increase at a critical $\hat{U}$. This feature seems to be due to non-negligible inertial effects (12).

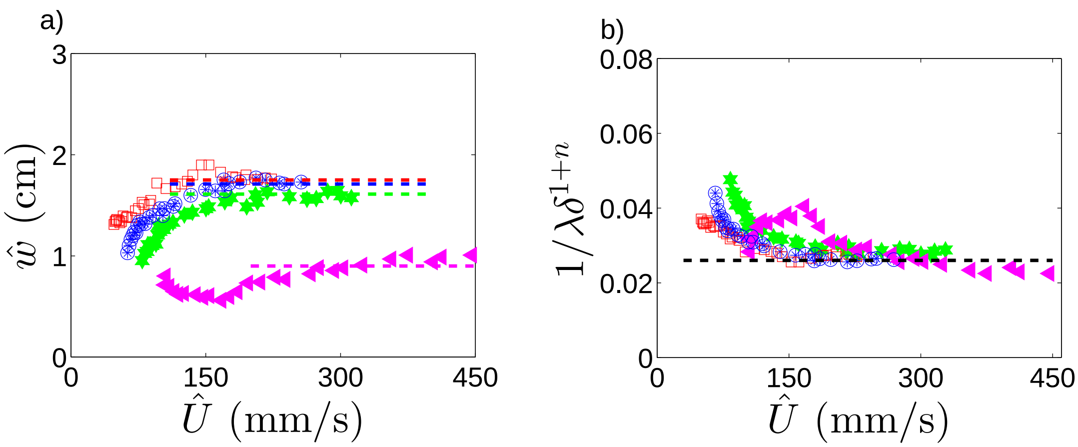

FIGURE 1.8 – Results for the elasto-inertial regime with the following experimental parameters: $\hat{b}$ = 1.5 (mm) & LCC (□), $\hat{b}$ = 1.5 (mm) & MCC (⊛), $\hat{b}$ = 1.5 (mm) & HCC (★), and $\hat{b}$ = 0.9 (mm) & MCC (◂). (a) The finger width as a function of the finger tip velocity. (b) Superposition of the experimental data when $1/\lambda\delta^{1+n}$ is used. The dashed line shows a plateau value of $1/\lambda\delta^{1+n} = 0.026$.

In terms of the finger width, another aspect is also observed, i.e., $\hat{w}$ eventually reaches almost a plateau value, which we will discuss first in this section. Figure 1.8a shows the variation of $\hat{w}$ with $\hat{U}$ for different Carbopol concentrations and channel thicknesses, for the data points belonging to the elasto-inertial regime. Although the results differ from one anther, one trend seems common: after the initial increase, all the curves seem to reach more or less plateau values. However, the plateau finger width for our fluid is significantly narrower than the classical plateau value of Newtonian fluids. For example, for the high Carbopol concentration and the fixed channel thickness $\hat{b}$ = 1.5 (mm), the dimensionless finger width reaches $\lambda \approx 0.24$, compared to $\lambda \approx 0.5$ reported for Newtonian fluids. One hypothesis to justify this discrepancy is that interfacial patterns may be modified due to anisotropy (88; 16; 4; 67) near the finger, resulting in reduced plateau values. This has been examined through using a thin wire inside the Hele-Shaw cell (88; 67), having a small bubble on the finger tip (16; 67), and grooving in the top/bottom plates of the channel (67). An anisotropy state may also exist as a result of the shear dependent viscosity in non-Newtonian fluids, which has been confirmed numerically

(24; 37). For example, the plateau value of λ for shear-thinning fluids at higher finger tip velocities is less than 0.5 because of the smaller viscosity value at the interface, which has been reported experimentally (42).

Figure. 1.8b interestingly shows that the curves can be superposed provided that $1/\lambda\delta^{1+n}$ is used as the dimensionless group, in which viscous effects are apparently absent. This dimensionless group shows that the finger width selection mechanism is completely different from that for Newtonian fluids, although we are unable to fully justify why $1/\lambda\delta^{1+n}$ enables the collapse of data.

- **Inertial effects**:

Let us attempt to quantify inertial effects and their role in the transition point where the width of the finger starts to increase. The relevant dimensionless number for this purpose is the Weber number defined as $We = \frac{\hat{\rho}\hat{U}^2\hat{b}}{\hat{\sigma}_{eff}}$, where $\hat{\rho}$ is the density of the Carbopol gel and $\hat{\sigma}_{eff}$ is the effective surface tension. At high shear rates (elasto-inertial regime) the effective surface tension ($\hat{\sigma}_{eff}$) is more relevant that the surface tension ($\hat{\sigma}$) since the normal stress exerts extra stress on the finger, which should be taken into account. The effective surface tension is calculated through (42):

$$\hat{\sigma}_{eff} = \hat{\sigma} + 1/2\ N_1(\hat{\dot{\gamma}})\ \hat{b}. \tag{1.7}$$

The Weber number quantifies the importance of inertial to surface tension stresses. Our investigation shows that the transition to inertial effects is governed by a modified Weber number (We^*) defined as:

$$We^* = We\ \delta^{1+n}. \tag{1.8}$$

Figure. 1.9a shows that by increasing the modified Weber number, λ starts to increase at a critical modified Weber number of $We^*{}_c \approx 76.5$ for all the experiments performed at different experimental conditions. Regarding the finger width for Newtonian fluids, it has been shown that the dimensionless group $Ca\ \delta^2$ can be modified to include inertial effects (12). Based on this idea, for our non-Newtonian fluid we propose a modified capillary number as a new dimensionless group to help collapse the λ data that belong to viscous and elasto-inertial regimes on the same graph:

$$Ca^* = \frac{Ca\ \delta^{1+n}}{1 + We^*/We^*_c}. \tag{1.9}$$

It can be concluded from equation (1.9) that when We^* is small, $Ca^* \to Ca\ \delta^{1+n}$, and when We^* is very large, $Ca^* \to \frac{We^*_c}{Re}$ (where $Re = \frac{\hat{\rho}\hat{U}\hat{b}}{\hat{\mu}}$), both of which seem to be reasonable limits. Furthermore, the Reynolds number varies in the range of $(2.7 - 81000) \times 10^{-7}$. Note that to calculate the capillary number (Ca), we have used the effective surface tension ($\hat{\sigma}_{eff}$), which is equal to $\hat{\sigma}$ for the yield stress and viscous regimes.

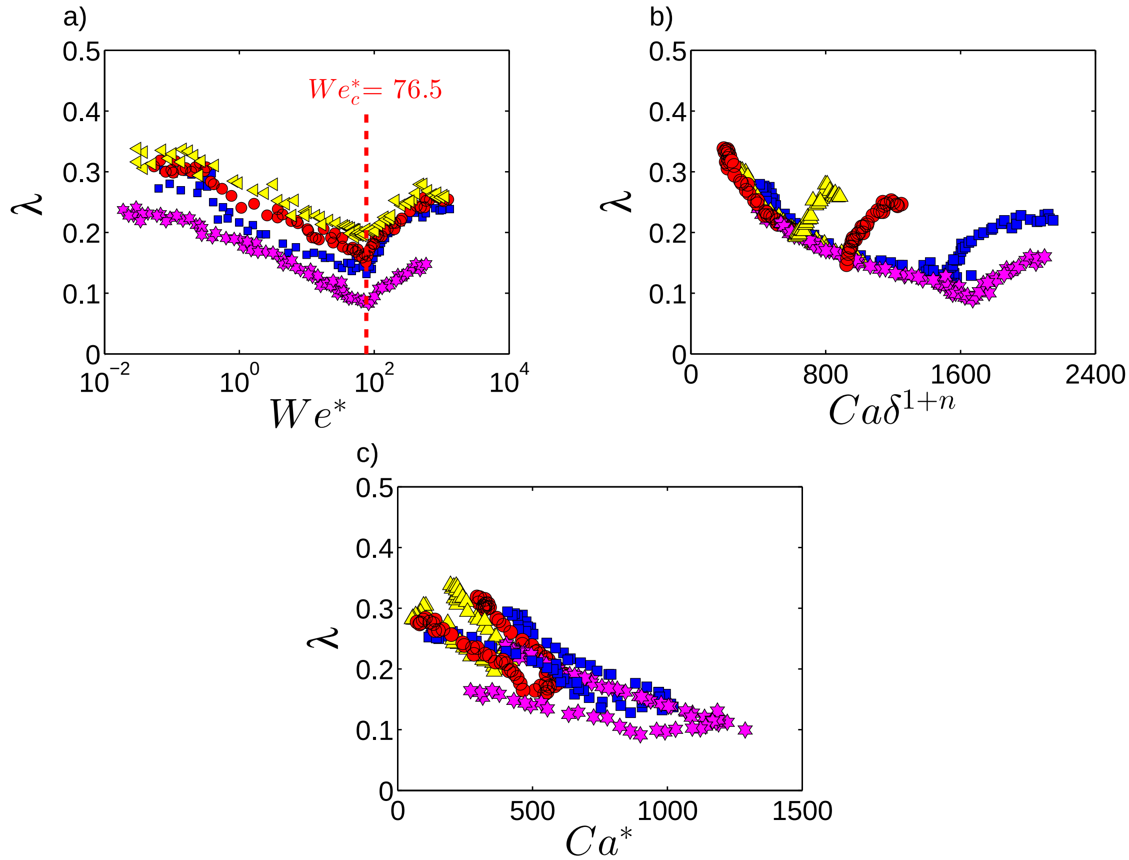

FIGURE 1.9 – The dimensionless finger width as a function different dimensionless groups for data at different aspect ratios and Carpool concentrations: (a) λ as a function We^*. (b) λ as a function $Ca\ \delta^{1+n}$. (c) λ as a function Ca^*. The data correspond to experiments with $\hat{b}$ = 1.5 (mm) & LCC (▲), $\hat{b}$ = 1.5 (mm) & MCC (●), $\hat{b}$ = 1.5 (mm) & HCC (■) and $\hat{b} = 0.9$ (mm) & MCC (★).

While Fig. 1.9b shows that λ corresponding to the experimental data points including viscous and inertial flows do not collapse versus $Ca\ \delta^{1+n}$, Fig. 1.9c shows that a good improvement with respect to the collapse of a wide range of experimental data can be achieved when Ca^* is used as the dimensionless group. However, the collapse onto a single curve is not perfect. One reason for the discrepancy might be that three-dimensional effects due to inertia have been ignored, while it is known such system can be considered two-dimensional when the inertia effects are negligible (69). Another reason may be related to the (non-uniform) thickness of the wetting film of the displaced non-Newtonian fluid, which was not taken into account in our analyzes.

- **Elastic effects**:

We have already shown that the Carbopol gel that we are using has elastic properties manifested at very large shear rates, captured by the relevant dimensionless number, i.e., the

Weissenberg number (Wi). Figure 1.10 classifies the experimental data points that belong to the elasto-inertial regime and those that do not, in the plane of Ca and Wi. It is seen that the data points of the elasto-inertial regime are clearly segregated as they are located at the higher Wi end. The transition to the elasto-inertial regime (with side-branching features) seems to be occurring at more or less $Wi \approx 0.13$, although a small dependency on Ca may be also recognized on the graph. At small Wi, the inelastic data points include both the yield stress regime (with a ramified structure) and the viscous regime (with a narrow single-finger).

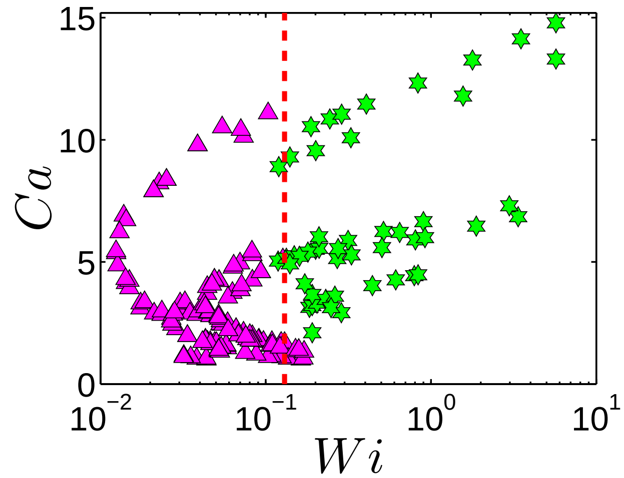

FIGURE 1.10 – The regimes classification based on elastic properties. Viscoelastic regime (★) and inelastic regime (▲). The vertical dashed line shows $Wi = 0.13$, which is roughly the transition to elasto-inertial regime.

For shear-thinning fluids, Kondic *et al.* (37) reported that at higher velocities the growth of shorter wavelengths is increased; consequently, more side branches are created. We have observed a similar feature for our visco-elasto-plastic fluid at larger shear rates. Loosely speaking, elasticity in elasto-inertial regime creates extra stresses in the finger sides (due to the first normal stress difference) that lets (shortwave) perturbations grow, leading to side branching patterns. Therefore, in this regime, the evolution of finger patterns is controlled by a competition between viscous and elastic forces.

Although we have so far observed the "indirect" influence of elasticity through changing the first normal stress difference (allowing for perturbations to grow), we expect major detectable elastic response to be only seen at extremely high shear rates, with significantly larger Wi. Unlike the flows at $Wi \sim O(1)$ where the deformations are observed to be totally irreversible, for larger Wi, we may expect to detect a real elastic response (which is at least partially reversible). Therefore, we set up an experiment at an extremely large finger tip velocity (i.e., 2000 (mm/s)), which corresponds to $Wi = 5.74$ and $\hat{\Lambda} = 18.7$ (ms) (i.e., the relaxation time). The ultra-high-speed camera was set to take 2000 images per second. Figure 1.11 depicts an

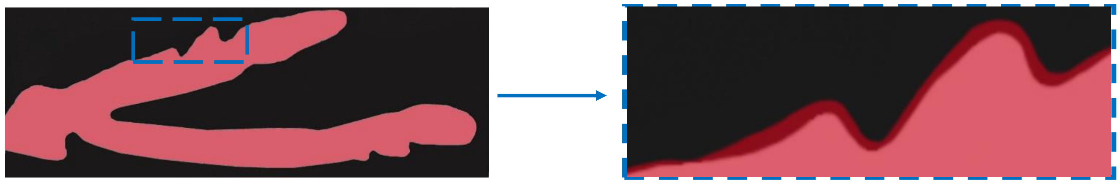

FIGURE 1.11 – An experimental snapshot showing the movement of the finger side due to an elastic response. The right image is zoomed-in on the indicated box of the left image. The red color indicates the displacing fluid (air) and the black color shows the displaced fluid (Carbopol). The dark red color shows the oscillation of the Carbopol layer within $\hat{t} = 0.358 - 0.4$ (ms). The images show the field of view of 5.8×17.5 (cm^2) (left) and of 4.3×1.25 (cm^2) (right).

experimental image which shows the elastic response of our gel. We observe that the side branches move back and forth when undergoing large stresses due to the extremely rapid air flow.

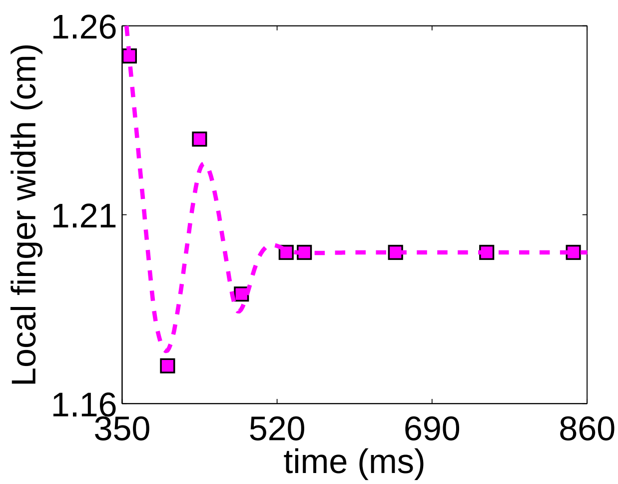

FIGURE 1.12 – The oscillation in the local finger width due to elastic response at different times with respect to the beginning of the experiment. The dashed line is smoothing spline fitted curve.

Fig. 1.12 shows that the variation of the local finger width versus time for the experiment of Fig. 1.11. Two effects can be seen: first, it is observed that the local finger width initially oscillates but it relaxes shortly after a few oscillations. Second, the deformation is not totally reversible, due to viscous dissipation. This experiment is also interesting in providing valuable information. For example, lengthwise, it can be seen that the maximum deviation is 6.4% compared to initial finger width. With regard to time, the time corresponding to the maximum deviation of the finger width is $\Delta\hat{t}_m \approx 42$ (ms) and the time needed for the finger to completely relax is $\Delta\hat{t}_m \approx 139$ (ms). The latter is interestingly in the order of the longest relaxation time.

1.6 Secondary features of the displacement flow

It must be accepted that the flow that we consider present various, complex features and we cannot cover all the flow aspects in a single study. However, there are secondary features of the displacement flow that are worth discussing in the present work. In this section, we attempt to introduce and explain two of these interesting features in the following two subsections below.

1.6.1 Static residual wall layers

The first secondary feature of the flow that we look into is related to the flow in the cross-section of the channel. Through a comparison between the flow volume measured by the flow meter and that calculated through image processing, we have found out that the Carbopol gel cannot be completely swept out by the air within the cross section of the channel. This implies the existence of wetting films of Carpool adjacent to the lower and the upper plates of the Hele-Shaw cell. Assuming a zero film thickness, image processing can deliver a mean imposed flow velocity, $\hat{V}_M$, which can be compared to the real mean imposed flow velocity, $\hat{V}$, measured by the flow meter. These two velocities can be simply related through

$$\frac{\hat{V}_M}{\hat{V}} = \frac{\hat{b} - 2\hat{t}_{ave}}{\hat{b}}, \tag{1.10}$$

where $\hat{t}_{ave}$ is the mean wall film thickness defined as $\hat{t}_{ave} = \frac{\hat{t}_u + \hat{t}_l}{2}$ with $\hat{t}_u$ and $\hat{t}_l$ being the wetting layer thicknesses in the upper and lower walls, respectively.

Figure 1.13a shows the dimensionless mean thickness of the wetting films ($t = \frac{\hat{t}_{ave}}{\hat{b}}$) versus the capillary number. It can be seen that by increasing the capillary number, t increases, which seems to be a reasonable effect: as the relative surface tension stress decreases the film layer thickness increases. At larger Ca (~ 10), it can be observed that the mean film thickness in the vicinity of the wall can reach up to %10 of the gap thickness while Tabeling & Libchaber (75) observed that the mean residual layer thickness for Newtonian fluids reached up to %1 of the gap thickness at small capillary number ($Ca < 5 \times 10^{-3}$). In this work, due to dealing with large capillary numbers in the presence of a yield stress (proportional to the Carbopol concentration), the wetting layer thickness is relatively large. Thus, expectedly our results do not follow the Bretherton's law, which is only applicable to Newtonian fluids in small capillary numbers and breaks down for large values of capillary numbers ($Ca > 10^{-2}$) (76).

Figure 1.13b shows the same data points as in Fig. 1.13a while the values of Bn are marked by colors and symbol sizes. This figure shows that increasing Bn generally results in decreasing t, which may seem counter-intuitive at a first glance. In fact, increasing Bn of the displaced fluid influences the plug ahead of the displacing finger and results in a reduction of the residual wall layer thickness (84). It should be noted that, for the ranges of the dimensionless numbers studied, the maximum variation of the film thickness with respect to the mean value

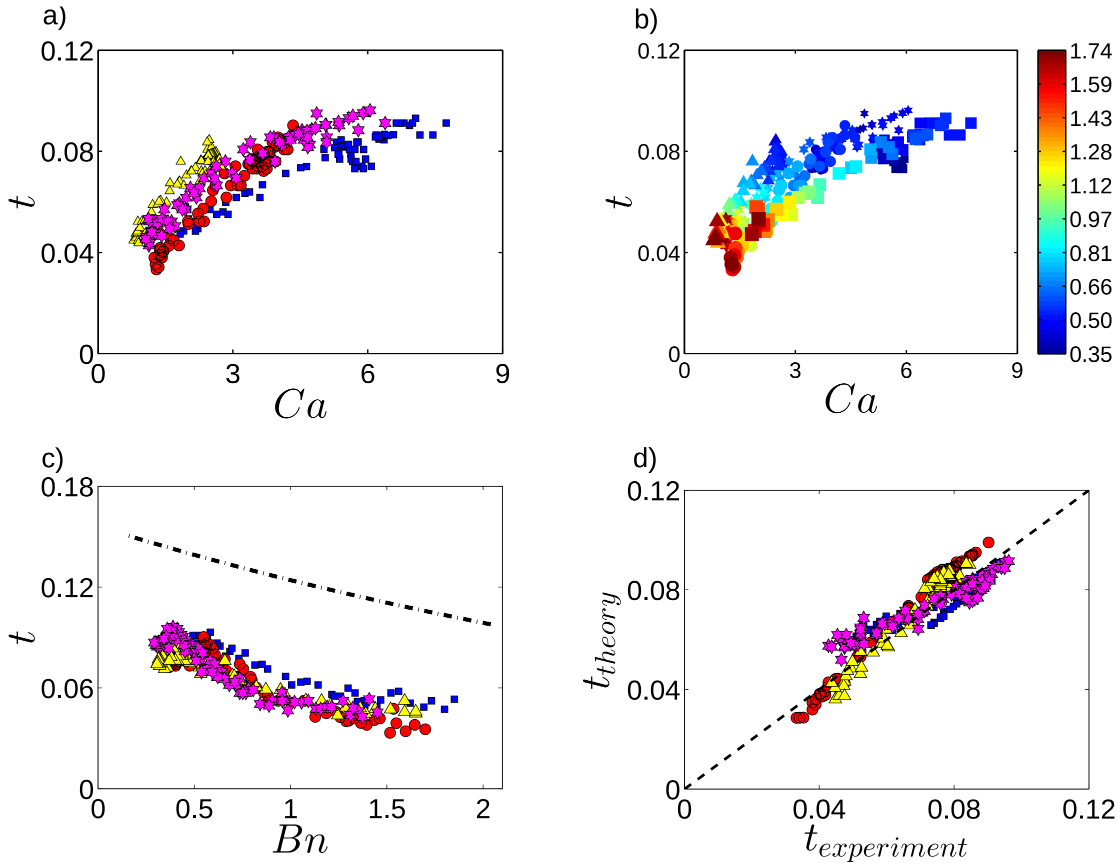

FIGURE 1.13 – Results for experimental data corresponding to $\hat{b}$ = 1.5 (mm) &LCC (▸), $\hat{b}$ = 1.5 (mm) & MCC (●), $\hat{b}$ = 1.5 (mm) and HCC (■), and $\hat{b}$ = 0.9 (mm) & MCC (★). (a) Thickness of wetting film (t) as a function of Ca. (b) Variation of Bn in the plane of t and Ca. The colors/symbol sizes illustrate the magnitude of Bn. (c) Variation of t versus Bn. The dash-dot line shows h_{circ} from equation (1.11), i.e., when $Ca \to \infty$. (d) Comparison between the experimental and theoretical prediction (equation (1.14)) of the wall layer thickness. The dashed line shows $t_{experiment} = t_{theory}$.

is ±0.048 (mm) and the variation of finger width is ≈ ±7.1 (mm). Therefore, the variation of film thickness does not have a significant effect on the finger.

After displacing finger tip has passed, the residual wall layers in our experiments do not seem to move; thus, it may be reasonable to assume that they are completely static. For miscible displacement flows at their immiscible limit (i.e., $Ca \to \infty$), static residual wall layers of viscoplastic fluids have been first analyzed by Allouche *et al.* (2). Their combined theoretical and computational study for symmetric 2D channel flows showed that the wall layer thickness can be well approximated by the recirculation layer thickness, h_{circ}, defined as a thickness at which a steadily displacing finger would advance with the same velocity as that of the center-line of the downstream flow. Provided that $t < h_{circ}$ a recirculatory region would occur in the channel center, in front of the displacing finger within the cross-section, which in return increases viscous dissipation. The flow prefers to avoid this situation. h_{circ} depends only on the Bingham number and it is defined as (2; 84):

$$h_{circ} = 1 - \frac{2Y}{Bn(1-Y)^2}, \tag{1.11}$$

where Y is found through the solution of

$$Y^3 - 3Y\left[1 + \frac{2}{Bn}\right] + 2 = 0, \tag{1.12}$$

for a given Bn. The residual wall layer thickness in the theory above shows an inverse relation to Bn, which is consistent with our experimental observations. In a recent computational study for channel flows, Swain *et al.* (74) have also showed that at low Bingham number ($Bn < 30$), increasing the Bingham number leads to decreasing the average residual layer thickness.

Using equation (1.11), h_{circ} has been calculated and superposed as a dash-dot line on Fig. 1.13c. The data points on this figure show the mean wetting layer thickness versus Bn. Although the trend is reasonable, h_{circ} overestimates the static wall layer thickness in our experiments, which is due to the presence of the non-negligible surface tension stress in our flows; in other words $Ca \sim O(1)$ in our experiments. In general $t = f(Bn, 1/Ca)$ and one may assume that $f(Bn, 0) = h_{circ}$. When $Ca \neq \infty$, using Taylor series, we can therefore write

$$t = f\left(Bn, \frac{1}{Ca}\right) = f\left(Bn, 0\right) + f'\left(Bn, 0\right)\frac{1}{Ca} + \frac{f''\left(Bn, 0\right)}{2}\frac{1}{Ca^2} + \frac{f'''\left(Bn, 0\right)}{6}\frac{1}{Ca^3} + \ldots, \tag{1.13}$$

for which the best fit from the experimental results furnishes

$$t \approx h_{circ} - \frac{0.024}{Ca} + \frac{0.098}{Ca^2} - \frac{0.126}{Ca^3}. \tag{1.14}$$

To test the accuracy of modified theoretical equation above, the predicted layer thicknesses using equation (1.14) versus the experimental layer thicknesses reported in Fig. 1.13c are presented in a parity plot, illustrated in Fig. 1.13d. This figure shows the modified equation is fairly successfully to predict the wall layer thickness, for a wide range of experiments at different values of Ca and Bn.

1.6.2 Network structure regime

One of the interesting features observed in some of ours experiments was a secondary flow aspect, which we term a *network structure* regime, associated to the formation of Carbopol network structures within the finger domain, after the displacing front had already passed. This effect was seen in the experiments conducted at lower concentrations of Carbopol and very high mean imposed velocities. In order to simplify the explanation of the network structure regime, we divide the process into 4 main stages, i.e., the thin residual layers formation (stage 1), the residual layers break up and formation of cavities (stage 2), the extension of cavity area (stage 3), and the final structure formation (stage 4).

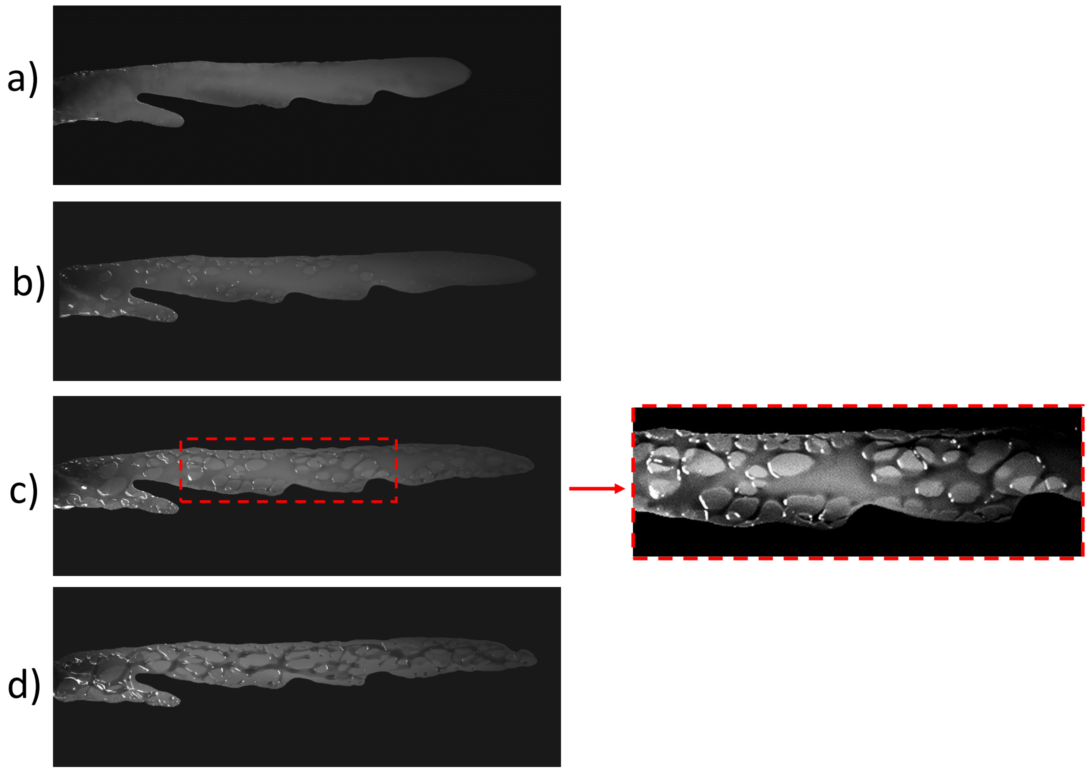

FIGURE 1.14 – An experimental snapshot (top view) showing 4 sequential steps of the process of the network structure formation within the finger domain. The experimental times are $1326, 1353, 1393, 1473$ (ms), from top to bottom. The mean imposed velocity is $\hat{V} = 34.6$ (mm/s) (the finger tip velocity is $\hat{U} = 315.3$ (mm/s)). The images correspond to the experiment with $\hat{b} = 0.9$ (mm) & LCC. The field of view for these snapshot is 22.8×5.6 (cm^2).

We now try to explain the 4-stage process step by step using Fig. 1.14, illustrating 4 sequential images (top view of the cell), for an experiment conducted with LCC at a large imposed air flow rate. These images were taken at 90 (fps). The first stage of the process, i.e., the formation of the thin residual layers, is straightforward. As the air displaces the Carbopol gel, a finger is formed. Within the channel cross-section, as the finger tip advances, two thin residual layers of the Carbopol gel are left behind on the upper/lower walls of channel. These residual layers within the finger domain can be distinguished by the gray color area in Fig. 1.14a (which means that in this area, both air and Carbopol are present). In this first stage, nothing in particular is observed inside the finger. After a few microseconds, as seen in Fig. 1.14b, a partial break up of the residual Carbopol layers is observed, which is perhaps one of the reason to form some cavities (i.e., stage 2). In the stage of the extension of cavity area (i.e., stage 3), in Fig. 1.14c, the break up of the residual layer continues and the area of cavities is increased. The extension stage continues until the thickness of the residual layer becomes constant and the final structure formation stage is reached (Fig. 1.14d). At this stage, a network of Carbopol structure is formed inside the finger domain.

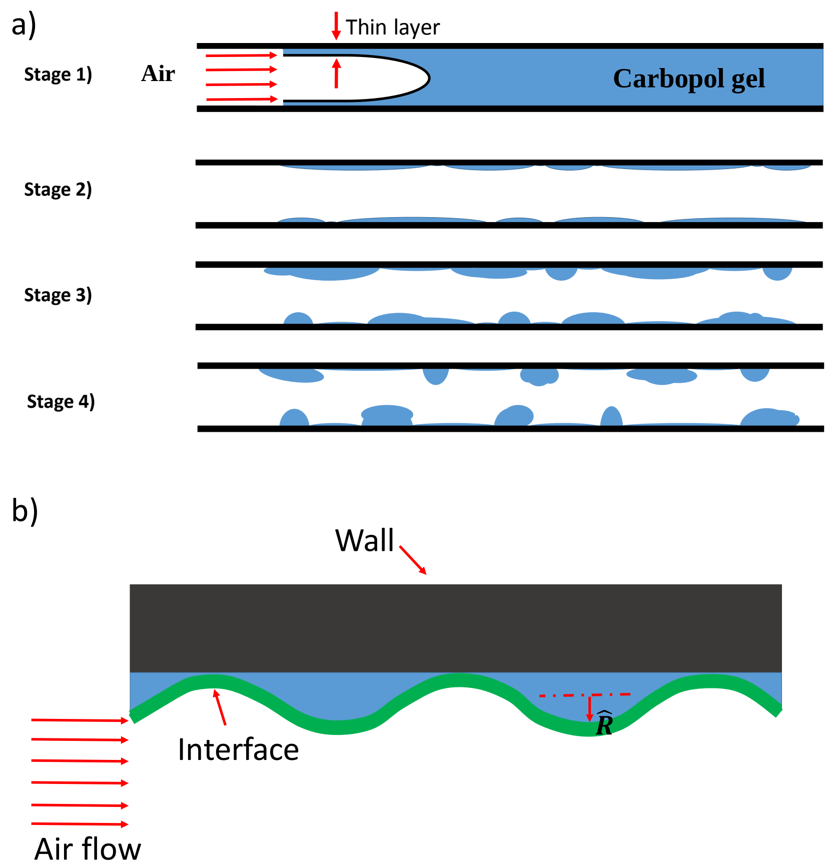

FIGURE 1.15 – (a) Schematic view of a probable 4-stage process of the formation of network structure regime (side channel view). (b) Schematic view of the intermediate stage of the network structure formation, as the residual layer breaks up into several pieces.

A schematic view of what we think is happening may be helpful. Figure 1.15a shows a schematic (cell side view) of the 4 sequential stages observed in the network structure regime. The top image is the formation of the thin residual layers of Carbopol gel, adjacent to the walls. In the second stage, the residual layers are broken perhaps since the wall shear stress overcomes the bonding strength in the Carbopol gel layers, causing the cavities to form. In the third stage, the remaining Carbopol pieces on the walls retract and the cavity area extends. Finally, in the final stage, i.e., the structure formation, the residual pieces are almost stationary (and the thickness of Carbopol pieces remains constant).

It seems that the residual layers break up is a key stage in the network structure regime. Two aspects may be important: non-uniformity of the residual layer and the bonding strength of Carbopol. Regarding the latter aspect, at low Carbopol concentrations, the large wall shear stresses induced by the air flow overcome the Carbopol bonding strength so that they are able to significantly weaken the structure of the residual film. Afterwards, the former aspect becomes important: due to the layer non-uniformity, the thin layer is vulnerable to instabilities caused by capillary pressure. Figure 1.15b illustrates a simple schematic of this step, where the residual layer adjacent to the upper wall is at the verge of break up. We may postulate that the air-Carbopol interface is non-uniform and wavy, due to the growth of perturbations of various wavelengths on the surface of the residual layer; see (45; 51; 23) for conceptually comparable phenomena in completely different contexts. In Fig. 1.15b, $\hat{R}$ indicates the local principal radius of the curvature of the sinusoidal perturbation waves. According to the Young-Laplace equation ($\Delta\hat{p} = \hat{\sigma}/\hat{R}$), the smaller the radius of curvature, the higher the pressure jump across the interface. We postulate that at this step, the radius is small so that capillary pressure at certain places is sufficiently large to rupture the weakened structure bonds, which, in return, leads to the break up of the residual layers. This results in the formation of several Carbopol pieces on the upper/lower walls of the channel.

The descriptions presented are compatible with our experimental observations in that at low Carbopol concentrations, the Carbopol layer naturally has a weaker bonding strength, causing the residual layers to break up more easily. For higher Carpool concentrations, the bonding strength is enhanced (79); therefore, the residual layer is able to resist the break up. Higher air imposed flow rates also increase the wall shear stresses, which may weaken the bonding strength of the Carbopol gel.

The network structure regime may be similar to the film rupture phenomena in which the thin polymer film rupture is caused by capillary pressure, usually when the film thickness is very small (86; 56; 73). Similar to the break up of residual layers, the film rupture processes in thin polymer films may lead to form diverse morphologies. Similar to the network structure regime, pattern formations through the film rupture depend on the polymer composition (or concentration) and the film thickness.

In order to provide further understanding about the network structure regime, characterizing the cavities versus time is useful. Figure 1.16a illustrates the variation in the number and the mean characteristic diameter of cavities versus time for a typical experiment, for which images are processed. It is interesting to note that the number of cavities is not monotonic versus time. Initially the cavities are quickly formed as the residual layer breaks into smaller pieces but the cavities eventually meet and merge with one another. The number of cavities stabilizes at a small plateau value as the network structure appears. On the other hand, the mean characteristic diameter of the cavities continuously increases and it finally reaches a nearly constant value.

The presence of cavities creates a highly non-uniform residual layer, to which we have also looked. Figure 1.16b shows the relative transverse mean light intensities in the finger domain for the 4 sequential images presented in Fig. 1.14, for which the images were converted to gray levels (between 0 to 255). The first image in Fig. 1.14 has been taken as a reference, to

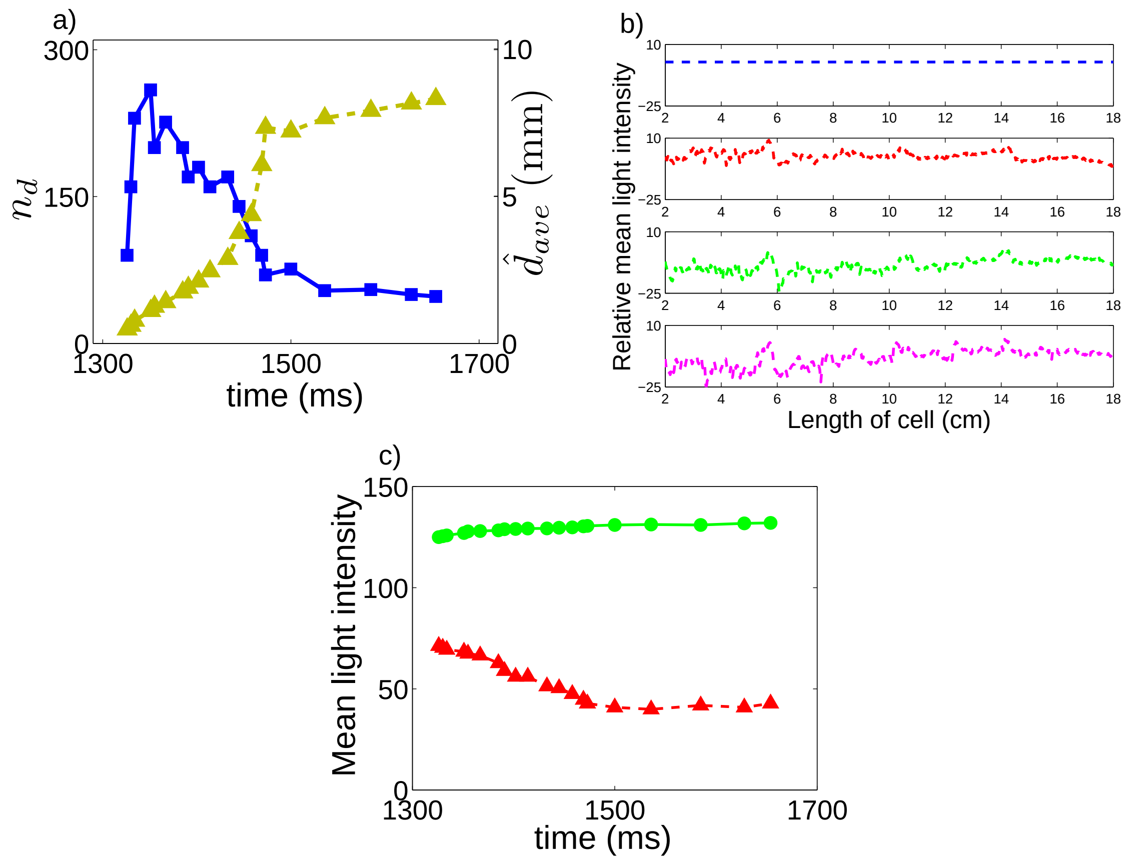

FIGURE 1.16 – (a) Variation in the total number of cavities (■) and the mean characteristic diameter of cavities (▲) versus time, in the network structure regime, for the same experiment as in Fig. 1.14. (b) Variation in relative mean light intensity versus length of cell for 4 sequential images of Fig. 1.14. (c) Variation in mean light intensity of cavities (•) and Carbopol pieces (▲) versus time.

which the relative mean light intensities are compared. Comparing the top and bottom plots in Fig. 1.16, and considering that the film layer thickness is proportional to the light intensity, it can be concluded that the residual layers are highly non-uniform.

In order to gain insight about the thickness of Carbopol pieces, Fig. 1.16c shows the variation of the mean light intensities of 10 areas, each covering 10×10 pixels randomly distributed in either the cavity area or the Carbopol pieces area, versus time. This figure shows that while the mean light intensity of cavities is almost constant, the mean light intensity of Carbopol pieces decreases initially with time but finally reaches a plateau value. This implies that the overall thickness of Carbopol pieces increases but eventually becomes constant.

Various areas in the finger domain can be observed in the network structure regime. In order to observe these areas more clearly, a sequence of images was obtained at 1000 (fps) and plotted in Fig. 1.17. The experiment was conducted with MCC at a very high imposed air flow rate (a video corresponding to this experiment is included in supplementary materials). In these images, 4 areas, marked by Roman numbers, can be distinguished. The first area (I) consists of the finger domain where thin wall layers are present. The seconds area (II) corresponds to a cavity formed on one of the walls. In the third area (III), cavities on both walls are observed. The forth area (IV) corresponds to pieces of Carbopol that are formed.

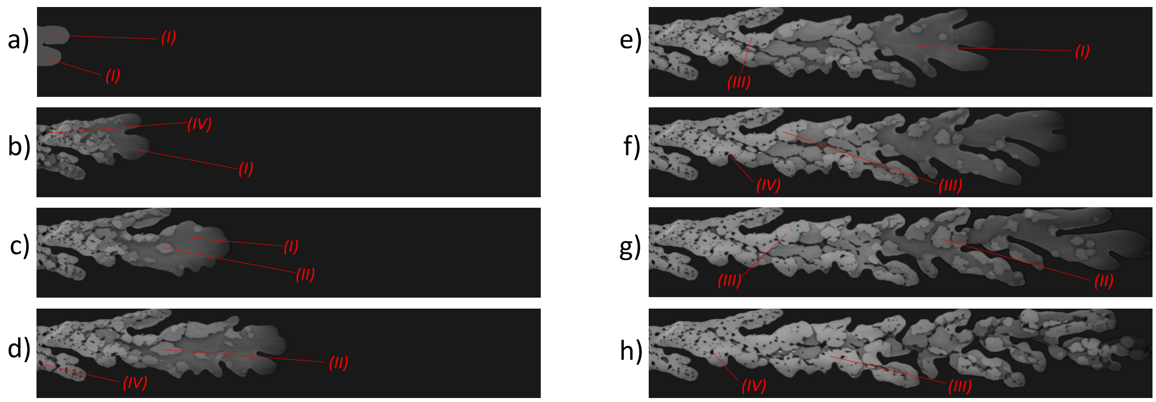

FIGURE 1.17 – Image sequence showing the finger evolution in the network structure regime. Different areas are explained in the text.

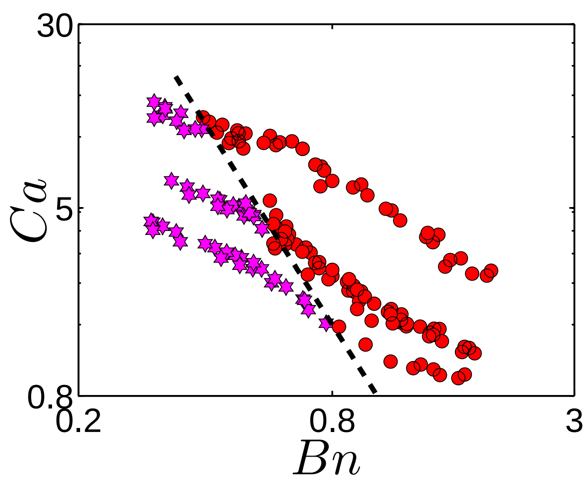

FIGURE 1.18 – A secondary flow regime classification based on the formation of a network structure inside the finger domain. The data correspond to the experiments for the network structure regime are marked by ★ and the ones without by •. The black dashed line indicates transition between the two regimes: $Ca = 0.86Bn^{-2.82}$.

Based on the descriptions mentioned earlier, it may be expected that the values of surface tension and the bonding strength of Carbopol (which is very loosely speaking proportional to the yield stress) to be the important parameters that delineate the boundary to the network structure regime. Therefore, at least Ca and Bn may be considered as the relevant dimensionless groups. Figure 1.18 plots the experimental data points in the plane of Ca versus Bn. Interestingly, the data belonging to the network structure regime are clearly segregated from the rest of the data in this figure. The transition seems to follow a line indicated by $Ca = 0.86Bn^{-2.82}$.

1.7 Summary

We have considered the Saffman-Taylor for non-Newtonian fluids in the Hele-Shaw cell. In this work, air displaced a Carbopol gel, which exhibits both viscoplastic and viscoelastic properties, in addition to shear-thinning effects. The problem is complex as a result of many important dimensionless numbers involved, i.e., the Bingham number (Bn), the capillary number (Ca), the Weber number We, the Weissenberg number (Wi), the aspect ratio (δ), and power-law index (n). We identify three distinct flow regimes: a yield stress regime, a viscous regime and an elasto-inertial regime, based on the morphological differences and finger width variations. These flow regimes and their transition boundaries are studied in depth. We have succeeded to provide a clear picture of the flow over a reasonable range of dimensionless groups. Some of the secondary features of the flow have been also discussed, including the thickness of the residual wall layers as well as an interesting novel pattern, termed the network structure regime. Table 1.4 provides a summary of the main dimensionless groups that our work has delivered to predict various flow features.

Dimensionless group	Significance	Critical value
We_c^*	Transition to inertial effects	76.5
$Ca\ \delta^{1+n}/(Bn - 0.5) : Bn > 0.5$	Transition between the yield stress and viscous regimes	550
Wi	Transition to elastic effects	0.13
$1/\lambda\delta^{1+n}$	Finger width plateau value	0.026
Ca^*	Enable collapse of λ from the viscous and elasto-inertial regimes	-
$\delta^{-2/3}\left(Ca\ Bn^*\right)^{-1/3}$	Enable collapse of λ from the yield stress regime	-
$t \approx h_{circ} - \frac{0.024}{Ca} + \frac{0.098}{Ca^2} - \frac{0.126}{Ca^3}$	Predict mean static residual wall layer thickness	- -
$Ca\ Bn^{2.82}$	Transition from the network structure regime	0.86

TABLE 1.4 – Important dimensionless groups that the present study has delivered.

Supplementary materials: This supplementary section includes two parts:

- Three vidoes showing the three main flow regimes: These videos show the finger evolution and the appearance of different flow patterns. The videos correspond to the experiment with $\hat{b} = 1.5$ (mm) & HCC. I) The yield stress regime: the mean imposed velocity is $\hat{V} = 1.8$ (mm/s) while the finger tip velocity is $\hat{U} = 8.3$ (mm/s). The field of view is 20.8×4.3 (cm^2). II) The viscous regime: the mean imposed velocity is $\hat{V} = 8.6$ (mm/s) while the finger tip velocity is $\hat{U} = 95.5$ (mm/s). The field of view is 19.6×3.7 (cm^2). III) The elasto-inertial regime: the mean imposed velocity is $\hat{V} = 41.7$ (mm/s) while the finger tip velocity is $\hat{U} = 215.2$ (mm/s). The field of view is 20.2×4.1 (cm^2).
- A video showing the network structure regime: The mean imposed velocity is $\hat{V} = 274$ (mm/s) while the finger tip velocity is $\hat{U} = 1068$ (mm/s). The images correspond to the experiment with $\hat{b} = 0.9$ (mm) & MCC. The field of view is 24.6×6.7 (cm^2).

1.8 Bibliography

[1] T.T. Al-Housseiny, P.A. Tsai, and H.A. Stone. Control of interfacial instabilities using flow geometry. *Nat. Phys.*, 8(10):747–750, 2012.

[2] M. Allouche, I. Frigaard, and G. Sona. Static wall layers in the displacement of two visco-plastic fluids in a plane channel. *J. Fluid Mech.*, 424(1):243–277, 2000.

[3] M.B. Amar and E.C. Poire. Pushing a non-Newtonian fluid in a Hele-Shaw cell: From fingers to needles. *Phys. Fluids*, 11(7):1757–1767, 1999.

[4] E. Ben-Jacob, R. Godbey, N.D. Goldenfeld, J. Koplik, H. Levine, T. Mueller, and L.M. Sander. Experimental demonstration of the role of anisotropy in interfacial pattern formation. *Phys. Rev. Lett.*, 55(12):1315, 1985.

[5] E. Ben-Jacob, H. Shmueli, O. Shochet, and A. Tenenbaum. Adaptive self-organization during growth of bacterial colonies. *Physica A*, 187(3):378–424, 1992.

[6] D. Bensimon, L.P. Kadanoff, S. Liang, B.I. Shraiman, and C. Tang. Viscous flows in two dimensions. *Rev. Mod. Phys.*, 58(4):977, 1986.

[7] S.H. Bittleston, J. Ferguson, and I.A. Frigaard. Mud removal and cement placement during primary cementing of an oil well–Laminar non-Newtonian displacements in an eccentric annular Hele-Shaw cell. *J. Eng. Math.*, 43(2-4):229–253, 2002.

[8] J. Boujlel and P. Coussot. Measuring the surface tension of yield stress fluids. *Soft Matter*, 9(25):5898–5908, 2013.

[9] R. Brandao, J.V. Fontana, and J.A. Miranda. Interfacial pattern formation in confined power-law fluids. *Phys. Rev. E*, 90(1):013013, 2014.

[10] F.P. Bretherton. The motion of long bubbles in tubes. *J. Fluid Mech.*, 10(2):166–188, 1961.

[11] A. Buka, P. Palffy-Muhoray, and Z. Racz. Viscous fingering in liquid crystals. *Phys. Rev. A*, 36(8):3984–3989, 1987.

[12] C. Chevalier, M.B. Amar, D. Bonn, and A. Lindner. Inertial effects on Saffman–Taylor viscous fingering. *J. Fluid Mech.*, 552:83–97, 2006.

[13] T. Chevalier, C. Chevalier, X. Clain, J.C. Dupla, J. Canou, S. Rodts, and P. Coussot. Darcy's law for yield stress fluid flowing through a porous medium. *J. non-Newt. Fluid Mech.*, 195:57–66, 2013.

[14] R.L. Chuoke, P. Van Meurs, and C. van der Poel. The instability of slow, immiscible, viscous liquid-liquid displacements in permeable media. *Trans. AIME*, 216:188–194, 1959.

[15] Y. Cinar, A. Riaz, H.A. Tchelepi, et al. Experimental study of CO2 injection into saline formations. In *SPE ATCE*, 2007.

[16] Y. Couder, N. Gerard, and M. Rabaud. Narrow fingers in the Saffman–Taylor instability. *Phys. Rev. A*, 34(6):5175, 1986.

[17] P. Coussot. Saffman–Taylor instability in yield-stress fluids. *J. Fluid Mech.*, 380:363–376, 1999.

[18] D. Q.M. Craig, S. Tamburic, G. Buckton, and J.M. Newton. An investigation into the structure and properties of Carbopol 934 gels using dielectric spectroscopy and oscillatory rheometry. *J. Cont. Rel.*, 30(3):213–223, 1994.

[19] M. M. Cross. Relation between viscoelasticity and shear-thinning behaviour in liquids. *Rheol. Acta*, 18(5):609–614, 1979.

[20] Y. Dimakopoulos and J. Tsamopoulos. Transient displacement of a viscoplastic material by air in straight and suddenly constricted tubes. *J. non-Newt. Fluid Mech.*, 112(1):43–75, 2003.

[21] B. Ebrahimi, P. Mostaghimi, H. Gholamian, and K. Sadeghy. Viscous fingering in yield stress fluids: a numerical study. *J. Eng. Math.*, 1–16, 2015.

[22] B. Ebrahimi, S.M. Taghavi, and K. Sadeghy. Two-phase viscous fingering of immiscible thixotropic fluids: A numerical study. *J. non-Newt. Fluid Mech.*, 218:40–52, 2015.

[23] J. Eggers and E. Villermaux. Physics of liquid jets. *Rep. Prog. Phys.*, 71(3):036601, 2008.

[24] P. Fast, L. Kondic, M.J Shelley, and P. Palffy-Muhoray. Pattern formation in non-Newtonian Hele–Shaw flow. *Phys. Fluids*, 13(5):1191–1212, 2001.

[25] J.V. Fontana, E.O. Dias, and J.A. Miranda. Controlling and minimizing fingering instabilities in non-Newtonian fluids. *Phys. Rev. E*, 89(1):013016, 2014.

[26] J. F. Freitas, E. J. Soares, and R. L. Thompson. Viscoplastic-viscoplastic displacement in a plane channel with interfacial tension effects. *Chem. Eng. Sci.*, 91:54–64, 2013.

[27] P. Gondret and M. Rabaud. Shear instability of two-fluid parallel flow in a Hele–Shaw cell. *Phys. Fluids*, 9(11):3267–3274, 1997.

[28] S. Hill et al. Channeling in packed columns. *Chem. Eng. Sci.*, 1(6):247–253, 1952.

[29] K.E. Holloway, P. Habdas, N. Semsarillar, K. Burfitt, and J.R. de Bruyn. Spreading and fingering in spin coating. *Phys. Rev. E*, 75(4, 2):046308, 2007.

[30] G.M. Homsy. Viscous fingering in porous media. *Annu. Rev. Fluid Mech.*, 19(1):271–311, 1987.

[31] P.C. Huzyak and K.W. Koelling. The penetration of a long bubble through a viscoelastic fluid in a tube. *J. non-Newt. Fluid Mech.*, 71(1):73–88, 1997.

[32] J. Ignes-Mullol, Zhao H., and J.V. Maher. Velocity fluctuations of fracture like disruptions of associating polymer solutions. *Phys. Rev. E*, 51(2):1338–1343, 1995.

[33] N. Kagei, D. Kanie, and M. Kawaguchi. Viscous fingering in shear thickening silica suspensions. *Phys. Fluids*, 17:0545103, 2005.

[34] D.A. Kessler, J. Koplik, and H. Levine. Pattern selection in fingered growth phenomena. *Adv. Phys.*, 37(3):255–339, 1988.

[35] J.Y. Kim, J.Y. Song, E.J. Lee, and S.K. Park. Rheological properties and microstructures of Carbopol gel network system. *Coll. Polym. Sci.*, 281(7):614–623, 2003.

[36] L. Kondic, P. Palffy-Muhoray, and M.J. Shelley. Models of non-Newtonian Hele-Shaw flow. *Phys. Rev. E*, 54(5):R4536, 1996.

[37] L. Kondic, M.J. Shelley, and P. Palffy-Muhoray. Non-Newtonian Hele-Shaw flow and the Saffman–Taylor instability. *Phys. Rev. Lett.*, 80(7):1433, 1998.

[38] C. H. Lee, V. Moturi, and Y. Lee. Thixotropic property in pharmaceutical formulations. *J. Cont. Rel.*, 136(2):88–98, 2009.

[39] E. Lemaire, P. Levitz, G. Daccord, and H. Van Damme. From viscous fingering to viscoelastic fracturing in colloidal fluids. *Phys. Rev. Lett.*, 67(15):2009, 1991.

[40] S. Li, J.S. Lowengrub, J. Fontana, and P. Palffy-Muhoray. Control of viscous fingering patterns in a radial Hele-Shaw cell. *Phys. Rev. Lett.*, 102(17):174501, 2009.

[41] A. Lindner, D. Bonn, and J. Meunier. Viscous fingering in a shear-thinning fluid. *Phys. Fluids*, 12(2):256–261, 2000.

[42] A. Lindner, D. Bonn, E.C. Poire, M.B Amar, and J. Meunier. Viscous fingering in non-Newtonian fluids. *J. Fluid Mech.*, 469:237–256, 2002.

[43] A. Lindner, P. Coussot, and D. Bonn. Viscous fingering in a yield stress fluid. *Phys. Rev. Lett.*, 85(2):314, 2000.

[44] A. Lindner, P. Coussot, and D. Bonn. Viscous fingering in a gel. In *Branching in Nature*, pages 433–438. Springer, 2001.

[45] D. Lukas, N. Pan, A. Sarkar, M. Weng, J. Chaloupek, E. Kostakova, L. Ocheretna, P. Mikes, M. Pociute, and E. Amler. Auto-model based computer simulation of Plateau–Rayleigh instability of mixtures of immiscible liquids. *Physica A*, 389(11):2164–2176, 2010.

[46] N. Maleki-Jirsaraei, A. Lindner, S. Rouhani, and D. Bonn. Saffman–Taylor instability in yield stress fluids. *J. Phys. Condens. Matter*, 17(14):S1219, 2005.

[47] S. Malhotra and M.M. Sharma. Impact of fluid elasticity on miscible viscous fingering. *Chem. Eng. Sci.*, 117:125–135, 2014.

[48] D.S. Malkus, J.A. Nohel, and B.J. Plohr. Analysis of new phenomena in shear flow of non-Newtonian fluids. *SIAM J. Appl. Math.*, 51(4):899–929, 1991.

[49] K.V. McCloud and J.V. Maher. Experimental perturbations to Saffman–Taylor flow. *Phys. Rep.*, 260(3):139–185, 1995.

[50] J.W. McLean and P.G. Saffman. The effect of surface tension on the shape of fingers in a Hele-Shaw cell. *J. Fluid Mech.*, 102:455–469, 1981.

[51] J. Meyer and D. Weihs. Capillary instability of an annular liquid jet. *J. Fluid Mech.*, 179(6):531–545, 1987.

[52] T.G. Mezger. *The rheology handbook: for users of rotational and oscillatory rheometers.* Vincentz Network GmbH & Co KG, 2006.

[53] K.B. Migler, H. Hervet, and L. Leger. Slip transition of a polymer melt under shear stress. *Phys. Rev. Lett.*, 70(3):287, 1993.

[54] R. Mollaabbasi and S.M. Taghavi. Buoyant displacement flows in slightly non-uniform channels. *J. Fluid Mech.*, 795:876–913, 2016.

[55] S. Mora and M. Manna. Saffman–Taylor instability for generalized Newtonian fluids. *Phys. Rev. E*, 80(1):016308, 2009.

[56] G. Narsimhan and E. Ruckenstein. Effect of bubble size distribution on the enrichment and collapse in foams. *Langmuir*, 2(4):494–508, 1986.

[57] J. Nase, D. Derks, and A. Lindner. Dynamic evolution of fingering patterns in a lifted Hele-Shaw cell. *Phys. Fluids*, 23(12):123101, 2011.

[58] S. Nguyen, R. Folch, V.K. Verma, H. Henry, and M. Plapp. Phase-field simulations of viscous fingering in shear-thinning fluids. *Phys. Fluids*, 22(10):103102, 2010.

[59] J. Nittmann, G. Daccord, and H.E Stanley. Fractal growth of viscous fingers: quantitative characterization of a fluid instability phenomenon. *Nature*, 314(6007):141–144, 1985.

[60] F.M. Orr and J.J. Taber. Use of carbon dioxide in enhanced oil recovery. *Science*, 224(4649):563–569, 1984.

[61] C.W. Park and G.M. Homsy. Two-phase displacement in Hele-Shaw cells: theory. *J. Fluid Mech.*, 139:291–308, 1984.

[62] H. Pascal. Rheological behaviour effect of non-Newtonian fluids on dynamic of moving interface in porous media. *Int. J. Eng. Sci.*, 22(3):227–241, 1984.

[63] J.M. Piau. Carbopol gels: Elastoviscoplastic and slippery glasses made of individual swollen sponges: Meso-and macroscopic properties, constitutive equations and scaling laws. *J. non-Newt. Fluid Mech.*, 144(1):1–29, 2007.

[64] D. Pihler-Puzovic, P. Illien, M. Heil, and A. Juel. Suppression of complex fingerlike patterns at the interface between air and a viscous fluid by elastic membranes. *Phys. Rev. Lett.*, 108(6):074502, 2012.

[65] E.C. Poire and M.B. Amar. Finger behavior of a shear thinning fluid in a Hele-Shaw cell. *Phys. Rev. Lett.*, 81(10):2048, 1998.

[66] A.J. Poslinski, P.R. Oehler, and V.K. Stokes. Isothermal gas-assisted displacement of viscoplastic liquids in tubes. *Polym. Eng. Sci.*, 35(11):877–892, 1995.

[67] M. Rabaud, Y. Couder, and N. Gerard. Dynamics and stability of anomalous Saffman–Taylor fingers. *Phys. Rev. A*, 37(3):935, 1988.

[68] A. Rathapon, A. Sirivat, P. Vayumhasuwan, and others. Viscoelastic properties of Carbopol 940 gels and their relationships to piroxicam diffusion coefficients in gel bases. *Pharm. Res.*, 22(12):2134–2140, 2005.

[69] D.A. Reinelt and P.G. Saffman. The penetration of a finger into a viscous fluid in a channel and tube. *SISC*, 6(3):542–561, 1985.

[70] G. Rousseaux, A. De Wit, and M. Martin. Viscous fingering in packed chromatographic columns: Linear stability analysis. *J. Chromatogr. A*, 1149(2):254–273, 2007.

[71] C. Ruyer-Quil. Inertial corrections to the darcy law in a Hele–Shaw cell. *C R Acad Sci IIb Mec*, 329(5):337–342, 2001.

[72] P.G. Saffman and G. Taylor. The penetration of a fluid into a porous medium or Hele-Shaw cell containing a more viscous liquid. In *Proc. R. Soc. A.*, 245, 312–329, 1958.

[73] A. Sehgal, V. Ferreiro, J.F. Douglas, E. J. Amis, and A. Karim. Pattern-directed dewetting of ultrathin polymer films. *Langmuir*, 18(18):7041–7048, 2002.

[74] P. A. P. Swain, G. Karapetsas, O.K. Matar, and K.C. Sahu. Numerical simulation of pressure-driven displacement of a viscoplastic material by a Newtonian fluid using the lattice Boltzmann method. *Eur. J. Mech. B-Fluid*, 49:197–207, 2015.

[75] P. Tabeling and A. Libchaber. Film draining and the Saffman–Taylor problem. *Phys. Rev. A*, 33(1):794, 1986.

[76] P. Tabeling, G. Zocchi, and A. Libchaber. An experimental study of the Saffman-Taylor instability. In *Physicochemical Hydrodynamics*, 515–525. Springer, 1988.

[77] G.I. Taylor. Cavitation of a viscous fluid in narrow passages. *J. Fluid Mech.*, 16(4):595–619, 1963.

[78] R.L. Thompson and E.J. Soares. Viscoplastic dimensionless numbers. *J. non-Newt. Fluid Mech.*, 2016.

[79] P.H.T. Uhlherr, J. Guo, C. Tiu, X.M. Zhang, J.Z.Q. Zhou, and T.N. Fang. The shear-induced solid–liquid transition in yield stress materials with chemically different structures. *J. non-Newt. Fluid Mech.*, 125(2):101–119, 2005.

[80] H. Van Damme, E. Alsac, C. Laroche, and L. Gatineau. On the respective roles of low surface tension and non-Newtonian rheological properties in fractal fingering. *Europhys. Lett.*, 5(1):25, 1988.

[81] H. Van Damme, E. Lemaire, Y. Ould, M. Abdelhaye, A. Mourchid, and P. Levitz. Pattern formation in particulate complex fluids: A guided tour. In *Non-linearity and breakdown in soft condensed matter*, 134–150. Springer, 1994.

[82] S. J. Weinstein, E.B. Dussan, and L.H. Ungar. A theoretical study of two-phase flow through a narrow gap with a moving contact line: Viscous fingering in a Hele-Shaw cell. *J. Fluid Mech.*, 221:53–76, 1990.

[83] A.R. White and T. Ward. Constant pressure gas-driven displacement of a shear-thinning liquid in a partially filled radial Hele-Shaw cell: Thin films, bursting and instability. *J. non-Newt. Fluid Mech.*, 206:18–28, 2014.

[84] K. Wielage-Burchard and IA. Frigaard. Static wall layers in plane channel displacement flows. *J. non-Newt. Fluid Mech.*, 166(5):245–261, 2011.

[85] R.A. Wooding and H.J. Morel-Seytoux. Multiphase fluid flow through porous media. *Annu. Rev. Fluid Mech.*, 8(1):233–274, 1976.

[86] T. Xia, Y. Qin, Y. Huang, T. Huang, J. Xu, and Y. Li. Sequence control of phase separation and dewetting in PS/PVME blend thin films by changing molecular weight of PS. *J. Chem. Phys*, 145(20):204903, 2016.

[87] J. Zilz, C. Schafer, C. Wagner, R.J. Poole, M.A. Alves, and A. Lindner. Serpentine channels: micro-rheometers for fluid relaxation times. *Lab Chip*, 14(2):351–358, 2014.

[88] G. Zocchi, B.E. Shaw, A. Libchaber, and L.P. Kadanoff. Finger narrowing under local perturbations in the Saffman–Taylor problem. *Phys. Rev. A*, 36(4):1894, 1987.

Chapitre 2

Viscous fingering of yield stress fluids: The effects of wettability

2.1 Résumé

Nous examinons expérimentalement le problème de la digitation visqueuse dans lequel une huile de silicone déplace un gel de Carbopol dans une cellule de Hele-Shaw rectangulaire. Contrairement aux cas traditionnels, le fluide de déplacement mouille parfaitement les parois de la cellule de Hele-Shaw. Alors que l'huile de silicone utilisée est un fluide Newtonien (à faible viscosité), le gel Carbopol utilisé est un fluide non-Newtonien (à haute viscosité), qui présente une gamme de comportements rhéologiques complexes, telle que le seuil d'écoulement, la rhéofluidification et les faibles élastique. Nous démontrons que les effets non-Newtoniens ainsi que les conditions de mouillabilité ont un impact significatif sur les modèles de digitation, que nous décrivons par une comparaison détaillée entre les déplacements mouillants (huile-Carbopol) et les déplacements non-mouillants (air-Carbopol). Nous analysons l'écoulement sous différentes perspectives, en utilisant les groupes sans dimension pertinents, y compris le nombre capillaire (Ca), le nombre de Bingham (Bn), le nombre de Weissenberg (Wi), le nombre de Weber (We), le rapport d'aspect du canal (δ) et l'indice en loi de puissance de la rhéofluidification (n). Nous réussissons à classer quatre régimes d'écoulement principaux par rapport à ces groupes sans dimension; un régime capillaire, un régime de contrainte d'écoulement, un régime visqueux et un régime élasto-inertiel. Le régime capillaire, observé à de très faibles vitesses, est un régime unique qui apparaît en raison d'une interaction entre la contrainte d'écoulement et les effets de tension interfaciale. Dans ce régime, la largeur du doigt est presque égale à la largeur de la cellule. Les autres régimes d'écoulement sont observés dans les deux déplacements mouillants et non mouillants, mais avec certaines différences critiques qui sont clairement expliquées dans le document.

2.2 Abstract

We consider experimentally the viscous fingering problem wherein a silicone oil displaces a Carbopol gel in a rectangular Hele-Shaw cell. Unlike traditional cases, the displacing fluid perfectly wets the walls of the Hele-Shaw cell. While the silicone oil used is a Newtonian fluid (with a small viscosity), the Carbopol gel employed is a non-Newtonian fluid (with a large viscosity), which exhibits an interesting range of complex rheology such as yield stress, shear-thinning and weakly-elastic behaviours. We demonstrate that non-Newtonian effects together with wettability conditions exert a significant impact on fingering patterns, which we describe through a detailed comparison between wetting displacements (oil-Carbopol) and non-wetting displacements (air-Carbopol). We analyze the flow from various perspectives, using the relevant dimensionless groups, including the capillary number (Ca), the Bingham number (Bn), the Weissenberg number (Wi), Weber number (We), the channel aspect ratio (δ), and the shear-thinning power-law index (n). We succeed in classifying four main flow regimes versus these dimensionless groups: a *capillary* regime, a *yield stress* regime, a *viscous* regime and an *elasto-inertial* regime. The capillary regime, observed at very low velocities, is a unique regime which appears due to an interplay between yield stress and interfacial tension effects. In this regime, the finger width is nearly equal to the cell width. The other flow regimes are observed in both wetting and non-wetting displacements, but with certain critical differences that are made clear in the paper.

2.3 Introduction

Multiphase flows in confined geometry are frequently studied in fluid mechanics, as they appear in a large number of natural and engineering systems (50). One particular problem of interest is the displacement of one fluid by another fluid of lower viscosity, for which the interface between the two fluids becomes unstable as the less-viscous fluid fingers into the more-viscous one. This phenomenon is called the classical *viscous fingering* instability or the *Saffman-Taylor* instability (104). Since a variety of interfacial patterns may appear due to fingering (130; 80; 50), the problem is fundamentally important in terms of pattern formation. Besides, fingering flows can also find many industrial applications: cleaning of gel-like waxy crude oil from pipelines during start-up flows (125); displacement of sugar liquors by water in the refining process of raw sugar (49); displacement of dense degassed magma by gas-rich magma in volcanoes (107); secondary and tertiary recovery of crude oil by injection of gas/water into reservoir (93; 65); annular displacement of drilling mud or spacer by cement slurry (89; 11); cleaning of processing equipment in food industry and rinsing pipes (129; 42); chromatographic separations(102).

Ignoring three-dimensional geometrical effects, two-dimensional features of viscous fingering in a traditional Hele-Shaw cell (or a porous medium) (50; 80) can be explained by Darcy's law :

$$\hat{v} = -\frac{\hat{b}^2}{12\hat{\mu}}\nabla\hat{p}, \tag{2.1}$$

where $\hat{b}$ and $\hat{\mu}$ are the Hele-Shaw cell gap thickness and shear viscosity, respectively[1]. This equation describes the relation between the two-dimensional velocity field averaged through the small gap ($\hat{v}$) and the local pressure ($\hat{p}$). When the interface is flat, the velocity of each incompressible fluid ($\nabla.\hat{v} = 0$) remains constant along the cell. For Newtonian fluids, Darcy's law is applicable and it can be even modified by considering interface shape effects (111), wall film thicknesses (94) and inertial effects (103; 45). For non-Newtonian fluids, however, the applicability of Darcy's law is limited (71; 100), making the understanding of viscous fingering more difficult for these fluids.

When the interface between the displacing and displaced fluids is perturbed, viscous fingers develop, grow and compete. One particular parameter to analyze the flow is the relative finger width, $\lambda = \hat{w}/\hat{W}$, with $\hat{w}$ and $\hat{W}$ being the average finger width and the cell width, respectively. λ depends on the flow parameters and provides a measure of displacement flow efficiency in viscous fingering. Experimentally and theoretically, Saffman and Taylor have shown in their seminal 1958 paper (104) that λ decreases with increasing the finger tip velocity ($\hat{U}$). Stronger interfacial tension forces result in larger λ, while increasing viscous forces lead to smaller λ (13; 74; 130; 50). These findings imply that the capillary number, $Ca = \hat{\mu}\hat{U}/\hat{\sigma}$, representing the ratio of these interfacial tension and viscous forces (133; 50), is a relevant flow dimensionless parameter. In fact, for Newtonian fluids in Hele-Shaw cells, using a combination of Ca and the aspect ratio (δ) as a control parameter ($Ca\delta^2$) results in a collapse of experimental datapoints, for which λ versus $Ca\delta^2$ follows a single curve for various flow parameters (112; 7; 72). In addition, at high $Ca\delta^2$, λ tends to an asymptotic value of 1/2 (82; 50; 60; 104). Both of these findings are in good agreement with theoretical predictions (82).

Non-Newtonian parameters remarkably affect the viscous finger problem in Hele-Shaw cells. The effects of shear-thinning (128; 38; 16; 15), shear-thickening (38; 87; 16; 15), yield stress (25; 96; 39; 40), elasticity (78; 52) and elasto-visco-plastic properties (36) have been investigated using numerical, analytical and experimental approaches. A number of exotic patterns, such as snowflake-like patterns (17) and branched, fractal, or fracture-like structures (90; 68; 53), have been observed. Many fluid types have been also considered, including gels (74), colloidal fluids (68), foams (95), liquid crystals (17), polymer solutions (76), granular suspensions (21), and emulsions (34). Shear-thinning effects create dendritic flow patterns (with side branching) and crack-like flow patterns (with angular branches and sharp finger tips) (62; 4). Shear-thickening properties may widen or narrow the finger (58). Elasticity results in thin and long fingers and reduce the average finger width (78). Viscoelastic features lead to peculiar patterns, altering displacement efficiency (68). Viscoplasticity drastically affects morphological patterns,

1. In this paper, we adopt the convention of denoting dimensional quantities with the ˆ symbol and dimensionless quantities without.

resulting in various flow regimes. For example, in a sequence of increasing $\hat{U}$, displacing a viscoplastic fluid (with relatively small elastic properties) by air results in a yield stress regime, a viscous regime and an elasto-inertial regime (36). Ramified fingering patterns appear in the yield stress regime (73; 36), while a single stable finger is observed in the viscous regime (73; 36), both in good agreement with numerical observations (32). In the elasto-inertial regime, weak elastic effects lead to side branching (77; 36), while inertial effects result in increasing the finger width (36). Relevant to our work, viscoplastic flows involving interfacial patterns in geometries other than the Hele-Shaw cell have also received significant attention (3; 31; 115; 2; 85; 110; 18; 35; 86; 114), which can provide further understanding about the complex nature of these flows.

Wettability, which is the tendency of a fluid to adhere to a solid surface, may become important in multiphase flows in Hele-Shaw cells or in porous media (46). Although wettability can significantly affect fluid-fluid interactions in the vicinity of solid surfaces (133), its effects are not well understood in the viscous fingering context. In fact, the majority of studies have entirely circumvented the question of wettability, for example through considering the displacement of a wetting fluid by a non-wetting one. In this case, a displacing fluid usually fingers through a displaced fluid that preferentially wets the Hele-Shaw cell so that the former does not interact with the upper and lower cell walls. The same is true for similar studies considering porous media flows (70). Certainly, wetting effects result in more complex behaviours. For example, Lenormand (69) have studied immiscible displacements in porous media (rectangular channel), for the case where the displacing fluid is more wetting to the solid surface, finding three different flow types due to wettability: a flow along the bulk of the channel, a flow along the corners and a film flow along the roughness of the walls. However, when the displaced fluid is more wetting to the solid surface, they have observed only a flow along the bulk of the channel. Other experimental studies (108) have also confirmed that qualitative morphological changes in displacement flows occur when the displacing fluid preferentially wets the flow geometry walls. Weinstein *et al.* (127) have also noted the difficulties of defining an appropriate hydrodynamic model for the case when both displacing and displaced fluids contact the solid surface.

In order to evaluate wettability, the contact angle, which is the angle where a fluid-fluid interface meets a solid surface, is typically measured. The contact angle is related to interfacial tensions (46), and its measurement is also used to study interface functionalities and surface features. The contact angle is a crucial parameter influencing immiscible displacement flows in porous media, with a variety of applications in geological carbon sequestration, heavy oil recovery, etc. Although in these processes the contact angle of oil-water is of relevance, most studies address the air-water contact angle, which for smooth solid surfaces varies in the range of $0°$ to $120°$ (46). Jung *et al.* (57) have considered, numerically and experimentally, immiscible displacement flows in a Hele-Shaw cell with cylindrical posts, for a wide range of contact angles.

They have found two different flow regimes with regard to changes in the contact angle, i.e., a capillary fingering regime and a stable interfacial displacement regime. Trojer *et al.* (118) have also shown that wettability significantly impacts fluid-fluid displacement patterns and the finger width in granular media. These and similar works consider Newtonian fluid flows, while the literature for non-Newtonian fluid flows with wettability effects is not developed.

Parameter	**Name**	**SI Unit**	**Range or Value**
$\hat{b}$	Gap thickness*	m	9×10^{-4} & 1.5×10^{-3}
$\hat{C}$	Carbopol concentration	% (wt/wt)	$(1 - 1.5) \times 10^{-3}$
$\hat{L}$	Channel length	m	2.6×10^{-1}
$\hat{U}$	Finger tip velocity	m/s	$(0 - 570) \times 10^{-3}$
$\hat{V}$	Mean imposed flow velocity (flow rate divided by channel cross-section)	m/s	$(0 - 196) \times 10^{-3}$
$\hat{W}$	Channel width	m	6.8×10^{-2}
$\hat{w}$	Finger width	m	$(1.09 - 6.42) \times 10^{-2}$
$\hat{\rho}_s$	Silicone oil density	kg/m^3	9.18×10^2
$\hat{\mu}_s$	Silicone oil viscosity	Pa.s	4.6×10^{-3}
$\hat{\rho}_c$	Carbopol density	kg/m^3	$\sim 9.985 \times 10^2$
$\hat{\mu}_c$	Carbopol viscosity	Pa.s	$(1.3 - 1591) \times 10^{-1}$
$\hat{\sigma}_{ac}$	Carbopol-air interfacial tension**	N/m	$(6.6) \times 10^{-2}$
$\hat{\sigma}_{ao}$	Silicone oil-air interfacial tension	N/m	$(1.97) \times 10^{-2}$
$\hat{\sigma}_{oc}$	Carbopol-silicone oil interfacial tension	N/m	$(3.7) \times 10^{-2}$
$\hat{\sigma}_{oc,\text{eff}}$	Effective interfacial tension of silicone oil and Carbopol	N/m N/m	$\sim (3.7 - 4.45) \times 10^{-2}$
$\hat{\sigma}_{ac,\text{eff}}$	Effective interfacial tension of air and Carbopol	N/m	$\sim (6.6 - 7.05) \times 10^{-2}$
$\hat{\tau}_y$	Carbopol yield stress	Pa	$5.4 - 13.7$
$\hat{\Lambda}$	Relaxation time	s	$(1.7 - 3635) \times 10^{-2}$
$\hat{\kappa}$	Carbopol consistency index	Pa.s^n	$5.7 - 11.6$

TABLE 2.1 – The ranges and values of the dimensional parameters in our work. *A number of additional experiments have been also performed in a cell with a larger gap thickness, $\hat{b}$ = 2.5 (mm), to enable the cell side-view visualization. **For convenience in this work, interfacial tension refers to both liquid-liquid interfacial tension or liquid-air surface tension.

Numerous studies have considered displacements in confined geometries (64; 126; 116; 5) but mainly for miscible fluid flows. In this work, we study experimentally the viscous fingering problem where a Carbopol gel is displaced by a silicone oil in a rectangular Hele-Shaw cell. The former is among the most popular types of laboratory fluids and exhibits various non-Newtonian features, such as yield stress, shear-thinning, weakly viscoelastic, and negligible thixotropic effects (22; 101; 99; 67). Unlike traditional studies, our displacing fluid (silicone oil) wets the Hele-Shaw cell walls as it fingers through the displaced fluid (Carbopol gel); therefore, our aim is to provide a fundamental understanding of how viscous fingering of non-

Newtonian fluids may be affected by wettability. To do so, our experiments cover a considerably wide range of flow parameters (see Tables 2.1 & 2.2 for definitions and ranges). In addition, as the problem is quite complex, we compare in great detail our experimental results with those of air displacing a Carbopol gel, with very similar flow parameters. As will be seen, this approach is effective in highlighting surprising similarities and critical differences between these displacements, while it also helps to explain which effects are primarily due to wettability.

Parameter	Name	Definition	Range or value
A_2	Relative wave amplitude	$\frac{\hat{a}_2}{\hat{W}}$	$(1.8 - 29) \times 10^{-2}$
B_2	Relative wavelength	$\frac{\hat{b}_2}{\hat{W}}$	$(9.05 - 22.25) \times 10^{-1}$
Bn	Bingham number	$\frac{\hat{\tau}_y}{\hat{\kappa}(\hat{V}/\hat{b})^n}$	$(1.06 - 38.7) \times 10^{-1}$
Ca	Capillary number	$\frac{\hat{\mu}_c \hat{U}}{\hat{\sigma}_{oc,\text{eff}}}$	$(2.5 - 114) \times 10^{-1}$
$\widetilde{Ca}$	Effective capillary number	$\frac{Ca}{Bn}$	$(2.3 - 5690) \times 10^{-2}$
$\widetilde{Ca}^*$	Modified capillary number	$\frac{\widetilde{Ca}\ \delta^{1+n}}{1+We^*/We^*_c}$	$(9.5 - 51880) \times 10^{-1}$
n	Power-law index	-	$0.31 - 0.35$
Re	Reynolds number	$\frac{\hat{\rho}_c \hat{U} \hat{b}}{\hat{\mu}_c}$	$(2.6 - 67000000) \times 10^{-7}$
We	Weber number	$\frac{\hat{\rho}_c \hat{U}^2 \hat{b}}{\hat{\sigma}_{oc,\text{eff}}}$	$(7.1 - 2819000000) \times 10^{-8}$
We^*	Modified Weber number	$We\ \delta^{1+n}$	$(2.12 - 451100000) \times 10^{-5}$
Wi	Weissenberg number	$\frac{\hat{\Lambda} \hat{U}}{\hat{b}}$	$(1.1 - 76) \times 10^{-2}$
δ	Aspect ratio	$\frac{\hat{W}}{\hat{b}}$	45.3 & 75.5
λ	Relative finger width	$\frac{\hat{w}}{\hat{W}}$	$(1.6 - 9.4) \times 10^{-1}$

TABLE 2.2 – The ranges and values of the dimensionless parameters in our work.

This manuscript is organized as follows. The details of our experimental setup, fluid preparations, characterizations, and producers are explained in §2.4. The main results are discussed in §2.5. Our brief conclusions are drawn in §2.6.

2.4 Experimental setup and descriptions

Our experiments were conducted in a traditional Hele-Shaw cell, made of two parallel flat plates with a very small gap. This flow geometry has a lot of applications in understanding classical fluid mechanics problems, but it can be also relevant in explaining fluid flows in microfluidic devices, rock fractures and porous media (50). Our rectangular Hele-Shaw cell was formed by two parallel, transparent, smooth acrylic plastic plates. Each plate thickness was 1/2 inch. A thin rubber was used to separate the plates. Note that in order to enable the cell side-view visualization, several additional experiments were also conducted in a cell with a larger gap thickness, for which all the rectangular sides were transparent plexiglas plates. The gap thickness between the plates was set using level screws, distributed along the cell sides.

In order to control the gap thickness, a digital level meter and a digital caliper were used. A general 3D schematic of the experimental cell (with the flow configuration) is demonstrated in Fig. 2.1a. The cell dimensions and some flow parameters are represented in Table 2.1.

The Hele-Shaw cell was initially filled with a more viscous fluid (Carbopol gel). Then, from the cell inlet, a less viscous displacing fluid (silicone oil [2]) was injected, in a laminar way. Note that, due to wetting effects, an oil-Carbopol displacement is novel and different from the more traditional air-Carbopol displacement: oil wets the walls as it pushes Carbopol gel, while air fingers through Carbopol gel since Carbopol gel wets the walls, as depicted in Figs. 2.1b and c. In addition, when oil displaces Carbopol gel (Fig. 2.1b), the interface moves as a concave meniscus (1; 106). However, when air displaces Carbopol gel (Fig. 2.1c), the interface advances as a convex meniscus, leaving behind a thin Carbopol film on the lower and upper plates (1; 50; 111). Note that these configurations (Fig. 2.1b & c) are only valid for specific conditions, as discussed in §2.5.2 and §2.5.4.

A camera (Basler acA2040-90um) was used to record the displacement process, from the cell top view (i.e., the $\hat{x}\hat{z}$-plane). For certain experiments at higher speeds, an ultra-high-speed camera (FASTCAM UX100) was used. The cameras were connected to computer for direct image acquisition and post processing. For visualization purposes, the displaced fluid was dyed by black ink (Fountain Pen India black ink). To augment the image quality, adjust the light and improve the light homogeneity, Light-Emitting Diode (LED) strips and a light diffuser panel were employed. The recorded images were analyzed using ImageJ, MATLAB and the camera software. The inlet mean imposed velocity was determined by a combined flow meter and flow controller system.

Certain verification experiments were performed to ensure that the Hele-Shaw cell was perfectly smooth and homogeneous, and no unwanted instability could be created due to the channel walls/boundaries. In these experiments, dyed water smoothly swept transparent water in a piston-like pattern with a stable interface (minimal diffusion), confirming the absence of unwanted instabilities due to wall imperfections.

2.4.1 Fluid preparations

Carbopol is widely used in cosmetic products and pharmaceutical industrials (101; 67; 61) thanks to its low toxicity, good receptibility and high viscosity at low concentrations (27). Carbopol can be also used as a gelling agent and thickener in systems where clarity is important, a good example of which may be non-Newtonian fluid flow experiments. Carbopol is available in a various grades, depending on the molecular weight distribution of polymer chains. The rheological properties of a Carbopol gel depends on the concentration and acidity of Carbopol.

2. Hereafter, silicone oil is called oil for convince.

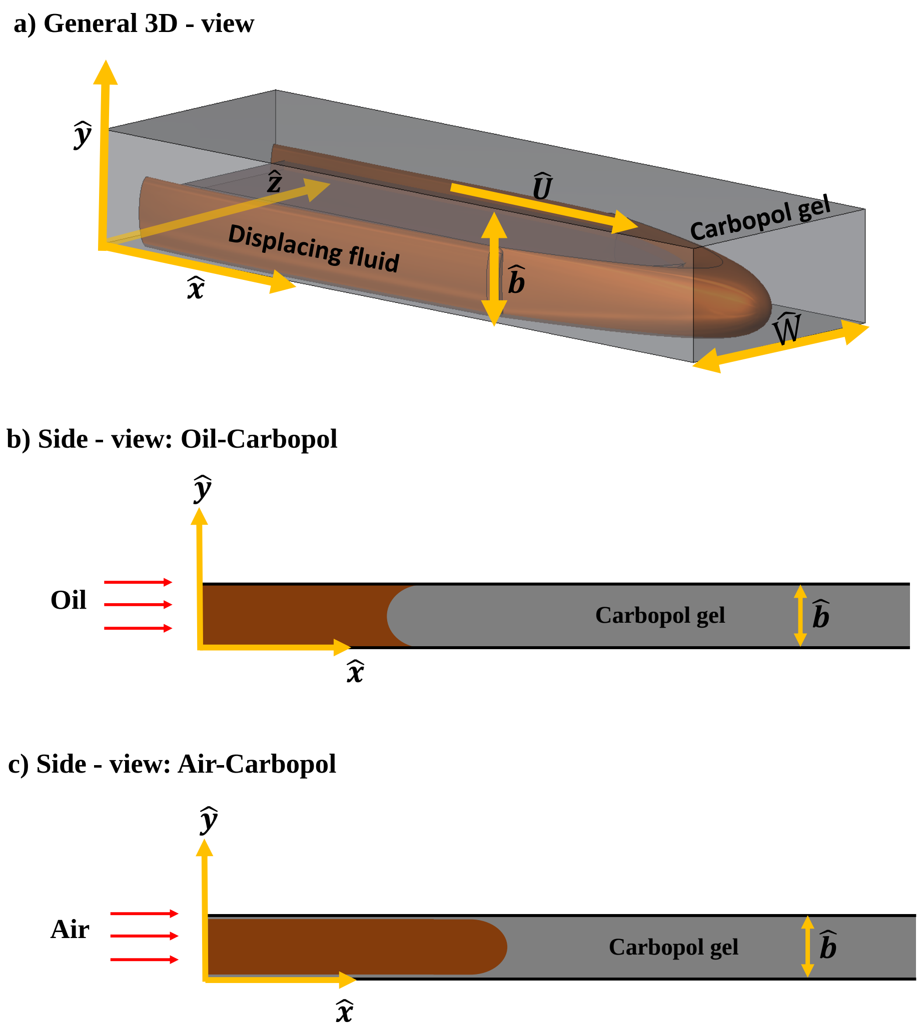

FIGURE 2.1 – (a) A 3D schematic view of the experimental set-up, showing our rectangular Hele-Shaw cell and the flow within. (b) A schematic side-view of oil displacing Carbopol (with a concave interface). (c) A schematic side-view of air displacing Carbopol (with a convex interface). Note the film of Carbopol left on the walls.

Our Carbopol gel was prepared using the following procedure: an appropriate amount of Carbopol powder (Carbomer 940, Making Cosmetics Co.) was initially dispersed in deionized water to create an acidic solution (see Table 2.3). The Carbopol solution was continuously stirred, and it was then neutralized at an intermediate pH by adding Sodium hydroxide. The base agent, NaOH, charges the polymer chains negatively, which subsequently repel one another and the solution eventually turns into a gel-like material due to swelling and jamming of polymer blobs (56). This gel possesses a yield stress, but has a density close to that of water.

2.4.2 Rheological characterization

In our experiments, a low viscosity Newtonian oil (Low Viscosity PDMS Silicone Fluid, 5cSt, Clearco Products Co.) displaced a non-Newtonian Carbopol gel, for which three different weight concentrations were used (see Table 2.3 for the compositions). These are conventionally called LCC (low Carbopol concentration), MCC (medium Carbopol concentration) and HCC (high Carbopol concentration) throughout the paper. Oscillatory and rotational rheometry tests were performed using a DHR-3 TA Instrument rheometer to measure the rheological properties of these gels. A parallel-plate geometry with a 40 (mm) plate diameter at a gap of 1 (mm) was typically employed. To eliminate wall slip, fine sandpapers were attached to the surfaces of the parallel plates (92; 113). The same loading procedure was used in all tests. Our rheological characterization approach as well as results were similar to those presented in Eslami and Taghavi (36), to which we refer for more details.

Carbopol solution	**Carbopol** %(wt/wt)	**NaOH** %(wt/wt)	$\hat{\tau}_y$ (Pa)	$\hat{\kappa}$ (Pa.s^n)	n	θ_{ac} (°)	θ_{oc} (°)
Low concentration (LCC)	0.10	0.029	5.4 ± 0.2	5.7 ± 0.4	0.32 ± 0.02	52 ± 2	117 ± 2
Medium concentration (MCC)	0.12	0.035	8.4 ± 0.2	7.7 ± 0.5	0.31 ± 0.02	54 ± 2	120 ± 3
High concentration (HCC)	0.15	0.043	13.7 ± 0.3	11.6 ± 0.5	0.35 ± 0.03	58 ± 3	121 ± 3

TABLE 2.3 – Carbopol composition, parameters determined from rheological measurements (assuming the Herschel-Bulkley model), and static contact angles for a Carbopol drop in oil (θ_{oc}) and for a Carbopol drop in air (θ_{ac}), in contact with an acrylic plastic substrate.

Fig. 2.2a shows the rheometer flow curves for the three Carbopol concentrations. As can be seen, each of these fluids clearly exhibits a yield stress at low shear rates. The solid lines superimposed on the datapoints are fitted using the Herschel-Bulkley model:

$$\hat{\tau} = \hat{\tau}_y + \hat{\kappa}\hat{\dot{\gamma}}^n, \tag{2.2}$$

where $\hat{\tau}_y$, $\hat{\kappa}$ and n are the yield stress, the fluid consistency index and the power-law index, respectively. Fig. 2.2a shows that the fitted Herschel-Bulkley model follows the experimental data in a satisfactory way, and that the yield stress value increases with increasing the Carbopol concentration. The Herschel-Bulkley viscosity ($\hat{\mu}_c$) can be defined as

$$\hat{\mu}_c = \hat{\tau}_y \left(\frac{\hat{b}}{\hat{U}}\right) + \hat{\kappa}\left(\frac{\hat{U}}{\hat{b}}\right)^{n-1}. \tag{2.3}$$

Low concentration Carbopol gels typically exhibit weak elastic properties (75; 27; 61), which can be characterized through analyzing the first normal stress difference, $\hat{N}_1$, or the normal stress coefficient (83):

$$\hat{\Psi}_1 = \hat{N}_1/\hat{\dot{\gamma}}^2. \tag{2.4}$$

Figure. 2.2b illustrates the first normal stress difference ($\hat{N}_1$) as a function of the shear rate ($\hat{\dot{\gamma}}$) for different Carbopol concentrations, showing that $\hat{N}_1$ becomes significant at larger shear rates and it increases with an increase in the Carbopol concentration. According to Barnes *et al.* (6), $\hat{N}_1$ may be excepted to exhibit a power-law behaviour, as observed in our case. The solid lines represent the following power-laws fitted to the datapoints in Fig. 2.2b, for HCC, MCC, LCC, respectively:

$$\hat{N}_1 = 1.35\hat{\dot{\gamma}}^{0.55}, \tag{2.5}$$

$$\hat{N}_1 = 1.09\hat{\dot{\gamma}}^{0.52}, \tag{2.6}$$

$$\hat{N}_1 = 0.58\hat{\dot{\gamma}}^{0.51}. \tag{2.7}$$

The variation of $\hat{N}_1$ versus $\hat{\dot{\gamma}}$ in our work is generally comparable with the experimental measurement of Peixinho *et al.* (98; 97) for 0.2% Carbopol concentration:

$$\hat{N}_1 = 0.16\Big[4.3\hat{\dot{\gamma}}^{0.47} + 7.2\Big]^{1.4}, \tag{2.8}$$

and it is also qualitatively in agreement with the trend proposed in the correlation formula of Piau (99) for 1% Carbopol concentration over $10^{-5} < \hat{\dot{\gamma}} < 10^2$ (see also (117)):

$$\hat{N}_1 = 102\left[1.31\hat{\dot{\gamma}}^{0.39} + 1\right]. \tag{2.9}$$

In order to quantify the viscoelastic behaviours of our samples under flow, the Weissenberg number is typically used:

$$Wi = \frac{\hat{\Lambda}\hat{U}}{\hat{b}}, \tag{2.10}$$

which represents the ratio of the relaxation time ($\hat{\Lambda}$) to the timescale of flow ($\hat{b}/\hat{U}$). One of the common method to find the relaxation time of our samples can be written as (10; 28; 135):

$$\hat{\Lambda} = \frac{\hat{\Psi}_1(\frac{\hat{U}}{\hat{b}})}{2\hat{\mu}_c(\frac{\hat{U}}{\hat{b}})}, \tag{2.11}$$

showing that the relaxation time of our samples is a function of the ratio between the normal stress coefficient ($\hat{\Psi}_1$) and the effective viscosity. For different Carbopol concentrations, the variation of $\hat{\Lambda}$ as a function of the characteristic shear rate ($\hat{U}/\hat{b}$) is plotted in Fig. 2.2c, showing a decreasing trend.

Alternatively, in place of Wi, the elasticity number, $El = Wi/Re$ (84; 81), which only depends on the fluid properties and the Hele-Shaw geometry, can be used to compare the competition between elastic and inertial stresses.

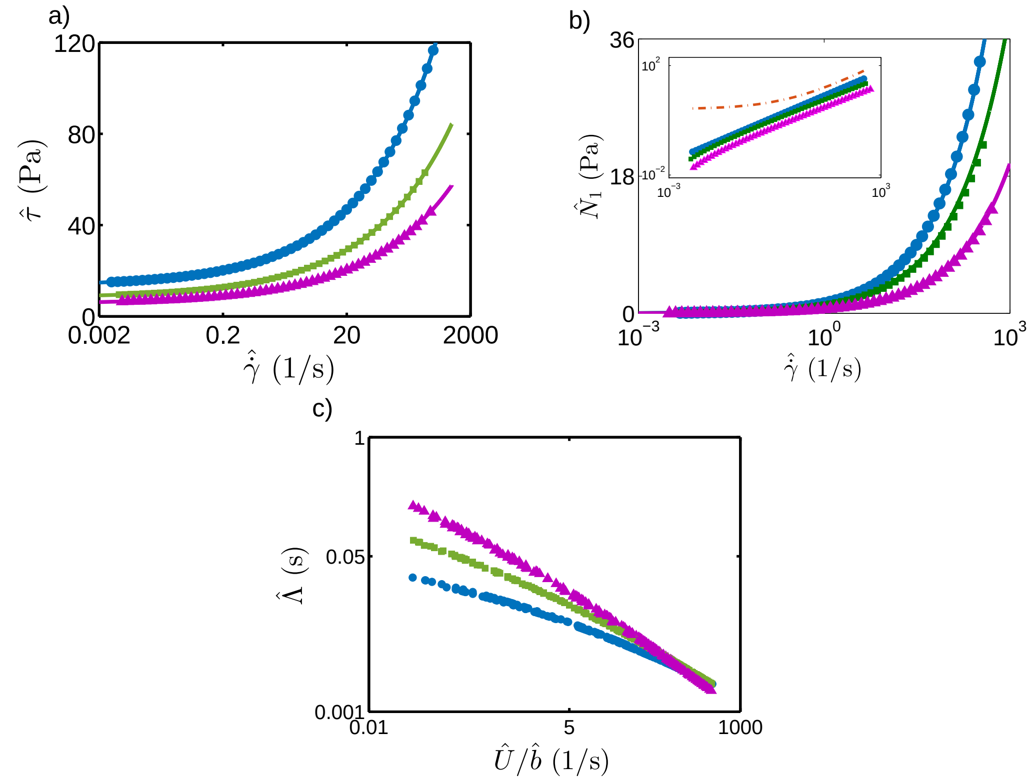

FIGURE 2.2 – (a) Flow curves of shear stress, $\hat{\tau}$, versus shear rate, $\hat{\dot{\gamma}}$. The lines correspond to the Herschel-Bulkley model parameters fitted to data. (b) First normal stress difference ($\hat{N}_1$) as a function of $\hat{\dot{\gamma}}$. The solid lines show the power-law fit corresponding to HCC ($\hat{N}_1 = 1.35\hat{\dot{\gamma}}^{0.55}$), MCC ($\hat{N}_1 = 1.09\hat{\dot{\gamma}}^{0.52}$) and LCC ($\hat{N}_1 = 0.58\hat{\dot{\gamma}}^{0.51}$). The inset presents the same data as in the main graph but in a logarithmic scale. The dash-dot line shows the variation of $\hat{N}_1$ as a function of $\hat{\dot{\gamma}}$ based on equation (2.8). (c) Relaxation time, $\hat{\Lambda}$, as a function of the characteristic shear rate ($\hat{U}/\hat{b}$) based on equation (2.11). The data correspond to HCC (●), MCC (■) and LCC (▲).

2.4.3 Wettability characterization

Our focus in this study is on the viscous finger problem in which oil displaces Carbopol gel. In this case, unlike most of traditional viscous fingering studies (e.g., using air and a viscous fluid), the effects of wettability becomes very crucial as the displacing fluid wets the wall during the displacement process. Therefore, before running displacement experiments, we needed to quantify relevant wettability effects associated to an oil-Carbopol system and, to provide further understanding, compare them to an air-Carbopol system. One way to evaluate the wettability is to measure contact angles, for which there exist a number of techniques, such as rising a liquid column in a capillary tube, reflection and deflection of rays by a liquid prism, direct photography, and interferential techniques (29). In the current study, we relied on a classical approach, i.e., measuring the wall contact angle based on the images of a small Carbopol gel drop placed on an acrylic plastic surface submerged into an oil-filled and air-filled

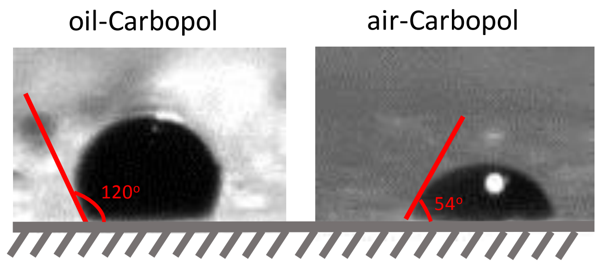

FIGURE 2.3 – Wall contact angle of a small drop of Carbopol (MCC) placed on an acrylic plastic plate submerged in an oil-filed reservoir (left) and in an air-filled reservoir (right). The field of view for each snapshot is 5.5×3.4 (mm^2).

reservoirs, which is a conventional method broadly used for the contact angle measurement of Carbopol drops (54; 105; 55). Finally, we processed the images using ImageJ and relying on a method proposed by Lamour *et al.* (66).

Fig. 2.3 illustrates an example of the results, in which the contact angle of a Carbopol drop in oil (θ_{oc}) is 120° while the contact angle of a Carbopol drop in air (θ_{ac}) is 54°. Note that a contact angle less than 90° implies that wetting of the substrate is favorable. On the other hand, a contact angle greater than 90° means that wetting of the substrate is unfavorable. In other words, a smaller contact angle represents a higher wettability (131). Therefore, the substrate's affinity to oil (in an oil-Carbopol system) is stronger than that to air (in an air-Carbopol system).

Due to the measurement technique adopted, it is necessary to ensure that the drop shape is not affected by the spreading and retraction of our yield stress fluid over the substrate. Fig. 2.4 presents the contact angle variations for air-Carbopol and oil-Carbopol drops versus time (starting from zero when the drop contacts the substrate), showing no considerable variations with time. This implies that the drops stop spreading at a given contact angle and there are no additional spreading or retractions thanks to the drop small sizes.

Table 2.3 provides the variation of θ_{oc} and θ_{ac} versus different Carbopol concentrations, showing only a small dependency of the contact angles on the Carbopol concentration. However, the contact angles are very different depending on whether oil or air surrounds the Carbopol drop. First, for all the measurements we found $\theta_{oc} > 90°$ and $\theta_{ac} < 90°$. Second, on average we have $\theta_{oc} \approx 119°$ and $\theta_{ac} \approx 55°$. These contact angles are generally comparable with those reported in the literature (54; 44).

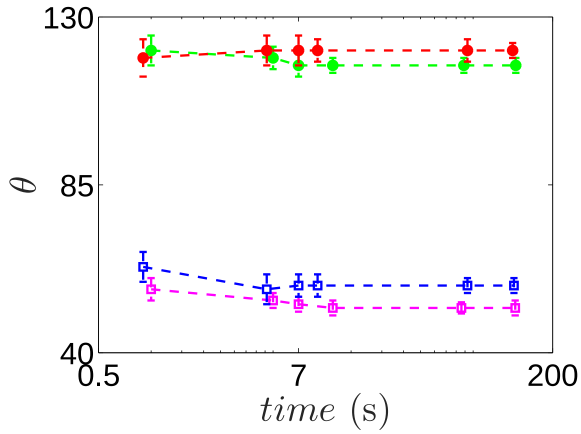

FIGURE 2.4 – Variation of the wall contact angle of a small drop versus time. The data correspond to experiments with oil-Carbopol (HCC) (•), oil-Carbopol (LCC) (•), air-Carbopol (HCC) (□) and air-Carbopol (LCC)(□). MCC results are not shown to make the presented datapoints visually distinguishable.

2.4.4 Interfacial tension characterization

Measuring the interfacial tension of viscoplastic fluids is difficult, which may be the reason why the interfacial tension is typically neglected in studying viscoplastic fluid flows over solid surfaces (26; 14). However, there are certainly cases, such as ours, in which the interfacial tension between the fluids involved must be quantified. There are a number of techniques for measuring the interfacial tension in simple fluids, such as the pendant drop method, the drop weight method, the Wilhelmy plate method, the maximum bubble pressure method, and the du Noüy ring method (26). These techniques are based on measuring residual stresses at vanishing velocities, for which viscous dissipation disappears. However, they may not be useful in the case of yield stress fluids, where finite residual stresses still exist at vanishing velocities (14). In addition, Truzzolillo *et al.* (120; 119) have recently focused on the interfacial tension between miscible fluids in Hele-Shaw flows, measuring the effective interfacial tension between the colloidal suspensions and their solvent, experimentally and theoretically. They have shown that the nature of colloidal fluids and the composition gradient at the interface significantly change the interfacial tension.

Considering the intricacy explained above, in order to obtain the oil-Carbopol interfacial tension, $\hat{\sigma}_{oc}$, we relied on an indirect approach, i.e., finding $\hat{\sigma}_{oc}$ through available measurements of relevant interfacial tensions and contact angles. The contact angle for two liquid systems can be related to interfacial tensions according to the Bartell-Osterhof equation (derived from the Young's law) (109; 46; 134), which we can write in our case as:

$$\hat{\sigma}_{oc}\cos(\theta_{oc}) = \hat{\sigma}_{ao}\cos(\theta_{ao}) - \hat{\sigma}_{ac}\cos(\theta_{ac}), \tag{2.12}$$

where the subscripts a, o and c represent air, oil and Carbopol gel, respectively. Therefore, we can estimate $\hat{\sigma}_{oc}$ provided that the following five parameters are known: θ_{oc}, θ_{ac}, θ_{ao}, $\hat{\sigma}_{ao}$, and $\hat{\sigma}_{ac}$. In the previous section, on average we found $\theta_{oc} \approx 119°$ and $\theta_{ac} \approx 55°$. We also measured θ_{ao} through the same technique explained earlier, finding on average $\theta_{ao} \approx 9.5°$. Also, for our low viscosity oil, the oil-air interfacial tension is $\hat{\sigma}_{ao} = 0.0197$ (N/m), given by the provider (Clearco Products). However, the reported values for $\hat{\sigma}_{ac}$ at low Carbopol concentrations slightly vary in the literature, for example 0.072 (N/m) (51), 0.069 (N/m) (79), 0.063 (N/m) (56), and 0.066 N/m (14). We took $\hat{\sigma}_{ac} = 0.066$ (N/m) and finally estimated the oil-Carbopol interfacial tension through equation (2.12) to be $\hat{\sigma}_{oc} \approx 0.037$ (N/m). This value is comparable with the oil-water interfacial tension (91; 109; 1).

For further confirmation on the value of $\hat{\sigma}_{oc}$, we relied on the findings of van Dijke and Sorbie (123) and Grate *et al.* (46), who demonstrated that there is a linear relationship between contact angle cosines in three-phase systems, which we can write in our case as:

$$\cos(\theta_{ac}) = \left[\frac{1 - (\hat{\sigma}_{ao} - \hat{\sigma}_{oc})/\hat{\sigma}_{ac}}{2}\right]\cos(\theta_{oc}) + \left[\frac{1 + (\hat{\sigma}_{ao} - \hat{\sigma}_{oc})/\hat{\sigma}_{ac}}{2}\right]. \tag{2.13}$$

Using the values of θ_{ac} and θ_{oc} at different Carbopol concentrations (Table 2.3) and through fitting a linear function, we determined the coefficients in equation (2.13) as $\cos(\theta_{ac}) = 1.57\cos(\theta_{oc}) + 1.31$, using which we again find $\hat{\sigma}_{oc} \approx 0.037$ (N/m). This value agrees well with findings of Varges *et al.* (124), who have recently determined the interfacial tension of Carbopol gel and various oils using simple empirical Antonow's rule.

Before we proceed, a clarification needs to be made on our approach to measure the contact angle, and subsequently determine the interfacial tension, for yield stress fluids. A natural question is how meaningful these contact angle measurements for our yield stress fluids are (see e.g., Fig. 2.3). This question is motivated by the fact the yield stress may also have a role in the drop final shape (and the contact angle) because of the presence of a non-zero internal shear stress, even at rest. In terms of forces, a drop shape is generally controlled by a balance between yield stress, interfacial tension and gravity. The latter is negligible in our case as we are dealing with small drops (also see the subsection below). The capillary and yield stress forces can be compared using the Bingham-capillary number (44; 105; 43; 55; 63):

$$B = \frac{\hat{\tau}_y \hat{\Gamma}}{\hat{\sigma}}, \tag{2.14}$$

where $\hat{\Gamma}$ denotes the characteristic system size, which in our case is the drop diameter. In our measurements, the drop volumes are small ($\leq 5\mu$l) and we find $0.07 < B < 0.18$ and $0.12 < B < 0.33$ for oil-Carbopol and air-Carbopol systems, respectively. Since $B < 1$, our drop shape is mainly controlled by the capillary forces whereas for $B \geq 1$ the yield stress forces would dominant. Therefore, our experiments are in the range where the contact angles can be properly defined based on the Young's law (43). These conclusions are in qualitative agreement with the literature. For example, German & Bertola (44) have experimentally found that for $B < 1$ the classical Young's law can describe the relationship between the interfacial tension and the contact angle of yield stress drops for various substrate conditions. For a yield stress flow driven by capillarity in horizontal tubes, Bertola (8) has used the Bingham-capillary to compare yield stress and capillary forces, revealing that a condition based on $B < 1$ and $B \geq 1$ determines whether the yield stress fluid moves in the tube. German & Bertola (44) have shown that, for $B < 1$, there is no notable dependency of the contact angles on the yield stress magnitude for different substrates, hydrophobic and hydrophilic surfaces, while for $B > 1$, the contact angle is clearly affected by the yield stress. Finally, Saidi *et al.* (105) have experimentally studied the properties of Carbopol drops at various conditions, finding that for $\hat{\tau}_y > 20$ (Pa), yield stress effects may dominate interfacial tension and gravity effects (note that in our work $\hat{\tau}_y \leq 13.7$ (Pa)).

2.4.5 Buoyancy effect characterization

An appropriate dimensionless parameter to quantify buoyancy effects in our work is the Bond number, which represents the ratio between gravitational and interfacial tension stresses:

$$Bo = \frac{\Delta\hat{\rho}\hat{g}\hat{b}^2}{\hat{\sigma}}, \tag{2.15}$$

where $\Delta\hat{\rho}$ is the density difference and $\hat{g}$ is the gravitational acceleration. To measure the densities of our experimental fluids, we used a high-precision density meter (Anton Paar DMA 35). For oil-Carbopol and air-Carbopol displacements, we found the Bond number to be $Bo < 0.04$ and $Bo < 0.3$, respectively, implying that buoyancy effects are negligible (30).

2.5 Results and discussion

Our main experimental findings are presented and discussed in this section. Approximately 900 experiments are conducted to cover a wide range of experimental parameters that include the imposed flow velocity, the Carbopol concentration and the cell gap thickness. Due to the presence of a large viscosity difference between the displacing and displaced fluids, oil (displacing fluid) penetrates into Carbopol gel (displaced fluid), presenting different flow patterns as well as various finger widths. Therefore, we analyze the results in two spirits:

i Analyzing flow morphological behaviours versus the flow parameters;

ii Analyzing the variation of the average finger width versus the flow parameters.

To unravel the difficulty of understanding our wetting displacement flows (oil displacing Carbopol gel), we compare the results against the corresponding non-wetting displacements with comparable parameters, in which air is used to displace Carbopol gel. Some of these non-wetting displacement results appeared in our recent work (36). For comparisons in which the non-wetting displacement results are not available in (36), either raw experimental data of air-Carbopol systems had to be analyzed or new experiments using air had to be performed. For a better comparison/presentation of the results, throughout the manuscript filled symbols, solid lines and solid arrows will be used to refer to oil-Carbopol displacements while hollow symbols, dashed lines and dashed arrows will be used to refer to air-Carbopol displacements, as given in Table 2.4. Finally, again for simplicity in presenting our experimental results, throughout the manuscript we rely on the following terminology:

— **Wetting displacement**: The displacing fluid is oil, which is more wetting to the solid surface than the displaced fluid (Carbopol solution).
— **Non-wetting displacement**: The displacing fluid is air, which is less wetting to the solid surface than the displaced fluid (Carbopol solution).

Oil-Carbopol result presentation	**Air-Carbopol result presentation**
Filled symbols (e.g., • and ★)	Hollow symbols (e.g., ∘ and ☆)
Solid line (–)	Dashed line (– – –)
Solid arrow ($\longrightarrow$)	Dashed arrow ($\dashrightarrow$)

TABLE 2.4 – The logic notations used in our work to present results.

2.5.1 General flow behaviours

When oil sweeps Carbopol gel, we observe four distinct flow patterns depending on the flow parameters. Fig. 2.5a presents these flow patterns for increasing values of the mean imposed flow velocity ($\hat{V}$) while the other flow parameters are kept constant:

— At very low $\hat{V}$, as the displacing fluid preferentially wets the Hele-Shaw cell, a tear-shaped finger is formed (top image in Fig. 2.5a). The finger is wide and the interface is smooth and uniform. As observed, the displacement efficiency is relatively large. Due to the significance of interfacial tension stresses, this flow can be called a *capillary* regime. This flow regime is not observed in non-wetting displacements and, to the best of our knowledge, it has not been previously reported in the literature of non-Newtonian viscous fingering.
— At low $\hat{V}$, the initial displacement finger frequently splits and the flow presents a ramified structure with several asymmetric fingers (second image in Fig. 2.5a). Due to the importance of the gel yield stress in destabilizing the finger, this flow regime can be called a *yield stress* regime. Interesting, this flow has been observed in non-wetting displacements (74; 36).
— At large $\hat{V}$, the flow presents a state which consists of a single, narrow viscous finger (third image in Fig. 2.5a). The narrow finger exhibits somewhat symmetry and it is found more or less in the middle of the channel. Contrary to the yield stress regime,

the finger tip splitting is completely suppressed and the flow regime in a sense is similar to that of classical Newtonian viscous fingers (74; 122). Therefore, this regime can be named a *viscous* regime, which has been also observed in non-wetting displacements (74; 36).

— Finally, at extremely high $\hat{V}$, an asymmetric displacing finger is typically formed in middle of the cell (bottom image of Fig. 2.5a). Although the main finger tip is not split, its sides are branched due to secondary instabilities. The side branches have various lengths and orientations. Previous studies have observed the same phenomenon in the context non-wetting displacements (77; 36), which they attributed to non-negligible elastic effects. Eslami and Taghavi (36) have also shown the finger width in this regime undergoes a sudden increase due to inertial effects. Therefore, this regime can be called an *elasto-inertial* regime.

Fig. 2.5b shows the corresponding non-wetting (air-Carbopol) displacement snapshots at imposed velocities comparable with Fig. 2.5a. A qualitative comparison may be useful. As can be seen, in a sequence of increasing $\hat{V}$, for both cases the flow morphology strongly depends on the imposed velocity. However, at very small $\hat{V}$, two completely different morphologies are observed depending on whether the displacing fluid wets the cell walls. For non-wetting displacement flows, a ramified structure pattern is observed, whereas for wetting displacement flows, a single, tear-shaped finger pattern is found. The magnitude of the finger width is much larger in the case of the latter. By slightly increasing $\hat{V}$, the flow pattern for wetting displacements remarkably changes: the flow transitions from a tear-shaped finger to a ramified structure pattern. For non-wetting displacements, the flow pattern remains the same (i.e., ramified structure). Although the flow regimes at this $\hat{V}$ are the same for wetting and non-wetting displacements, the finger width seems larger in the case of the wetting one. At high velocities, both cases present a single finger, for which at least visually the wetting condition does not seem to affect the flow pattern, although the wider finger still belongs to the wetting case. Finally, at very high $\hat{V}$, for both cases there exist a single finger with side branches. However, the orientation of the branches for wetting and non-wetting displacements is different, which we will discuss further towards the end of the paper. This is in line with general findings in the literature arguing that a wettability condition (contact angle) alteration can dramatically change displacement flow patterns in Hele-Shaw cells (118) or in porous media (108).

It must be noted that the aforementioned flow regimes in Figs. 2.5a and b are determined based on visual observations to distinguish among various morphological behaviours. However, Fig. 2.5c shows that these flow regimes also correspond to distinguishable behaviours in the variations of the finger width, as a quantitative measurement. In addition, we will see later in the paper that these different morphologies correspond quite well to the appropriate regions in the planes made with the dimensionless groups that are expected to control the flow dynamics.

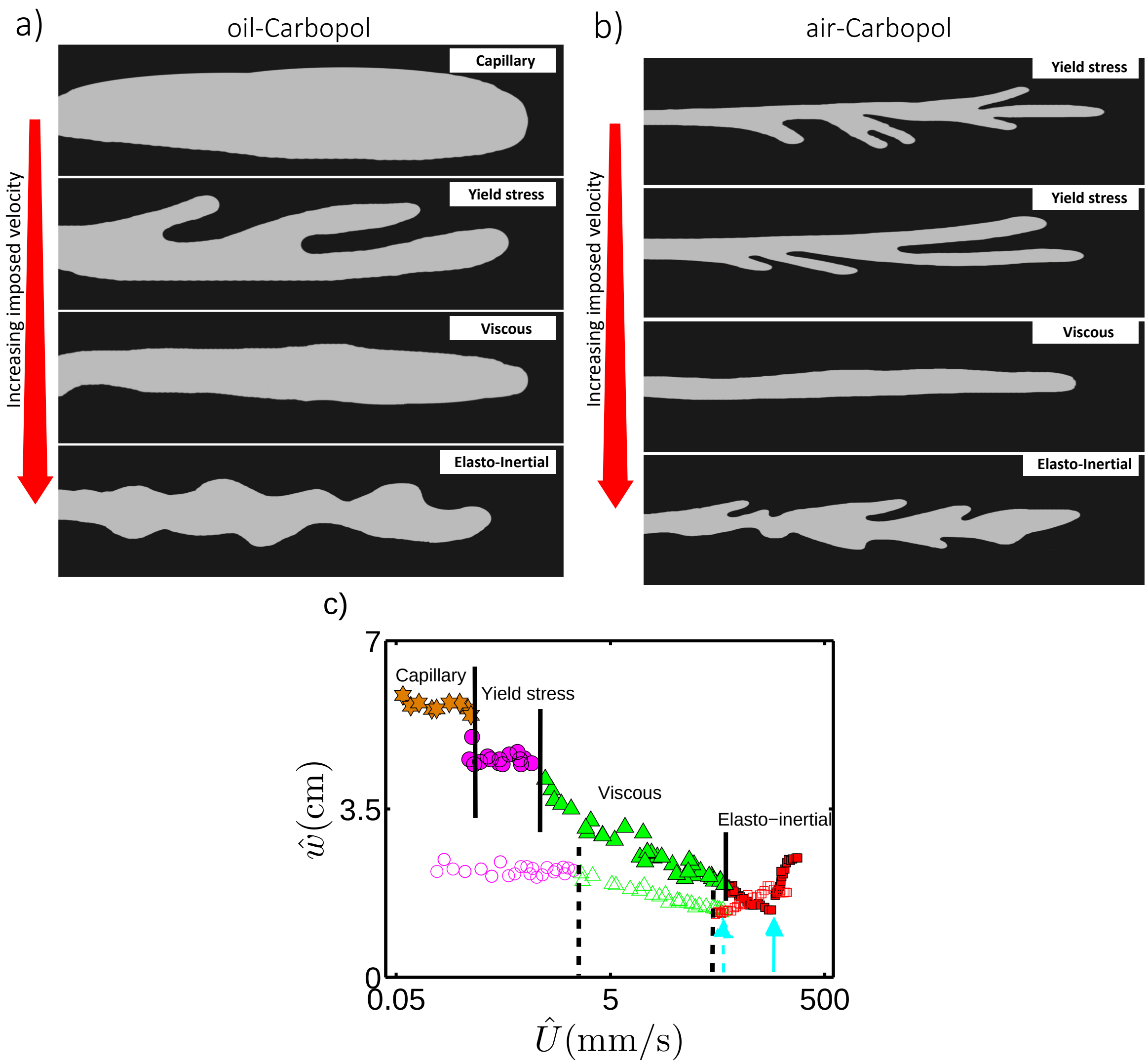

FIGURE 2.5 – Experimental results of the displacement of an LCC gel by (a) oil and by (b) air, in a Hele-Shaw cell geometry with $\hat{b} = 1.5$ (mm). The oil/air flows from left to right. In both (a) and (b), the mean imposed velocities are $\hat{V} = 0.09, 0.3, 5.7, 29$ (mm/s), from top to bottom. The field of view for each snapshot is 6.12×22.05 (cm^2). (c) Variation of the finger width, $\hat{w}$, versus the finger tip velocity, $\hat{U}$. Different flow regimes are marked: capillary (★); yield stress (●,○); viscous (▲,△), and elasto-inertial (■, □). Note that the capillary regime is not observed for air-Carbopol displacements. The vertical solid (dashed) lines show transition boundaries for oil-Carbopol (air-Carbopol) displacements. The solid (dashed) arrow indicates the critical point where inertial effects start to become important, for displacements of Carbopol gel by oil (air).

Note that although the aforementioned patterns and regimes were explained as a function of the mean imposed velocity ($\hat{V}$), they can be equally described versus the finger tip velocity ($\hat{U}$), since $\hat{V}$ and $\hat{U}$ are proportional. Therefore, for the rest of the paper $\hat{U}$ will be employed as the flow characteristic velocity, which can also be used to properly define the capillary number.

In wetting displacement flow experiments, we observe four different flow regimes (i.e., capillary, yield stress, viscous, and elasto-inertial regimes), depending on the experimental parameters such as the imposed velocity, the Carbopol concentration, the gap thickness, the wettability condition, etc. Although we will later deliver proper flow regime classifications versus the flow dimensionless groups, to make sense of the appearance each regime versus the finger velocity, let us provide the following very rough estimations (averaged over six different experimental conditions):

— Capillary regime: $\hat{U} < 0.35$ (mm/s)
— Yield stress regime: $0.35 \leq \hat{U} < 4.5$ (mm/s)
— Viscous regime: $4.5 \leq \hat{U} < 65$ (mm/s)
— Elasto-inertial regime: $\hat{U} \geq 65$ (mm/s)

Let us now analyze the average finger width[3], $\hat{w}$, versus the finger tip velocity, $\hat{U}$, for the various flow regimes and patterns observed in wetting displacements and compare them with non-wetting displacements. The variation of $\hat{w}$ as a function of $\hat{U}$ is plotted in Fig. 2.5c. The four (three) different filled (hollow) symbols on this graph illustrate the above-mentioned flow regimes for oil (air) displacement flows. The variation of $\hat{w}$ versus $\hat{U}$ in wetting and non-wetting displacement flows seem to follow the same trend. However, at very low $\hat{U}$, the capillary regime is only observed for wetting displacements. For the same values of imposed velocity, the corresponding non-wetting displacements present a yield stress regime, with ramified fingers and with much smaller $\hat{w}$. For both cases, $\hat{w}$ remains almost independent of $\hat{U}$. At slightly larger $\hat{U}$, the flow pattern of wetting displacements changes to the yield stress regime with ramified fingers. In this regime $\hat{w}$ is almost independent of $\hat{U}$, for wetting and non-wetting cases. At larger $\hat{U}$, for both wetting and non-wetting cases, the flow enters a viscous regime, in which $\hat{w}$ continuously decreases with $\hat{U}$. Finally, at very large $\hat{U}$, the flow transitions into an elasto-inertial regime with side branches, in which a non-monotonic variation of $\hat{w}$ versus $\hat{U}$ is also observed: initially $\hat{w}$ decreases, but after a critical velocity, it suddenly increases. At higher $\hat{U}$, the values of $\hat{w}$ for wetting and non-wetting displacements approach one another. Note that although $\hat{w}$ undergoes a non-monotonic variation, the flow morphology does not change within this regime.

It is natural to study the effects of the flow parameters, namely the channel thickness and the Carbopol concentration, on the variation of $\hat{w}$ versus $\hat{U}$, as carried out in Fig. 2.6. By increasing the channel thickness, the finger width increases for wetting displacements (Fig. 2.6a).

3. For simplicity throughout the paper, we refer to the average finger width by the "finger width".

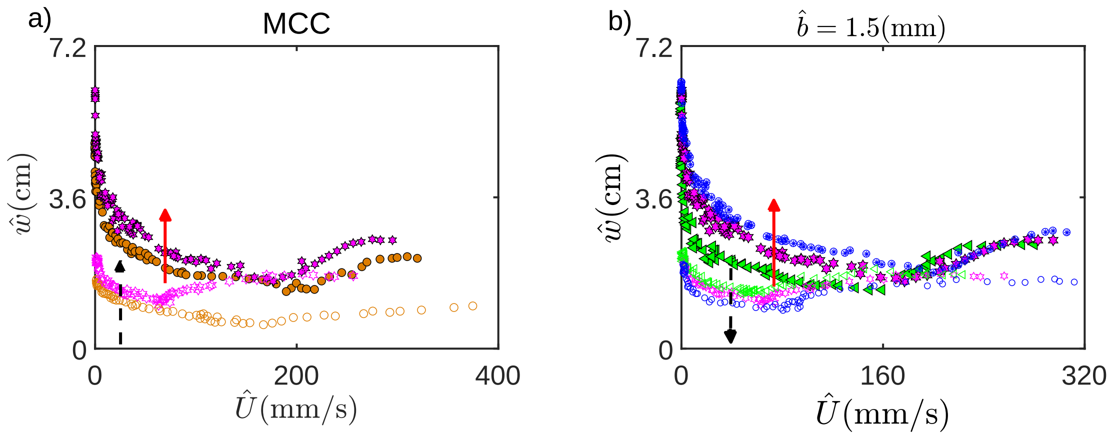

FIGURE 2.6 – (a) Variation of $\hat{w}$ versus $\hat{U}$, for different channel thicknesses and at a fixed Carbopol concentration, MCC. The data correspond to experiments with $\hat{b}$ = 0.9 (mm) (●, ○) and $\hat{b}$ = 1.5 (mm) (★, ☆). The channel thickness in wetting (non-wetting) displacement flows increases in the solid (dashed) arrow direction. (b) Variation of $\hat{w}$ versus $\hat{U}$, for different Carbopol concentrations and at a fixed channel thickness, $\hat{b}$ = 1.5 (mm). The data correspond to experiments with LCC (◂, ◃), MCC (★, ☆), HCC (⊛, ∘). The Carbopol concentration in wetting (non-wetting) displacement flows increases in the solid (dashed) arrow direction.

The same effect is seen in non-wetting displacements (Fig. 2.6a). Thus, the effects of the channel thickness on the finger width does not seem to be a function of the wettability behaviour. By increasing the Carbopol concentration, the finger width decreases in non-wetting displacements (Fig. 2.6b). However, for wetting displacements, increasing the Carbopol concentration results in increasing the finger width, for most of the parameter ranges (except for very small velocities). This is a striking finding since, at least based on the morphological behaviours, the effects of wetting seemed to be limited to very small velocities (capillary regime). However, these effects seem to be still present to significantly affect the flow even at large velocities. Therefore, the finger width selection mechanism for the oil-Carbopol system seems to be different from the air-Carbopol system.

Looking again at Fig. 2.6, it can be noted that, for a given velocity, the values of $\hat{w}$ in wetting displacements are larger with respect to their corresponding values in non-wetting displacements, for various Carbopol concentrations and channel thicknesses. This implies that in comparable conditions an oil-Carbopol displacement is more efficient than an air-Carbopol displacement, regardless of the flow pattern. This observation is in line with the general findings in the literature. For example, for Newtonian displacements in porous media, it has been found that when the invading fluid is wetting, the finger width is larger than when the defending fluid is wetting (108). In addition, for fluid-fluid displacements in granular media, it has been demonstrated that increasing wettability of the displacing fluid stabilizes the invasion and increases the finger width at all capillary numbers (118).

2.5.2 Main flow regimes

As explained, our wetting displacement flows exhibit four different flow regimes, the understanding of which is crucial from a physical and practical point of view. In the following subsections, we will explain these regimes in detail.

Capillary regime

Since the capillary regime has not been reported before in the context of non-Newtonian viscous fingering, it is useful to study its displacement flow features. However, before doing so, it seems necessary to describe the origin of this regime in wetting displacements, through specifying three critical differences between wetting and non-wetting displacements.

First of all, in our experiments the invading fluid with a lower viscosity wets the walls of the Hele-Shaw cell, unlike more traditional viscous fingering experiments where the defending fluid wets the walls and the invading one leaves behind a wetting thin film of the displaced fluid on the walls (compare Figs. 2.1b and c). The thickness of this film remarkably affects the flow in non-wetting displacements and it is a function of Ca for Newtonian fluids (111; 112) and of Ca and Bn for viscoplastic fluids (36). Furthermore, the mean residual film thickness for non-wetting viscoplastic fluid flows is larger than their Newtonian counterparts (36). Our experimental results show that these residual films are not observed in the capillary regime in wetting yield stress displacements.

FIGURE 2.7 – Experimental side-view snapshots showing the interface shape for HCC in a cell with $\hat{b} = 2.5$ (mm) for air-Carbopol (left) and oil-Carbopol (right) displacements. The field of view in each snapshot is 3.94×18.63 (mm^2). The oil/air flows from left to right. The mean imposed velocity is $\hat{V} \approx 0.04$ (mm/s), in both cases.

Second, there is another difference that is more pronounced at small capillary numbers (or at very low velocities), which we explained earlier using Fig. 2.1. In wetting displacements in certain cases, we postulated that the interface in the $\hat{x}\hat{y}$-plane (Fig. 2.1b) advances as a concave meniscus (106) as a result of the wetting properties of the displacing fluid. In non-wetting displacements, on the other hand, the interface moves as a convex meniscus (Fig. 2.1c). We now try confirm this picture for yield stress displacements using Fig. 2.7, illustrating the side-view of wetting and non-wetting displacements, for experiments conducted with HCC. To obtain these side-view results (i.e., the $\hat{x}\hat{y}$-plane), a macro lens (zoom 7000 NAVITAR) is used along with our high-speed camera. At a small imposed velocity ($\hat{V} \approx 0.04$ (mm/s)), the solid-air-Carbopol contact angle (e.g., 51°) is smaller than 90° while the solid-oil-Carbopol contact angle (e.g., 129°) is larger than 90°, confirming our general expectations for the specific case of yield stress displacements. These findings are conceptually in agreement with the recent literature showing the formation of a convex meniscus in non-wetting displacements of yield stress fluids (see Fig. 2 in (132)) and a concave meniscus in wetting displacements of colloid-polymer mixtures (see Fig. 4b in (106)).

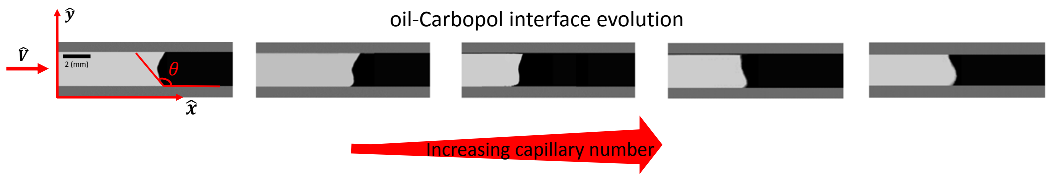

FIGURE 2.8 – Oil-Carbopol interface evolution, from side-view, versus Ca at a given channel thicknesses ($\hat{b}$ = 2.5 (mm)) and a fixed Carbopol concentration, HCC. The capillary numbers are $Ca = 0.78, 0.86, 0.92, 0.97, 1.04$, from left to right. The field of view in each snapshot is 3.94×12.93 (mm^2).

Third, it is worth pointing out that the evolution of the curvature of the advancing interface with the imposed velocity (i.e., change in the dynamic contact angle) for wetting and non-wetting displacements is quite different. For wetting cases, the dynamic contact angle may significantly differ from the static one, as it can vary as a function of the interface speed (24). For Newtonian fluids in the case of a completely wetting fluid we have ${\theta_d}^3 \propto U$, which is known as Tanner's law (33; 9; 19) (with $\theta_d = \pi - \theta$). In addition, several experimental studies (24; 47; 12) have been conducted on the measurement of the dynamic contact angle as a function of the interface velocity and fluid properties, demonstrating that θ_d changes with Ca for Newtonian fluids. We observe similar evolution behaviours in oil-Carbopol displacements as Ca increases, as shown in Fig. 2.8. The oil-Carbopol interface initially advances as a concave meniscus while its shape changes with Ca. The dynamic contact angles on the top and bottom walls are not completely symmetric, which may be due to presence of yield stress and buoyancy effects. The latter may appear as the gap thickness has been increased for visualization purposes ($\hat{b}$ = 2.5 (mm)) (similarly, for yield stress displacements, Zhang *et al.* (132) have shown that by increasing the gap thickness the interface curvature slightly changes but it keeps its overall curvature sign). It can be seen from Fig. 2.8 that the dynamic contact angle of the meniscus, θ_d, generally increases with increasing Ca (from left to right in Fig. 2.8), meaning that the curvature of the meniscus decreases by increasing Ca. Increasing the capillary number further will lead to decreasing the meniscus curvature even more and eventually changing a curvature sign (i.e., concave to convex). Our experimental results will further clarify how that this change in the curvature sign can be associated to the transition between the capillary and yield stress regimes.

Let us analyze in more detail the variation of θ_d versus the other parameters. For the case of a partially wetting Newtonian displacement, there exists a simple relation between θ_d and Ca

(41):

$$\tan\theta_d = 3.4(Ca)^{1/3}\,, \tag{2.16}$$

and for the case of a completely wetting Newtonian displacement (59):

$$\tan\theta_d = 7.48(Ca)^{1/3}\,. \tag{2.17}$$

Note that these relations will break down when θ_d approaches 90° due to the nature of the tangent function. For oil-Carbopol displacements, Fig. 2.9a presents the variation of $\tan\theta_d$ versus Ca, in which the mean value of θ_d on the top and bottom walls is employed. In general, it can be seen that θ_d strongly increases with Ca and that $\tan\theta_d$ can be also affected by the Carbopol concentration. For comparison purposes, the theoretical Newtonian results of equations (2.16) and (2.17) are also superimposed on the graph. Although the trends are the similar, the yield stress results do not fall in the Newtonian lines. While the power-law for Newtonian fluids is 1/3, for yield stress fluids, the fitted lines would follow a power-law larger than one (not shown). There are possible explanations for this discrepancy. First of all, in contrast to Newtonian cases where a small capillary number ($10^{-7} < Ca < 10^{-1}$) is common (33), in our oil-Carbopol flows, we find $Ca > 0.1$ primarily due to the large effective viscosity of Carbopol. In addition, the results can be affected by the viscosity ratio (i.e., the effective viscosity ratio of Carbopol and oil) in the current work, which is larger than that in Newtonian cases. For example, Levache & Bartolo (70) have analyzed the variation of the meniscus shape in wetting Newtonian displacements, finding that both Ca and the viscosity ratio control the dynamic interface deformation. In fact, they have demonstrated that the value of viscosity ratio has a notable, non-monotonic impact on the meniscus characteristics. Fig. 2.9b shows the variation of $\tan\theta_d$ as a function of the Bingham number for two different Carbopol concentrations. As seen, there exists a significant dependency of $\tan\theta_d$ on Bn. By increasing Bn, $\tan\theta_d$ decreases, implying that at larger Bingham numbers the interface moves as a concave meniscus and that by decreasing Bn the interface tends towards a convex meniscus.

Our findings on the within-the-gap evolution of the interface shape with Ca are qualitatively in agreement with the general literature results. In wetting displacements, the balance between the pressure drop across the interface and the capillary pressure can change the interface curvature in the vicinity of wall (133). By increasing the imposed velocity, the pressure drop across the interface is increased; consequently, according to the Young-Laplace equation, the radius of curvature decreases. For wetting displacements, Setu *et al.* (106) have numerically and experimentally studied the development of viscous fingering in colloid-polymer mixtures, and they quantified the interface shape evolution as a function of the capillary number. At a small Ca, the interface moves as a concave meniscus but increasing Ca results in a change in the interface shape, eventually leading to a convex form at large Ca. Zhao *et al.* (133) have also considered wetting displacements in porous media, finding that θ_d increases with increasing Ca.

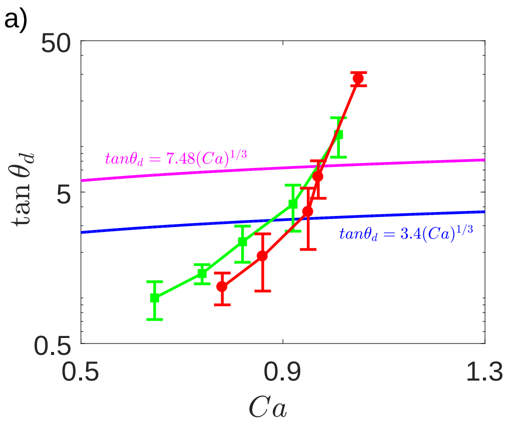

FIGURE 2.9 – Variation of $\tan\theta_d$ versus (a) Ca and (b) Bn at a given channel thickness ($\hat{b}$ = 2.5 (mm)) for oil-Carbopol displacements. The data correspond to experiments with HCC (●) and MCC (■). In (a) the solid lines present the theoretical results of equation (2.16) and equation (2.17) for Newtonian fluids.

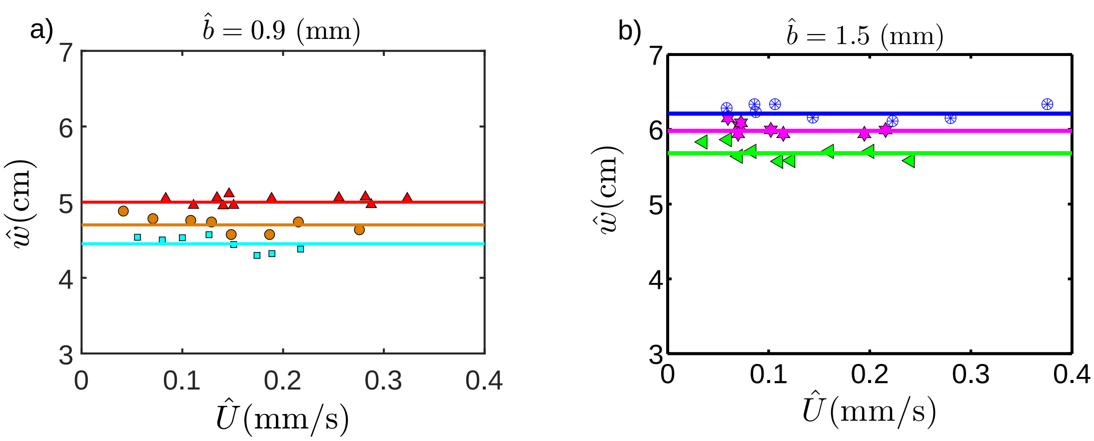

FIGURE 2.10 – (a) & (b) Variation of $\hat{w}$ versus $\hat{U}$ in the capillary regime, for oil-Carbopol displacements. The data correspond to experiments at $\hat{b}$ = 0.9 (mm) with LCC (■), MCC (●) and HCC (▲) and at $\hat{b}$ = 1.5 (mm) with LCC (◂), MCC (★), HCC (⊛). The horizontal lines show the mean values of $\hat{w}$. Note that in air-Carbopol displacements, the capillary regime is not observed.

Based on the discussions above, it seems that the cross over from the capillary regime (at very low velocities) to the yield stress regime (at low velocity) in wetting displacements may be linked to complex changes in the interface shape (and curvature) within the cell gap. In fact, it is known that the interface shape in the $\hat{x}\hat{y}$-plane (side-view) may have a notable impact on the viscous fingering features in the $\hat{x}\hat{z}$-plane (e.g., finger morphology, finger width, etc.). For example, it has been shown that the viscous fingering instability can be suppressed due to the concave meniscus in the $\hat{x}\hat{y}$-plane (106). The stabilizing effects of wettability at lower capillary numbers have been also experimentally shown for Newtonian displacements (118).

Therefore, at lower capillary numbers, in general the flow behaviours in the $\hat{x}\hat{y}$-plane and the $\hat{x}\hat{z}$-plane are entangled, implying that 3D effects should be considered to fully understand the flow.

We can now return to describing the flows features the capillary flow regime, mainly based on the finger width. The capillary regime in our experiments is associated with a quasi-steady removal of the displaced fluid and a wide, tear-shaped finger. The variation of the finger width versus the finger tip velocity in this regime is shown in Fig. 2.10. For a given parameter set, the finger width is almost independent of $\hat{U}$. Increasing the Carbopol concentration seems to only slightly increase $\hat{w}$, for both channel thicknesses ($\hat{b}$). However, increasing $\hat{b}$ from 0.9 (mm) to 1.5 (mm) appears to be more influential: when the channel thickness is larger, the finger width is also larger.

In addition to the finger width, as an indicator of the displacement efficiency, the variation of the dynamic contact angle can be also quantified to provide further understanding about the capillary regime, e.g. through analyzing the variation in the relative mean light intensity across the interface (cell top view), as discussed in §2.5.4.

Similarities of the capillary regime in Newtonian and yield stress fluid displacements As mentioned earlier, the capillary flow regime is not observed in non-wetting displacements and it has not been previously reported in the literature of non-Newtonian viscous fingering. To give a broader understanding of the capillary regime, here, we explain how the injection of a wetting fluid into a yield stress fluid has certain similarities with the injection of a wetting fluid into a Newtonian fluid.

First of all, the wettability generally stabilizes the displacement in both Newtonian and yield stress fluids, in particular, at lower imposed velocities. In wetting yield stress displacements, at very small capillary number, there exists a single stable finger, compared to ramified structures observed for non-wetting displacements (see e.g., Fig. 2.5a & b). This stabilization effect may be compared to that in Newtonian displacements. For example, Trojer *et al.* (118) have experimentally studied Newtonian displacements in a wide range of contact angles and capillary numbers, revealing the stabilizing effects of wettability at lower Ca, as it delays the development of instabilities to higher capillary numbers. For immiscible displacements at very small Ca in a Hele-Shaw cell with cylindrical posts, Jung *et al.* (57) have also shown that the interface between two fluids remains smooth and stable when the displacing fluid wets the medium.

Second, the finger widths in wetting displacements are larger with respect to their corresponding values in non-wetting displacements for both Newtonian and yield stress fluids. Regarding the latter, we observe in Fig. 2.5c that the values of $\hat{w}$ at small Ca are much larger for wetting displacements. For Newtonian fluids, a comparison between experimental results of oil-Glycerol displacements (wetting Newtonian) compared against non-wetting displacements shows that the finger width in wetting cases are larger than their corresponding values for non-wetting flows (results are not shown for brevity).

Finally, the displacement efficiency of wetting displacements are in general higher than their corresponding non-wetting flows for both Newtonian and yield stress cases. For yield stress fluids, this can be visually observed through comparing the top images in Fig. 2.5a and Fig. 2.5b. For Newtonian fluids, Zhao *et al.* (133) have demonstrated that increasing the medium affinity to the displacing fluid leads to a more efficient fluid displacement. In addition, Stokes *et al.* (108) have shown that, for Newtonian flows in a Hele-Shaw cell packed with unconsolidated glass beads, the displacement is more efficient when the displacing fluid preferentially wets the medium.

Although, as explained above, there are certain similarities between wetting Newtonian and yield stress displacements, compared to their corresponding non-wetting flows, there are also unique features due to the role played by the yield stress in wetting yield stress displacements. We will return later to look into these features in more detail.

Yield stress regime

Yield stress fluid flows in confined geometries have been generally studied under the assumption that wettability does not affect the flow, essentially considering non-wetting displacements, except for very specific situations such as thin film flows and droplet impact (26). In addition, a majority of studies have focused on the case of viscous effects being dominant, partly due to the lack of clear data on the effective interfacial tension of yield stress materials (26). When yield stress effects dominate, using linear stability analysis, some valuable theoretical works deliver a criterion for the instability onset as well as the maximum growth wavelength for yield stress fluids (25), extending their classical Newtonian counterparts (23). However, there is a serious lack of such studies for wetting displacements.

Although wetting and non-wetting displacements are inherently different, our experimental results of wetting displacements reveal the existence of the yield stress regime at relatively low finger velocities, which is well studied theoretically and experimentally for non-wetting displacements (73; 74; 77; 36). This regime is associated with the yield stress dominated fingering and is referred to as the yield stress regime since the yield point is not exceeded everywhere in the flow (73). In our wetting displacements at low velocities, we also observe that the yield stress has a significant role, leading to frequent tip-splittings and branched patterns. Figs. 2.11a and b show the variation of the finger width versus the finger tip velocity for the yield stress regime. The wetting and non-wetting displacement results are marked by filled and hollow symbols, respectively. At a given Carbopol concentration or at a fixed channel thickness, the finger width is independent of the finger tip velocity for both wetting and non-wetting

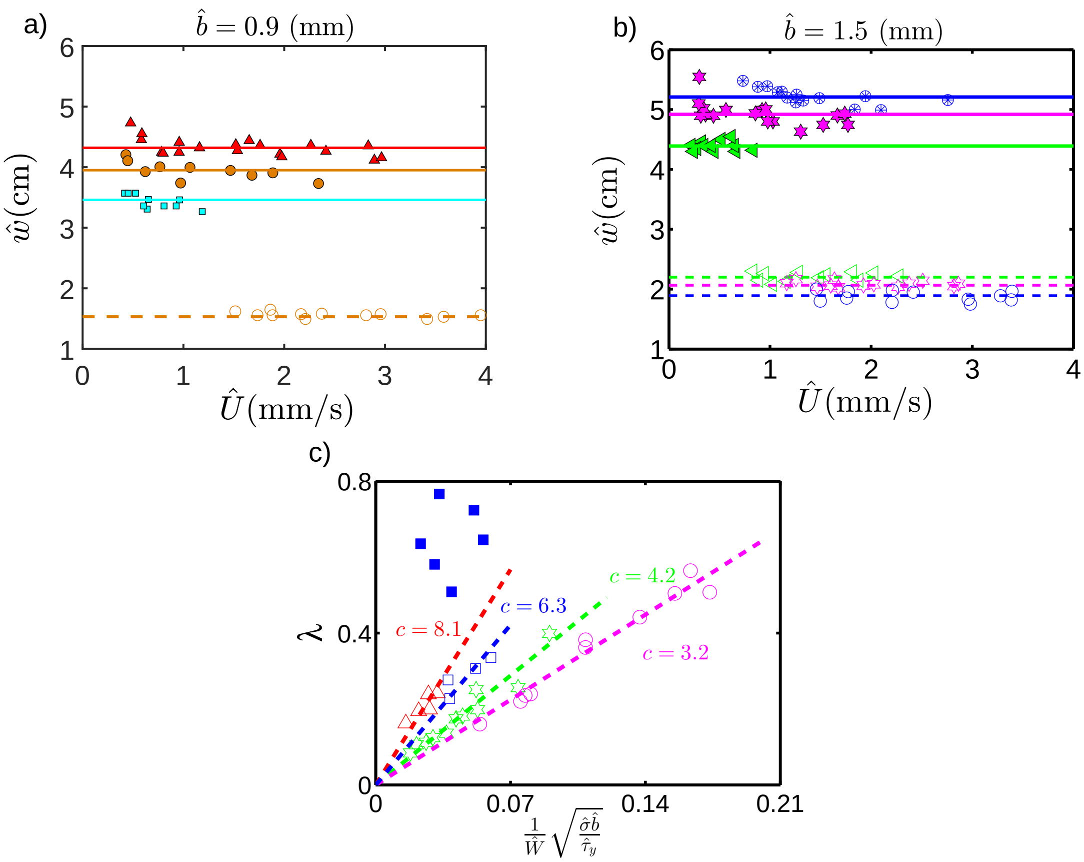

FIGURE 2.11 – (a) & (b) Variation of $\hat{w}$ versus $\hat{U}$ in the yield stress regime, for oil (filled symbols) and air (hollow symbols). The horizontal lines and dashed lines show the mean values of $\hat{w}$. The data correspond to experiments at $\hat{b} = 1.5$ (mm) with LCC (◂, ◁), MCC (★, ☆), HCC (⊛, ∘) and at $\hat{b} = 0.9$ (mm) with LCC (■), MCC (•, ∘) and HCC (▲). (c) Dimensionless mean finger width, λ, as a function of a dimensionless control parameter, $\lambda = \frac{c}{\hat{W}}\sqrt{\frac{\hat{\sigma}\hat{b}}{\hat{\tau}_y}}$, with c being the coefficient of the linear fit. Our wetting displacement results (■) against non-wetting results from (73) (☆), (32) (∘), (77) (△), and (36) (□).

cases. We also note that both the channel thickness and the Carbopol concentration slightly affect the mean finger width value and that the finger width for the wetting displacements lie above the non-wetting ones. It must be noted that for non-wetting displacements at these flow conditions (i.e., large aspect ratio and small Bond numbers), the finger width in the yield stress regime (lower velocities) does not depend on the channel width (73).

It has been extensively shown that, for non-wetting displacements in the yield stress regime, the finger width shortly after destabilization corresponds to $\hat{\lambda}_m$, which is the wavelength of the maximum growth, which theoretically follows (73; 77; 25):

$$\hat{\lambda}_m \propto \sqrt{\frac{\hat{\sigma}\hat{b}}{\hat{\tau}_y}}, \tag{2.18}$$

implying that $\hat{w}$ is independent of $\hat{U}$ and $\hat{W}$ and one can therefore write $\hat{w} \propto \sqrt{\frac{\hat{\sigma}\hat{b}}{\hat{\tau}_y}}$. Based on this argument, Fig. 2.11c plots the dimensionless mean finger width, λ, as a function of an appropriate dimensionless parameter:

$$\lambda = \frac{\hat{w}}{\hat{W}} \propto \frac{1}{\hat{W}}\sqrt{\frac{\hat{\sigma}\hat{b}}{\hat{\tau}_y}}. \tag{2.19}$$

In addition to our wetting displacement results, several numerical and experimental non-wetting displacement results from the literature (73; 77; 32; 36) have been also added on the graph. Interesting, for all the non-wetting displacement results, there are linear relations between the control parameter and the dimensionless mean finger width, i.e., $\lambda = c\frac{1}{\hat{W}}\sqrt{\frac{\hat{\sigma}\hat{b}}{\hat{\tau}_y}}$, with c being the coefficient of the linear fit. Nevertheless, λ for oil-Carbopol displacements (filled squares) does follow a linear line and it therefore does not scale with the control parameter used for non-wetting displacements. This means that, although there are similarities in terms of the existence of the yield stress regime in both wetting and non-wetting displacements, the current theoretical relations developed for non-wetting displacements are incapable of predicting the finger width of wetting displacements in this regime.

Before we proceed to the next flow regime, it is worth noting that the values of c are not the same for the four sets of non-wetting displacement results shown in Fig. 2.11c, a feature which may be attributed to the effective interfacial tension that instead must be used in the control parameter definition. For instance, Tabeling & Libchaber (111) employed a modified interfacial tension by considering the film left behind the fingers, finding a better agreement between theoretical and experimental results of the finger width.

Viscous regime

At higher velocities, as oil sweeps Carbopol gel, the flow transitions from a yield stress dominated regime to a viscous dominated regime, where both the flow morphology and the finger width (displacement efficiency) change significantly. First, instead of the ramified structures in the yield stress regime, a single finger in the middle of the channel is formed. Second, the finger width is no longer independent of the finger tip velocity; instead $\hat{w}$ continuously decreases with $\hat{U}$.

Although the flow is complex, the viscous regime may be understood through finding a proper control parameter that results in a reasonable collapse of the finger width values onto a master curve, for a wide range of parameters. Nevertheless, non-wetting displacements have been the subject of almost all the previous works attempting to find such a control parameter. For example, for Newtonian flows, $Ca\delta^2$ has been found to be the appropriate dimensionless group (50; 82; 111; 121). For viscoplastic fluids with strong shear-thinning effects ($n \leq 0.65$), $Ca\delta$ has been suggested (73). More recently, it has been demonstrated that a better control parameter for viscoplastic fluids may be $Ca\delta^{1+n}$ (36), which also satisfies the Newtonian limit ($n \to 1$).

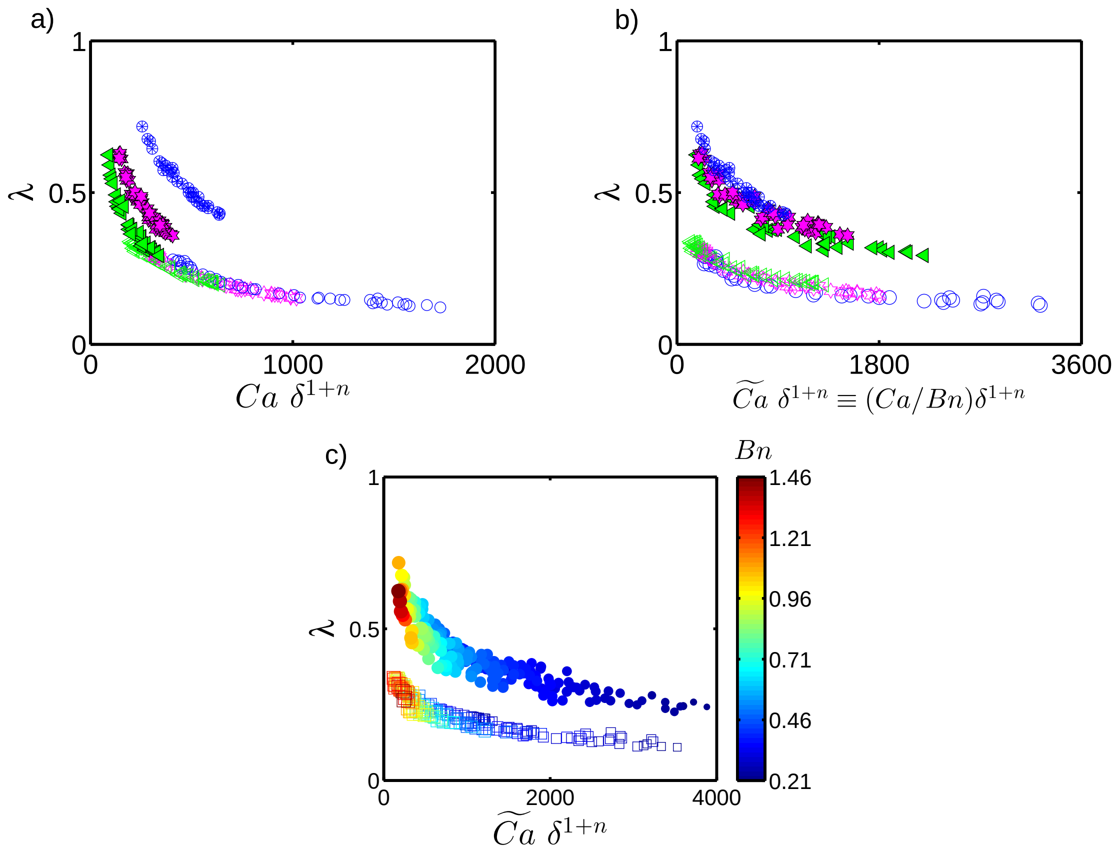

FIGURE 2.12 – (a) Variation of λ versus $Ca\delta^{1+n}$, at different Carbopol concentrations, with three data sets of oil-Carbopol and three data sets of air-Carbopol displacement results. The data correspond to experiments at $\hat{b}$ = 1.5 (mm) with LCC (◂, ◁), MCC (★, ☆), HCC (⊛, ∘). (b) λ as a function $\widetilde{Ca}\delta^{1+n}$, with the same parameters as in (a), showing a collapse of data for oil-Carbopol and air-Carbopol displacements. (c) λ as a function $\widetilde{Ca}\delta^{1+n}$, with various Carbopol concentrations and channel thicknesses, for six data sets of wetting displacements (filled bullets) and four data sets of non-wetting displacements (hollow squares). The change in Bn is illustrated by the size and color.

Fig. 2.12a shows the variation of λ versus $Ca\delta^{1+n}$ for a given channel thickness, for three Carbopol concentrations. While for non-wetting displacements the finger width values perfectly collapse on a single curve, for wetting displacements the finger width values do not collapse. This highlights one more time that, in the viscous regime, the effects of wettability are still important. We observed earlier the opposite effect of increasing the Carbopol concentration for wetting and non-wetting displacements (see Fig. 2.6). Therefore, as increasing the Carbopol concentration is equivalent to increasing the yield stress, it makes sense to assume that the control parameter may need to be modified by considering the Bingham number. To this aim, therefore, let us define an effective capillary number:

$$\widetilde{Ca} = \frac{Ca}{Bn}. \tag{2.20}$$

Fig. 2.12b presents the variation of λ versus $\widetilde{Ca}\delta^{1+n}$. As can be seen, a satisfactory collapse of data can be achieved for wetting displacements (oil-Carbopol). Interestingly, using $\widetilde{Ca}\delta^{1+n}$ still enables the collapse of data for the non-wetting displacements (air-Carbopol). This implies that the control parameter proposed is general in the sense that it perfectly works for both wetting and non-wetting displacement flows. Finally, Fig. 2.12c shows the variation of λ versus $\widetilde{Ca}\delta^{1+n}$ for many experimental data sets. The Bingham number values are also superposed as color bars onto this graph. This figure emphasizes that there is a neat collapse of experimental data, even though the datapoints have very different values of Ca and Bn.

Elasto-inertial regime

At higher velocities, the flow transitions from a viscous dominated regime to a regime in which both elastic and inertial effects come to play. Before presenting various flow features of the elasto-inertial regime, it is worth clarifying the importance of elastic and inertial effects in this regime.

— Elastic effects: Elastic stresses affect the morphology of the formed finger. In particular, the finger shape is different from that of the viscous finger in that side branching patterns are observed. For non-wetting displacements, this feature is attributed to the presence of a non-zero first normal stress difference, creating extra pressure on the finger side at high shear rates (77; 36). This also implies that an effective interfacial tension that takes into account the first normal stress difference must be considered for this regime.

— Inertial effects: Inertial stresses affect the finger width. In contrast to the viscous regime, by increasing the velocity in the elasto-regime, the finger width non-monotonically varies versus the finger tip velocity. For non-wetting displacements, this feature has been observed for both Newtonian fluids (20) and non-Newtonian fluids (36).

It is necessary to emphasize that our "elasto-inertial" flows should not be confused with the other types of elasto-inertial flows widely found in the literature, wherein the flows are governed by an interplay between elastic and inertial forces and these forces are quite strong. In contrast, due to our experimental parameters (geometry, scales, fluids, etc.) elastic and inertial forces in our work are quite weak compared to those in the literature of highly viscoelastic fluid flows. In addition, the term"elasto-inertial" in our work does not mean a balance between these forces. Therefore, our terminology is merely a simple convention to state that elastic forces (manifested through the first normal stress difference) and inertial forces both come to play a role in exhibiting certain features in the flow.

Figs. 2.13a and b show the variation of the finger width versus the finger tip velocity in the elasto-inertial regime in wetting displacements, at two fixed channel thicknesses: $\hat{b}$ = 0.9 (mm) and $\hat{b}$ = 1.5 (mm). The variation of $\hat{w}$ as a function of $\hat{U}$ in this regime is not monotonic; in

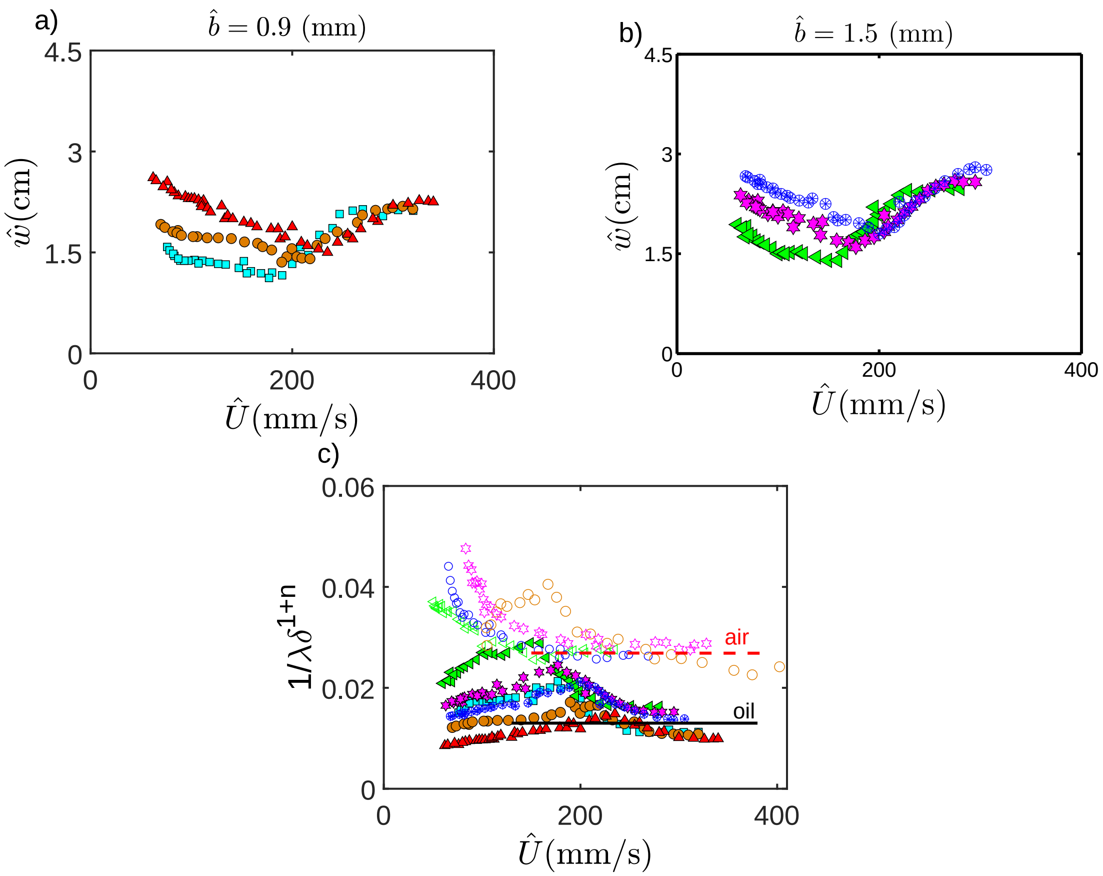

FIGURE 2.13 – (a) & (b) Variation of $\hat{w}$ versus $\hat{U}$ in the elasto-inertial regime in wetting displacements. (c) Superposition of experimental data for wetting and non-wetting displacements at large $\hat{U}$ when $1/\lambda\delta^{1+n}$ is used. The line marks the plateau value ($1/\lambda\delta^{1+n} = 0.014$) for oil and the dashed line marks the plateau value ($1/\lambda\delta^{1+n} = 0.026$) for air. The data correspond to experiments at $\hat{b} = 1.5$ (mm) with LCC (◂, ◁), MCC (★, ☆), HCC (⊛, ∘) and at $\hat{b} = 0.9$ (mm) with LCC (■), MCC (•, ∘) and HCC (▲).

particular three stages are observed. Initially $\hat{w}$ decreases, suddenly starts to increase, and finally reaches a plateau value. The latter seems to be independent of the Carbopol concentration but depends on the channel thickness. The plateau values in these wetting displacements can be compared to their non-wetting counterparts; For example, at $\hat{b} = 0.9$ (mm), the relative finger width reaches $\lambda \approx 0.31$, while Eslami and Taghavi (36) have reported the plateau value for non-wetting displacements to be $\lambda \approx 0.24$. In order to analyze the plateau stage, they have also proposed $1/\lambda\delta^{1+n}$ as the control parameter, proposed by (36), which appropriately takes into account the effects of the channel thickness on the finger width. Figure 2.13c plots the variation of $1/\lambda\delta^{1+n}$, versus $\hat{U}$ in the elasto-inertial regime, for various conditions. As seen, $1/\lambda\delta^{1+n}$ enables a reasonable collapse of the finger widths in the plateau stage. This figure also reveals that the trends in wetting and non-wetting displacements are similar, although the plateau values for oil ($1/\lambda\delta^{1+n} = 0.014$) and air ($1/\lambda\delta^{1+n} = 0.026$) are remarkably different.

Let us look further into the effects of inertial stresses on the finger width, resulting in an increase in $\hat{w}$ at a critical velocity. For non-wetting displacements of Newtonian fluids, Chevalier *et al.* (20) experimentally observed that the finger width at high velocities increases due to inertia, a featured that can be quantified by the Weber number, We. Eslami and Taghavi (36) extended the work of Chevalier *et al.* (20) to non-Newtonian fluids, demonstrating that the appropriate form of the Weber number in the elasto-inertial regime is a modified version defined as

$$We^* = \frac{\hat{\rho}_c \hat{U}^2 \hat{b}}{\hat{\sigma}_{oc,\text{eff}}} \times \delta^{1+n}, \tag{2.21}$$

where $\hat{\sigma}_{\text{eff}}$ denotes the effective interfacial tension (72):

$$\hat{\sigma}_{oc,\text{eff}} = \hat{\sigma}_{oc} + 1/2\ \hat{N}_1(\hat{\dot{\gamma}})\ \hat{b}. \tag{2.22}$$

Note that this relation takes into account the first normal stress difference, $\hat{N}_1$, as it becomes relevant at higher shear rates.

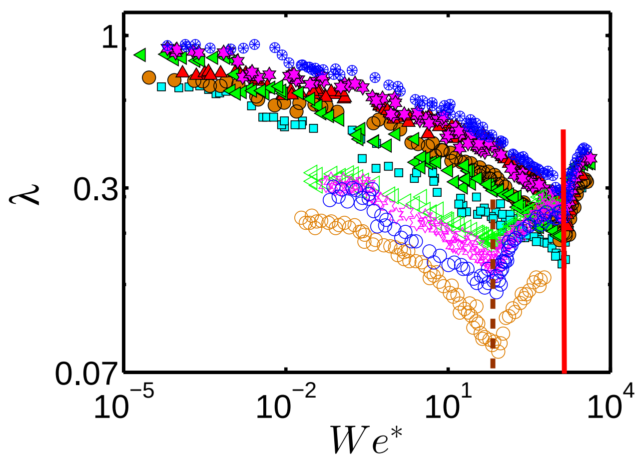

FIGURE 2.14 – λ as a function of We^*. The data correspond to experiments at $\hat{b} = 1.5$ (mm) with LCC (◂, ◁), MCC (★, ☆), HCC (⊛, ∘) and at $\hat{b} = 0.9$ (mm) with LCC (■), MCC (●, ∘) and HCC (▲). The solid (dashed) line shows the critical modified Weber number $We_c^* \approx 1480$ ($We_c^* \approx 76.5$) for oil-Carbopol (air-Carbopol) displacement flows.

Fig. 2.14 shows the variation of the dimensionless finger width (λ) versus the modified Weber number (We^*) for different experimental conditions. For wetting displacements, by increasing We^*, λ starts to increase at $We_c^* \approx 1480$, for all the experiments conducted at different experimental conditions. For non-wetting displacements, although the same trend is observed, the critical condition occurs at $We_c^* \approx 76.5$. These critical values are remarkably different, which may be related to the effects of the density ratio between the displacing and displaced fluids. In order to consider the density ratio, we can rely on the Atwood number defined as

$$At = \frac{\hat{\rho}_{\text{displaced}} - \hat{\rho}_{\text{displacing}}}{\hat{\rho}_{\text{displaced}} + \hat{\rho}_{\text{displacing}}}. \tag{2.23}$$

Now, we can define a new dimensionless group as $At \times We^*$, for which the critical value for the oil-Carbopol system is $At \times We_c^* \approx 63$, which is now much more comparable with that of the air-Carbopol system, i.e., $At \times We_c^* \approx 76$.

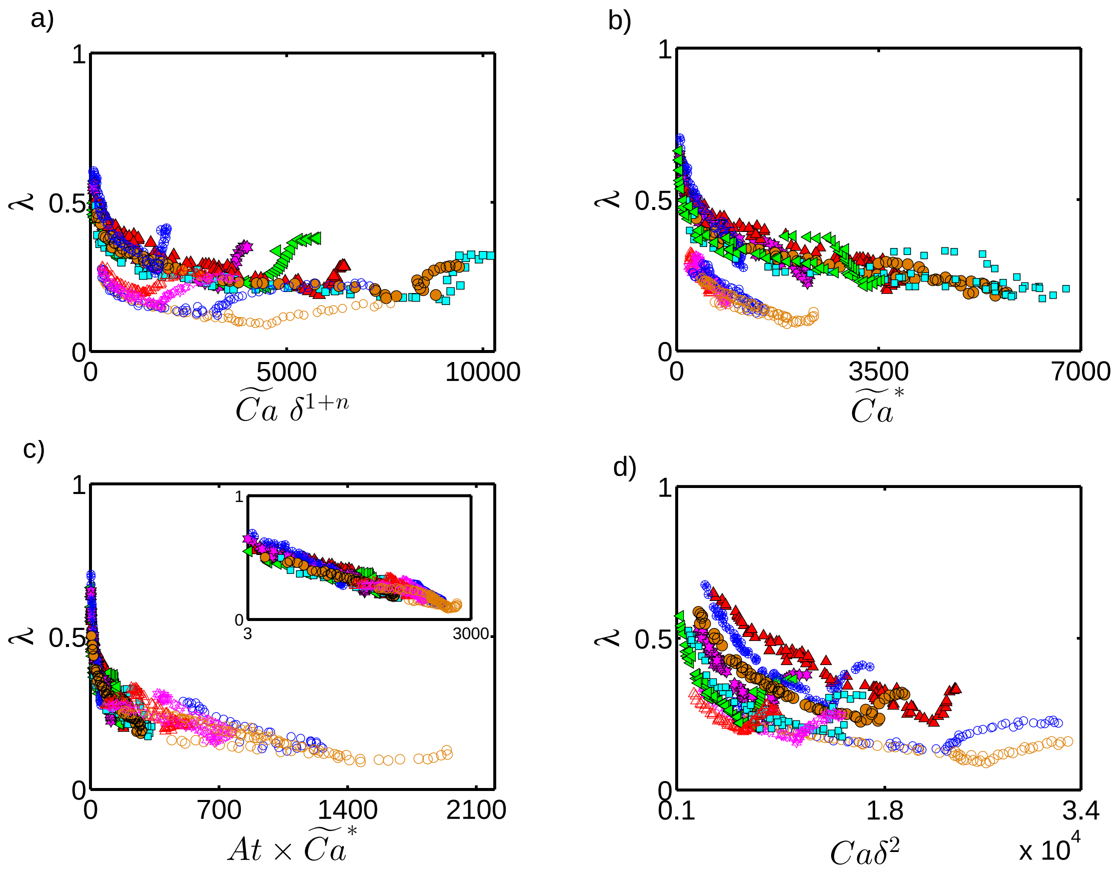

FIGURE 2.15 – The dimensionless finger width as a function of different dimensionless groups for data at different aspect ratios and Carpool concentrations: (a) λ as a function of $\widetilde{Ca}\delta^{1+n}$. (b) λ as a function of $\widetilde{Ca}^*$. (c) λ as a function of $At \times \widetilde{Ca}^*$. (d) λ as a function of $Ca\delta^2$. The inset shows the same data as in the main graph but a logarithmic scale. The data correspond to experiments at $\hat{b} = 1.5$ (mm) with LCC (◂, ◁), MCC (★, ☆), HCC (⊛, ∘) and at $\hat{b} = 0.9$ (mm) with LCC (■), MCC (•, ∘) and HCC (▲).

2.5.3 A comprehensive master curve

A valuable contribution of the current work can be providing a comprehensive master curve, enabling a collapse of data for both wetting and non-wetting flows. Let us start our discussion with Fig. 2.15a, showing λ as a function of $\widetilde{Ca}\delta^{1+n}$ at various experimental conditions, for the viscous and elasto-inertial flow regimes. Although at low velocities, λ versus $\widetilde{Ca}\delta^{1+n}$ follows a principal curve, at higher velocities the values of λ deviate from the principal curve. This trend is the same for both wetting and non-wetting displacements. Since the deviation is mainly due to inertial effects, following Chevalier *et al.* (20) and Eslami and Taghavi (36), the capillary number can be modified in order to include inertial effects (through We^*):

$$\widetilde{Ca}^* = \frac{\widetilde{Ca}\ \delta^{1+n}}{1 + We^*/We_c^*}, \tag{2.24}$$

For wetting displacements, Fig. 2.15b shows that a reasonable of collapse of λ versus $\widetilde{Ca}^*$ can become possible for a wide range of $\widetilde{Ca}^*$. A perfect collapse may never be possible unless three-dimensional effects can be considered. For non-wetting displacements, the collapse of data appears to be reasonable. However, the results of λ follow different curves for wetting and non-wetting cases, which can be due to the different density ratios. Thus, it is reasonable to define a new dimensionless group such as $At \times \widetilde{Ca}^*$, as depicted in Fig. 2.15c, where the results follows a single comprehensive master curve!

In order to highlight the value of the new dimensionless group proposed ($At \times \widetilde{Ca}^*$), the relative finger width (λ) as a function of the classical viscous fingering control parameter ($Ca\delta^2$) is plotted in Fig. 2.15d. As can be seen, the datapoints do not fall on one curve.

2.5.4 Transitions between regimes

Through performing a large number of wetting displacement flow experiments, we observed four different flow regimes (i.e., capillary, yield stress, viscous, and elasto-inertial regimes). Through finding the transition boundaries, it is possible to quantify where these flow regimes occur in the planes of the governing dimensionless groups. Fig. 2.16a depicts the four regimes for wetting displacements in the plane of $Ca\delta^{1+n}$ and Bn, which has been shown to be a suitable plane to classify non-wetting displacement (36). Using such a plane may be justified by noting that these dimensionless groups include the effects of capillary, yield and viscous stresses, as well as the shear-thinning and aspect ratio effects. However, as can be seen, the different regimes are not fully segregated. In what follows, we will attempt to introduce suitable additional dimensionless groups/planes to separate these four regimes and quantify their transition boundaries, as summarized in Figs. 2.16b, c and d.

Transition between the capillary and yield stress regimes

Although Ca and Bn may be assumed to be the reasonable dimensionless numbers to quantify the transition between the capillary and yield stress regimes, Fig. 2.16a shows that simply using these numbers is unable to separate the yield stress and capillary datapoints. This issue lies in the fact the dynamic contact angle varies with the dimensionless parameters (including Ca and Bn) and affects the dynamics of the flow as well as the transition. Therefore, let us first quantify the variation in the dynamic contact angle versus the dimensionless numbers.

A number of experiments in §2.5.2 visualizing the displacement within the channel cross section showed that, as the capillary number (or the imposed flow) increases, the dynamic contact

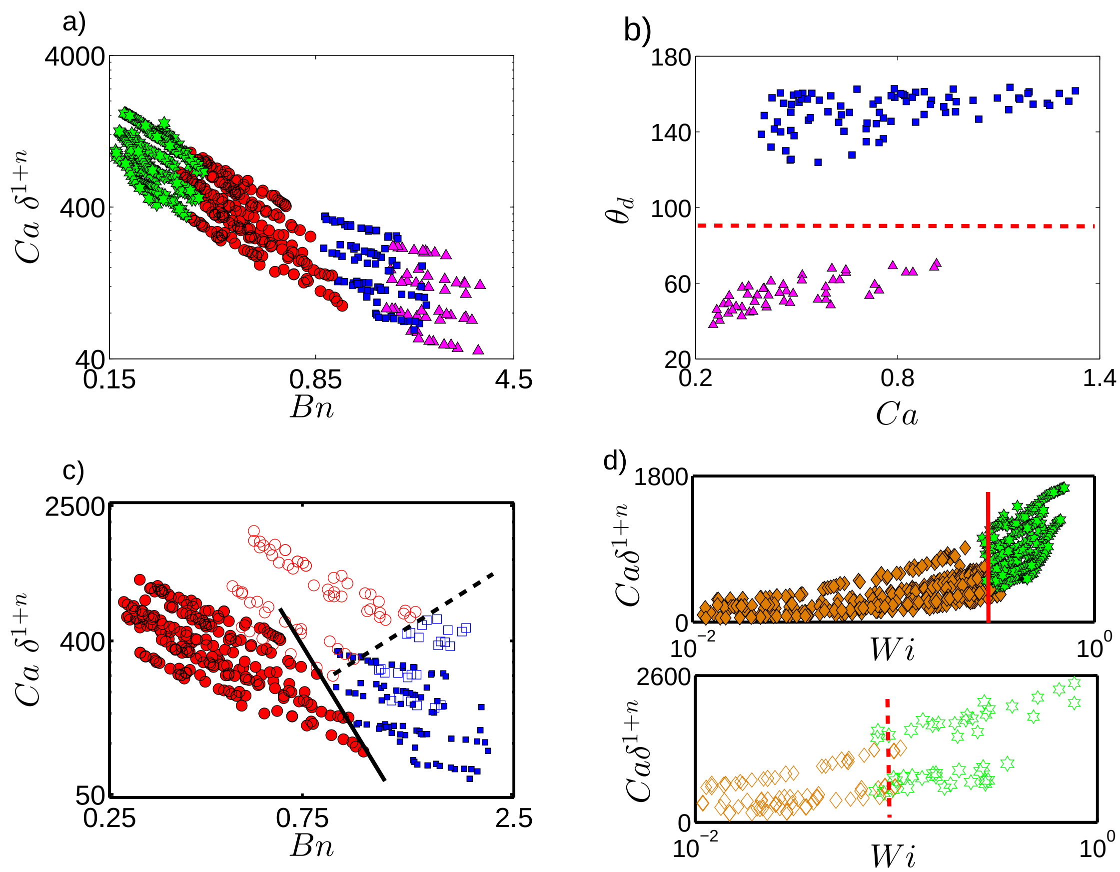

FIGURE 2.16 – (a) Four different flow regimes observed in wetting displacements, in the plane of $Ca\delta^{1+n}$ and Bn. (b) The yield stress and capillary regimes in the plane of Ca and θ_d. The horizontal line at $\theta_d \approx 90°$ separates the data corresponding to the capillary and yield stress regimes. Note that the capillary regime is not observed for non-wetting displacement flows. (c) The viscous and yield stress regimes, for wetting flows (filled symbols) and non-wetting flows (hollow symbols), in the plane of $Ca\delta^{1+n}$ and Bn. The transition between the yield stress and viscous regimes is marked by the oblique solid (dashed) line for oil-Carbopol (air-Carbopol) displacements, for which slope is $Ca\delta^{1+n}/Bn = -1050$ ($Ca\delta^{1+n}/Bn = 550$). Neglecting the small dependency on $Ca\delta^{1+n}$, the transition for wetting flows (non-wetting flows) occurs roughly at $Bn_c \approx 1$ ($Bn_c \approx 1.25$). The symbols correspond to the capillary (▲), yield stress (■, □), viscous (•, ∘), elasto-inertial (★, ☆) regimes. In (d), inelastic flows (including the capillary, yield stress and the viscous regimes) are marked by (♦,◊). In (d), for wetting (non-wetting) displacements, the vertical solid (dashed) line marks $Wi_c = 0.33$ ($Wi_c = 0.09$), which is roughly the transition to the elasto-inertial regime.

angles increases and the meniscus eventually transitions from concave to convex, which more or less coincides with the transition from the capillary to yield stress regime. However, analyzing the dynamic contact angle within the channel cross-section for all the experiments requires an access to a large amount of data in the $\hat{x}\hat{y}$-plane (side-view), which is not always possible due to technical/experimental measurement limitations. Nevertheless, these data can be also roughly estimated by taking digital images from the $\hat{x}\hat{z}$-plane (top-view) and processing them.

To do so, let us analyze the $\hat{x}\hat{z}$-plane images by looking into the variation of the relative mean light intensity ($\bar{I}$) in the middle of a developed finger. For two different conditions, Figs. 2.17c and d show the variation of $\bar{I}$ versus the channel length for a concave interface (corresponding to the schematic in Fig. 2.17a) and a convex interface (corresponding to the schematic in Fig. 2.17b), respectively. For both cases, $\bar{I}$ undergoes a sudden decrease over a small length, marked by $\hat{\ell}$ in all subfigures. In almost all the experiments, the concave interface (the capillary regime) has a sharper variation compared to the convex interface (in the yield stress regime). The solid-oil-Carbopol dynamic contact angle, θ_d, can be very crudely estimated using the following relation:

$$\theta_d \approx \arctan\,(\frac{\hat{b}}{2\hat{\ell}}), \tag{2.25}$$

in which conventionally $\hat{\ell}$ has a positive value for a concave interface and a negative value for a convex interface, as schematically depicted in Figs. 2.17a and b. Fig. 2.18a plots $\tan\theta_d$ versus Ca for the capillary regime datapoints, using our indirect measurement approach (i.e., estimation based on the variation of $\bar{I}$). To ensure that our approach to estimate θ_d provides reasonable results, a few direct measurement results already presented in Fig. 2.9a are superimposed on this graph, showing a reasonable comparison.

Before we proceed, let us remind that the analysis presented in Fig. 2.17 is an approximation and that even the relatively reasonable agreement between the data from direct (side view) and indirect (top view) measurements may not provide full certainty on the underlying hypotheses in terms of different typical lengths of concave and convex interfaces.

Figs. 2.18b shows the variation of θ_d versus Ca, for the capillary and yield stress regime datapoints. By increasing Ca, for a given condition, θ_d increases, eventually becoming convex ($\theta_d > 90°$) as the transition occurs. An opposite trend would be seen versus Bn (not shown for brevity). Therefore, finding the transition from the capillary to yield stress regime can reduced to the critical point where $\theta_d = f(Ca, Bn) \approx 90°$. For the six specific experimental conditions presented in Fig. 2.18b, the transitions of $\theta_d \approx 90°$ for LCC, MCC and HCC for $\hat{b} = 0.9$ (mm) respectively occur at $Ca \approx 0.33$, 0.45, 0.71 and for $\hat{b} = 1.5$ (mm) at $Ca \approx 0.42$, 0.54, 0.92.

To summarize the findings described above, Fig. 2.16b displays the data corresponding to the capillary (triangle) and yield stress (square) regimes, which are clearly segregated in the plane of Ca and θ_d. The horizontal line superimposed on Fig. 2.16b marks the transition between the capillary and yield stress regimes at $\theta_d \approx 90°$. Note that this transition corresponds to a significant change in the displacement flow efficiency and the displacement flow morphology. For the yield stress regime, there exists more than one finger in the Hele-Shaw cell for a considerable period of time, while for the capillary regime, there is only a single, wide finger propagating through the cell.

The transition between the capillary and yield stress regimes may be also better understood

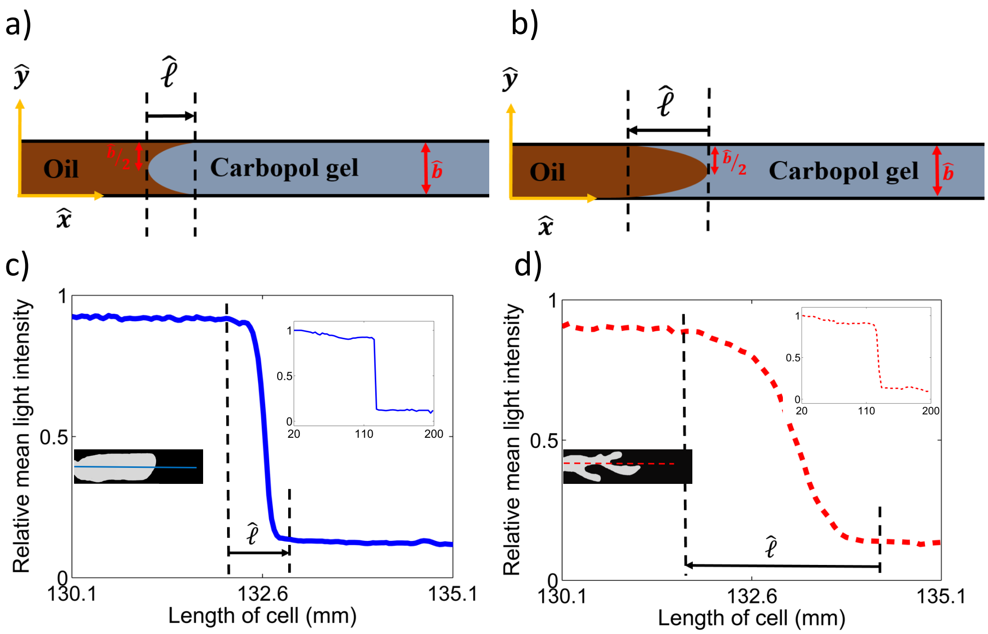

FIGURE 2.17 – A schematic side-view of oil displacing Carbopol with (a) a concave interface and (b) a convex interface. A typical variation in the relative mean light intensity versus length of cell for (c) a concave interface and (d) a convex interface. The upper insets show the same data as in the main graphs but for a longer cell length. The corresponding experimental snapshots (as lower insets) show the displacement of HCC Carbopol gel by oil in a cell with $\hat{b}$ = 0.9 (mm). The oil flows from left to right. The field of view in each snapshot is 6.03×23.3 (cm^2). The solid line and dashed line passing in the middle of the cell mark where the relative mean light intensities are calculated.

using a scaling augment. In the capillary regime, the wetting capillary stress dominates the flow, removing almost entirely the Carbopol gel and resulting in a finger width close to the channel width. Within the channel cross-section in this regime, the capillary stress associated to wetting can be written as $\frac{2\hat{\sigma}\cos\theta_d}{\hat{b}}$, which is larger than the yield stress ($\hat{\tau}_y$). As the imposed flow increases, $\cos\theta_d$ continuously decreases and at some point the yield stress exceeds the capillary stress and thus dominates the flow afterwards. Such critical transition can be crudely written as

$$\frac{2\hat{\sigma}\cos\theta_d}{\hat{b}} \sim \hat{\tau}_y \Rightarrow \theta_d \sim \arccos\left(\frac{\hat{\tau}_y\hat{b}}{2\hat{\sigma}}\right), \tag{2.26}$$

which using the average values for $\hat{b}$ and $\hat{\tau}_y$ in our experiments yields a critical value of $\theta_d \approx 81°$, in qualitative agreement with the above discussions.

It seems that the appearance of the capillary regime and in particular the tear-shaped finger formation at low velocities are caused by a combination of wetting and yield stress effects. In order to demonstrate that the latter is indeed an important factor, Figs. 2.19a and b compare an oil-Carbopol displacement (shear-thinning with a yield stress) with an oil-Xanthan gum

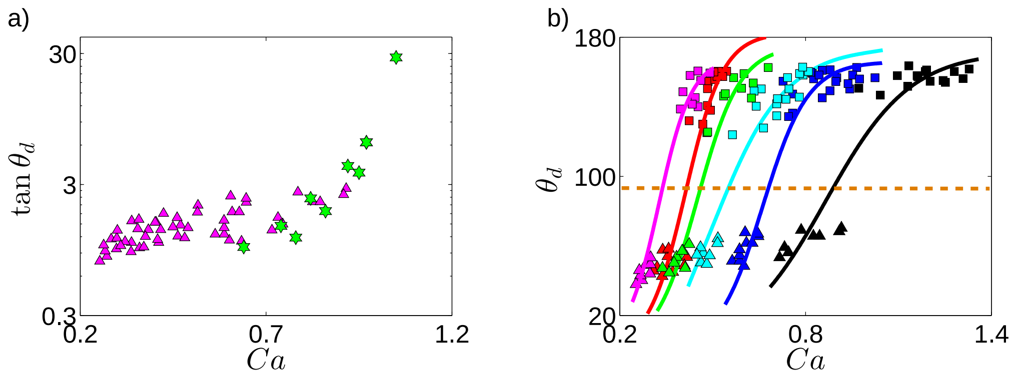

FIGURE 2.18 – (a) Variation of $\tan\theta_d$ versus Ca in the capillary regime, estimated using the indirect approach (i.e., analyzing the variation of $\bar{I}$). The datapoints (★) from the direct measurement (from Fig. 2.9a) are also superposed. (b) Variation of θ_d as a function of Ca. The symbols correspond to the yield stress regime (square symbols) and the capillary regime (triangle symbols). The data correspond to experiments at $\hat{b}$ = 0.9 (mm) with LCC (▲, ■), MCC (▲, ■), HCC (▲, ■) and at $\hat{b}$ = 1.5 (mm) with LCC (▲, ■), MCC (▲, ■) and HCC (▲, ■). The lines in subfigure (b) are fitted curves (as eye guides) for each set of experiments. The horizontal dashed line shows $\theta_d = 90°$.

displacement (shear-thinning without a yield stress). The oil-Carbopol displacement presents a capillary regime. The experimental conditions are identical in terms of the imposed flow velocity ($\hat{V} \approx 0.11$ (mm/s)), the channel thickness and the effective shear rates ($\hat{U}/\hat{b} = 0.1 \pm 0.02$ (1/s)), and they are also quite similar in terms of the overall viscosity of the displaced phase as illustrated in Fig. 2.19c (the rheology of the Xanthan solution follows $\hat{\tau} = 12.9\ \hat{\dot{\gamma}}^{0.25}$). At this very small imposed velocity, the oil-Carbopol displacement exhibits a wide tear-shaped finger, while the oil-Xanthan displacement displays a narrow finger. This significant difference implies that, in addition to wettability, the yield stress of the displaced fluid has also an important role in the existence of the capillary regime, for which the displacement is the most efficient.

After comparing the yield stress and shear-thinning displacements, a similar comparison can be also made between wetting displacements for yield stress fluids and Newtonian fluids, for range of capillary numbers. Fig. 2.20 compares λ versus Ca for Carbopol displacements ($\hat{\tau}_y \approx 13$ (Pa)) against their corresponding Glycerol cases ($\hat{\tau}_y = 0$). Two differences may be distinguished between these flows: First, the finger widths in the oil-Carbopol displacement are all larger than their corresponding values in the oil-Glycerol displacement. Second, λ in the yield stress displacement seems to be constant, while it seems to slowly decrease in the Newtonian counterpart. A conclusion drawn from Fig. 2.19 and Fig. 2.20 can be that the yield stress has a crucial role in the capillary regime in wetting displacements.

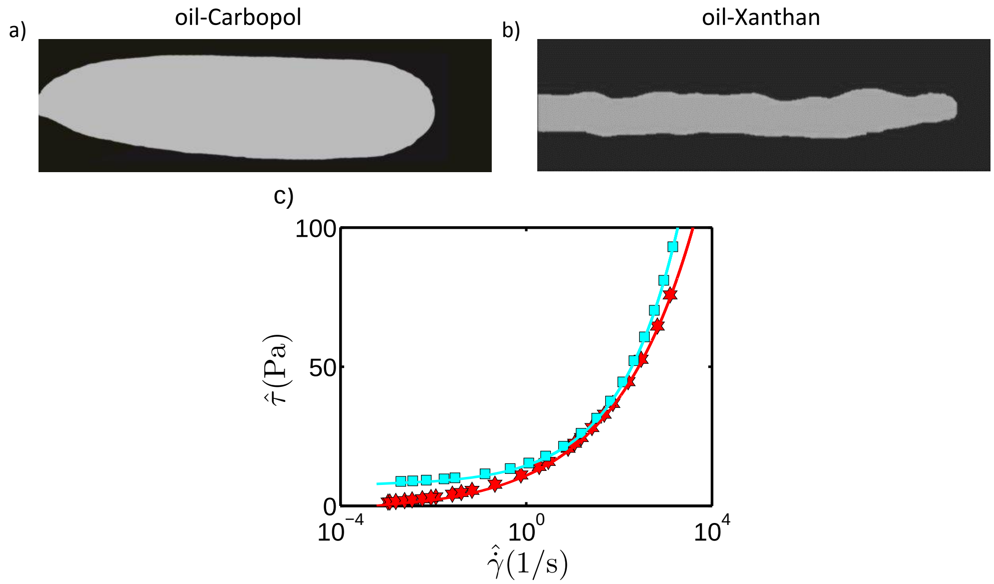

FIGURE 2.19 – Experimental results of the displacement of (a) MCC Carbopol gel and (b) Xanthan gum solution, by oil in a cell with $\hat{b} = 1.5$ (mm). The oil flows from left to right. The mean imposed velocity is $\hat{V} \approx 0.11$ (mm/s), in both cases. The field of view in each snapshot is 6.6×21.3 (cm^2). (c) Flow curves of shear stress, $\hat{\tau}$, versus shear rate, $\hat{\dot{\gamma}}$ for the MCC Carbopol gel (■) in comparison with the Xanthan gum solution (★). The lines correspond to the Herschel-Bulkley model parameters fitted to data.

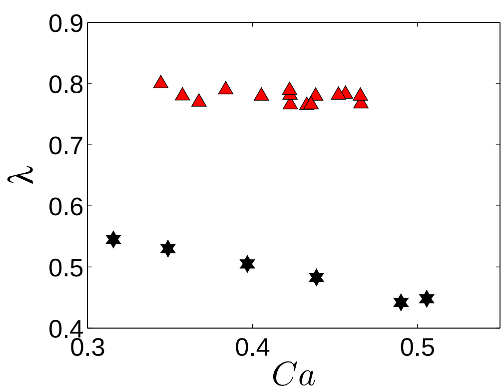

FIGURE 2.20 – Variation of λ as a function of Ca for the displacement of HCC Carbopol gel and Glycerol solution, by oil in a cell with $\hat{b} = 0.9$ (mm). The data correspond to experiments with HCC (▲) and Newtonian fluid (oil-Glycerol) (★).

Transition between the viscous and yield stress regimes

The transition between the yield stress and viscous regimes is governed by an interplay between capillary, yield and viscous stresses, which can be grouped into $Ca\delta^{1+n}$ and Bn. Figure 2.16c classifies the experimental datapoints in the plane of $Ca\delta^{1+n}$ and Bn, where the yield stress and viscous regimes are segregated, for both wetting and non-wetting displacements. The transitions for wetting flows and non-wetting displacement occur roughly at $Bn_c \approx 1$ and $Bn_c \approx 1.25$, respectively, which are close. However, the oblique solid and dashed lines illustrating the accurate transition boundaries for wetting and non-wetting displacements have opposite slopes. Figure 2.16c confirms that the transition largely depends on Bn: at smaller and larger Bn, the viscous and yield stress regimes are observed, respectively. However, the precise transition value also slightly depends on $Ca\delta^{1+n}$. Note that the transition between the yield stress and viscous regimes corresponds to significant changes in the variation of the finger width as well as the flow morphology.

Transition between the elasto-inertial and inelastic regimes

By entering the elasto-inertial regime, the finger in the middle of cell exhibits a tendency towards side branching and wavy-like interfacial patterns. For non-wetting displacements, these features have been linked to the presence of a first normal stress difference (77), which is non-zero when elastic effects become relevant, leading to finger side oscillations. The appropriate dimensionless group to capture the elastic properties of Carbopol gel at very large shear rates can be the Weissenberg number (Wi).

Figure 2.16d classifies the elasto-inertial and inelastic regimes in our wetting displacement flows, in the plane of $Ca\delta^{1+n}$ and Wi. Non-wetting displacement results have been also superimposed on the graph. Note that the inelastic regime already includes the capillary, yield stress and viscous regimes. As can be seen, the elasto-inertial and inelastic regimes are clearly segregated, while the former is reasonably observed at higher Wi. Also, the transition boundary occurs roughly at $Wi_c \approx 0.33$ and it does not seem to highly depend on $Ca\delta^{1+n}$. The same trend is observed for non-wetting displacements, although the transition occurs at $Wi_c \approx 0.09$, which is nearly four times smaller than that of the wetting displacements. However, using the average Reynolds number at transition points, the transition boundary can be also described versus the elasticity number, $El = Wi/Re$, for which we find $El_c \approx 10.3$ for oil-Carbopol displacement, which is more comparable with $El_c \approx 8.4$ for air-Carbopol displacements.

Finally, it is worth emphasizing the usefulness of Fig. 2.16c & d in classifying different regimes: (i) Although the flows that we are dealing with are quite complex, using only three dimensionless groups (i.e., Bn, $Ca\delta^{1+n}$ and Wi), we are able to quantify the appearance of various flow regimes for both wetting and non-wetting displacements. It is also important to note that our data cover ~ 1400 individual experiment. (ii) The dimensionless groups used clearly show which forces are dominant in governing the flow dynamics. For example, Fig. 2.16d, inelastic and elasto-inertial regimes are reasonably separated versus Wi, showing the onset of the appearance of elastic effects. Meanwhile, elasto-inertial flows correspond to small Bn wherein yield stress effects are negligible (see e.g., Fig. 2.16a). (iii) Although the critical transition boundaries in these figures are crude, the results still show a significant effect of wettability on the value and sign of these critical transitions.

2.5.5 A closer look at side branches in the elasto-inertial regime: a secondary flow feature

We have so far explored the main flow regimes and their characteristics; however, our complex flows exhibit secondary flow features, which are worth discussing in terms of wetting and non-wetting displacements. Here, we focus on explaining some of these secondary features in the elasto-inertial regime.

Spatial frequency and period of side branches

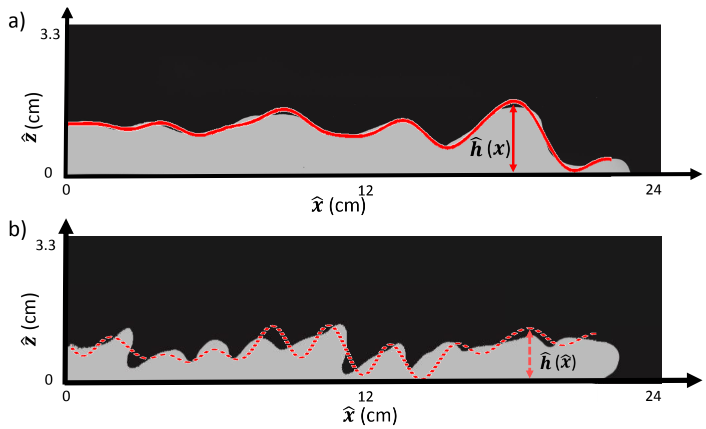

FIGURE 2.21 – Experimental snapshots showing the oscillation of the finger side due to secondary instabilities in the elasto-inertial regime (top view $\hat{x}\hat{z}$-plane). The finger upper half is shown. (a) Oil displaces Carbopol gel, from left to right. (b) Air displaces Carbopol gel, from left to right. The field of view of 3.36×24.05 (cm^2) in both images. The red solid (dashed) curve shows the result of applying equation (2.27) for the oil (air) flow. Note that here the origin of the $\hat{z}$-axis is shifted to the cell middle.

As discussed earlier, for both wetting and non-wetting displacements with $Wi \gtrsim O(1)$, the finger sides become wavy due to secondary instabilities. Thus, it is worth analyzing these waves in order to gain an indirect understanding of the nature of these instabilities. After the displacing fluid tip has exited the cell, the finger wavy patterns are permanent footprints, for which the amplitude and the wavelength can be quantified. To do so, we rely on a "sum of sines" model, to fit the following periodic functions on the interface on the upper half of the finger:

$$\hat{h}(\hat{x}) = \sum_{i=1}^{m} \hat{a}_i \sin\left(\frac{2\pi}{\hat{b}_i}\hat{x} + \hat{c}_i\right), \tag{2.27}$$

where $\hat{a}$, $\hat{b}$ and $\hat{c}$ are the amplitude, the wavelength and the phase constant, respectively. Also, m is the number of terms in the sine series. Our analysis shows that increasing m beyond 3 does not have a significant impact on the coefficients of the fitted sinusoidal curve. Thus, for simplicity we fix $m = 3$. Note that our analysis of the results shows that the first term in the series (27) is much smaller than the following terms. Therefore, to analyze the "waviness" of the interface, we consider $\hat{a}_2$ and $\hat{b}_2$. It should be mentioned that the above equation is closely related to the Fourier series, expect that it does not include a constant (intercept) term but it includes the phase constant. Fig. 2.21 depicts a typical displacing finger (the upper half) in the elasto-inertial regime when the finger tip meets the cell end. Through fitting equation (2.27), the overall interface shape can be crudely captured for both wetting (solid curve) and non-wetting (dashed curve) displacements.

Figs. 2.22a provide an understanding about the variation of the wave amplitude as a function of We^*, for both wetting and non-wetting displacements. Fig. 2.22a shows the dimensionless wave amplitude ($A_2 = \frac{\hat{a}_2}{\hat{W}}$) versus the modified Weber number for the oil-Carbopol system. The results show that the balance between interfacial tension and inertia effects can affect the wave amplitude value. For wetting displacements, by increasing the modified Weber number, A_2 gradually increases, implying that increasing inertial effects initially results in enhancing the side wave amplitude. However, by increasing the inertial effects further, A_2 becomes nearly constant after a critical Weber number, which interestingly is nearly the same as the critical value found for the transition to considerable inertial effects, i.e., We_c^* (see Fig. 2.14). The same trend is observed for non-wetting displacements (see Fig. 2.22b). Finally, the trend for A_3 is more or less similar to A_2 (not shown for brevity).

Our findings of Figs. 2.22a and b can be qualitatively compared with the literature results. First, these figures showed that in general decreasing interfacial tension (compared to inertial stresses) leads to an increase in A_2. Through analyzing weakly shear-thinning displacements with $Wi \sim O(1)$, Fast & Shelley (37) have computationally shown that decreasing interfacial tension leads to enhancement the growth rates of perturbations. Second, Figs. 2.22a and b showed that at higher inertia, the wave amplitude does not grow with We^*. This is qualitatively in agreement with the findings of He & Belmonte (48) who have proposed a mathematical model to investigate the impacts of inertia on the Saffman-Taylor instability, revealing that inertia stabilizes the flow and may contribute to suppressing the amplitude of disturbances.

Unlike A_2, the variation of the dimensionless wavelength ($B_2 = \frac{\hat{b}_2}{\hat{W}}$) versus We^* for oil-Carbopol and air-Carbopol flows would be scattered and would not show a definitive trend versus We^* (the results are not shown for brevity). Instead, Figs. 2.22c and d attempt to provide an understanding about B_2, through plotting its variation as a function of Wi, Bn and $Ca\delta^{1+n}$, where the values of B_2 are marked by colors and symbol sizes. Although no monotonic trend can be still recognized, the following rather qualitative conclusions may be drawn from these figures for wetting and non-wetting displacements: (i) B_2 in general decreases with Bn, implying that higher yield stress values augment the wavelength; (ii) B_2 in general increases with Wi, implying that more branches can be formed when elastic effects (manifested through

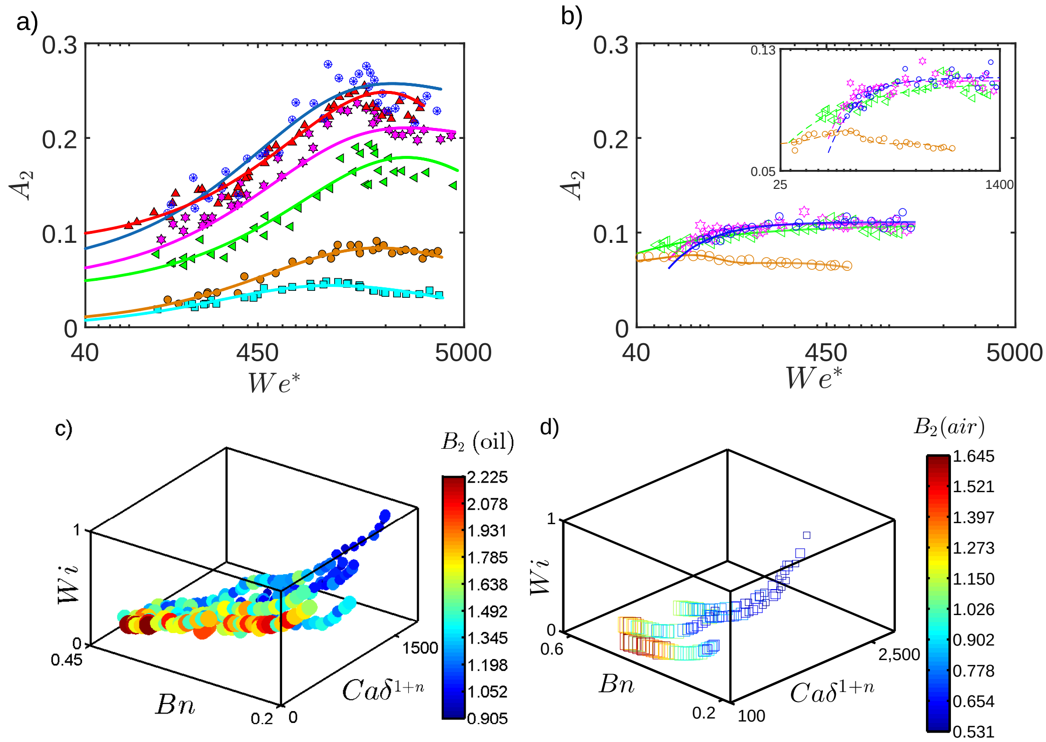

FIGURE 2.22 – (a) A_2 versus We^* for oil-Carbopol displacements. (b) A_2 versus We^* for air-Carbopol displacements. In (a&b), the data correspond to experiments at $\hat{b}$ = 1.5 (mm) with LCC (◂, ◁), MCC (★, ☆), HCC (⊛, ∘) and at $\hat{b}$ = 0.9 (mm) with LCC (■), MCC (•, ∘) and HCC (▲). (c&d) B_2 in the plane of Wi, Bn and $Ca\delta^{1+n}$ for (c) oil and (d) air displacements. The values of B_2 are marked by the symbol size and colors. The lines in (a&b) are fitted curves (as eye guides) using Curve Fitting Toolbox of MATLAB.

the first normal stress difference) are larger; (iii) B_2 in general increases with $Ca\delta^{1+n}$, so there are relatively more branches when interfacial tensions forces are relatively weaker; (iv) Finally, at the same conditions, in general the wavelength in wetting displacements is larger than that in non-wetting displacements.

Gap thickness (mm)	**Concentration**	**$\bar{B}_2$ for oil**	**$\bar{B}_2$ for air**
1.5	LCC	1.5 ± 0.3	1.2 ± 0.3
1.5	MCC	1.3 ± 0.2	1.0 ± 0.3
1.5	HCC	1.1 ± 0.2	0.8 ± 0.2
0.9	LCC	1.8 ± 0.2	Not available
0.9	MCC	1.6 ± 0.2	0.7 ± 0.1
0.9	HCC	1.3 ± 0.1	Not available

TABLE 2.5 – $\bar{B}_2$ (i.e., the mean value of $\bar{B}_2$ for different velocities) of for oil and air displacements for given values of the channel thickness and the Carbopol concentration.

To compare more quantitatively B_2 values for wetting and non-wetting displacements, Table 2.5 presents its mean value over different velocities ($\bar{B}_2$), for given values of the channel thickness and the Carbopol concentration. It is evident that $\bar{B}_2$ for the oil-Carbopol system is larger than that for the air-Carbopol system. Loosely speaking, this implies that there are relatively more side branches in the air-Carbopol system.

Our findings on the characteristics of side branches are qualitatively in agreement with the general literature results. For example, Mora & Manna (88) have studied viscoelastic displacements (with small elastic effects) through a linear stability analysis, demonstrating that the perturbation growth rate is a function of the elastic modulus and the gap thickness. They have also shown that a competition between elasticity and viscosity controls the interface shape: higher elasticity results in more branched and fracture-like patterns. Kondic *et al.* (62) have reported that, for shear-thinning flows with $Wi \sim O(1)$, higher velocities increase the growth of shorter wavelengths, eventually resulting in more side branches. They have also found that a higher capillary number leads to an increase in the growth of shorter wavelengths, creating a noticeable side branching. Finally, Malhotra & Sharma (78) have experimentally studied miscible viscoelastic displacements using a Fourier transformation, finding that elasticity leads to a decrease in the instability wavelength.

We end this subsection by reminding the reader that our approach in analyzing side branches in the elasto-inertial regime has been quite crude. Evidently, to provide a deep understanding of the effects of the dimensionless groups, such as Wi, We^*, Bn and $Ca\delta^{1+n}$, a detailed stability analysis of the flow seems necessary, regardless of whether or not this is feasible with our current theoretical tools.

Orientation of side branches

Our experimental images show that, depending on the flow parameters and wetting and non-wetting conditions, side branches may exhibit different orientations with the respect to the main finger direction. To shed further light on wetting effects in the elasto-inertial regime, these orientations may be studied by defining an angle associated to side branches. For simplicity of the analysis, let us focus on the upper finger side, although we note that side branches are typically asymmetrical. Fig. 2.23 shows typical experiments in which a side branching pattern is observed. In order to quantify the orientation of the side branches, we use the following procedure coded in MATLAB. First, we find the interface between the fluids. Second, we locate the interface peaks and find theirs height as well as widths at half height. To eliminate noises, we filter any peak whose height is smaller than 1 (mm). Finally, we define a side branch angle, β, using the slope of a line passing through the peak and the peak width at half height. To make a comparison possible between different experiments, for a given experiment, we calculate the average of all the side branch angles ($\bar{\beta}$).

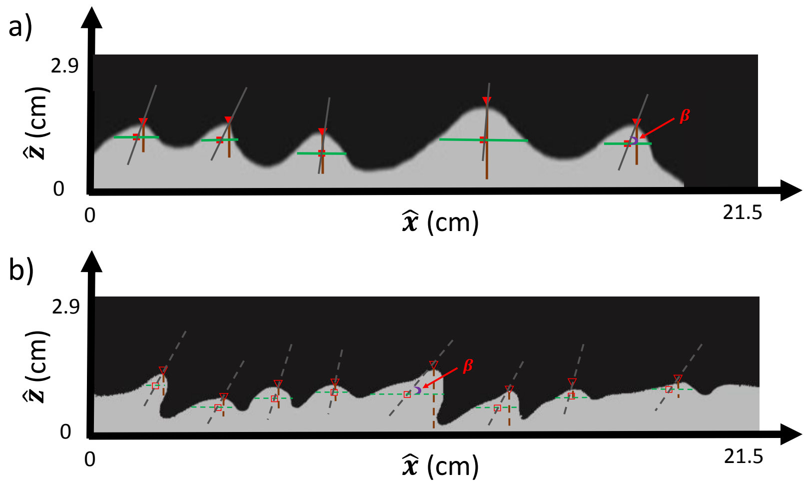

FIGURE 2.23 – Orientation of side branches for (a) wetting and (b) non-wetting displacements. The oil/air flows from left to right. For oil (air), the peak heights and the peak widths at half height are shown by the brown vertical solid (dashed) lines and the green horizontal solid (dashed) lines, respectively. For oil (air), each peak is marked by ▼ (▽) while the center of each peak width at half height is marked by ■ (□). For oil (air), each peak angle, β, is defined using the slope of the oblique solid (dashed) line, passing through the peak and the peak width at half height. Note that any peak whose height is smaller than 1 (mm) is filtered. Also note that here the origin of the $\hat{z}$-axis is shifted to the cell middle. Both images show a field of view of 2.95×21.53 (cm^2).

Fig. 2.24a compares $\bar{\beta}_{oil}$ and $\bar{\beta}_{air}$ for wetting and non-wetting displacements, respectively, at the same experimental conditions. The line shows $\bar{\beta}_{air} = \bar{\beta}_{oil}$. Contour values of Wi are also superposed as color bars onto this graph. Fig. 2.24b also makes a comparison between $\bar{\beta}_{air}$ and $\bar{\beta}_{oil}$ on average for given values of the channel thickness and the Carbopol concentration. Based on Fig. 2.24, our rather qualitative findings on the characteristics of side branches can be summarized as follows: (i) Depending strongly on the experimental conditions, the side branches have the different orientation values for both wetting and non-wetting displacements. The branch orientations also non-monotonically vary versus the Wi and other governing dimensionless numbers (not shown for brevity). (ii) The orientations for oil and air cover different ranges, i.e., $66° < \bar{\beta}_{oil} < 88°$ and $27° < \bar{\beta}_{oil} < 80°$. This means that, for the same parameter ranges, $\bar{\beta}_{air}$ is relatively more sensitive to the experimental conditions and that wettability conditions strongly affect the orientation of side branches. (iii) In most cases, for the same experimental parameters, $\bar{\beta}_{oil}$ is larger than $\bar{\beta}_{air}$. (iv) For a few experiments, $\bar{\beta}_{air} > \bar{\beta}_{oil}$. Interestingly, almost all these experiments correspond to large Wi. This implies that only when the elastic effects (manifested through the first normal stress difference) are very stronger, it may become possible for the non-wetting displacement to induce a side branch orientation larger than the corresponding value in the wetting displacement. (v) For oil-Carbopol displacements, on average $\bar{\bar{\beta}}_{oil} \approx 76°$, which compared to air-Carbopol displacements (with $\bar{\bar{\beta}}_{air} \approx 60°$) is relatively closer to 90°. This implies that, for oil-Carbopol displacements in general, side branches are relatively more perpendicular with respect to the main finger direction.

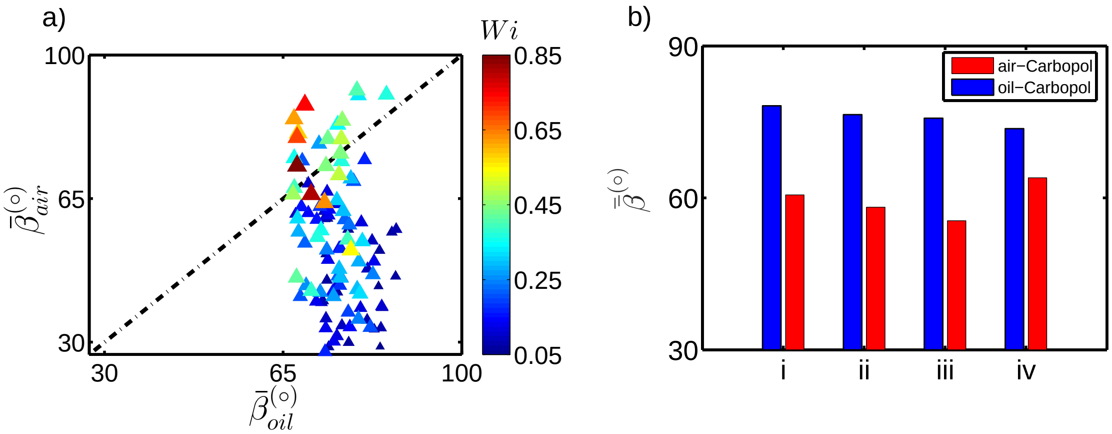

FIGURE 2.24 – (a) Comparison among $\bar{\beta}_{oil}$ and $\bar{\beta}_{air}$ for wetting and non-wetting displacements, respectively, with the same experimental conditions (i.e., same channel thickness, imposed flow velocity, and Carbopol concentration). The values of Wi are marked by the symbol size and colors. Dashed line shows $\bar{\beta}_{oil} = \bar{\beta}_{air}$. (b) $\bar{\bar{\beta}}$ (the mean value of $\bar{\beta}$ for different imposed velocities) for oil and air displacements at (i) $\hat{b} = 1.5$ (mm) with HCC; (ii) $\hat{b} = 1.5$ (mm) with MCC; (iii) $\hat{b} = 1.5$ (mm) with LCC ; and (iv) $\hat{b} = 0.9$ (mm) with MCC.

Dimensionless group	**Significance**	**Critical value Oil**	**Critical value Air**
We_c^*	Transition to inertial effects	1480	76.5
$At \times We_c^*$	Transition to inertial effects (while considering density ratios)	76 6	63
$Ca\delta^{1+n}/Bn$	Slope of transition line between yield stress and viscous regimes	-1050	550
Bn_c	Transition between yield stress and viscous regimes (crude)	1	1.25
$\theta_d = f(Ca, Bn)$	Transition between capillary and yield stress regimes	≈ 90°	Not applicable
Wi_c, El_c	Transition to elastic effects	0.33, 10.3	0.09, 8.4
$1/\lambda\delta^{1+n}$	Finger width plateau value	0.014	0.026
$At \times \widetilde{Ca}^*$	Enabling collapse of λ for viscous and elasto-inertial regimes in both wetting & non-wetting regimes	-	-

TABLE 2.6 – Important critical dimensionless groups for wetting (oil-Carbopol) displacement that the present study has delivered, in comparison with non-wetting (air-Carbopol) displacements. Some dimensionless group values for non-wetting (air-Carbopol) displacements are from (36).

2.6 Summary

Using an experimental approach, we have investigated the Saffman-Taylor (viscous fingering) instability wherein a Newtonian fluid pushes a non-Newtonian fluid, within a Hele-Shaw cell. Unlike most of the traditional studies, we have focused on displacements where the displacing fluid wets the cell walls. A less viscous fluid (oil) displaces a more viscous fluid (Carbopol gel), which shows viscoplastic, viscoelastic and shear-thinning behaviours. Through analyzing different flow patterns and the variation of the finger width, we have identified four displacement flow regimes: the capillary, yield stress, viscous and elasto-inertial regimes, for which we have also quantified the transition boundaries. To provide a deeper understanding, when possible, we have also made detailed comparisons between our results and the corresponding non-wetting displacement results (i.e., air displacing Carbopol gel), for each regime. We have succeeded in characterizing complex viscous fingering behaviours in terms of various governing dimensionless numbers: the capillary number (Ca), the Bingham number (Bn), the Weissenberg number (Wi), the Weber number (We), the channel aspect ratio ($\delta \gg 1$), and the shear-thinning power-law index (n). We have found that the wettability may have a significant impact on the flow patterns and the displacement flow efficiency. A summary of the main governing dimensionless numbers predicting various flow features are presented in Table 2.6.

2.7 Bibliography

[1] T.T. Al-Housseiny, P.A. Tsai, and H.A. Stone. Control of interfacial instabilities using flow geometry. *Nat. Phys.*, 8(10):747–750, 2012.

[2] K. Alba, S.M. Taghavi, and I.A. Frigaard. A weighted residual method for two-layer non-Newtonian channel flows: steady-state results and their stability. *J. Fluid Mech.*, 731:509–544, 2013.

[3] M. Allouche, I.A. Frigaard, and G. Sona. Static wall layers in the displacement of two visco-plastic fluids in a plane channel. *J. Fluid Mech.*, 424(1):243–277, 2000.

[4] M.B. Amar and E.C. Poire. Pushing a non-Newtonian fluid in a Hele-Shaw cell: From fingers to needles. *Phys. Fluids*, 11(7):1757–1767, 1999.

[5] A. Amiri, F. Larachi, and S.M. Taghavi. Buoyant miscible displacement flows in vertical pipe. *Phys. Fluids*, 28(10):102105, 2016.

[6] H. A Barnes, J.F. Hutton, and K. Walters. *An introduction to rheology.* 1989.

[7] D. Bensimon, L.P. Kadanoff, S. Liang, B.I. Shraiman, and C. Tang. Viscous flows in two dimensions. *Rev. Mod. Phys.*, 58(4):977, 1986.

[8] V. Bertola. Wicking with a yield stress fluid. *J. Phys. Condens. Matter.*, 21(3):035107, 2008.

[9] J. Bico and D. Quéré. Falling slugs. *J. Col. Inter. Sci.*, 243(1):262–264, 2001.

[10] R. J. Binnington, and D.V. Boger. Constant viscosity elastic liquids. *J. Rheol.*, 29(6):887-904, 1985.

[11] S.H. Bittleston, J. Ferguson, and I.A. Frigaard. Mud removal and cement placement during primary cementing of an oil well–Laminar non-Newtonian displacements in an eccentric annular Hele-Shaw cell. *J. Eng. Math.*, 43(2-4):229–253, 2002.

[12] T.D. Blake and Y.D. Shikhmurzaev. Dynamic wetting by liquids of different viscosity. *J. Col. Inter. Sci.*, 253(1):196–202, 2002.

[13] D. Bonn, H. Kellay, M.B. Amar, and J. Meunier. Viscous finger widening with surfactants and polymers. *Phys. Rev. Lett.*, 75(11):21–32, 1995.

[14] J. Boujlel and P. Coussot. Measuring the surface tension of yield stress fluids. *Soft. Matter.*, 9(25):5898–5908, 2013.

[15] R. Brandao, J. V. Fontana, and J. Miranda. Stretch flow of confined non-Newtonian fluids: Nonlinear fingering dynamics. *Phys. Rev. E.*, 88(6):063003, 2013.

[16] R. Brandao, J.V. Fontana, and J.A. Miranda. Interfacial pattern formation in confined power-law fluids. *Phys. Rev. E.*, 90(1):013013, 2014.

[17] A. Buka, P. Palffy-Muhoray, and Z. Racz. Viscous fingering in liquid crystals. *Phys. Rev. A.*, 36(8):3984–3989, 1987.

[18] H.M. Caliman, E.J. Soares, and R.L. Thompson. An experimental investigation on the Newtonian-Newtonian and viscoplastic-Newtonian displacement in a capillary tube. *J. non-Newt. Fluid Mech.*, 247:207–220, 2017.

[19] R. Chebbi. Deformation of advancing gas–liquid interfaces in capillary tubes. *J. Col. Inter. Sci.*, 265(1):166–173, 2003.

[20] C. Chevalier, M.B. Amar, D. Bonn, and A. Lindner. Inertial effects on Saffman–Taylor viscous fingering. *J. Fluid Mech.*, 552:83–97, 2006.

[21] C. Chevalier, A. Lindner, and E. Clement. Destabilization of a Saffman-Taylor fingerlike pattern in a granular suspension. *Phys. Rev. Lett.*, 99(17):174501, 2007.

[22] T. Chevalier, C. Chevalier, X. Clain, J.C. Dupla, J. Canou, S. Rodts, and P. Coussot. Darcy's law for yield stress fluid flowing through a porous medium. *J. non-Newt. Fluid Mech.*, 195:57–66, 2013.

[23] R.L. Chuoke, P. Van Meurs, and C. van der Poel. The instability of slow, immiscible, viscous liquid-liquid displacements in permeable media. *Trans. AIME.*, 216:188–94, 1959.

[24] T.A. Coney and W.J. Masica. Effect of flow rate on the dynamic contact angle for wetting liquids. *NASA TN D-5115*, 1969.

[25] P. Coussot. Saffman-Taylor instability in yield-stress fluids. *J. Fluid Mech.*, 380:363–376, 1999.

[26] P. Coussot. Yield stress fluid flows: A review of experimental data. *J. non-Newt. Fluid Mech.*, 211:31–49, 2014.

[27] D. Q.M. Craig, S. Tamburic, G. Buckton, and J.M. Newton. An investigation into the structure and properties of Carbopol 934 gels using dielectric spectroscopy and oscillatory rheometry. *J. Cont. Rel.*, 30(3):213–223, 1994.

[28] M.M. Cross. Relation between viscoelasticity and shear-thinning behaviour in liquids. *Rheol. Acta.*, 18(5):609–614, 1979.

[29] P.G. de Gennes. Wetting: statics and dynamics. *Rev. Mod. Phys.*, 57(3):827, 1985.

[30] A. de Lozar, A.L. Hazel, and A. Juel. Scaling properties of coating flows in rectangular channels. *Phys. Rev. Lett.*, 99(23):234501, 2007.

[31] D.A. de Sousa, E.J. Soares, R.S de Queiroz, and R.L. Thompson. Numerical investigation on gas-displacement of a shear-thinning liquid and a visco-plastic material in capillary tubes. *J. non-Newt. Fluid Mech.*, 144(2):149–159, 2007.

[32] B. Ebrahimi, P. Mostaghimi, H. Gholamian, and K. Sadeghy. Viscous fingering in yield stress fluids: a numerical study. *J. Eng. Math.*, 97(1):161–176, 2016.

[33] J. Eggers and H.A. Stone. Characteristic lengths at moving contact lines for a perfectly wetting fluid: the influence of speed on the dynamic contact angle. *J. Fluid Mech.*, 505:309–321, 2004.

[34] S. Enjamoori, J. Azaiez, and B.B. Maini. Experimental investigation of viscous fingering instabilities in emulsions displacements. *Int. J. Emerg. Multi. Fluid Sci.*, 2(4), 2010.

[35] A. Eslami, I.A. Frigaard, and S.M. Taghavi. Viscoplastic fluid displacement flows in horizontal channels: Numerical simulations. *J. non-Newt. Fluid Mech.*, 249:79–96, 2017.

[36] A. Eslami and S.M. Taghavi. Viscous fingering regimes in elasto-visco-plastic fluids. *J. non-Newt. Fluid Mech.*, 243:79–94, 2017.

[37] P. Fast and M.J. Shelley. A moving overset grid method for interface dynamics applied to non-Newtonian Hele–Shaw flow. *J. Comput. Phys.*, 195(1):117–142, 2004.

[38] J.V. Fontana, E.O. Dias, and J.A. Miranda. Controlling and minimizing fingering instabilities in non-Newtonian fluids. *Phys. Rev. E.*, 89(1):013016, 2014.

[39] J.V. Fontana, S.A. Lira, and J.A. Miranda. Radial viscous fingering in yield stress fluids: Onset of pattern formation. *Phys. Rev. E.*, 87(1):013016, 2013.

[40] J.V. Fontana and J.A. Miranda. Finger competition in lifting Hele-Shaw flows with a yield stress fluid. *Phys. Rev. E.*, 88(2):023001, 2013.

[41] G. Fritz. On the dynamic contact angle in the case of complete wetting. *Z. Angew. Phys.*, 19:374–381, 1965.

[42] P.J. Fryer, G.K. Christian, and W. Liu. How hygiene happens: physics and chemistry of cleaning. *Int. J. Dairy. Technol.*, 59(2):76–84, 2006.

[43] B. Géraud, L. Jørgensen, L. Petit, H. Delanoë-Ayari, P. Jop, and C. Barentin. Capillary rise of yield-stress fluids. *E.P.L.*, 107(5):58002, 2014.

[44] G. German and V. Bertola. The spreading behaviour of capillary driven yield-stress drops. *Coll. Surf. A. Physic chem. Eng. Asp.*, 366(1-3):18–26, 2010.

[45] P. Gondret and M. Rabaud. Shear instability of two-fluid parallel flow in a Hele–Shaw cell. *Phys. Fluids*, 9(11):3267–3274, 1997.

[46] J.W. Grate, K.J. Dehoff, M.G. Warner, J.W. Pittman, T.W. Wietsma, C. Zhang, and M. Oostrom. Correlation of oil-water and air–water contact angles of diverse silanized surfaces and relationship to fluid interfacial tensions. *Langmuir.*, 28(18):7182–7188, 2012.

[47] E.B. Gutoff and C.E. Kendrick. Dynamic contact angles. *AlChE. J.*, 28(3):459–466, 1982.

[48] A. He and A. Belmonte. Inertial effects on viscous fingering in the complex plane. *J. Fluid Mech.*, 668:436–445, 2011.

[49] S. Hill et al. Channeling in packed columns. *Chem. Eng. Sci.*, 1(6):247–253, 1952.

[50] G.M. Homsy. Viscous fingering in porous media. *Annu. Rev. Fluid Mech.*, 19(1):271–311, 1987.

[51] R.Y.Z. Hu, A.T.A. Wang, and J.P. Hartnett. Surface tension measurement of aqueous polymer solutions. *Exp. Therm. Fluid Sci.*, 4(6):723–729, 1991.

[52] P.C. Huzyak and K.W. Koelling. The penetration of a long bubble through a viscoelastic fluid in a tube. *J. non-Newt. Fluid Mech.*, 71(1):73–88, 1997.

[53] J. Ignes-Mullol, Zhao H., and J.V. Maher. Velocity fluctuations of fracture like disruptions of associating polymer solutions. *Phys. Rev. E.*, 51(2):1338–1343, 1995.

[54] M. Jalaal, N.J. Balmforth, and B. Stoeber. Slip of spreading viscoplastic droplets. *Langmuir.*, 31(44):12071–12075, 2015.

[55] L. Jørgensen. *Wetting of yield-stress fluids: capillary bridges and drop spreading.* PhD thesis, Université de Lyon, 2016.

[56] L. Jørgensen, M. Le Merrer, H. Delanoë-Ayari, and C. Barentin. Yield stress and elasticity influence on surface tension measurements. *Soft. Matter.*, 11(25):5111–5121, 2015.

[57] M. Jung, M. Brinkmann, R. Seemann, and M.S.and Herminghaus S. Hiller, T. de La Lama. Wettability controls slow immiscible displacement through local interfacial instabilities. *Phys. Rev. Fluids*, 1(7):074202, 2016.

[58] N. Kagei, D. Kanie, and M. Kawaguchi. Viscous fingering in shear thickening silica suspensions. *Phys. Fluids*, 17:0545103, 2005.

[59] S. Kalliadasis and H.C. Chang. Apparent dynamic contact angle of an advancing gas–liquid meniscus. *Phys. Fluids*, 6(1):12–23, 1994.

[60] D.A. Kessler, J. Koplik, and H. Levine. Pattern selection in fingered growth phenomena. *Adv. Phys.*, 37(3):255–339, 1988.

[61] J.Y. Kim, J.Y. Song, E.J. Lee, and S.K. Park. Rheological properties and microstructures of Carbopol gel network system. *Colloid. Polym. Sci.*, 281(7):614–623, 2003.

[62] L. Kondic, M.J. Shelley, and P. Palffy-Muhoray. Non-Newtonian Hele-Shaw flow and the Saffman–Taylor instability. *Phys. Rev. Lett.*, 80(7):1433, 1998.

[63] B. Laborie, F. Rouyer, D.E. Angelescu, and E. Lorenceau. Yield-stress fluid deposition in circular channels. *J. Fluid Mech.*, 818:838–851, 2017.

[64] E. Lajeunesse, J. Martin, N. Rakotomalala, D. Salin, and Y.C. Yortsos. Miscible displacement in a Hele-Shaw cell at high rates. *J. Fluid Mech.*, 398:299–319, 1999.

[65] L.W. Lake. *Enhanced oil recovery.* Prentice Hall, 1989.

[66] G. Lamour, A. Hamraoui, A. Buvailo, Y. Xing, S. Keuleyan, V. Prakash, A. Eftekhari-Bafrooei, and E. Borguet. Contact angle measurements using a simplified experimental setup. *J. Chem. Educ.*, 87(12):1403–1407, 2010.

[67] C. H. Lee, V. Moturi, and Y. Lee. Thixotropic property in pharmaceutical formulations. *J. Cont. Rel.*, 136(2):88–98, 2009.

[68] E. Lemaire, P. Levitz, G. Daccord, and H. Van Damme. From viscous fingering to viscoelastic fracturing in colloidal fluids. *Phys. Rev. Lett.*, 67(15):2009, 1991.

[69] R. Lenormand. Liquids in porous media. *J. Phys. Condens. Matter.*, 2(S):SA79, 1990.

[70] B. Levaché and D. Bartolo. Revisiting the Saffman-Taylor experiment: imbibition patterns and liquid-entrainment transitions. *Phys. Rev. Lett.*, 113(4):044501, 2014.

[71] A. Lindner, D. Bonn, and J. Meunier. Viscous fingering in a shear-thinning fluid. *Phys. Fluids*, 12(2):256–261, 2000.

[72] A. Lindner, D. Bonn, E.C. Poire, M.B Amar, and J. Meunier. Viscous fingering in non-Newtonian fluids. *J. Fluid Mech.*, 469:237–256, 2002.

[73] A. Lindner, P. Coussot, and D. Bonn. Viscous fingering in a yield stress fluid. *Phys. Rev. Lett.*, 85(2):314, 2000.

[74] A. Lindner, P. Coussot, and D. Bonn. Viscous fingering in a gel. In *Branching in Nature*, pages 433–438. Springer, 2001.

[75] W.F. Lopez, M. F. Naccache, and P. R. de Souza Mendes. Rising bubbles in yield stress materials. *J. Rheol.*, 62(1):209–219, 2018.

[76] K. Makino, M. Kawaguchi, K. Aoyama, and T. Kato. Transition of viscous fingering patterns in polymer solutions. *Phys. Fluids*, 7(3):455–457, 1995.

[77] N. Maleki-Jirsaraei, A. Lindner, S. Rouhani, and D. Bonn. Saffman–Taylor instability in yield stress fluids. *J. Phys. Condens. Matter.*, 17(14):S1219, 2005.

[78] S. Malhotra and M.M. Sharma. Impact of fluid elasticity on miscible viscous fingering. *Chem. Eng. Sci.*, 117:125–135, 2014.

[79] R.M. Manglik, V.M. Wasekar, and J. Zhang. Dynamic and equilibrium surface tension of aqueous surfactant and polymeric solutions. *Exp. Therm. Fluid Sci.*, 25(1):55–64, 2001.

[80] K.V. McCloud and J.V. Maher. Experimental perturbations to Saffman–Taylor flow. *Phys. Rep.*, 260(3):139–185, 1995.

[81] G.H. McKinley. Dimensionless groups for understanding free surface flows of complex fluids. *Rheol. Bulletin*, 683–696, 2005.

[82] J.W. McLean and P.G. Saffman. The effect of surface tension on the shape of fingers in a Hele-Shaw cell. *J. Fluid Mech.*, 102:455–469, 1981.

[83] T.G. Mezger. *The rheology handbook: for users of rotational and oscillatory rheometers.* Vincentz Network GmbH & Co KG, 2006.

[84] H. Mohammadigoushki and S.J. Muller. Inertio-elastic instability in Taylor-Couette flow of a model wormlike micellar system. *J. Rheol.*, 61(4):683–696, 2017.

[85] G.V.L. Moisés, M.F. Naccache, K. Alba, and I.A. Frigaard. Isodense displacement flow of viscoplastic fluids along a pipe. *J. non-Newt. Fluid Mech.*, 236:91–103, 2016.

[86] R. Mollaabbasi and S.M. Taghavi. Buoyant displacement flows in slightly non-uniform channels. *J. Fluid Mech.*, 795:876–913, 2016.

[87] S. Mora and M. Manna. Saffman–Taylor instability for generalized Newtonian fluids. *Phys. Rev. E.*, 80(1):016308, 2009.

[88] S. Mora and M.l. Manna. From viscous fingering to elastic instabilities. *J. non-Newt. Fluid Mech.*, 173:30–39, 2012.

[89] E.B. Nelson and D. Guillot. *Well Cementing, 2nd Edition.* Schlumberger Educational Services, 2006.

[90] J. Nittmann, G. Daccord, and H.E Stanley. Fractal growth of viscous fingers: quantitative characterization of a fluid instability phenomenon. *Nature*, 314(6007):141–144, 1985.

[91] E. Nowak, N.M. Kovalchuk, Z. Che, and M.J.H. Simmons. Effect of surfactant concentration and viscosity of outer phase during the coalescence of a surfactant-laden drop with a surfactant-free drop. *Colloids. Surf. A. Physic chem. Eng. Asp.*, 505:124–131, 2016.

[92] F.K. Oppong and J.R. de Bruyn. Diffusion of microscopic tracer particles in a yield-stress fluid. *J. non-Newt. Fluid Mech.*, 142(1):104–111, 2007.

[93] F.M. Orr and J.J. Taber. Use of carbon dioxide in enhanced oil recovery. *Science.*, 224(4649):563–569, 1984.

[94] C.W. Park and G.M. Homsy. Two-phase displacement in Hele-Shaw cells: theory. *J. Fluid Mech.*, 139:291–308, 1984.

[95] S.S. Park and D.J. Durian. Viscous and elastic fingering instabilities in foam. *Phys. Rev. Lett.*, 72(21):3347, 1994.

[96] H. Pascal. Rheological behaviour effect of non-Newtonian fluids on dynamic of moving interface in porous media. *Int. J. Eng. Sci.*, 22(3):227–241, 1984.

[97] J. Peixinho, C. Desaubry, and M. Lebouche. Heat transfer of a non-Newtonian fluid (Carbopol aqueous solution) in transitional pipe flow. *Int. J. Heat Mass Transf.*, 51(1-2):198–209, 2008.

[98] J. Peixinho, C. Nouar, C. Desaubry, and B. Théron. Laminar transitional and turbulent flow of yield stress fluid in a pipe. *J. non-Newt. Fluid Mech.*, 128(2-3):172–184, 2005.

[99] J.M. Piau. Carbopol gels: Elastoviscoplastic and slippery glasses made of individual swollen sponges: Meso-and macroscopic properties, constitutive equations and scaling laws. *J. non-Newt. Fluid Mech.*, 144(1):1–29, 2007.

[100] E.C. Poire and M.B. Amar. Finger behavior of a shear thinning fluid in a Hele-Shaw cell. *Phys. Rev. Lett.*, 81(10):2048, 1998.

[101] A. Rathapon, A. Sirivat, P. Vayumhasuwan, and others. Viscoelastic properties of Carbopol 940 gels and their relationships to piroxicam diffusion coefficients in gel bases. *Pharm. Res.*, 22(12):2134–2140, 2005.

[102] G. Rousseaux, A. De Wit, and M. Martin. Viscous fingering in packed chromatographic columns: Linear stability analysis. *J. Chromatogr. A.*, 1149(2):254–273, 2007.

[103] C. Ruyer-Quil. Inertial corrections to the Darcy law in a Hele–Shaw cell. *C. R. Acad. Sci. IIb. Mec.*, 329(5):337–342, 2001.

[104] P.G. Saffman and G. Taylor. The penetration of a fluid into a porous medium or Hele-Shaw cell containing a more viscous liquid. In *Proc. R. Soc. A.*, 245, 312–329, 1958.

[105] A.R. Saïdi, C. Martin, and A. Magnin. Influence of yield stress on the fluid droplet impact control. *J. non-Newt. Fluid Mech.*, 165(11-12):596–606, 2010.

[106] S.A. Setu, I. Zacharoudiou, G.J. Davies, D. Bartolo, S. Moulinet, A.A. Louis, J.M. Yeomans, and D.G. Aarts. Viscous fingering at ultralow interfacial tension. *Soft. Matter.*, 9(44):10599–10605, 2013.

[107] D. S. Stevenson and S. Blake. Modelling the dynamics and thermodynamics of volcanic degassing. *Bull. Volcanol.*, 60(4):307–317, 1998.

[108] J.P. Stokes, D.A. Weitz, J.P. Gollub, A. Dougherty, M.O. Robbins, P.M. Chaikin, and H.M. Lindsay. Interfacial stability of immiscible displacement in a porous medium. *Phys. Rev. Lett.*, 57(14):1718, 1986.

[109] T. Svitova, O. Theodoly, S. Christiano, R.M. Hill, and C.J. Radke. Wetting behavior of silicone oils on solid substrates immersed in aqueous electrolyte solutions. *Langmuir*, 18(18):6821–6829, 2002.

[110] P. A.P. Swain, G. Karapetsas, O.K. Matar, and K.C. Sahu. Numerical simulation of pressure-driven displacement of a viscoplastic material by a Newtonian fluid using the lattice Boltzmann method. *Eur. J. Mech. B. Fluid*, 49:197–207, 2015.

[111] P. Tabeling and A. Libchaber. Film draining and the Saffman–Taylor problem. *Phys. Rev. A.*, 33(1):794, 1986.

[112] P. Tabeling, G. Zocchi, and A. Libchaber. An experimental study of the Saffman-Taylor instability. In *Physicochemical Hydrodynamics*, pages 515–525. Springer, 1988.

[113] H. Tabuteau, P. Coussot, and J.R. de Bruyn. Drag force on a sphere in steady motion through a yield-stress fluid. *J. Rheol.*, 51(1):125–137, 2007.

[114] S.M. Taghavi. A two-layer model for buoyant displacement flows in a channel with wall slip. *J. Fluid Mech.*, 852:602–640, 2018.

[115] S.M. Taghavi, K. Alba, M. Moyers-Gonzalez, and I.A. Frigaard. Incomplete fluid-fluid displacement of yield stress fluids in near-horizontal pipes: experiments and theory. *J. non-Newt. Fluid Mech.*, 167-168:59–74, 2012.

[116] S.M. Taghavi, R. Mollaabbasi, and Y. St-Hilaire. Buoyant miscible displacement flows in rectangular channels. *J. Fluid Mech.*, 826:676–713, 2017.

[117] N.W. Taylor and E.B. Bagley. Rheology of dispersions of swollen gel particles. *J. Polymer Sci. Polymer Phys. Ed.*, 13(6):1133–1144, 1975.

[118] M. Trojer, M.L. Szulczewski, and R. Juanes. Stabilizing fluid-fluid displacements in porous media through wettability alteration. *Phys. Rev. Applied*, 3(5): 054008, 2015.

[119] D. Truzzolillo, S. Mora, C. Dupas, and L. Cipelletti. Off-equilibrium surface tension in colloidal suspensions. *Phys. Rev. Lett.*, 112(12):128303, 2014.

[120] D. Truzzolillo, S. Mora, C. Dupas, and L. Cipelletti. Nonequilibrium interfacial tension in simple and complex fluids. *Phys. Rev. X.*, 6(4):041057, 2016.

[121] H. Van Damme, E. Alsac, C. Laroche, and L. Gatineau. On the respective roles of low surface tension and non-Newtonian rheological properties in fractal fingering. *Europhys. Lett.*, 5(1):25, 1988.

[122] H. Van Damme, E. Lemaire, Y. Ould, M. Abdelhaye, A. Mourchid, and P. Levitz. Pattern formation in particulate complex fluids: A guided tour. In *Non-linearity and breakdown in soft condensed matter*, pages 134–150. Springer, 1994.

[123] M.I.J. Van Dijke and K.S. Sorbie. The relation between interfacial tensions and wettability in three-phase systems: consequences for pore occupancy and relative permeability. *J. Pet. Sci. Eng.*, 33(1-3):39–48, 2002.

[124] P.R. Varges, B.S. Fonseca, C.M. Costa, M.F. Naccache, P.R. de Souza Mendes, and H.A. Pinho. Exchange flows between yield stress materials and Newtonian oils. *J. non-Newt. Fluid Mech.*, 261:123–135, 2018.

[125] G. Vinay. *Modélisation du redémarrage des écoulements de bruts paraffiniques dans les conduites pétrolieres.* PhD thesis, École Nationale Supérieure des Mines de Paris, 2005.

[126] E. Walling, R. Mollaabbasi, and S.M. Taghavi. Buoyant miscible displacement flows in a non-uniform Hele-Shaw cell. *Phys. Rev. Fluids*, 3(3):034003, 2018.

[127] S. J. Weinstein, E.B. Dussan, and L.H. Ungar. A theoretical study of two-phase flow through a narrow gap with a moving contact line: Viscous fingering in a Hele-Shaw cell. *J. Fluid Mech.*, 221:53–76, 1990.

[128] A.R. White and T. Ward. Constant pressure gas-driven displacement of a shear-thinning liquid in a partially filled radial Hele-Shaw cell: Thin films, bursting and instability. *J. non-Newt. Fluid Mech.*, 206:18–28, 2014.

[129] J. Wiklund, M. Stading, and C. Trägårdh. Monitoring liquid displacement of model and industrial fluids in pipes by in-line ultrasonic rheometry. *J. Food Eng.*, 99(3):330–337, 2010.

[130] R.A. Wooding and H.J. Morel-Seytoux. Multiphase fluid flow through porous media. *Annu. Rev. Fluid Mech.*, 8(1):233–274, 1976.

[131] Y. Yuan and T.R Lee. Contact angle and wetting properties. In *Surface science techniques*, 3–34. Springer, 2013.

[132] X. Zhang, O. Fadoul, E. Lorenceau, and P. Coussot. Yielding and flow of soft-jammed systems in elongation. *Phys. Rev. Lett.*, 120(4):048001, 2018.

[133] B. Zhao, C.W. MacMinn, and R. Juanes. Wettability control on multiphase flow in patterned microfluidics. *Proc. Natl. Acad. Sci. U.S.A.*, 113(37):10251–10256, 2016.

[134] D. Zhou and M. Blunt. Effect of spreading coefficient on the distribution of light non-aqueous phase liquid in the subsurface. *J. Contam. Hydrol.*, 25(1-2):1–19, 1997.

[135] J. Zilz, C. Schafer, C. Wagner, R.J. Poole, M.A. Alves, and A. Lindner. Serpentine channels: micro-rheometers for fluid relaxation times. *Lab. Chip.*, 14(2):351–358, 2014.

Chapitre 3

Controlling branched fingering patterns in viscous fingering of yield stress fluids

3.1 Résumé

L'instabilité de digitation visqueuse des fluides à seuil dans les canaux à section rectangulaire est étudiée expérimentalement dans laquelle, contrairement aux fluides Newtoniens, des modèles de digitation ramifiés sont observés. En modifiant légèrement l'entrefer de la cellule sur une large gamme de largeurs de canaux, nous montrons que la présence de la flottabilité différente et différents rapports d'aspect de section entraînent des comportements d'écoulement fondamentalement différents. Nous trouvons que seul un nouveau paramètre (ET), proposé ici, peut bien expliquer la morphologie de la digitation visqueuse pour un large spectre de nombres d'obligations dépendant du rapport de format Bo^* lorsque la valeur est inférieure à une valeur critique (Bo_c^*); cependant, la formation du modèle de digitation ramifiés est entravée si le Bo^* dépasse Bo_c^*. De plus, nous pouvons classer deux modèles de flux généraux observés, à savoir les modèles de digitation ramifiés et les modèles à un seul doigt, par rapport à ET et Bo^*. De plus, nous présentons une courbe principale complète utilisant un paramètre mis à l'échelle ($Ca\delta^{1+n}$), permettant d'afficher toutes les données de largeur de digitation pour différents paramètres de flux.

3.2 Abstract

The viscous fingering instability of yield stress fluids in rectangular cross-section channels is experimentally studied wherein, unlike Newtonian fluids, branched fingering patterns are observed. By slightly varying the gap thickness of the cell over a wide range of channel widths, we demonstrate that the presence of buoyancy and the cross-section aspect ratio variations

result in fundamentally different flow behaviours. We find that only a novel parameter (ET), proposed here, can successfully explain the morphology of viscous fingering for a wide spectrum of aspect ratio-dependent Bond number Bo^* when below a critical value (Bo_c^*); however, the formation of the branched fingering pattern is hindered if the Bo^* exceeds Bo_c^*. Moreover, we are able to classify two general flow patterns observed, namely the branched fingering and the single finger patterns, versus ET and Bo^*. In addition, we present a comprehensive master curve using a scaled parameter ($Ca\delta^{1+n}$), enabling a collapse of all finger width data for various flow parameters.

3.3 Introduction

During two-phase flow in confined geometries, the interface is often rendered unstable and a variety of interfacial flow patterns are formed. Among these interfacial flows, the classical viscous fingering or Saffman-Taylor instability is of interest. This instability occurs when a fluid displaces another fluid of higher viscosity. In the landmark 1958 paper, Saffman and Taylor (1) experimentally and theoretically studied the viscous fingering in a traditional Hele-Shaw cell (2). This simple cell (i.e., quasi-two-dimensional channel) can provide considerable insights into the key features of hydrodynamic interfacial instabilities and pattern formation. Aside from the beauty and complexity of the flow patterns, the attention devoted to these interfacial flows can be associated with their observation in a variety of industrial applications and natural phenomena. Prominent examples includes oil and gas industries (3; 4), food processing (5; 6), and biomedical and biotechnological applications (7; 8).

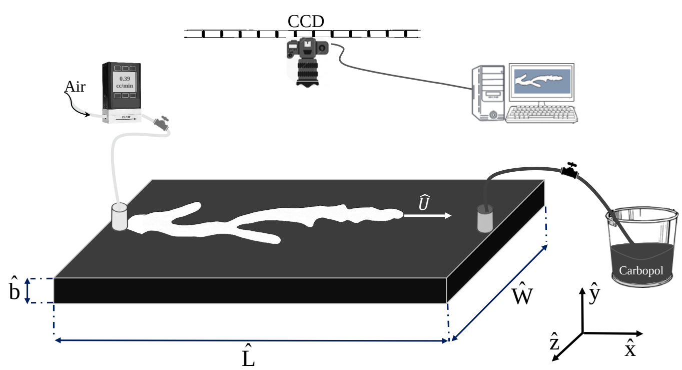

FIGURE 3.1 – A 3D schematic view of the experimental set-up: air is injected into Carbopol gel. The imposed velocity is determined by an Alicat mass flow controller. Also for recording the finger behaviours, a Basler high speed camera mounted on top of the cell is used.

In the past several decades, Newtonian fluid flows have been considered in the rectangular Hele-Shaw cell where an air finger propagates through the cell initially filled with a viscous fluid. The finger width ($\hat{w}$) [1] decreases monotonically with the capillary number ($Ca = \frac{\hat{\mu}\hat{U}}{\hat{\sigma}}$), representing the ratio of surface tension and viscous forces, where $\hat{\mu}$, $\hat{U}$ and $\hat{\sigma}$ denote the viscosity of the viscous fluid, the finger tip velocity and the surface tension, respectively. However, the finger width tends to an asymptotic plateau value of about half the cell width ($\hat{W}/2$) at high values of Ca. For Newtonian fluids, there is only one independent dimensionless parameter that largely describes the flow ($Ca\delta^2$). This parameter is a combination of the aspect ratio of the Hele-Shaw cell ($\delta = \frac{\hat{W}}{\hat{b}}$) and Ca. $Ca\delta^2$ acts as a control parameter in a way that the measurements of the relative finger width ($\lambda = \frac{\hat{w}}{\hat{W}}$) follow the same master curve for different fluid parameters. Experimental and theoretical studies have addressed the aforementioned findings at higher aspect ratios ($\delta > 20$), for which the buoyancy effects were negligible (10; 11; 12).

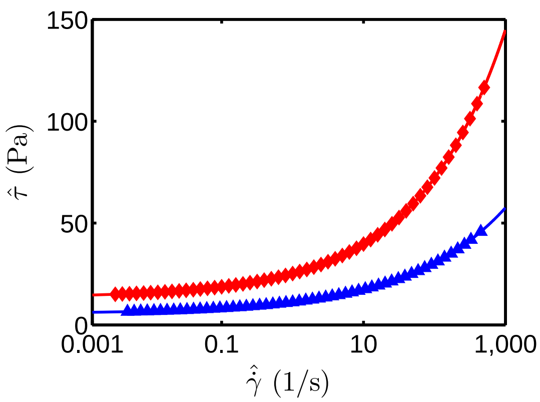

FIGURE 3.2 – Flow curves of shear stress, $\hat{\tau}$, versus shear rate, $\hat{\dot{\gamma}}$. The lines correspond to the Herschel-Bulkley model parameters fitted to data. The data correspond to high Carbopol concentration (♦)($\hat{\tau} = 13.7 + 11.6\ \hat{\dot{\gamma}}^{0.35}$) and low Carbopol concentration (▲)($\hat{\tau} = 5.4 + 5.7\ \hat{\dot{\gamma}}^{0.32}$).

Despite a vast majority of the experimental and theoretical investigations on the flows in either high aspect ratios of the cross section of the cell ($\delta \gg 1$) or in low aspect ratios ($\delta \cong 1$) (2; 13; 14), a few studies on the intermediate range of aspect ratios have been reported in the literature (15; 16). Nevertheless, this intermediate range is important due to pharmaceutical and food applications of interfacial flows in microchannels with intermediate aspect ratios ($1 \leq \delta \leq 10$) (17; 18).

In a majority of previous studies, the buoyancy effects have been negligible. There have been relatively few research works considering the gravitational effects on flow features in confined geometries. These have mainly drawn the attention to the impacts of buoyancy on the thickness of residual thin liquid films on the solid surface and the formation of non-uniform liquid films (13; 14). In order to assess the relative magnitudes of buoyancy and interfacial tension effects, the Bond number ($Bo = \frac{\hat{\rho}\hat{g}\hat{b}^2}{\hat{\sigma}}$) has been employed where $\hat{\rho}$ is the density of the viscous

1. In this Letter, we adopt the convention of denoting dimensional quantities with the ˆ symbol.

fluid and $\hat{g}$ is the gravitational acceleration.

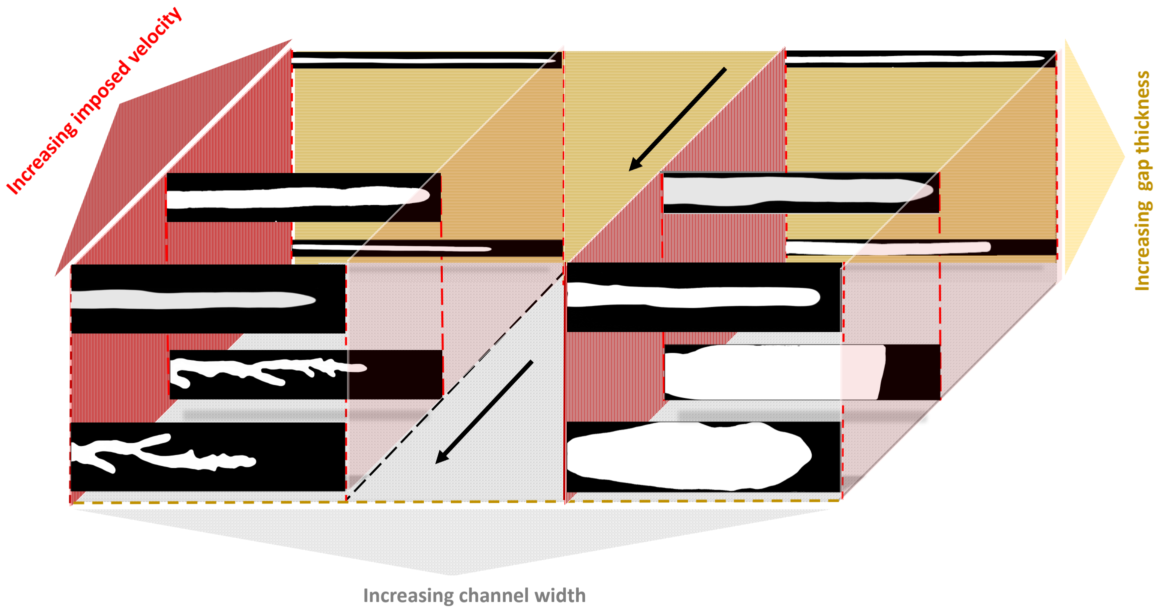

FIGURE 3.3 – Diagram of the different flow patterns as a function of the gap thickness, the channel width and the imposed velocity at the low Carbopol concentration. The air flows from left to right.

It has been shown that the viscous fingering instability is strikingly modified in yield stress fluids, in terms of both the morphological pattern and the finger width (19; 20; 21; 22; 23). In contradiction to the classical Newtonian viscous fingering, in particular, branched fingering patterns are formed in yield stress fluids at lower imposed velocities. In addition, $\hat{w}$ is independent of the imposed velocity and the channel width. For yield stress fluids, the formation of finger branching patterns may be attributed to the existence of unyielded zones in some regions behind the main finger front (23; 19).

In this letter, we demonstrate the formation of different fingering patterns emerging from the injection of air into a channel filled with a yield stress fluid. For the first time, we show that buoyancy exerts a remarkable impact on the fingering pattern in yield stress fluids so that the branched fingering pattern cannot appear at high Bo. Moreover, we present the effect of δ on the viscous fingering instability, illustrating the smaller values of δ either inhibit or trigger the formation of ramified structure patterns. We also show the influence of the aspect ratio on the relative finger width, highlighting that λ does not scale with the classical control parameter especially at low δ.

3.4 Experimental descriptions

Here, we study the fingering instability for two different Carbopol concentrations, i.e., a common laboratory yield stress fluid. The rheological behaviour of Carbopol gels is measured by a DHR-3 TA Instrument rheometer using a parallel-plate geometry (gap 1 mm, diameter 40 mm). Fine sandpapers are attached to the plates to eliminate wall slip. The shear behaviour of Carbopol gel is described by the Herschel-Bulkley model ($\hat{\tau} = \hat{\tau}_y + \hat{\kappa}\hat{\dot{\gamma}}^n$), a well-known constitutive equation for viscoplastic fluids, including the fluid consistency index ($\hat{\kappa}$) and the power-law index (n) (see Fig. 3.2). In addition to yield stress, the Carbopol gels used clearly exhibit strong shear-thinning behaviours ($n < 0.4$), implying the remarkable deviation from Newtonian viscosity behaviours.

We systematically investigate the effects of the cell width, gap thickness, imposed velocity ($\hat{V}$) and Carbopol concentration on the viscous fingering features in the rectangular cell. The experiments are conducted in several rectangular channels made of glass plates, each of length 50 cm (see Fig. 3.1), for which the gap thickness ($0.1 \leq \hat{b} \leq 5.5$ mm) and the channel width ($3 \leq \hat{W} \leq 120$ mm) are varied. The cell is initially filled with a dyed Carbopol gel. Then, through a hole drilled at the center of the upper plate, air is injected. The air imposed velocity is controlled via a mass flow controller and the interface evolution is recorded with a CCD camera, from the cell top view.

3.5 Results and discussions

Fig. 3.3 shows two general flow patterns as a function of $\hat{b}$, $\hat{W}$ and $\hat{V}$, for which the Carbopol concentration is constant. A ramified structure patten and a single finger pattern are observed. As seen, for larger values of $\hat{W}$ and small $\hat{b}$, and when $\hat{V}$ is low, the initial finger frequently splits and forms several asymmetric fingers. Consequently, the branched fingering pattern is observed. Nevertheless, at high velocities, a single, stable finger appears with a shape that is very similar to that of a classical Newtonian viscous finger. These phenomena have been reported in the literature (19; 20; 21; 22). For a wide range of velocities, even at very low velocities, we observed that by decreasing the cell width the branched fingering pattern does not appear. This significant difference implies that, apart from the presence of the yield stress, the aspect ratio (δ) also has a substantial role in the appearance of this flow pattern at lower velocities. For small $\hat{b}$ and $\hat{V}$ and when reaching a critical aspect ratio ($\delta_c \approx 25$), a destabilization of the displacing finger occurs, which leads to the formation of the ramified fingering patterns.

Surprisingly, Fig. 3.3 also presents that slightly increasing $\hat{b}$ has significant impacts on the flow pattern. As can be seen, contrary to what is the case for smaller gap thicknesses, the finger tip splitting is completely suppressed and therefore a single finger is formed, regardless of the imposed velocity and the cell width.

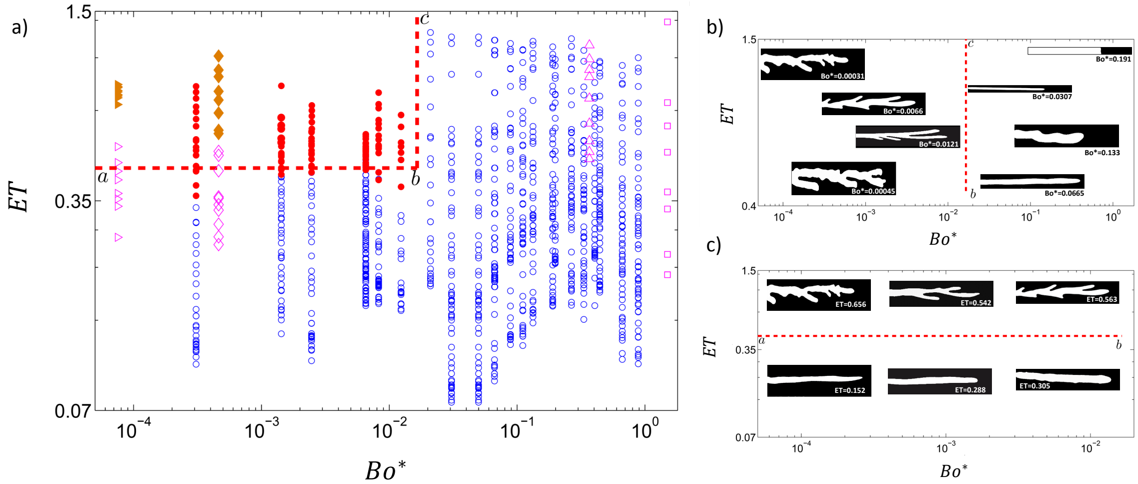

FIGURE 3.4 – (a) Two different flow patterns observed, in the plane of Bo^* and ET. The symbols correspond to the branched fingering patterns (●) and the single finger patterns (○). The horizontal line (ab) at $ET \approx 0.45$ and the vertical line (bc) at $Bo^* \approx 0.02$ separate the data corresponding to the two patterns. The single and branched fingering flow data points from the literature are also superposed. The symbols correspond to the single finger (hollow symbols) and the branched fingering (filled symbols). The data are from (20) (▸,▷), (19) (♦,◊), (24) (△) and (25) (□). Several experimental snapshots corresponding to the branched fingering and single finger patterns are presented in (b) and (c). Subfigures (b) and (c) show the effect of Bo^* (above critical ET) and ET on the flow patterns, respectively. The lines (bc) and (ab) represent the same lines as the main graph in (a).

The branched fingering pattern can appear only at smaller velocities, for which the yield stress is predominant and consequently the displaced fluid is not yielded everywhere (19). Thus, the initial finger splits without feeling the surroundings and the ramified structure pattern is observed due to the presence of yield stress ($\hat{\tau}_y$). On the other hand, at higher velocities, the flow pattern formation is mainly controlled by balancing the surface tension stress ($\frac{\hat{\sigma}}{\hat{b}}$) and the viscous stress ($\frac{\hat{\mu}\hat{U}}{\hat{b}}$) (quantified by Ca). In order to consider all the effects, we defined an appropriate dimensionless number as

$$ET = \frac{\sqrt{\hat{\tau}_y \hat{b} \hat{\sigma}}}{\hat{\mu}\hat{U}} \sim \frac{\sqrt{f_{\text{yield stress}} \cdot f_{\text{surface}}}}{f_{\text{viscous}}} \equiv \sqrt{\frac{Bn}{Ca}}, \tag{3.1}$$

where f denotes force or stress. The viscosity is defined as $\hat{\mu} = \hat{\tau}_y \left(\frac{\hat{b}}{\hat{U}}\right) + \hat{\kappa}\left(\frac{\hat{U}}{\hat{b}}\right)^{n-1}$. The Bingham number ($Bn = \frac{\hat{\tau}_y}{\hat{\mu}\frac{\hat{U}}{\hat{b}}}$) represents a dimensionless yield stress number that is zero in the Newtonian case (26). Moreover, the values of both buoyancy and cell width can dramatically affect the flow morphology. These effects are captured by by Bo and δ, which can be combined into

$$Bo^* = \frac{Bo}{\delta} \equiv \frac{Ar}{La}, \tag{3.2}$$

where the modified Bond number (Bo^*) is equivalent to the combination of the Archimedes number ($Ar = \frac{\hat{\rho}^2 \hat{g} \hat{b}^3}{\hat{\mu}^2}$) and the Laplace number ($\frac{\hat{\rho}\hat{\sigma}\hat{W}}{\hat{\mu}^2}$). It is worth noting that, in contrast to ET, both Ar and La are independent of the imposed velocity. Fig. 3.4a classifies the experimental data points in the plane of ET and Bo^*. A horizontal dashed line (ab) and a vertical dashed line (bc) are superimposed on the graph. As seen, the two flow patterns are clearly segregated on the sides of the lines, over a wide range of flow parameters. When Bo^* is large, the pattern formation does not depend on ET and the single finger patterns are observed (see Fig. 3.4b). The transition boundary (bc) occurs roughly at $Bo_c^* \approx 0.02$. On the other side, before reaching Bo_c^*, a small increment in ET corresponds to significant changes in the flow morphology (see Fig. 3.4c). The transition between the branched and single finger patterns roughly occurs at $ET \approx 0.45$. Fig. 3.4a also demonstrates that the proposed dimensionless groups, in terms of the classification, are in good agreement with several experimental studies from the literature superposed on the graph (20; 19; 25; 24).

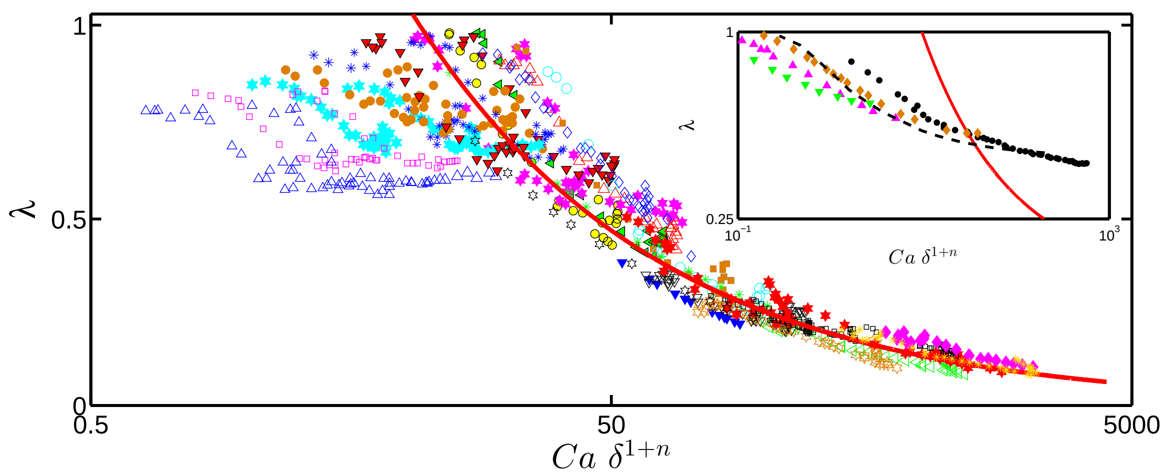

FIGURE 3.5 – λ as a function $Ca\delta^{1+n}$ for data at different channel widths, gap thicknesses and Carpool concentrations. The data correspond to experiments with both low and high Carbopol concentrations at various $\delta = \frac{\hat{W}\,(\mathrm{mm})}{\hat{b}\,(\mathrm{mm})}$: $\frac{4.5}{3}$ (△), $\frac{6}{3}$ (□), $\frac{9}{3}$ (★), $\frac{12}{3}$ (●), $\frac{15}{3}$ (∗), $\frac{21}{3}$ (▼), $\frac{30}{3}$ (★), $\frac{36}{3}$ (●), $\frac{45}{3}$ (◀), $\frac{60}{3}$ (■), $\frac{130}{3}$ (★), $\frac{60}{0.2}$ (♦), $\frac{60}{0.3}$ (∗), $\frac{60}{0.5}$ (◁), $\frac{60}{1}$ (☆), $\frac{60}{1.5}$ (▽), $\frac{60}{2.1}$ (○), $\frac{60}{4.33}$ (△), $\frac{60}{5.5}$ (◊), $\frac{20}{0.9}$ (☆), $\frac{25}{0.9}$ (∗), $\frac{68}{1.5}$ (□) and $\frac{40}{1.5}$(▼). The datapoints seem to follow a solid red curve indicated by $\lambda = 2.82\left(Ca\delta^{1+n}\right)^{-0.46}$. The inset shows Newtonian results from the literature in the plane of λ and $Ca\delta^{1+n}$ (for Newtonian fluids the control parameter turns into $Ca\delta^2$). The results are from (12)(δ = 65 (●)), (15) (δ = 1 (▼), δ = 1.99 (▲), δ = 6 (♦)). The theoretical results of (11) are shown using the black dashed curve. The red solid line is the same as the one in the main graph.

It has been found that for yield stress fluids, the finger width datapoints (λ) cannot collapse using the classical Newtonian control parameter ($Ca\delta^2$) (19). Recently, it has been shown that $Ca\delta^{1+n}$ is a relevant parameter in viscous fingering of yield stress fluids (21). The variation of λ versus $Ca\delta^{1+n}$ in our experiments for different experimental conditions is shown in Fig. 3.5, illustrating a reasonable collapse of data for larger aspect ratios. Nevertheless, for smaller δ, the data do not collapse onto the master curve when the gap thickness is large. It means that in this case buoyancy notably affects the finger width. As seen, the rest of the data falls on the master curve ($\lambda = 2.82 \left(Ca\delta^{1+n}\right)^{-0.46}$).

Our findings on the influences of buoyancy and the aspect ratio on viscous fingering of yield stress fluids are qualitatively in agreement with the theoretical and experimental results in the Newtonian viscous fingering literature (15; 16; 11; 12). It has been indicated that for the Newtonian cases, when δ is small ($\delta \leq 6$), the values of λ do not superpose using $Ca\delta^2$ (see the inset of Fig. 3.5) (15). Earlier studies have also shown that λ versus $Ca\delta^2$ follows the Newtonian principal curve for $\delta > 20$, valid for negligible buoyancy (11; 12). The inset in Fig. 3.5 compares quantitatively Newtonian and yield stress fluid flow results, showing completely different master curves.

3.6 Summary

In conclusion, we have demonstrated that the viscous fingering instability of yield stress fluids can be dramatically modified by buoyancy and the aspect ratio, as these drastically affect the flows patterns and the displacement efficiency captured by the finger width. We have found that the flow morphology is governed not only by the velocity, but also by the gap thickness and the cell width. The destabilization of the finger can be damped at high values of Bo^* and at smaller ET, offering an opportunity to control the yield stress flow behaviour. We have also found that the scaling parameter governing the finger in yield stress fluids ($Ca\delta^{1+n}$) is relevant for the cells with $\delta > 6$.

3.7 Bibliography

[1] P.G. Saffman and G. Taylor. The penetration of a fluid into a porous medium or Hele-Shaw cell containing a more viscous liquid. In *Proc. R. Soc. A.*, 245, 312–329, 1958.

[2] G.M. Homsy. Viscous fingering in porous media. *Annu. Rev. Fluid Mech.*, 19(1):271–311, 1987.

[3] F.M. Orr and J.J. Taber. Use of carbon dioxide in enhanced oil recovery. *Science*, 224(4649):563–569, 1984.

[4] L.W. Lake. *Enhanced oil recovery.* Prentice Hall, 1989.

[5] S. Hill et al. Channeling in packed columns. *Chem. Eng. Sci.*, 1(6):247–253, 1952.

[6] P.J. Fryer, G.K. Christian, and W. Liu. How hygiene happens: physics and chemistry of cleaning. *Int. J. Dairy. Technol.*, 59(2):76–84, 2006.

[7] P.D. Howell, S.L. Waters, and J.B. Grotberg. The propagation of a liquid bolus along a liquid-lined flexible tube. *J. Fluid Mech.*, 406:309–335, 2000.

[8] N.G. Cogan and J.P Keener. Channel formation in gels. *SIAM J. Appl. Math.*, 65(6):1839–1854, 2005.

[9] In this Letter, we adopt the convention of denoting dimensional quantities with the ˆ symbol.

[10] P. Tabeling and A. Libchaber. Film draining and the Saffman–Taylor problem. *Phys. Rev. A.*, 33(1):794, 1986.

[11] J.W. McLean and P.G. Saffman. The effect of surface tension on the shape of fingers in a Hele-Shaw cell. *J. Fluid Mech.*, 102:455–469, 1981.

[12] P. Tabeling, G. Zocchi, and A. Libchaber. An experimental study of the Saffman-Taylor instability. *J. Fluid Mech.*, 177:67–82, 1987.

[13] O. Atasi, S. Khodaparast, B. Scheid, and H.A. Stone. Effect of buoyancy on the motion of long bubbles in horizontal tubes. *Phys. Rev. Fluids*, 2(9):094304, 2017.

[14] M. Magnini, S. Khodaparast, O.K. Matar, H.A. Stone, and J.R. Thome. Dynamics of long gas bubbles rising in a vertical tube in a cocurrent liquid flow. *Phys. Rev. Fluids*, 4(2):023601, 2019.

[15] A. de Lozar, A.L. Hazel, and A. Juel. Scaling properties of coating flows in rectangular channels. *Phys. Rev. Lett.*, 99(23):234501, 2007.

[16] A. De Lozar, A. Juel, and A.L. Hazel. The steady propagation of an air finger into a rectangular tube. *J. Fluid Mech.*, 614:173–195, 2008.

[17] G.M. Whitesides and A.D. Stroock. Flexible methods for microfluidics. *Phys. Today.*, 54(6):42–48.

[18] C.N. Baroud and H. Willaime. Multiphase flows in microfluidics. *C. R. Phys.*, 5(5):547–555, 2004.

[19] A. Lindner, P. Coussot, and D. Bonn. Viscous fingering in a yield stress fluid. *Phys. Rev. Lett.*, 85(2):314, 2000.

[20] N. Maleki-Jirsaraei, A. Lindner, S. Rouhani, and D. Bonn. Saffman–Taylor instability in yield stress fluids. *J. Phys. Condens. Matter.*, 17(14):S1219, 2005.

[21] A. Eslami and S.M. Taghavi. Viscous fingering regimes in elasto-visco-plastic fluids. *J. non-Newt. Fluid Mech.*, 243:79–94, 2017.

[22] A. Eslami and S.M. Taghavi. Viscous fingering of yield stress fluids: The effects of wettability. *J. non-Newt. Fluid Mech.*, 264:25–47, 2019.

[23] P. Coussot. Saffman-Taylor instability in yield-stress fluids. *J. Fluid Mech.*, 380:363–376, 1999.

[24] H.M. Caliman, E.J. Soares, and R.L. Thompson. An experimental investigation on the Newtonian-Newtonian and viscoplastic-Newtonian displacement in a capillary tube. *J. non-Newt. Fluid Mech.*, 247:207–220, 2017.

[25] D.A. de Sousa, E.J. Soares, R.S. de Queiroz, and R.L. Thompson. Numerical investigation on gas-displacement of a shear-thinning liquid and a visco-plastic material in capillary tubes. *J. non-Newt. Fluid Mech.*, 144(2):149–159, 2007.

[26] R.L. Thompson and E.J. Soares. Viscoplastic dimensionless numbers. *J. non-Newt. Fluid Mech.*, 238:57–64, 2016.

Chapitre 4

Viscoplastic fluid displacement flows in horizontal channels: Numerical simulations

4.1 Résumé

Nous analysons par simulation numérique les écoulement à déplacement iso-visqueux d'un fluide de Bingham par un fluide de Newton dans un canal plan horizontal. Nous considérons un flux de déplacement léger-lourd avec un flux imposé laminaire. Nous analysons l'écoulement sous différentes perspectives, en utilisant les trois paramètres sans dimension qui décrivent en termes généraux l'écoulement : le nombre de Bingham (Bn), le nombre de Froude (Fr) et le nombre de Reynolds (Re). En particulier, nous sommes en mesure de classer trois classes pour les principaux régimes d'écoulement, à savoir, déplacements «center-type»/«slump- type», «back flow»/«no-back flow» et déplacement «stable/instable», pour lesquels nous quantifions également leurs limites de transition par rapport aux nombres sans dimension susmentionnés. Nous montrons que la formation d'un flux peut éventuellement conduire à un certain nombre de modèles d'écoulement, tels que des formes sinusoïdales et des formes de périodiques. De plus, nous étudions en profondeur une caractéristique intéressante exclusivement associée aux écoulement à déplacement viscoplastiques, à savoir la formation de couches résiduelles statiques sur les parois supérieure/inférieure du canal. Nous étudions également l'évolution des caractéristiques principales d'écoulement à déplacement et nous classifions certaines caractéristiques secondaires d'écoulement liées au front de tête, telles que les fronts de type bouchon, inertiel, semi-détachés et totalement détachés. Enfin, nous quantifions la vitesse du front de tête pendant longtemps.

4.2 Abstract

We study numerically iso-viscous displacement flows of a Bingham fluid by a Newtonian fluid in a horizontal plane channel. We consider a heavy-light displacement flow with a laminar imposed flow. We analyze the flow from various perspectives, using the three dimensionless parameters that largely describe the flow: the Bingham number (Bn), the densimetric Froude number (Fr) and the Reynolds number (Re). In particular, we are able to categorize three classes for the main flow regimes, viz., *center*-type and *slump*-type, *no-back-flow* and *temporary-back-flow*, and *stable* and *unstable* displacements, for which we also quantify their transition boundaries versus the aforementioned dimensionless numbers. We show that the appearance of unstable flows can eventually lead to a number of different flow patterns, such as *sinusoidal* shaped wave and *periodic-detachment* forms. In addition, we study in depth an interesting feature exclusively associated to viscoplastic fluid displacements, i.e., the formation of static residual layers on the upper/lower walls of the channel. We also study the evolution of the key displacement flow features, i.e., the trailing and leading fronts, and classify certain secondary flow features related to the leading front, such as *plug-like*, *inertial tip*, *semi-detached* and *fully-detached* fronts. Finally, we quantify the velocity of the leading front at long times.

4.3 Introduction

Displacement flow in a confined geometry is one of the most common processes appearing in diverse physical, chemical, biological, geophysical, and engineering systems. These fascinating flows are studied from various perspectives thanks to their numerous applications. Examples may includes : sugar refining (displacement of sugar liquors by water in pipe (21)); printing devices (displacement of lubrication oil in printing rollers (58)); carbon sequestration (injection of carbon dioxide into saline aquifer (10)); chromatographic separations (displacement of fluids with different viscosities in packed chromatographic columns (47)); enhanced oil recovery (displacement of oil by injection of gas or water into reservoir (39; 27)); coating (spreading and fingering of silicone oil in spin coating (22)); adhesives (penetrating air into oil during lifting a circular cell (37)). Displacement flows sometimes occur in industrial processes where it is essential to remove a gelled-like material (i.e., typically viscoplastic) from interior geometries. Examples include: oil & gas well cementing (displacement of drilling mud by cement slurry in annulus (38; 6)); gas-assisted injection molding (plastic manufacturing (41)); biomedical applications (propagation of a liquid bolus along a tube (24) and clearing of mucus plugs in alveoli (25)); cleaning of equipments, environmental surfaces and stubborn soil (8); food processing (rinsing pipes and cleaning processing machineries (62; 18)); waxy crude oil pipeline restarts (cleaning the paraffin of crude oil from pipelines (59)); biofilms applications (biological and biotechnological polymer gels (11)). The fluids involved in these processes can have different properties, e.g., different densities. Displacement flows between miscible liquids frequently occur. Typical flow geometries include pipe, annulus, channel, etc. In this work, we numerically consider buoyant miscible displacement flows of a viscoplastic fluid by a Newtonian one, where the imposed flow is laminar.

A miscible displacement flow, i.e., the focus of our work, is fundamentally different from an immiscible one. When the displacing and displaced fluids are immiscible (i.e., $\hat{\sigma} > 0$, with $\hat{\sigma}$ being the surface tension coefficient), the density and viscosity remain constant in each phase and a pressure jump at the interface is considered. However, when the displacing and displaced fluids are miscible, there is no interface, *per se*, between the phases so that diffusion and mixing between them need to be considered. In this case, a relevant dimensionless flow parameter is therefore the Péclet number, Pe, (see Table 4.1 for the definition), which represents the ratio between advective and molecular diffusive transports. The diffusion between the displacement flow phases becomes important when Pe is small, while at large Pe the degree of molecular diffusive transport compared to advective transport is very small, implying that the two fluids do not have sufficient time to mix in a typical displacement flow process. Previous studies (45; 9) have shown that, in the absence of flow instabilities, the flow at high-Pe approaches its immiscible counterpart at the zero surface tension limit ($\hat{\sigma} \to 0$) and consequently the interface between the two fluids remains quite sharp. Knowing that many of displacement flow applications occur at large Pe, from a modeling perspective, $Pe \to \infty$ provides a good approximation to the flow behaviors. Note that the fluids can still mix due to hydrodynamic effects (e.g., instabilities, secondary flows). In a numerical framework, mixing at the grid level is dominated by numerical diffusion.

Buoyant miscible displacement flows for Newtonian fluids have been studied in detail, for various flow geometries such as circular pipes, 2D channels and Hele-Shaw cells. Here, we briefly review a few of the relevant studies. For example, Seon *et al.* (50) have studied these flows at the limit of zero imposed flow velocity (i.e., an *exchange* flow) in inclined pipes, revealing the competition between buoyant, viscous and inertial forces that result in the formation of various flow regimes (e.g., a viscous-dominated or an inertial-dominated regime). In a series of studies, Taghavi *et al.* (57; 56; 54) have considered numerically, analytically and experimentally buoyant miscible displacement flows in near-horizontal pipes and 2D channels, for a wide range of flow parameters (e.g., Re, Fr and pipe/channel inclination), and they have quantified the appearance of different flow regimes when an imposed flow is added to an exchange flow. Earlier studies such as Chen & Meiburg (9) have analyzed displacement flows in capillary tubes at the limit of high-Pe, using numerical approaches. Sahu *et al.* (49) have considered these flows along inclined channel, finding that mixing and displacement rates are improved with increasing Fr and the density ratio between the two fluids. Amiri *et al.* (5) have recently focused on vertical pipe flows, observing a stabilizing effect of the imposed flow for small density differences.

Due to complex rheological behaviors of non-Newtonian fluids, the literature of non-Newtonian displacement flows is less developed compared to that for Newtonian fluids. For these flows, a majority of studies concern the well-known Saffman-Taylor instability (or the *viscous fingering* instability) and the associated pattern formations in the Hele-Shaw geometry (see review by McCloud (33)). The effects of various non-Newtonian parameters, such as yield stress (28; 31; 12; 43), shear-thinning (60; 16; 7), shear-thickening (16; 36; 7), elasticity (32; 26) and elaso-visco-plastic properties (15), on displacement flows have been investigated numerically, experimentally and analytically. Fluid viscoelasticity has been shown to create peculiar patterns and affect the efficiency of displacement flows. Interfacial instabilities for viscoplastic displacements have been studied first by Pascal (43; 42; 44) in the context of porous media. The Hele-Shaw cell viscoplastic displacement regimes have been classified by Lindner *et al.* (28; 29), who have shown that at low imposed flow rates yield stress effects are dominant and ramified structure patterns are formed. At high imposed flow rates, viscous effects are dominant and smooth displacing fingers appear (28; 31). At extremely high imposed flow rates, yield stress effects are completely eliminated and side-branching patterns are exhibited (28; 31; 15).

Non-Newtonian displacement flows in geometries other than the Hele-Shaw cell have been less explored. de Sousa *et al.* (13) numerically analyzed displacement flows of viscoplastic materials in capillary tubes. They found that the value of residual layers of viscoplastic fluids on the wall is decreased by increasing the dimensionless yield stress value. Freitas *et al.* (17) studied immiscible viscoplastic-viscoplastic displacement flows in a capillary plane channel, using numerical approaches. They showed that the dimensionless yield stress number of the displaced fluid (with respect to the one of the displacing fluid) has a significant impact on the residual layer thickness. Gabard & Hulin (19) studied the effects of non-Newtonian rheology on vertical tube displacements. They showed that the transient residual film thickness for shear-thinning fluids is larger than that for viscoplastic fluids. Papaioannou *et al.* (40) studied displacement of a viscoplastic fluid by air in a pipe, demonstrating that a detachment of the viscoplastic material from the solid wall can take place at sufficiently large Bingham numbers (see Table 4.1). Swain *et al.* (51) studied computationally viscoplastic displacement flows in 2D channels. They showed that interfacial instabilities are decreased by increasing the yield stress and the flow index (which characterizes the shear-thinning tendency) of the displaced fluid. In addition, they mentioned that increments in the flow index lead to increasing the size of the unyielded region. Dimakopoulos & Tsamopoulos (14) considered the displacement of a viscoplastic material by a Newtonian fluid in straight tubes (symmetric) and suddenly constricted tubes (asymmetric). They found that unyielded regions arise in front of the displacing fluid and near the recirculation corners for straight and constricted tubes, respectively. Moisés *et al.* (34) experimentally investigated the residual layer variation amplitude in a horizontal pipe when a Newtonian fluid displaces a viscoplastic fluid. They found that the competition between the ratio of inertia to viscous forces of the viscoplastic fluid leads to three different flow regimes, with smooth, wavy or corrugated interface, respectively. Taghavi *et al.* (55) studied semi-analytically heavy-light & light-heavy displacements of viscoplastic fluids in near-horizontal 2D channels. They demonstrated that a yield stress in the displacing fluid enhances the displacement flow efficiency and a yield stress in the displaced fluid leads to decreasing the displacement flow efficiency. Taghavi *et al.* (53) and Alba *et al.* (2) performed experiments for yield stress fluid displacement flows, at near-horizontal and highly-inclined pipes, respectively. They analyzed displacement flow exotic patterns at the condition when the yield stress in the displacing fluid is much larger than the typical viscous stress. They identified two different patterns for heavy-light displacement flows: (1) a *center*-type and (2) a *slump*-type displacement flow regime, based on the density ratio between the two fluids. The experimental-theoretical approach of Alba & Frigaard (1) confirmed the formation of the two aforementioned flow patterns for these fluids. In addition, they found that the front velocity in the slump-type case is larger than the center-type case.

A crucial aspect associated of viscoplastic displacements is the formation of static residual layers of the displaced fluid on the walls of the flow geometry. These layers are hard-to-remove especially from interior sections. The phenomenon of static residual layers usually occurs when the yield stress of the displacing fluid is smaller than that of the displaced fluid (4). A relevant early work in this context is that of Poslinski *et al.* (46), who experimentally studied the displacement of a viscoplastic fluid by a Newtonian fluid (air) in a tube, finding that the residual layer thickness is much larger in comparison with Newtonian fluids (increasing up to 0.35 of the tube radius at high imposed flow rates). Allouche *et al.* (4) showed that, unlike Newtonian fluids, the residual wall layers for viscoplastic fluids can be completely static due to their yield stress. Using a combined theoretical and computational approach, they quantified the residual wall layer thickness for a symmetric displacement flow of two Bingham fluids flowing in a 2D channel. Wielage-Burchard & Frigaard (61) studied computationally the effects of the Reynolds number (Re), the Bingham number (Bn) and the viscosity ratio (m) on the static layer thickness for iso-dense displacements. They mentioned that the static residual wall layers are quasi-uniform, but they did not provide information about the location/time of the appearance of these layers. Mollaabbasi and Taghavi (35) analytically studied viscoplastic fluid displacement flows in non-uniform 2D channels, showing that the channel convergence/divergence decreases/increases the static residual wall layer thickness.

The outline of this manuscript is as follows. Below in §4.4, the problem setting is discussed. The details of the computational methodology and the benchmarking of our code are explained in §4.5. Our main results are presented in §4.6. The paper ends with a brief summary in §4.7.

4.4 Problem setting

Our computational study was performed in a plane channel, as represented in Fig. 4.1. Figure 4.1a shows a schematic of the flow geometry, with the initial flow configuration and the notation used in this manuscript. The displacement of a Bingham fluid (fluid L in Fig. 4.1) by a

Newtonian one (fluid H in Fig. 4.1) along a channel of width $\hat{D}$ is considered.[1] The viscosity ratio (m), defined as the ratio of the plastic viscosity ($\hat{\mu}_L$) to the Newtonian fluid's viscosity ($\hat{\mu}_H$), is one. The fluids have different densities: the displacing fluid is denser than the displaced fluid. After the onset of displacement flow, the displacement flow configuration has two fronts: a *leading* front and a *trailing* front, as depicted in Fig. 4.1b. Cartesian coordinates $(\hat{x}, \hat{y})$ are considered with $\hat{x}$ representing the stream-wise direction. The dimensionless equations of motion are

$$[1+\phi At]Re\left[\frac{\partial}{\partial t}\mathbf{u}+(\mathbf{u}.\nabla)\,\mathbf{u}\right] = -\nabla p+\nabla.\boldsymbol{\tau}+\frac{\phi Re}{Fr^2}\mathbf{e}_g, \tag{4.1}$$

$$\nabla.\mathbf{u} = 0, \tag{4.2}$$

$$C_t+\mathbf{u}\cdot\nabla C = \frac{1}{Pe}\nabla^2 C, \tag{4.3}$$

where $\mathbf{u}$, p and $\boldsymbol{\tau}$ are the velocity, the pressure and the deviatoric stress, respectively. Here $\mathbf{e}_g = (0,-1)$ and the function $\phi(C) = 2C-1$ varies linearly between -1 and 1 for $C \in [0,1]$. No slip boundary conditions are applied at the walls. The fully developed velocity profile (plane Poiseuille profile) and the outflow boundary conditions are prescribed at the inlet ($x = -L/4$) and the outlet ($x = 3L/4$) of the channel, respectively.

The governing dimensionless numbers that appear in (4.1-4.3) are the Reynolds number (Re), the densimetric Froude number (Fr), the Atwood number (At) and the Péclet number (Pe). The Atwood number is a dimensionless density difference, shown as $At = (\hat{\rho}_H-\hat{\rho}_L)/(\hat{\rho}_H+\hat{\rho}_L)$, in which the density of the displacing fluid is represented by $\hat{\rho}_H$ and that of the displaced fluid by $\hat{\rho}_L$. Since $\hat{\rho}_H > \hat{\rho}_L$ (i.e., the heavy fluid pushes the light fluid), $At > 0$ in this paper. In addition, displacement flows with small density differences are considered, for which the Boussinesq approximation is implemented. The other parameters are defined in Table 4.1.

The constitutive law for the displacing Newtonian fluid is presented as $\tau(\boldsymbol{u}) = \dot{\gamma}(\boldsymbol{u})$ with $\dot{\gamma} = \nabla\mathbf{u}+(\nabla\mathbf{u})^T$. For the displaced Bingham fluid, the constitutive law includes a yield stress and it is written as

$$\tau_2(\mathbf{u}) = m\left[1+\frac{Bn}{\dot{\gamma}(\mathbf{u})}\right]\dot{\gamma}(\mathbf{u}) \Leftrightarrow \tau_2(\mathbf{u}) > mBn, \tag{4.4}$$

$$\dot{\gamma}(\mathbf{u}) = 0 \Leftrightarrow \tau_2(\mathbf{u}) \leq mBn, \tag{4.5}$$

where the second invariants, $\dot{\gamma}(\mathbf{u})$ and $\tau_2(\mathbf{u})$, are defined by

$$\dot{\gamma}(\mathbf{u}) = \left[\frac{1}{2}\sum_{i,j=1}^{2}[\dot{\gamma}_{ij}(\mathbf{u})]^2\right]^{1/2},$$

$$\tau_2(\mathbf{u}) = \left[\frac{1}{2}\sum_{i,j=1}^{2}[\tau_{2,ij}(\mathbf{u})]^2\right]^{1/2}, \tag{4.6}$$

1. In this paper we adopt the convention of denoting dimensional quantities with the ˆ symbol and dimensionless quantities without.

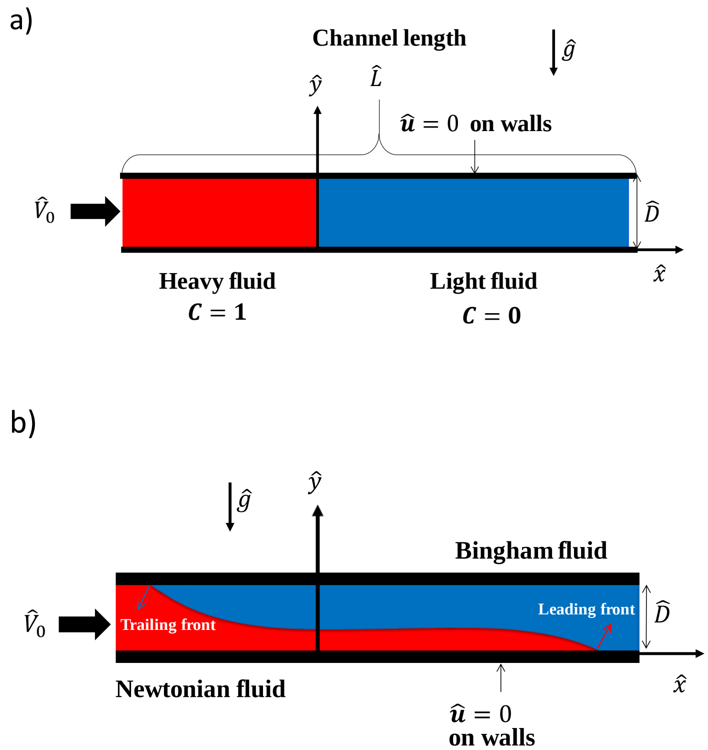

FIGURE 4.1 – Schematic view of the numerical domain (a) at the initial flow configuration and (b) after the onset of displacement flow.

where m is the viscosity ratio. Table 4.1 shows the ranges of the dimensionless parameters used in our work. As can be seen, our study (with ~ 400 simulations performed) covers a wide range of these parameters.

4.5 Computational code

The system (4.1-4.5) was discretized using a mixed finite element-finite volume method, using the classical augmented Lagrangian approach of (20) to resolve unyielded zones. More details of the numerical method are explained in (61; 48). The present numerical algorithm was implemented in C++ and solved using PELICANS (available at https://gforge.irsn.fr/gf/project/pelicans/), which is an open source, object oriented platform to solve PDEs. PELICANS is shared under the CeCILL free software license agreement (http://www.cecill.info/licences/Licence_CeCILL_V2-en.html, 2010). More details about using this platform for displacement flow simulations are given in (57; 61).

In our simulations, 63,000 mesh cells (1500 × 42) were typically used while the meshes (regular rectangular) in the y-direction were refined slightly towards the channel walls. The initial

Parameter	Name	Definition	Range or value
Bn	Bingham number	$\frac{\hat{\tau}_y \hat{D}}{\hat{\mu}_L \hat{V}_0}$	0 – 200
Fr	Densimetric Froude number	$\frac{\hat{V}_0}{\sqrt{At\hat{g}\hat{D}}}$	0.1 – 1000
m	Viscosity ratio	$\frac{\hat{\eta}_L}{\hat{\eta}_H}$	1
Re	Reynolds number	$\frac{\hat{V}_0 \hat{D}}{\hat{\nu}}$	50 – 500
δ	Aspect ratio	$\frac{\hat{L}}{\hat{D}}$	100
Pe	Péclet number	$\frac{\hat{V}_0 \hat{D}}{\hat{D}_m}$	$\gg 1$

TABLE 4.1 – Definitions and ranges of the dimensionless parameters used in this manuscript. Here, $\hat{V}_0$ is the mean imposed velocity. In the definition of the Reynolds number, $\hat{\nu} = \hat{\eta}_H/\hat{\rho}$ with $\hat{\eta}_H$ being the viscosity of the heavy fluid and $\hat{\rho} = (\hat{\rho}_L + \hat{\rho}_H)/2$. In the definition of the Péclet number, $\hat{D}_m$ is the molecular diffusivity. m is 1 everywhere, unless otherwise stated. Hereafter, the densimetric Froude number, denoted by Fr, is called the Froude number for convenience.

interface between the two fluids was placed at distance $L/4$ from the channel inlet in the computational domain (see also Fig. 4.1a).

The most obvious global feature of the displacement flow is the average value of the concentration, defined as

$$\bar{C}(t) = \frac{1}{L} \int_0^1 \int_{-L/4}^{3L/4} C(x,y,t) dx dy. \tag{4.7}$$

For different mesh densities, the dependency of $\left(1 - \bar{C}(t)\right) / \left(1 - \bar{C}(0)\right)$ and the position of the displacing front, x_{front}, for parameters $Bn = 100$, $Re = 50$ and $Fr = 1000$, are given in Fig. 4.2a and 4.2b, respectively. Obviously at $t = 0$, the quantity $\left(1 - \bar{C}(t)\right) / \left(1 - \bar{C}(0)\right)$ approaches unity and it decreases with time as more displacing fluid (with $C = 1$) is introduced into the computational domain. As can be seen, for small mesh sizes, a good convergence for the variation of $\left(1 - \bar{C}(t)\right) / \left(1 - \bar{C}(0)\right)$ is achieved.

As Fig. 4.1a illustrates, initially (at $t = 0$) an imaginary gate valve separates the two fluids at $x = 0$, meaning that interface between two fluids is distinct and sharp at the beginning of the displacement process. At $t > 0$, due to the mean imposed flow rate, the heavy layer starts to push the light fluid. Initially, the axial position of the displacing front (x_{front}) is zero and as the time progresses the distance between x_{front} and the initial interface position increases. Fig. 4.2b displays x_{front} versus time for the same mesh densities as in Fig. 4.2a. It is evident that the position of the displacing front varies only slightly with the mesh sizes chosen. Comparing 13,600 mesh cells (400 × 34) to 71,400 mesh cells (2100 × 34), the maximum relative error is 3.81% for the final value of displacing front position. Mesh refinement from 1500 × 42 to 2100 × 34 leads to a small deviation of 0.75%.

Moreover, to illustrate that our results are not affected by the mesh density, simulations with two different mesh densities are performed. Fig. 4.2c and Fig. 4.2d display the concentration colormaps, at different times for Bn = 100, Re = 300 and Fr = 0.1, for 63,000 mesh cells (1500 × 42) and 71,400 mesh cells (2100 × 34), respectively. For these conditions, the front detachment phenomenon (due to flow instabilities) is observed. As seen, there exists good agreement between the results of the two simulations, in which the mesh refinement results in a small deviation of 1.54% in the mean wavelength of 10 interfacial waves (closest to the channel end) at t = 40.

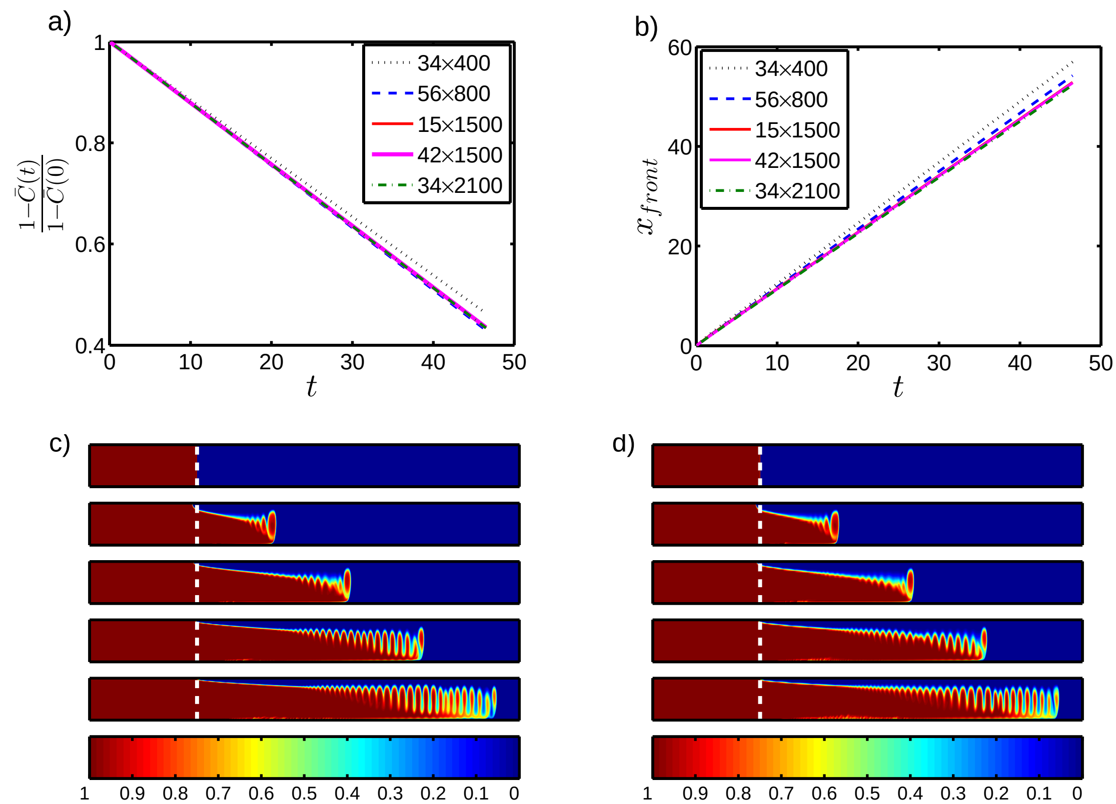

FIGURE 4.2 – (a) Evolution of $\frac{1-\bar{C}(t)}{1-\bar{C}(0)}$ versus time for different mesh sizes for Bn = 100, Re = 50 and Fr = 1000. (b) Evolution of the position of the displacing front, x_{front}, versus time for different mesh sizes for the same simulation. (c)&(d) Concentration colormaps at $t = [0, 10, ..., 40]$ for Bn = 5, Re = 200 and Fr = 0.5 for the mesh size (c) 1500 × 42 and d) 2100 × 34. The domain size shown is 1 × 100.

4.5.1 Code benchmarking

We have validated our code by comparing our results against those obtained in Taghavi *et al.* (52; 54) and Alba *et al.* (3) for Newtonian displacement flows. For the Bingham fluids, we have benchmarked our code against the results of Wielage-Burchard & Frigaard (61), who considered iso-dense displacement flows of a Bingham fluid (i.e., $Fr \to \infty$). Fig. 4.3a shows an example where our results are compared against those of Wielage-Burchard & Frigaard (61), with $Re = 100$, $Fr = 1000$. As can be seen, the results obtained from our code follow precisely the results presented in (61). Fig. 4.3b shows a qualitative comparison against the results of Swain *et al.* (51), who investigated the displacement flow of a viscoplastic fluid by a lighter Newtonian fluid in a 2D channel via a multiphase lattice Boltzmann method. This subfigure shows the concentration colormaps of a displacement flow in a horizontal channel for $Bn = 10$, $Re = 100$, $m = 2$ and $Fr = 7.071$ (note that for comparison against the results of Swain *et al.* (51), we have performed a light-heavy displacement simulation). The overall behaviors are quite similar to those reported in Fig. 2 given in (51): due to the imposed flow, first the displacing finger penetrates into the bulk of the displaced fluid in a symmetric way but soon the finger becomes slightly asymmetric under the effect of gravity. In addition, we observe the appearance of *Kelvin-Helmholtz*-like instabilities, more or less in the same spatial locations as in (51).

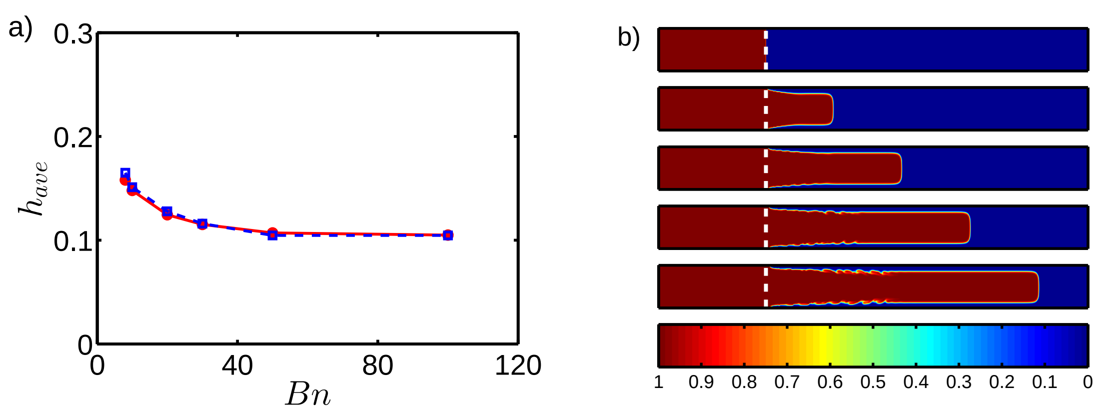

FIGURE 4.3 – Code benchmarking: (a) The average static residual wall layer thickness, $h_{ave} = (h_u + h_l)/2$, from our simulation ($\square$) at $Re = 100$ and $Fr = 1000$ against the results of (61) ($\bullet$) for $Re = 100$ and $Fr = \infty$. (b) Concentration colormaps of the displacement flow at times $t = [0, 7, ..., 28]$ for $Bn = 10$, $Re = 100$, $m = 2$ and $Fr = 7.071$. The last image at the bottom of the subfigure is the colorbar of the concentration values (here and elsewhere). The white broken lines display the position of the initial interface $x = 0$ (here and later). The domain size shown is 1×100 (unless otherwise stated). The images in this subfigure can be qualitatively compared with Fig. 2 in (51). To validate the code against the results of Swain *et al.* (51), we have exceptionally considered a light-heavy displacement flow.

4.6 Results and discussions

In this section, we present and discuss our main findings for a wide range of the flow parameters. In a typical simulation, as time progresses, depending on the imposed mean velocity, the heavy fluid penetrates into the light fluid and displaces it. During the displacement process, various interesting patterns are formed at the interface between the two fluids, which we will explain below in more detail. Our simulation results can be divided in three subcategories: i) quantifying static residual wall layers; ii) quantifying the main displacement flow regimes; and iii) analyzing displacement front velocities.

4.6.1 Note of the effects of Bn on displacement flows

Before we proceed with presenting various flow features in the following subsection, it is worth discussing general effects of considering a yield stress fluid as the displaced entity in place of a Newtonian fluid. This can help clarify two aspects: (a) the difference of our work with the large body of recent computational studies, considering Newtonian displacements in channels; (b) general effects that could be expected before analyzing all the simulations results.

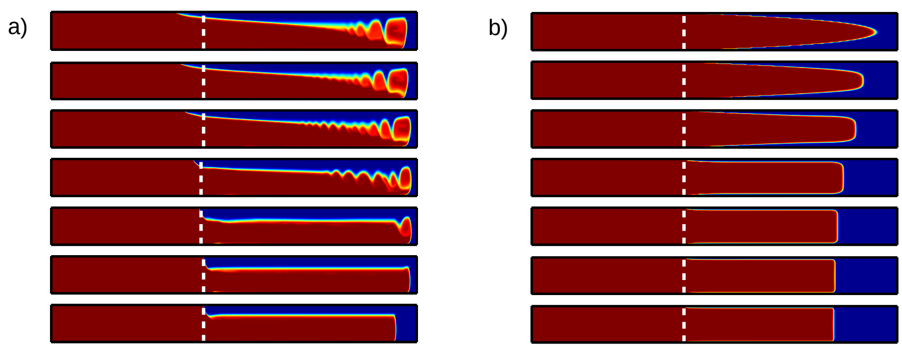

FIGURE 4.4 – Panorama of concentration colormaps at $t = 16$ and $Re = 400$ for (a) $Fr = 0.5$ and (b) $Fr = 100$. The rows from top to bottom show $Bn = 0$, $Bn = 2$, $Bn = 5$, $Bn = 20$, $Bn = 50$, $Bn = 100$, $Bn = 200$. The domain size shown is 1×60.

Fig. 4.4 presents panoramas of the concentration colormaps at a given time, for fixed Re and Fr. By increasing Bn, the displacement flow morphology changes significantly. Fig. 4.4a shows that, at small Fr, by increasing Bn the interfacial instabilities decrease and the yield stress damps the interfacial waves. In addition, the trailing front, which moves upwards at small Bn, completely stops moving at larger Bn. However, the variation in Bn does not seem to influence the slumping form, which is close to a 2-layer flow. Finally, as will be illustrated in the following sections, at large Bn the displaced layer above the displacing finger becomes static (motionless).

Fig. 4.4b shows that, at large Fr, at $Bn = 0$ (i.e., the Newtonian limit) the displacement is nearly symmetric (e.g., the displacing finger advances approximately along the center of the channel) and that the displacing finger resembles a Poiseuille-like profile. At larger Bn, the flow remains symmetric, although the front shape changes and resembles a plug-like profile. Moreover, while at $Bn = 0$ there are no static wall layers, these layers are formed at larger Bn. The thickness of the static layers seems to decrease with Bn.

4.6.2 Static residual wall layers

As discussed in the introduction section, static residual wall layers are of great significance in viscoplastic fluid displacement flows. In this subsection, we focus on describing qualitative and quantitative features of these layers in our computational results.

Fig. 4.5 shows examples of our results, for $Bn = 50$, $Re = 500$ and $Fr = 1$. Initially at $x = 0$, the displacing and displaced fluids are completely separated by an imaginary gate valve. As time grows, due to a combined effect of the imposed flow and the density ratio, the heavy fluid penetrates through the light fluid and attempts to push it out of the channel. Fig. 4.5a displays the concentration colormaps of the displacement flow for various times. As can be seen in this subfigure, at longer spatial positions with respect to the initial gate valve, the displaced layers adjacent to the walls become apparently static. Accordingly, the displacing finger moves in a narrower channel (created by the upper and lower static layers) and advances significantly faster than the mean imposed flow. Fig. 4.5b shows the shear stress colormaps at the same times as the colormaps of concentration, revealing that the stress field asymmetry results in asymmetric static layers on the top/bottom walls.

For convenience, let us call the spatial locations where the static residual layers become uniform as the upper static distance (x_u) and the lower static distance (x_l), for upper and lower static residual layers, respectively. Similarly, let us call the associated uniform static layer thicknesses as the upper static layer thickness (h_u) and the lower static layer thickness (h_l). In order to better understand the definitions of h_u, h_l, x_u and x_l, at a given large time (here $t = 40$), they are plotted in Fig. 4.5c, where a few velocity vectors are also plotted. As seen, the displaced fluid layers close to the top and lower walls are entirely static, where the concentration of displacing fluid is zero. This means that the displaced fluid layers have a zero velocity and therefore h_u and h_l can be computed. Initially, the static layer thicknesses vary with x but reach plateau values after certain distance x, where uniform static residual layers in the upper and lower walls appear.

Fig. 4.5d shows the speed contours, $V = \sqrt{{V_x}^2 + {V_y}^2}$, at $t = 40$, where V_x and V_y denote the stream-wise and depthwise velocity components, respectively. The velocity profile is evidently similar to a Poiseuille profile before the gate valve location such that the high speed regions remain towards the channel center. After the gate valve, the speed contours are zero within the displaced fluid layers adjacent the upper and lower walls, which means that the remaining

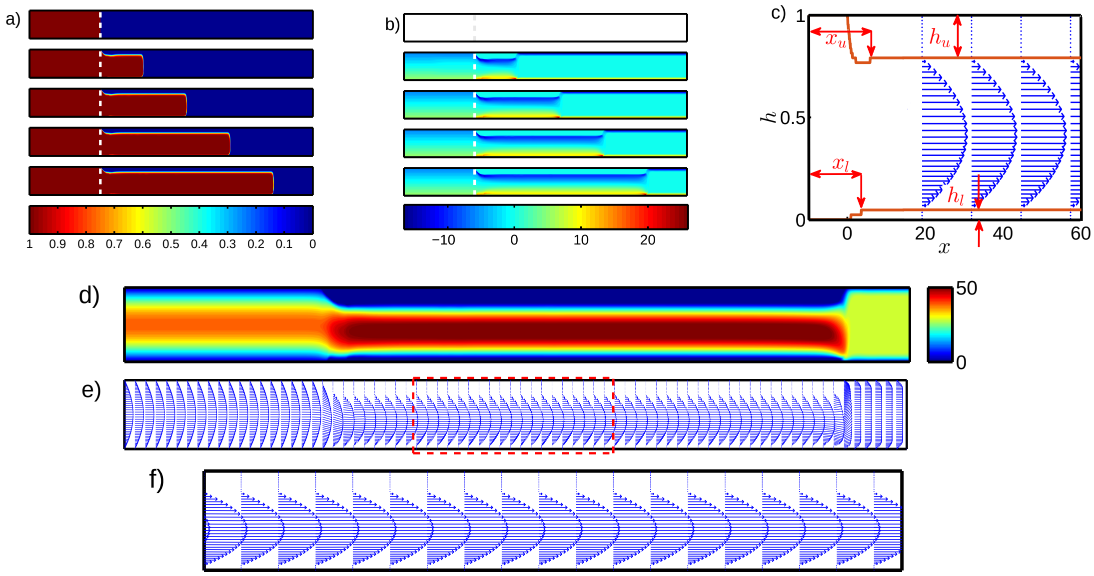

FIGURE 4.5 – Computational results for Bn = 50, Re = 500 and Fr = 1; (a) Concentration colormaps at times $t = [0, 10, ..., 40]$; (b) Shear stress colormaps at times $t = [0, 10, ..., 40]$; (c) Interface heights (lower and upper layers) at $t = 40$: h_u and h_l show the thickness of upper and lower static layers, respectively. The red arrows indicate the position at which uniform static layers appear, with x_u indicating the upper static distance and x_l the lower static distance. (d) Speed contours: $V = \sqrt{{V_x}^2 + {V_y}^2}$. (e) Velocity vectors. (f) The image is zoomed-in on the indicated box of subfigure (e).

displaced layers are completely static. Fig. 4.5e and Fig. 4.5f show the velocity vector fields along the channel length, confirming that the existence of completely static residual layers wherein the velocity is zero. It should be noted that the velocity profiles within the displaced fluid further downstream (where the displacing front has not reached) are similar to a typical *plug-type* profile of a Bingham fluid in a channel. The velocity profiles of displacing fluid in the finger are similar to a stable viscous profile over a narrower channel; however, inertial effects exist at the displacing front.

Our study is mainly governed by Re, Bn and Fr. Thus, it is logical to attempt to quantify the effects of these parameters on the upper and lower static residual layers in our displacement flows. Fig. 4.6 shows the effects of varying the Bingham number on the thicknesses of the upper and lower static residual layers, for various Reynolds and Froude numbers. There are missing data for certain flows at very small Froude numbers for which there are no uniform static residual layers formed. The subfigures demonstrate that for a wide ranges of Re and Fr, increasing Bn generally results in decreasing both h_u and h_l. In fact, increasing Bn of the displaced fluid influences the plug ahead of the displacing finger and results in a reduction of the static residual wall layer thickness (61). The subfigures in Fig. 4.6a show that the upper static residual layer thickness decreases as Fr increases, whereas the ones in Fig. 4.6b show that

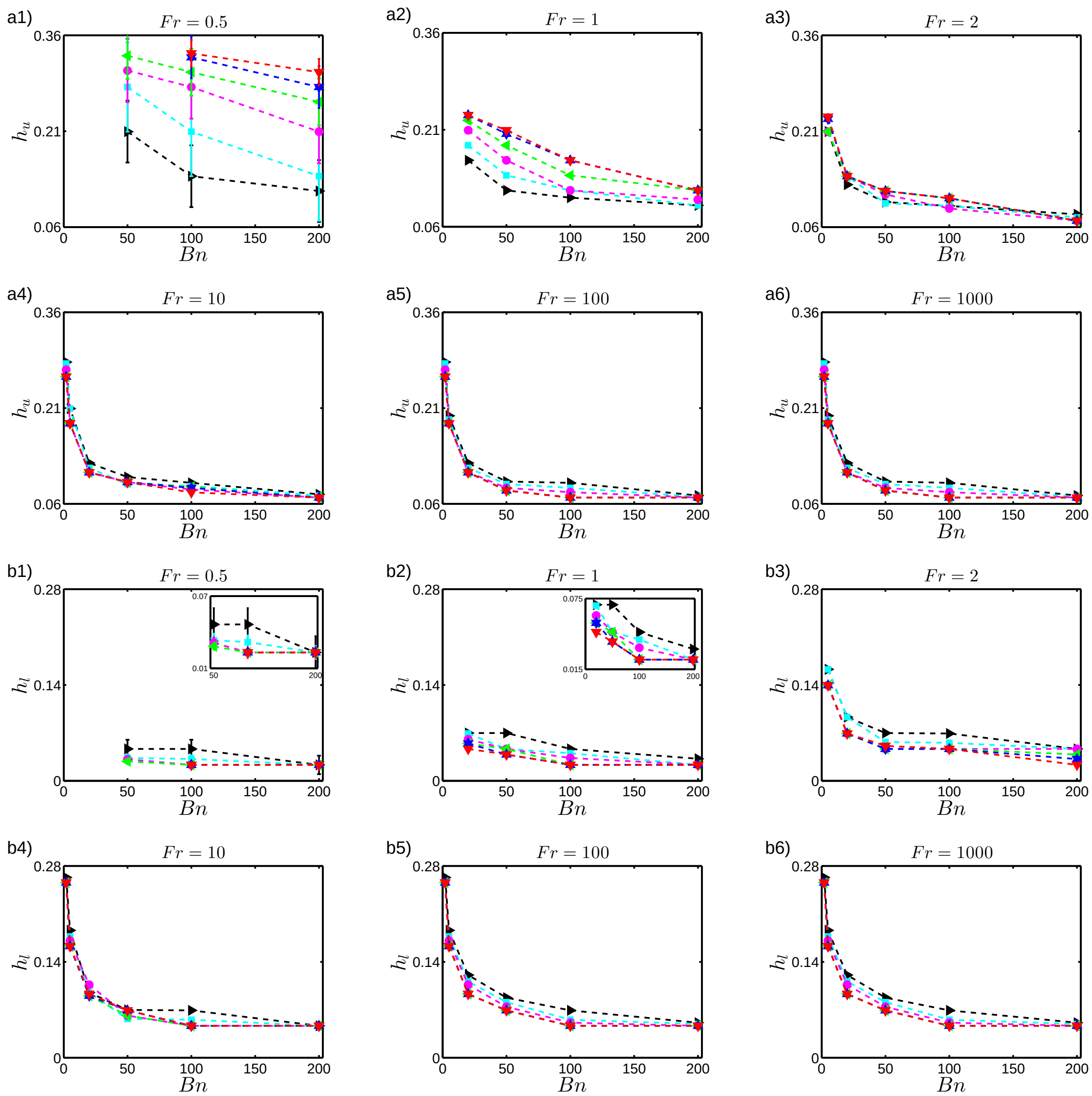

FIGURE 4.6 – Effects of Bn, Fr and Re on static residual layer thicknesses: (a) h_u and (b) h_l. The data correspond to Re = 50 (▸), Re = 100 (■), Re = 200 (•), Re = 300 (◂), Re = 400 (⋆) and Re = 500 (▼). In this and the following figures, the error-bars (estimated through the standard deviation of the static layer thicknesses) are shown in one graph only, while the error-bars of the other data are more or less similar (not shown). The insets are zoomed at the variation of the lower static thickness.

the lower layer thickness is enhanced by increasing Fr. These effects may be expected since increasing Fr is equivalent to decreasing the density difference, an effect which progressively pushes the displacing finger towards the channel center.

Comparison among different subfigures in Fig. 4.6a and Fig. 4.6b reveals useful information. For example, for various Fr the effect of Re on h_u is not monotonic: h_u increases by increasing Re at small Fr, while h_u decreases by increasing Re at large Fr. The effect of Re on h_l is more or less monotonic such that by increasing Re, h_l decreases for all values of Fr.

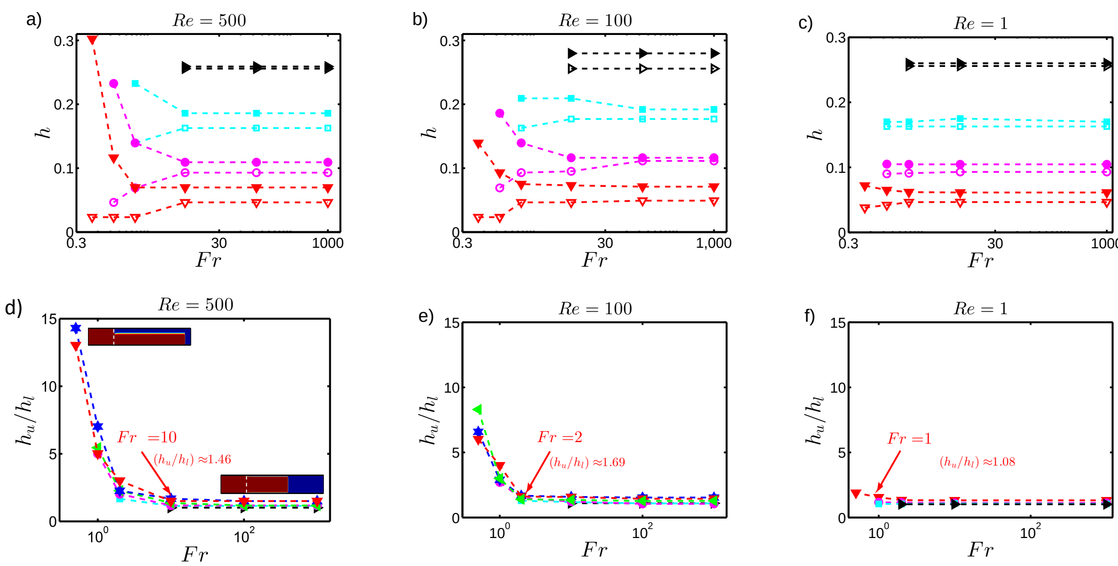

FIGURE 4.7 – The upper row shows the variation of h_u (filled symbols) and h_l (hollow symbols) versus Fr for different values of Bn at: (a) Re = 500; (b) Re = 100; (c) Re = 1. The lower row shows the variation of h_u/h_l versus Fr for: (d) Re = 500; (e) Re = 100; (f) Re = 1. The data correspond to Bn = 2 (▸), Bn = 5 (■), Bn = 20 (●), Bn = 50 (◂), Bn = 100 (⋆), Bn = 200 (▼).

In order to better observe some of the effects explained, Figs. 4.7a-c show the variations in h_u and h_l for increasing Froude numbers, for different Bn, at fixed Re = 500, Re = 100 and Re = 1. These subfigures show that, for a given Bn, h_u decreases initially with Fr but finally reaches a plateau value. On the other hand, h_l increases by increasing Fr but eventually becomes constant. Although the observed behaviors for h_u and h_l at Re = 500, Re = 100 and Re = 1 are more or less the same, the plateau values are reached at different values of Fr.

The ratio of the upper to lower static layer thickness (h_u/h_l) may help gain further insight about the formation of these layers as well as the overall displacement flow. Fig. 4.7d, Fig. 4.7e and Fig. 4.7f show the variation of h_u/h_l versus Fr for three Re and different Bn. At Re = 500 (Fig. 4.7d), initially h_u/h_l sharply decreases with Fr but eventually reaches a near-plateau value for all Bn. One may find the value of Fr when the plateau state is reached roughly at Fr = 10, where $h_u/h_l \approx 1.46$. As illustrated by the superimposed snapshot images, this transition point also interestingly corresponds to a significant change in the flow morphology: at low Fr (when $h_u \gg h_l$), a *slump-type* displacement regime is observed where the displacing finger is found more or less near the lower wall of the channel; at high Fr (when $h_u \approx h_l$), a *center-type* displacement regime is found where the displacing finger appears approximately in the middle of the channel. For $Re = 100$, as seen in Fig. 4.7e, $Fr = 2$, for which $h_u/h_l \approx 1.69$. Fig. 4.7f displays the variation of h_u/h_l versus Bn for $Re = 1$. At these conditions the flow is more or less symmetric about the channel center and h_u/h_l tends to unity. Two other conclusions drawn from Fig. 4.7d, Fig. 4.7e and Fig. 4.7f can be summarized as: (1) the value of Fr (when the plateau state is observed) is a function of Re and (2) h_u/h_l is more or less independent of Bn.

• **Comparison between our simulations and theoretical models from the literature**:

In recent years, there has been some progress in analyzing static residual layers of viscoplastic fluids. In this subsection, we will explain a few of the previous studies and attempt to make comparison between their findings and our simulation results.

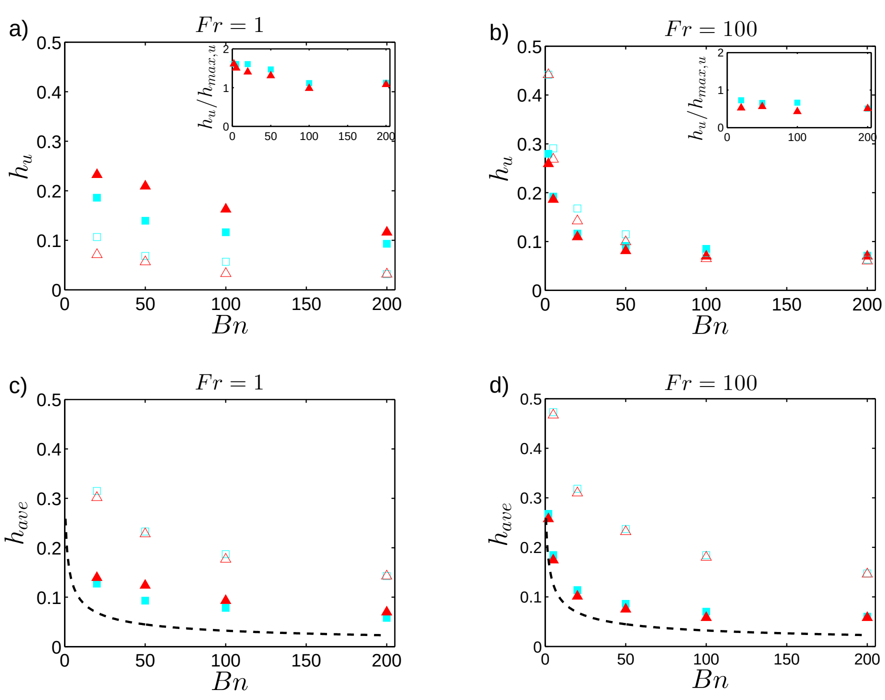

FIGURE 4.8 – Comparison among static layer thicknesses from our simulation results (filled symbols), h_{circ} (dashed line) and $h_{max,u}$ or $h_{max,ave}$ (hollow symbols). The upper row shows h_u and the bottom row shows the mean value of the lower and upper static layer thicknesses ($h_{ave} = \frac{h_u+h_l}{2}$). The data correspond to $Re = 100$ (■) and $Re = 500$ (▲). The insets indicate the ratio of the simulation upper layer thickness to the upper maximal static layer thickness, h_u/h_{max}, versus Bn for the same datapoints as in the main graphs.

Allouche *et al.* (4) were first to rigorously investigate theoretically and computationally static residual wall layers of Bingham fluids. For miscible displacement flows in a 2D channel and in symmetric configurations, they showed that the static wall layer thickness can be predicted via the recirculation layer thickness, h_{circ}, which is a thickness corresponding to a steadily displacing finger advancing with the speed equal to that of the downstream flow center-line. Upon the condition that $h < h_{circ}$, a recirculatory region ahead of the displacing finger would occur, increasing viscous dissipation as a response. Therefore, Allouche *et al.* (4) concluded that the displacement flow adjusts to avoid such situation. h_{circ} is defined by the downstream flow, as follows (4; 61):

$$h_{circ} = 1 - \frac{2Y}{Bn(1-Y)^2}, \tag{4.8}$$

where Y can be found by the solution of

$$Y^3 - 3Y\left[1 + \frac{2}{Bn}\right] + 2 = 0, \tag{4.9}$$

for a given Bn. The aforementioned theory suggests that the residual wall layer thickness has an inverse relation to Bn, which is consistent with our simulation results.

Taghavi *et al.* (55) also studied analytically the maximal static residual wall layer thickness, h_{max}, for 2D viscoplastic displacement flows in a slumping 2-layer configuration. They used a lubrication/thin-film approximation to quantify these layers in near horizontal channel inclinations, showing that, for Bingham fluids, the layer thickness depends on the ratio of the yield stress of the fluids and the ratio of axial buoyancy stress to the yield stress of the displaced fluid. In our context (i.e., a strictly horizontal channel), the axial buoyancy stress, which depends on the interface slope, would be negligible at long times, implying that h_{max} is controlled by the Bingham number only. Here we extend their analysis of h_{max} for our asymmetric configuration. We crudely can assume that the upper maximal static residual wall layer thickness, $h_{max,u}$, is a function of the Bingham number and the centerline of the displacing fluid layer (behind the front) donated as y_0 (obtained from our simulations). Therefore, $h_{max,u}$ can be found as

$$h_{max,u} = (\frac{12 - 12y_0}{Bn})^{1/3}. \tag{4.10}$$

Fig. 4.8a and Fig. 4.8b compare our numerical simulation results of the static layer thickness with $h_{max,u}$, as explained above. It can be seen that, first of all, the variation of our results versus Bn appears to follow the same trend as $h_{max,u}$. However, the results indicate that at small Froude number ($Fr = 1$) the model underestimates the static layer thickness whereas at large Froude number ($Fr = 100$), the model overestimates the static layer thickness. In fact, using $h_{max,u}$ is not a precise model since, among other factors, it does not take into account the recirculatory front region and variation of Fr. Fig. 4.8c and Fig. 4.8d demonstrate that the trends of our results and h_{circ} are similar, both decreasing with Bn. However, the calculation of h_{circ} through the symmetric 3-layer model does not fully agree with our simulation results, at least due to following reasons: First, our flow is asymmetric with the respect to the channel center-line; Second, our simulations are run for a wide range of Fr, which is not included in h_{circ}; Third, our displacement flows are run at considerable Re, which is absent in the analysis of h_{circ}. In addition, $h_{max,ave}$ (extended form the analysis above) is also unable to predict the average static layer thickness.

• **Static layer distance**:

In this subsection, we explain our main findings about the distance from the gate valve where uniform static layers appear in the channel. For a typical simulation, we study the impact of Re, Bn and Fr on the upper and lower static distances.

Fig. 4.9 shows the effects of varying the Bingham number on x_u and x_l for various Reynolds and Froude numbers. For a wide range of Re and Fr, increasing Bn generally results in decreasing both x_u and x_l. This means that for larger Bingham numbers, the static residual layers become uniform closer to the initial interface. Furthermore, by increasing Re generally (not always) x_u and x_l increase. It seems that the locations wherein the uniform static layer appear are controlled by a balance between the yield (stabilizing) and inertial stresses (destabilizing). The interplay between these stresses results in creating uniform static layers such that when the yield stress is large the distance between the imaginary gate valve and the uniform static layers is small and vice versa. Moreover, Fig. 4.9 shows that the variations of x_u and x_l as a function of Re and Bn are monotonic at large Fr, while non-monotonic behaviors are observed at small Fr. The latter slightly strange feature may be attributed to large buoyancy effects.

Fig. 4.10 shows the ratio of lower to upper static distances, x_l/x_u, for different Fr, Bn and Re. The upper row shows that increasing the Froude number (from $Fr = 1$ to $Fr = 100$) leads to the fact that all the curves reach more or less $x_l/x_u \approx 1$, implying that the flow becomes progressively more symmetric as Fr increases (or the density difference decreasing); thus, the uniform static layers are formed at the same upper and lower locations. However, the lower row shows the same trend appears if Bn decreases. Increasing Bn also helps the formation of static layers close to initial interface of two fluids (both x_u and x_l become small). Regarding the effect of Re on x_l/x_u, we have not succeeded to reach to a definitive conclusion.

4.6.3 Main flow regimes

Our displacement flows present a variety of fascinating, complex behaviors; therefore, it is useful to try to classify various flow regime observed.

• **Center-type and slump-type regimes**:

One example of the flow regimes that appear in our simulations is the classification of slump-type and center-type flow regimes, which we briefly explained earlier. In the center-type regime

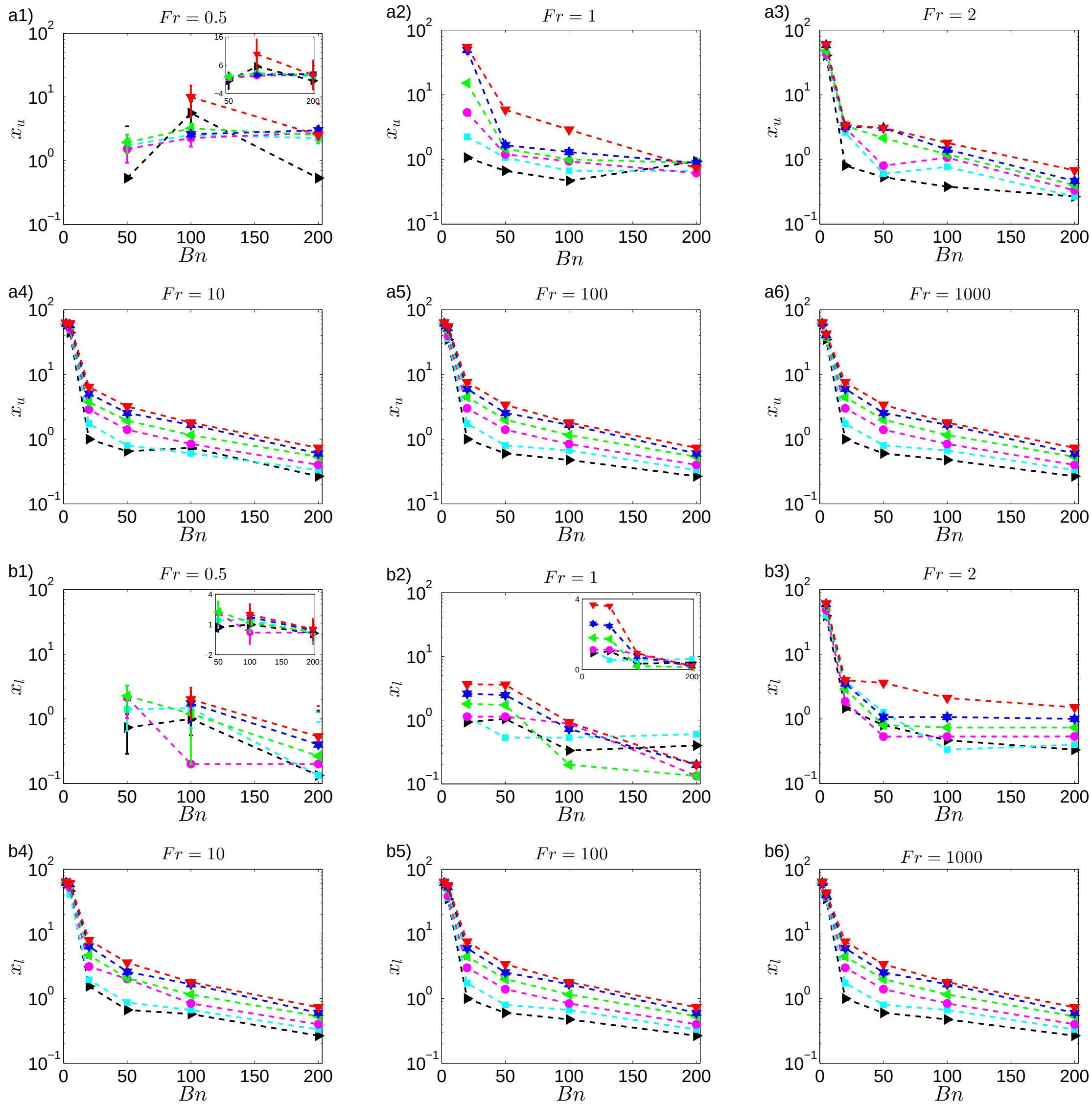

FIGURE 4.9 – Effects of Bn, Fr and Re on (a) x_u and (b) x_l. The data correspond to Re = 50 (▸), Re = 100 (■), Re = 200 (●), Re = 300 (◂), Re = 400 ($\star$), Re = 500 (▼). The insets display the same data as in the main graphs but with a linear scale.

($h_u/h_l \to 1$), the heavy displacing fluid flows as a finger more or less in the middle of the channel, while in the slump-type regime ($h_u/h_l \gg 1$) the displacing layer moves closer to the lower region of the channel, below the bulk of the displaced fluid. We observed that slump-type displacements appear at large density differences (small Fr), more or less independent of Bn. The latter is a feature that has been seen experimentally by Taghavi *et al.* (53), but it has never been quantified computationally. Our simulations show that beyond a transition value of Fr, the ratio of the upper to lower static layer thickness is not much affected by Re and remains at $h_u/h_l \approx 1.6$, on average. We have used this criterion to identify the slump- and center-type regimes. The flow deemed to be slump-type if $h_u/h_l > 1.6$, and is center-type otherwise.

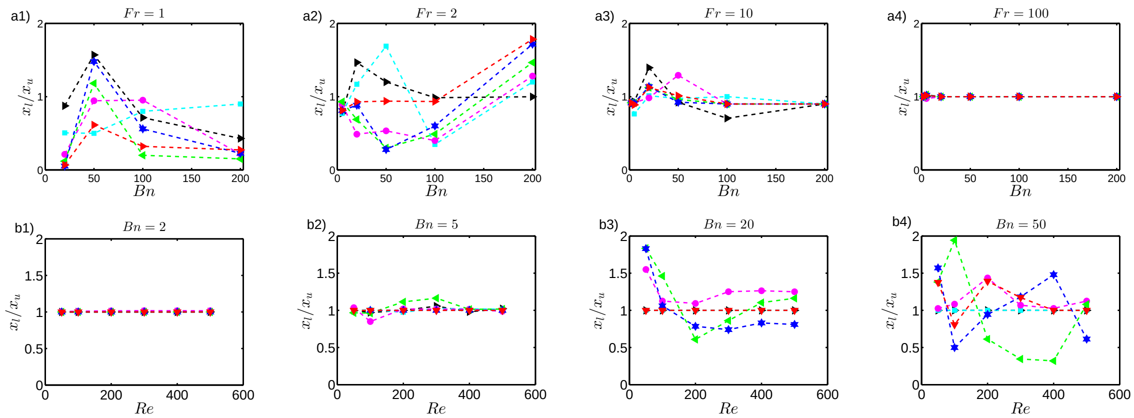

FIGURE 4.10 – The ratio x_l/x_u. In the upper row, the data correspond to $Re = 50$ (▸), $Re = 100$ (■), $Re = 200$ (•), $Re = 300$ (◂), $Re = 400$ (⋆), $Re = 500$ (▼). In the lower row, the data correspond to $Fr = 0.5$ (▸), $Fr = 1$ (■), $Fr = 2$ (•), $Fr = 10$ (◂), $Fr = 100$ (⋆), $Fr = 1000$ (▼).

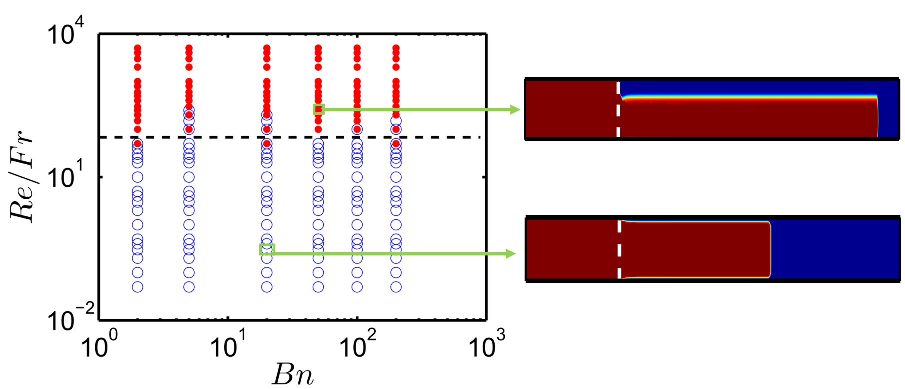

FIGURE 4.11 – Regime classification based on the class of the slump-type (•) and center-type (∘) regimes. The dashed line represents $Re/Fr = 60$. Snapshot images belong to $Bn = 20$, $Re = 500$, and $Fr = 1000$ at $t = 8.9$ (center-type) and $Bn = 50$, $Re = 500$, and $Fr = 2$ at $t = 12.7$ (slump-type).

Fig. 4.11 shows our simulation datapoints that belong to different flow regimes in the plane of Re/Fr and Bn. The slump-type and center-type regimes are marked by different symbols. A horizontal dashed line at $Re/Fr = 60$ is superimposed on this figure, which approximately separates the two regimes. It is interesting to compare the specified value of $Re/Fr = 60$ for displacements in a 2D channel, with the experimental results of Taghavi *et al.* (53), who found the threshold of $Re/Fr = 600$ for circular pipe displacements, i.e. buoyancy is apparently more effective in the channel than the pipe.

• **No-back-flow and temporary-back-flow regimes**:

Another type of flow regime that is phenomenologically important is the class of no-back-flow and temporary-back-flow displacement regimes. In a typical simulation, the leading front always moves forward downstream the channel, advecting a large portion of the displaced fluid outwards. However, the trailing front can move upstream against the direction of the imposed flow, due to buoyancy forces. In our simulations, we have observed two behaviors for the trailing front: i) the trailing front neither moves downstream nor upstream (no-back-flow regime); ii) the trailing front advances upstream against the mean flow but stops and does not significantly move afterwards, for the rest of the simulation time (temporary-back-flow regime). The relevance of back-flow regimes is that they are frequently associated with interfacial instability.

In relation to our work but for Newtonian fluids, Taghavi *et al.* (57) have also studied in depth the movement of the trailing front in displacement flows and they have quantified various possible movements of the trailing front for near-horizontal pipe/channel inclinations.

Fig. 4.12a and Fig. 4.12b show the concentration colormaps as time evolves, for a no-back-flow displacement and a temporary-back-flow displacement, respectively. In Fig. 4.12a the trailing front seems to be pinned to the upper wall, so that its speed is zero throughout the simulation. In Fig. 4.12b, the trailing front initially moves upward but its speed gradually decreases until it becomes zero. The explanation for this behavior may be simple: the buoyancy stress associated to the interface slope is initially large but it decreases as the interface elongates and eventually reaches zero when the interface becomes nearly parallel to the channel walls. Fig. 4.12c and Fig. 4.12d show the spatiotemporal diagram of the depth-averaged concentration values, where the advancement of the trailing and leading fronts with time are clearly observed.

Let us classify our results based on the appearance of the no-back-flow and temporary-back-flow regimes. In order to find the suitable dimensionless groups governing the transition between the no-back-flow and temporary-back-flow displacement flows, various combinations of the dimensionless numbers were examined. Fig. 4.13 classifies the simulation data points in the plane of Fr and Re/Bn, where the two regimes are clearly segregated. Temporary-back-flows are observed for higher Fr. Although at smaller Fr and fixed Re, more temporary-back-flows are observed if Bn decrease, in general the transition between the regimes has only a small dependency on Bn, implying the dominance of a buoyancy-inertia balance (quantified by Fr) for the back flow behaviors.

• **Stable and unstable flow regimes**:

We frequently observe unstable flows in our displacement simulations, forming a variety of flows patterns. Thus, it is useful to study unstable flows in more detail and classify them

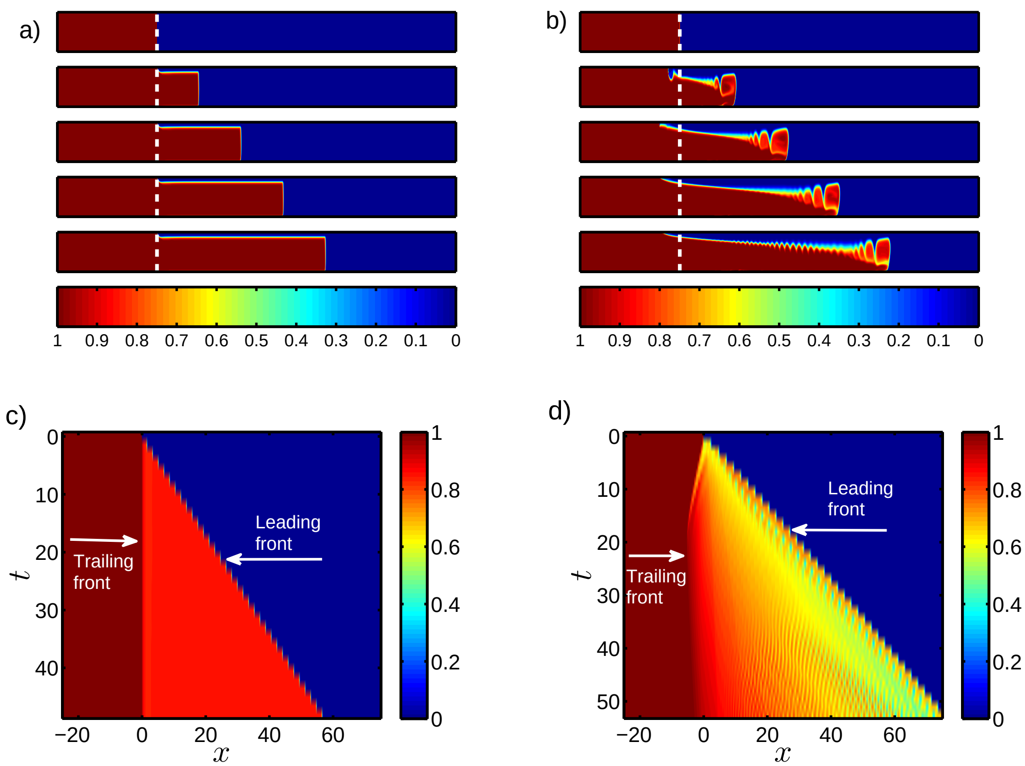

FIGURE 4.12 – Concentration colormaps at $t = [0, 8, ..., 32]$ for (a) $Bn = 200$, $Re = 100$ and $Fr = 0.5$ (a case without a back flow) and (b) $Bn = 2$, $Re = 500$ and $Fr = 0.5$ (a case with a back flow). (c) & (d) Spatiotemporal diagrams of the depth-averaged concentration values for the same simulations as in (a) & (b). The size of the domain shown is 1×76, starting from before the gate valve at $x = -12$.

versus the dimensionless groups.

Fig. 4.14 shows two examples of unstable displacement flows, leading to two different patterns. Concentration colormaps and velocity vectors are shown. At least in their initial stages, the origin of the two forms of instabilities observed can be attributed to Kelvin-Helmholtz-like mechanism. Typically, when instabilities are present in slump-type flows, *sinusoidal* shaped wave regions are observed along the interface between the two fluids. This is demonstrated in Fig. 4.14a, and the wave appear similar in form to internal gravity waves. For center-type flows that are unstable, as demonstrated in Fig. 4.14b, the instabilities arise at two sides of the displacing finger forming symmetric waves. These instabilities grow (often into roll waves) and the fluids eventually mix at the interface. For the case shown in Fig. 4.14b the growths of the interfacial waves become significant at $t \approx 31$.

When buoyant and inertial effects are strong, instabilities can grow significantly, resulting in a pattern that we call *periodic-detachment*. In this flow pattern, large pieces of the displacing fluid are cut from the bulk displacing fluid. Using 7 sequential time frames, Fig. 4.15 details the

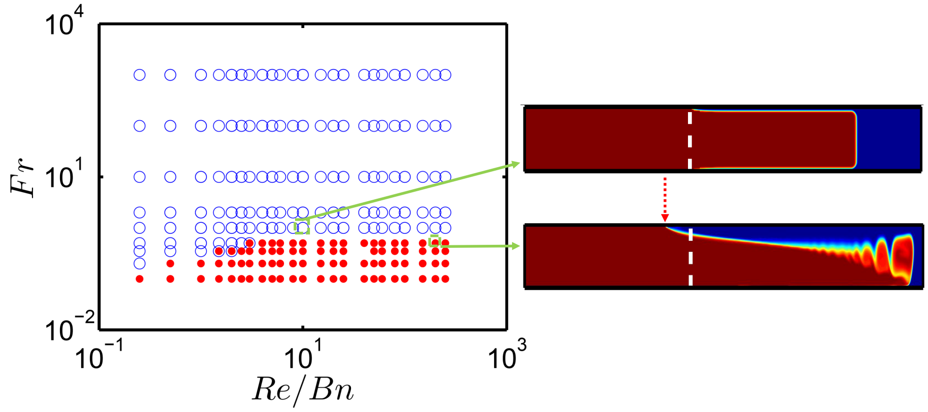

FIGURE 4.13 – Flow regime classification based on appearing back flows. The data corresponding to the temporary-back-flow regime are marked by (●) and the no-back-flow regime by (∘). Snapshot images belong to $Bn = 2$, $Re = 400$, and $Fr = 0.5$ at $t = 7.3$ (temporary-back-flow) and $Bn = 50$, $Re = 500$, and $Fr = 1$ at $t = 10.6$ (no-back-flow). The broken red arrow indicates the location of trailing front. The domain size shown is 1×60.

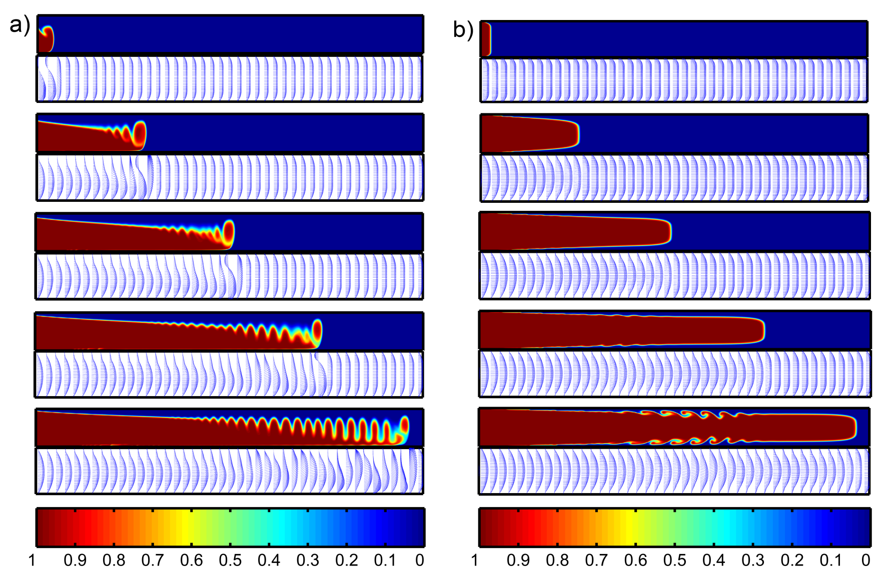

FIGURE 4.14 – Concentration colormaps and velocity vectors at $t = [6.8, 13.85, ..., 35]$ for (a) $Bn = 5$, $Re = 200$ and $Fr = 0.5$ and (b) $Bn = 5$, $Re = 500$ and $Fr = 10$, showing two types of unstable displacements. The domain size shown is 1×57, starting from the gate valve position at $x = 0$.

detachment process as times grows, for a simulation with $Bn = 100$, $Re = 300$ and $Fr = 0.2$ (the videos corresponding to these simulations are included in the supplementary materials). As can

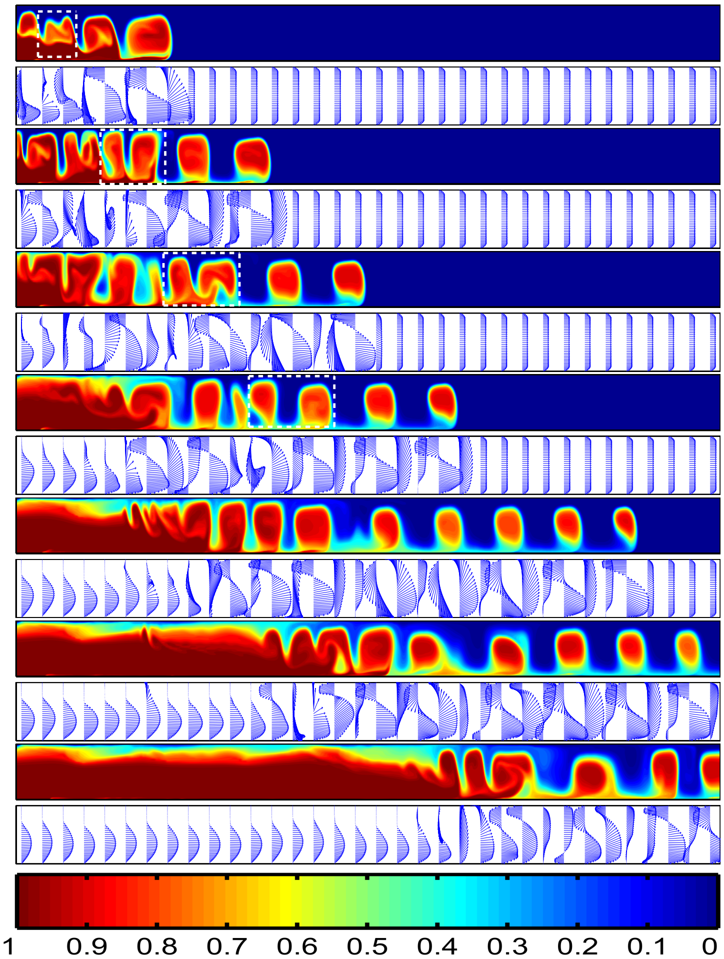

FIGURE 4.15 – Concentration colormaps and velocity vectors, at $t = [4, 6, 8, 10, 14, 19, 26]$ for $Bn = 100$, $Re = 300$ and $Fr = 0.2$, showing 7 sequential steps in a displacement flow with periodic detachment. The domain size shown is 1×50, starting from the gate valve position at $x = 0$.

be seen, the number, the size and the mean concentration of the segments change with time. For instance, by tracking the first segment (from the top to the bottom image), the size of the separated segment is clearly reduced over time. Generally, after being cut from the displacing bulk, the Newtonian core is encapsulated by the surrounding Bingham fluid. The encapsulated part gradually mixes with the displaced fluid over longer times and becomes smaller. Since the mean concentration of each formed segment is a function of time, the mixing degree between the two fluids is time-dependent. Furthermore, the number of segments increases with time, not only due to the formation of new segments near the bulk of the displacing fluid, but also thanks to flow instabilities which may divide each segment (e.g. see the highlighted boxed-region in Fig. 4.15). Regarding the velocity vectors, they obviously fluctuate with time and location, both inside and outside of the segments. It should also be noted that the variation in the mean spacing length between the segments can be quantified as the function of Re, Fr

and Bn. For example, the mean spacing length has an inverse relation with the Bingham and Froude numbers whereas it grows with the Reynolds number.

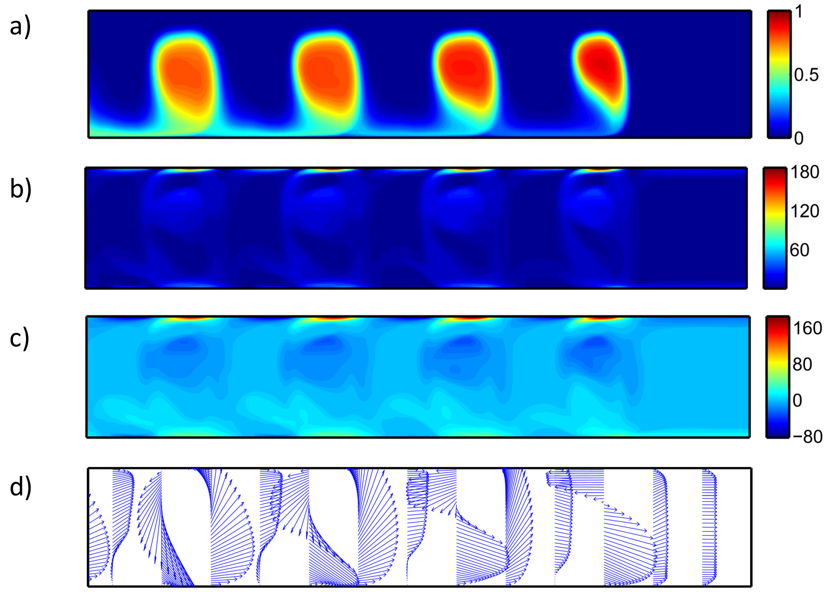

FIGURE 4.16 – Colormaps of (a) concentration, (b) stress (second invariant of the deviatoric stress) and (c) shear stress, as well as (d) velocity vectors, at $t = [13]$ for $Bn = 100$, $Re = 300$ and $Fr = 0.2$, showing a displacement flow with periodic detachment. The domain size shown is 1×18, starting from $x = 25$.

The concentration, deviatoric stress and shear stress colormaps are plotted in Fig. 4.16a-c for a displacement flow with a periodic detachment pattern. As can be seen, the concentration and stress vary from the center of each segment towards the outer surface. Moreover, while the segments are more or less separated from one other, the stress at the upper wall is maximum locally. The asymmetric stress field results in asymmetric segments. The velocity corresponding (Fig. 4.16d) to each segment is also different. Furthermore, the positive shear stress values are close to the upper/lower walls and the negative values are observed within the segments. It is interesting to note that after cutting the Newtonian fluid pieces from the bulk, the shear stress locally exceeds the yield stress at the upper wall, while it does not necessarily do so at the lower wall. Finally, before rupturing and within the pure yield stress fluid, the shear stress values are symmetric with respect to the channel center with different signs; the maximum positive/negative shear stresses are in the vicinity of the lower/upper walls.

Alba *et al.* (2) experimentally studied the miscible displacement flows of a viscoplastic fluid by a Newtonian fluid through a long inclined pipe. For slump-type flows, they observed break-up of the displaced layer. Our periodic detachment pattern has certain similarities with the "ripped-type" displacement observed in their experimental study. For example, in both phenomena, large fluid pieces are cut from the bulk fluid and the detached pieces appear to decrease in size following the initial break-up. Also the breakage becomes weak when buoyancy effects are smaller. The periodic detachment processes (similar to the break up of viscoplastic layers) leads to form diverse morphologies. However, Alba *et al.* (2) observed the breakage of the viscoplastic layer (Carbopol gel) in all slump-type displacement, which is caused by a fast-moving front (and thin layer) of the displacing fluid advancing along the bottom of the pipe. Here the periodic detachment flow occurs when the Froude number is very small (buoyant and inertial effects are strong) wherein the Newtonian fluid is ruptured. Furthermore, the leading front segments are almost separated from one other and the boundaries between the segments are more or less clear, i.e. the thin layer of displacing fluid is cut here, whereas the thin layers in the experiments mentioned are not completely segregated. Generally, after cutting the pieces of the Newtonian fluid from the bulk, the Newtonian core is encapsulated by the surrounding yield stress fluid. Despite these differences, which may be largely due to geometry (pipe vs channel), we believe the breakage/rupture mechanisms are similar to those observed experimentally.

The encapsulated parts move at different speeds and we can see in Fig. 4.16d, both that there is considerable motion within the capsules and that the Bingham fluid between the capsules does not become fully unyielded. This, although conceptually similar to the visco-plastic lubrication flows of Hormozi *et al.* (23) or the encapsulation studies of Maleki *et al.* (30), our flows are far from fully developed.

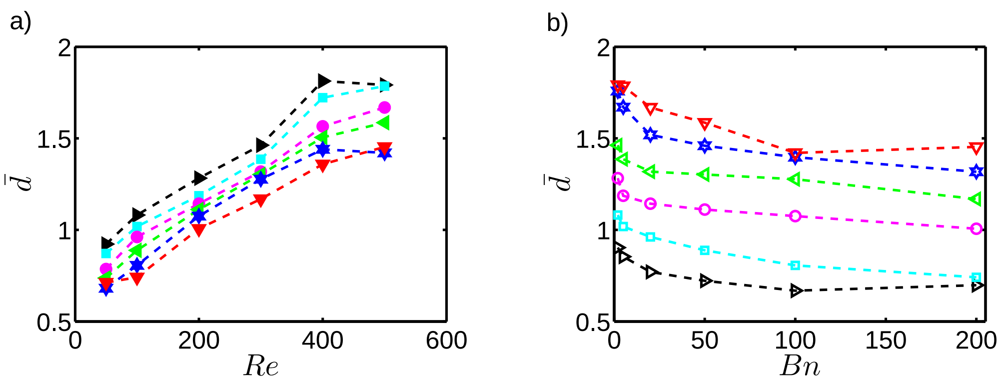

FIGURE 4.17 – The mean characteristic diameter of detached segments ($\bar{d}$) at Fr = 0.1; (a) versus Re with the data corresponding to Bn = 2 (▸), Bn = 5 (■), Bn = 20 (•), Bn = 50 (◂), Bn = 100 (⋆), Bn = 200 (▾); (b) versus Bn with the data corresponding to Re = 50 (▷), Re = 100 (□), Re = 200 (•), Re = 300 (◁), Re = 400(⋆), Re = 500 (▽). $\bar{d}$ is calculated using $\bar{d} = \sqrt{\frac{4A}{\pi}}$, where A is the segment area.

To give a broader understanding of the detached segments, characterizing them versus Bn, Re and Fr can be useful. Fig 4.17a and Fig. 4.17b illustrate the variation in the mean characteristic diameter of the segments ($\bar{d}$) versus Re and Bn, respectively. It is interesting to note that $\bar{d}$ monotonically increases with Re. Initially, $\bar{d}$ is controlled by a balance between the yield and buoyancy stresses. At larger Re, inertia competes with the yield stress to balance buoyancy; thus $\bar{d}$ increases. In fact, our simulations show that the number of segments is generally reduced by increasing Re whereas their areas are enhanced. Fig. 4.17b shows that by increasing Bn, $\bar{d}$ decreases generally, although the effects of Bn are less significant compared to those of Re.

There is also another subtle effect caused by increasing Re, i.e., the augmentation of the mixing degree between the segments and the surrounding fluid. As Re increases, the separated segments mix more with the displaced fluid so that their concentration decreases.

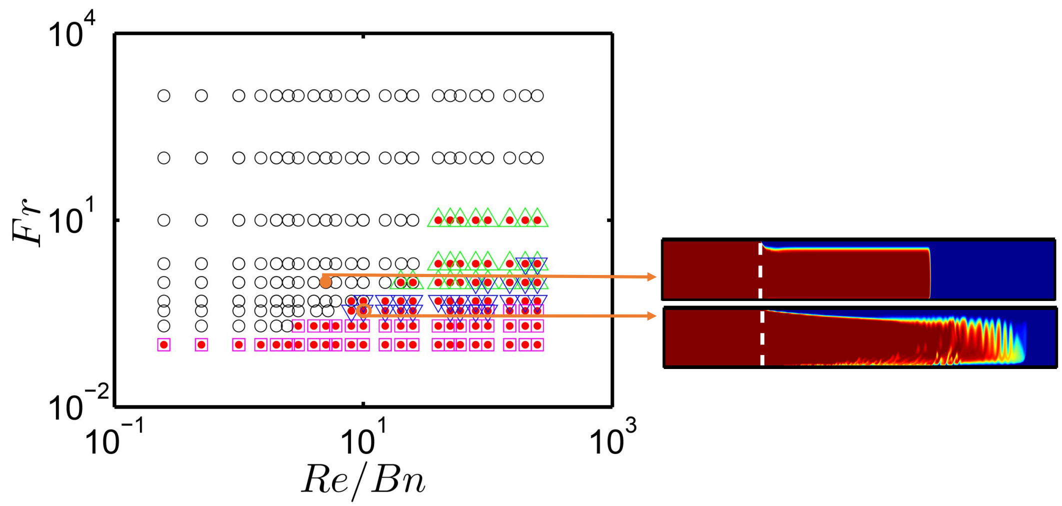

FIGURE 4.18 – Flow regime classification based on stable/unstable flows. The stable datapoints are marked by (∘) and the unstable ones by (•). Two snapshots corresponding to a stable flow (Bn = 100, Re = 500, and Fr = 1 at t = 32) and an unstable flow (Bn = 5, Re = 50, and Fr = 0.35 at t = 40) are included. Within the unstable displacement flows, the ones with the periodic-detachment patterns are marked by (□), the semi-detached patterns by (▽) and the sinusoidal shaped wave patterns by (△).

Now we can return to providing the stable/unstable regime classification based on the dimensionless groups. Fig. 4.18 shows the data corresponding to stable (black hollow) and unstable (red filled) flows, which are completely segregated in the plane of Fr versus Re/Bn, over a wide range of these parameters. For the stable flows, there is almost a sharp transition between purely displacing and displaced fluid regions. For these flows, the location and concentration of the *interface* and front are clear. Approximately, there is no wave at the interface between the Bingham and Newtonian fluids. However, for unstable cases, there exist waves observed in the concentration field and there is no distinct boundary between the two pure fluids.

In general, stable displacements are located at higher Fr. The transition between stable and unstable displacement flow regimes highly depends on Bn, which may be expected. At fixed Re, by increasing Bn, the transition Froude number decreases since instabilities are damped by the large yield stress. The displacement flows with $Fr \geq 100$ are generally stable, regardless of Re and Bn, within the ranges explored.

4.6.4 Leading front features

The behaviors of the leading front are of importance from both the physical and practical points of view. At least four different leading order behaviors can be distinguished for the fronts: plug-like, inertial tip, semi-detached, and fully-detached fronts. Fig. 4.19 classifies these front patterns in the plane of Fr and Re/Bn, and gives illustrative examples. In the following subsections, we will review these front behaviors in detail.

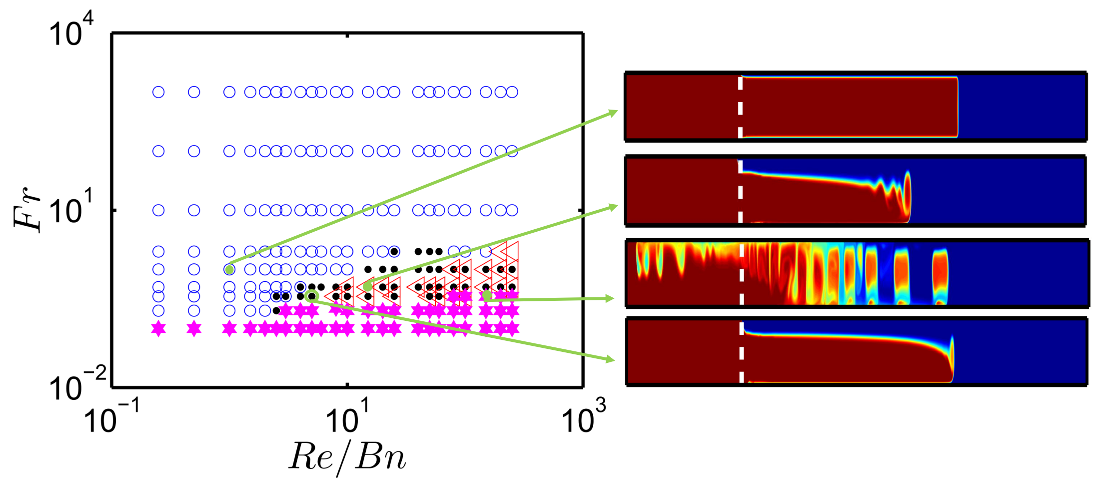

FIGURE 4.19 – Classification of front patterns: plug-like ($\circ$), inertial tip ($\bullet$), semi-detached ($\triangleleft$) and fully-detached ($\star$). Four snapshots corresponding to a plug front pattern ($Bn = 100$, $Re = 200$, and $Fr = 1$ at $t = 35$), inertial tip pattern ($Bn = 20$, $Re = 100$, and $Fr = 0.35$ at $t = 28$), semi-detached pattern ($Bn = 20$, $Re = 300$, and $Fr = 0.5$ at $t = 20$) and fully-detached front pattern ($Bn = 2$, $Re = 300$, and $Fr = 0.35$ at $t = 16$) are included.

• **Plug-like front**:

As mentioned earlier, channel flow displacement simulations in the current study cover a wide range of yield stresses, i.e., $Bn = [2 - 200]$. For considerable yield stress values, the displacing front pattern resembles that of a plug flow. Fig. 4.20a and Fig. 4.20b display the concentration colormaps and velocity vectors for two typical cases. As can be seen, plug-like fronts can appear within the flow regimes that are either center-type or slump-type, depending on the buoyancy. Although the displacing front is plug-like due to the large yield stress in both cases, there seems to be a smooth transition between two shear flow regimes, seen from the velocity vectors. For the slump-type case the mean static layer thickness ($\frac{h_u+h_l}{2} \approx 0.2$) is larger than in the center-type case ($\frac{h_u+h_l}{2} \approx 0.1$).

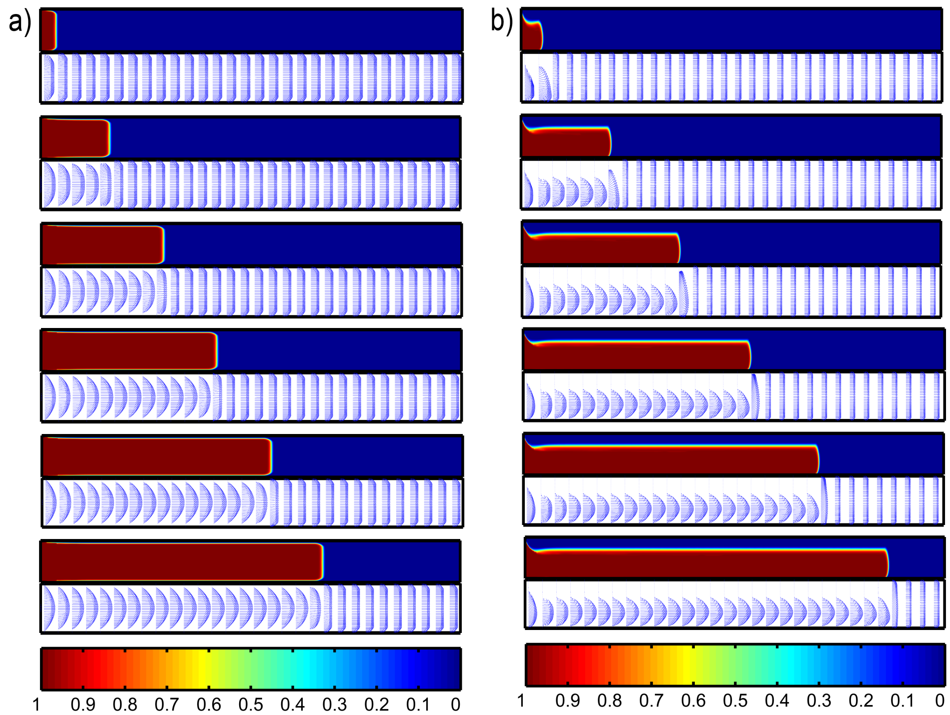

FIGURE 4.20 – (a) & (b) Concentration colormaps and velocity vectors at $t = [3.5, 7.2, ..., 22]$ for (a) $Bn = 50$, $Re = 400$ and $Fr = 100$ and (b) $Bn = 200$, $Re = 500$ and $Fr = 0.5$, showing two examples of the plug-like front. The domain size shown is 1×40, starting from the gate valve position at $x = 0$.

• **Inertial tip front**:

One of the interesting behaviors observed in our numerical simulations is the appearance an inertial tip pattern at the displacing front. For example, Fig. 4.21a and Fig. 4.21b display the concentration colormaps for two simulations, showing an inertial tip front for $Bn = 20$, $Re = 100$, $Fr = 0.5$ and $Bn = 2$, $Re = 400$, $Fr = 1$, respectively. The inertial tip at the displacing front starts to form approximately at $t = 4$ and extends gradually. It can be seen from these subfigures that the displacing layers slump towards the bottom of the channel, while the front itself moves slightly upward. The velocity vectors show that the inertial effects are quite present at the displacing front, leading to the formation of the front inertial tip pattern. A similar type of front pattern has been previously observed in Newtonian displacements (3), although the front is much more dispersive in Newtonian cases. In our work, the yield stress of the displaced fluids limits the dispersivity at the front, leading to the formation of a *clean* inertial tip pattern. Moreover, it can be seen that the size and the shape of the inertial tip region are enhanced by increasing Re and decreasing Bn.

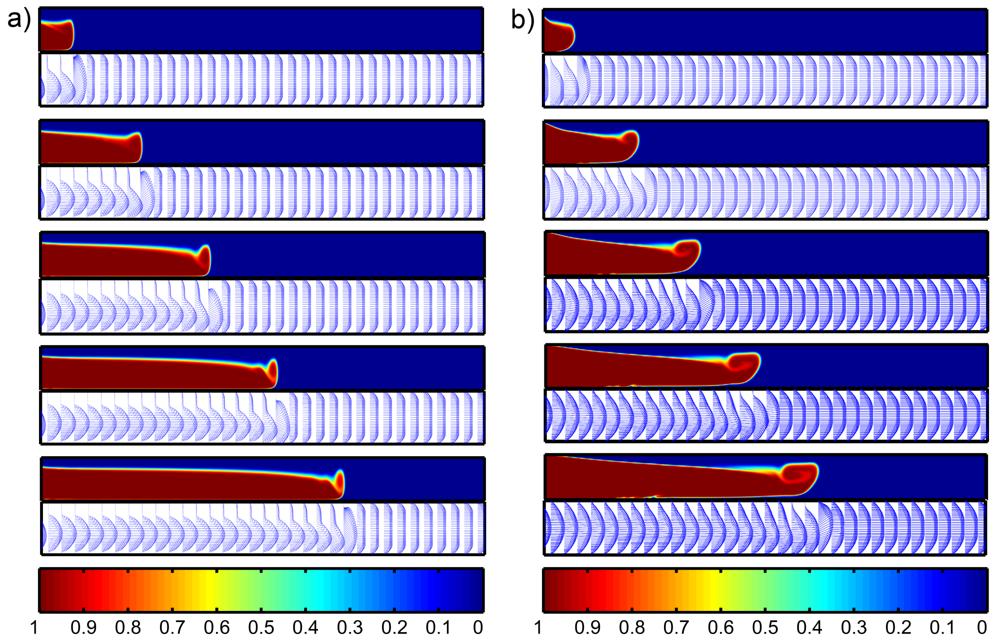

FIGURE 4.21 – Concentration colormaps and velocity vectors at $t = [3, 6.25, ..., 16]$ for: (a) $Bn = 20$, $Re = 100$ and $Fr = 0.5$ and (b) $Bn = 2$, $Re = 400$ and $Fr = 1$, showing two examples with an inertial tip pattern. The domain size shown is 1×44, starting from the gate valve position at $x = 0$.

• **Semi-detached and fully-detached fronts**:

As discussed earlier in detail, an interesting phenomenon observed in some of our simulations is that pieces of the displacing front are cut from the rest of displacing finger, forming separated segments of the heavy fluid advected within the displaced fluid. The detachment process nearly always starts at the front. For example, Fig. 4.22a shows the concentration colormaps and velocity vectors, at different times for $Bn = 100$, $Re = 300$ and $Fr = 0.1$, in which the front detachment phenomenon due to flow instabilities is seen. As discussed earlier, the detachment process periodically continues so that separated segments are continuously formed. Each detached segment moves faster than the bulk of the displacing fluid, although each may have a different size and a different speed. The velocity field is quite unstable and the velocity profiles around each segment fluctuate with time. Finally, although in this work we focus mainly on the leading front, we can also notice the formation of separated segments of the displaced fluid, moving backward. These segments are clearly smaller, have smaller speeds and usually mix much more quickly with the surrounding fluid.

Fig. 4.22b illustrates the leading and trailing front velocities, for the same simulation as in Fig. 4.22a. Since the fronts are periodically formed, these velocities correspond to fastest

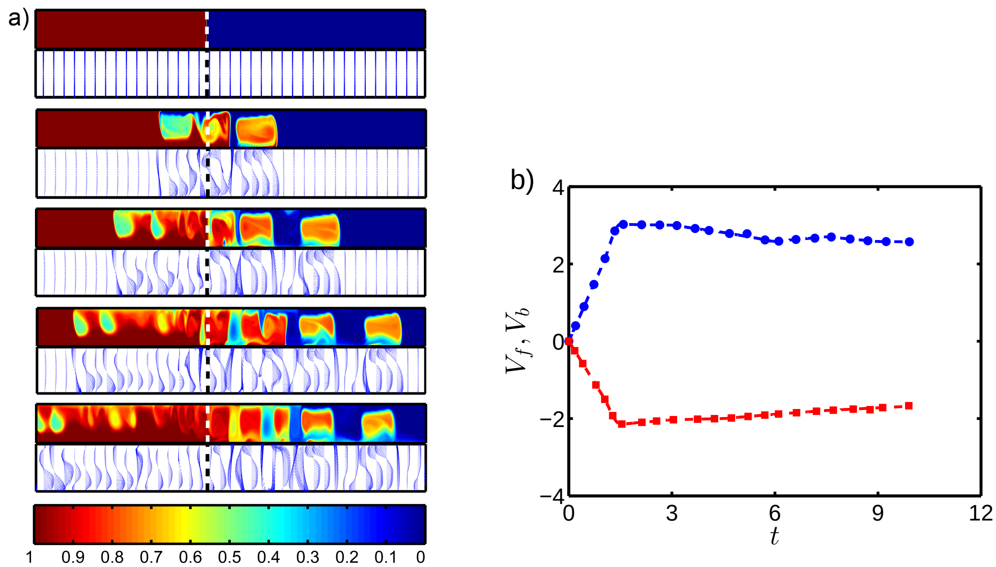

FIGURE 4.22 – (a) Concentration colormaps and velocity vectors, at $t = [0, 2.5, ..., 10]$ for $Bn = 100$, $Re = 300$ and $Fr = 0.1$, showing a front detachment configuration. The domain size shown is 1×60, starting from $x = -25$. (b) Evolution of the leading (•) and trailing (■) front velocities for the same simulation.

advancing segments of the displacing and displaced fluids. Initially, the leading front velocity rapidly increases from 0, and after a peak, starts to slowly decrease (perhaps due to partial mixing). This implies that the speed of the most advanced piece of the displacing fluid (within the displaced one) remains significant. On the other hand, the absolute value of the trailing front velocity increases with time, but slows down afterwards. The absolute trailing front velocity decreases (due to very strong mixing) until it reaches zero at very long times (not shown).

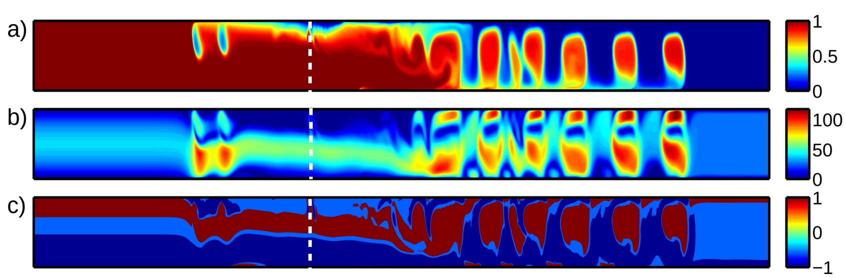

FIGURE 4.23 – Simulation results at $t = 10$, for $Bn = 50$, $Re = 200$ and $Fr = 0.2$, showing a detachment configuration: (a) Concentration colormaps; (b) Speed contours $V = \left(\sqrt{{V_x}^2 + {V_y}^2}\right)$; (c) Vorticity contours $\left(\omega = \frac{\partial V_y}{\partial x} - \frac{\partial V_x}{\partial y}\right)$. The domain size shown is 1×66, starting from $x = -25$.

In order to provide further understanding about how the front is detached, let us look into Fig. 4.23 showing the contours of concentration, velocity and vorticity, at $t = 10$ for $Bn = 50$,

Re = 200 and Fr = 0.2. Fig. 4.23a shows that the separated segments of the displacing fluid have progressively smaller areas along the channel length. Fig. 4.23b illustrates the absolute speed contours. The flow velocity profile is far from both a Poiseuille flow and a plug flow. High speed regions are observed within the separated segments. Fig. 4.23c shows the vorticity contours. Positive vorticity values are within the separated segments and negative vorticity values are outside. However, before and after each segment, small islands of positive vorticity values can be also observed close to the upper/lower walls. Therefore, temporarily flow reversals do occur in the vicinity of the upper/lower walls, due to a mix of buoyancy and interfacial instabilities.

• **Leading front velocity**:

It is interesting to investigate the leading front velocity as a function of the dimensionless numbers of the flow. In our large aspect ratio channel, the leading front velocity can provide an indication to how efficiency the displacement process is. Generally, one may expect that when the leading front velocity approaches unity, the displacement efficiency tends to 100%. Details about methods of the calculation of V_f can found in (54; 3).

Let us start with analyzing the effects of the dimensionless numbers on the leading front velocity. Fig. 4.24a and Fig. 4.24b show the variation of V_f versus Bn (for different Fr) at two fixed Re = 100 and Re = 300, respectively. Note that for some cases at very small Fr, the front velocity highly fluctuates with time and cannot reach a plateau value; these datapoints are not included in the figure. As can be seen, V_f decreases by increasing Bn (in other words by increasing the yield stress). The explanation for this behavior is that by increasing Bn the thickness of the static residual layers of the displaced fluid generally decreases, which therefore implies that V_f needs to decrease as well. The other effect that can be seen is that V_f generally decreases with Fr. The interpretation of this behavior is that, for fixed Re (i.e., constant ratio of inertial to viscous forces), V_f decreases when buoyancy forces decrease (as Fr increase). As Fr decreases, these forces act as additional driving forces (in addition to the imposed flow), improving V_f and worsening the displacement efficiency. Fig. 4.24c and Fig. 4.24d show the variation of V_f versus Fr (for different Bn) at two fixed Re = 100 and Re = 300. For fixed Bn, it can be seen that at small Fr, V_f highly depends on Fr, since buoyancy forces are significant. Initially, V_f sharply decreases with Fr but becomes independent of it at very large Fr values, where the displacement flow approaches an iso-density, symmetric three-layer displacement flow.

Fig. 4.25 shows the effects of Re on V_f for Bn and Fr. It is interesting to note that Re has opposite effects on V_f, at small and large Fr: by increasing Re the leading front velocity increases at small Fr, but the opposite is true at large Fr.

At fixed, large value of Fr, as the displacing finger is more towards the channel center, the

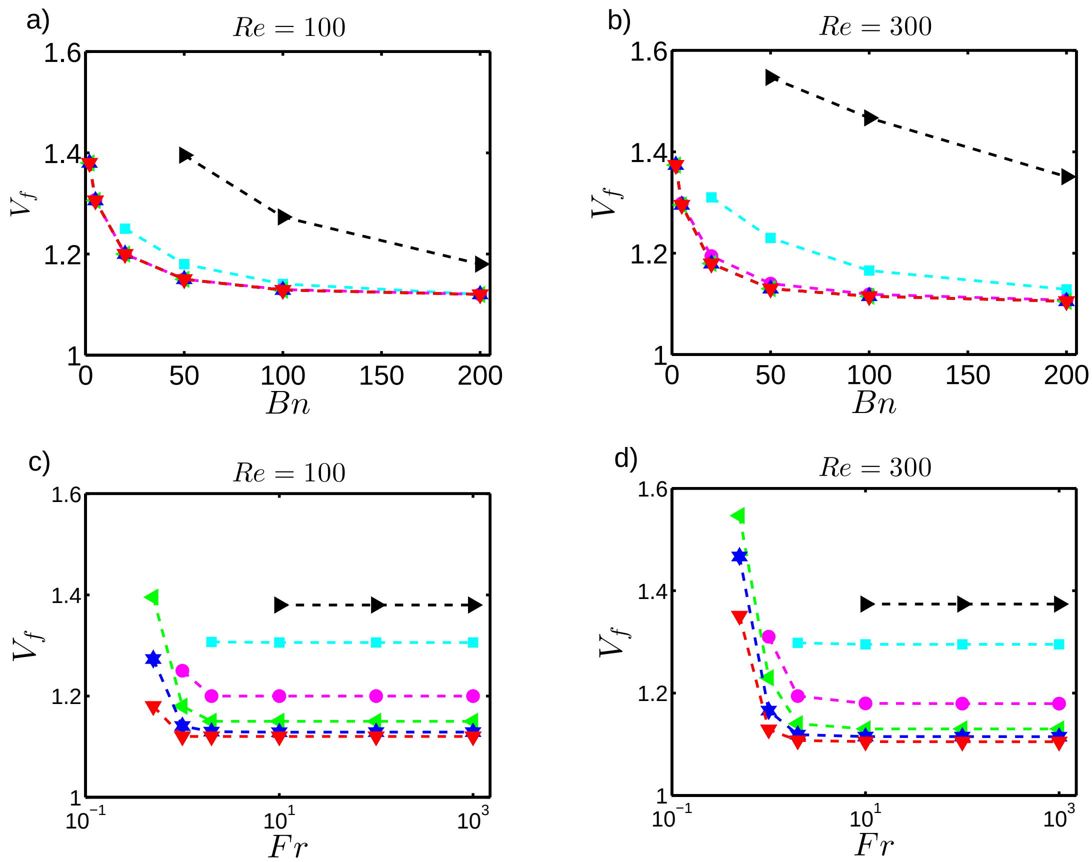

FIGURE 4.24 – Effects of the dimensionless groups on the leading front velocity for at (a)&(c) $Re = 100$ and (b)&(d) $Re = 300$. In the top row the data correspond to $Fr = 0.5$ (▸), $Fr = 1$ (■), $Fr = 2$ (•), $Fr = 10$ (◂), $Fr = 100$ (⋆), $Fr = 1000$ (▾) and in the bottom row to $Bn = 2$ (▸), $Bn = 5$ (■), (•)$Bn = 20$, (◂) $Bn = 50$, $Bn = 100$ (⋆), $Bn = 200$ (▾).

upper/lower static layers are affected by Re to the extent that increasing Re leads to decreasing the static layer thickness (due to inertial dissipation). More rigorously, Wielage-Burchard & Frigaard (61) have shown that, for $Fr \to \infty$, increasing Re improves the rate of energy production of the steady flow, resulting in decreasing the residual wall layer thicknesses. Since the static layer effects are dominant at larger Fr, V_f decreases with Re. On the other hand, at small Fr, the displacing finger is more towards channel center (i.e., the flow approaches a two-layer displacement). In this case, for fixed Bn and Fr, increasing Re may be interpreted as increasing buoyancy, which is a significant driving force at small Fr. Thus, since buoyant effects dominate the flow, V_f increases with Re.

Fig. 4.26 presents the variation of V_f, as a function of Fr, Bn and Re, where V_f values are marked by the symbol size and colors. It is seen that increasing Bn generally results in decreasing V_f, and that the variation of V_f is not monotonic versus Re. Moreover, the variation of V_f with Fr is negligible for $Fr \geqslant 5$.

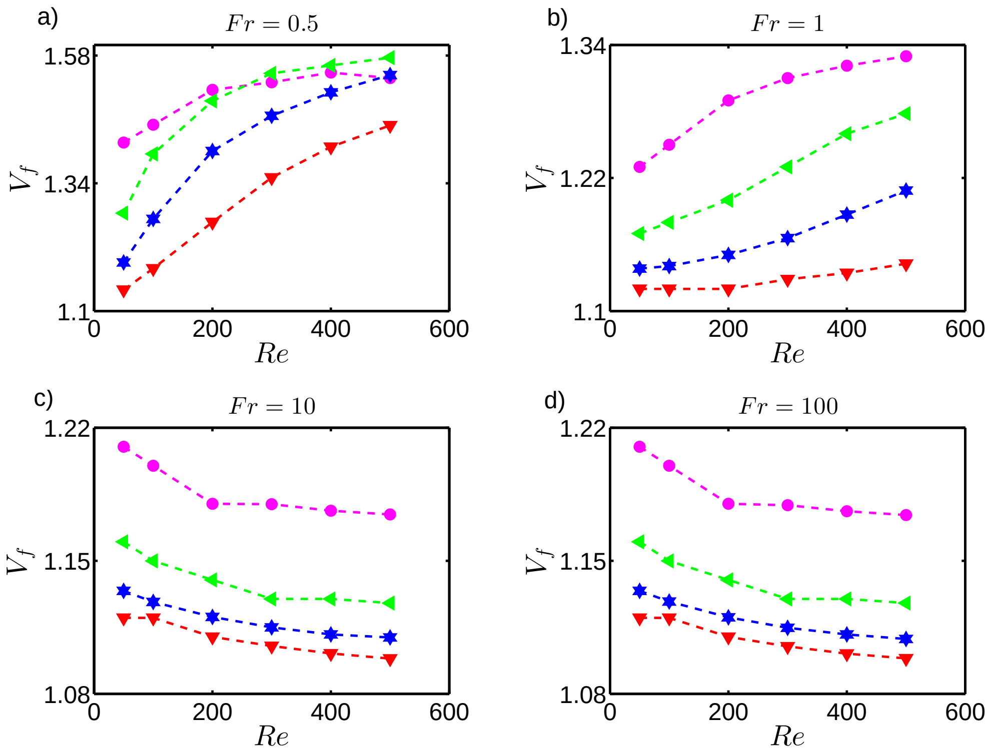

FIGURE 4.25 – Variation of V_f versus Re for (a) Fr = 0.5; (b) Fr = 1; (c) Fr = 10; and (d) Fr = 100. The data correspond to Bn = 20 (●), Bn = 50 (◂), Bn = 100 (⋆), Bn = 200 (▼).

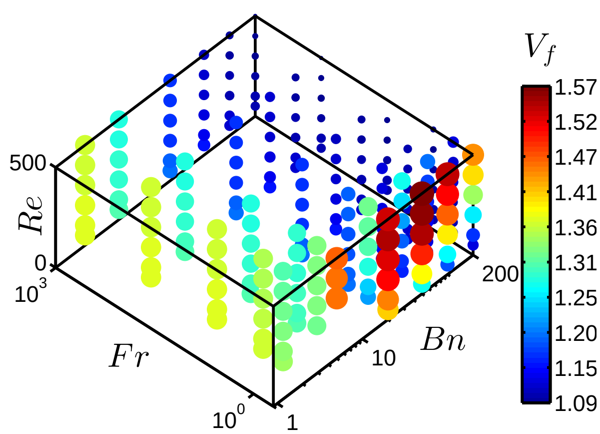

FIGURE 4.26 – Effects of Re, Bn and Fr on V_f, the values of which are marked by the symbol size and colors.

4.7 Summary

Using numerical simulations, we have considered displacement flows of a Bingham fluid by a Newtonian fluid, along a 2D uniform plane channel wherein the heavier fluid pushes the lighter fluid. The long-time behaviors of the displacement flow have been characterized in

Regime class	**Ref. figure**	**Appropriate dimensionless group**	**Comments**
Center- or slump-type	Fig. 4.11	Re/Fr	•In center-type: $h_u \approx h_l$ & in slump-type: $h_u/h_l \gg 1$ •Important threshold: $h_u/h_l \approx 1.6$ •Transition from slump- to center-type: $Re/Fr \approx 60$ •Transition independent of Bn & $\hat{V}_0$
Temporary- or no-back-flow	Fig. 4.18	Re/Bn & Fr	•For Bingham fluids, no-back-flows likely occur •Temporary-back-flows observed at small Fr •At smaller Fr, by increasing Bn, no-back-flows increasingly observed •Transition with small dependency on Bn.
Stable or unstable	Fig. 4.13	Re/Bn & Fr	•Stable (unstable) flows with (no) clear boundary between phases •Unstable (stable) flows with (no) wave at interface •Transition with significant dependency on Bn
Front patterns	Fig. 4.19	Re/Bn & Fr	•Main front patterns: plug-like, inertial tip, semi-detached, fully-detached •For Bingham fluid, plug-like flows likely occur •At large Fr front pattern independent of Re/Bn

TABLE 4.2 – Summary of the main observations.

the terms of three important dimensionless numbers: the Reynolds number (Re), the Bingham number (Bn) and the densimetric Froude number (Fr). Details associated with various displacement flow behaviors have been uncovered. First, static residual wall layers of the displaced fluid have been discussed. In particular, the upper/lower thicknesses of the residual wall layers as well as the upper/lower locations where uniform static layers appear have been quantified. Next, the main displacement regimes have been introduced, in the three classes of slump-type/center-type, no-back-flow/temporary-back-flow and stable/unstable displacements. Moreover, the characteristics of the leading front have been looked into in detail. For example, various front patterns observed, e.g., plug-like, inertial tip, semi-detached and fully-detached fronts, have been studied. Finally, the leading front velocity has been quantified as a function of the dimensionless numbers. A summary of the main observations is presented in Table 4.2.

Supplementary materials: This supplementary section includes videos showing the concentration colormap, the velocity vectors, the absolute speed contours and the vorticity contours in a displacement flow in a periodic-detachment regime. The numerical simulation is run for $Bn = 100$, $Re = 300$ and $Fr = 0.2$. The domain size shown is 1×50, starting from the gate valve position at $x = 0$.

4.8 Bibliography

[1] K. Alba and I.A. Frigaard. Dynamics of the removal of viscoplastic fluids from inclined pipes. *J. non-Newt. Fluid Mech.*, 229:43–58, 2016.

[2] K. Alba, S.M. Taghavi, J.R. de Bruyn, and I.A. Frigaard. Incomplete fluid-fluid displacement of yield-stress fluids. part 2: Highly inclined pipes. *J. non-Newt. Fluid Mech.*, 201:80–93, 2013.

[3] K. Alba, S.M. Taghavi, and I.A. Frigaard. Miscible heavy-light displacement flows in an inclined two-dimensional channel: A numerical approach. *Phys. Fluids*, 26(12):122104, 2014.

[4] M. Allouche, I. Frigaard, and G. Sona. Static wall layers in the displacement of two visco-plastic fluids in a plane channel. *J. Fluid Mech.*, 424(1):243–277, 2000.

[5] A. Amiri, F. Larachi, and S.M. Taghavi. Buoyant miscible displacement flows in vertical pipe. *Phys. Fluids*, 28(10):102105, 2016.

[6] S.H. Bittleston, J. Ferguson, and I.A. Frigaard. Mud removal and cement placement during primary cementing of an oil well–Laminar non-Newtonian displacements in an eccentric annular Hele-Shaw cell. *J. Eng. Math.*, 43(2-4):229–253, 2002.

[7] R. Brandao, J.V. Fontana, and J.A. Miranda. Interfacial pattern formation in confined power-law fluids. *Phys. Rev. E*, 90(1):013013, 2014.

[8] D. Burfoot, K.E. Middleton, and J.T. Holah. Removal of biofilms and stubborn soil by pressure washing. *Trends Food Sci. Technol.*, 20:S45–S47, 2009.

[9] C.Y. Chen and E Meiburg. Miscible displacements in capillary tubes. part 2. numerical simulations. *J. Fluid Mech.*, 326:57–90, 1996.

[10] Y. Cinar, A. Riaz, H.A. Tchelepi, et al. Experimental study of CO2 injection into saline formations. In *SPE ATCE*, 2007.

[11] N.G. Cogan and J.P Keener. Channel formation in gels. *SIAM J. Appl. Math.*, 65(6):1839–1854, 2005.

[12] P. Coussot. Saffman–Taylor instability in yield-stress fluids. *J. Fluid Mech.*, 380:363–376, 1999.

[13] D.A. de Sousa, E.J. Soares, R.S de Queiroz, and R.L. Thompson. Numerical investigation on gas-displacement of a shear-thinning liquid and a visco-plastic material in capillary tubes. *J. non-Newt. Fluid Mech.*, 144(2):149–159, 2007.

[14] Y. Dimakopoulos and J. Tsamopoulos. Transient displacement of a viscoplastic material by air in straight and suddenly constricted tubes. *J. non-Newt. Fluid Mech.*, 112(1):43–75, 2003.

[15] A. Eslami and S.M. Taghavi. Viscous fingering regimes in elasto-visco-plastic fluids. *J. non-Newt. Fluid Mech.*, 243:79–94, 2017.

[16] J.V. Fontana, E.O. Dias, and J.A. Miranda. Controlling and minimizing fingering instabilities in non-Newtonian fluids. *Phys. Rev. E*, 89(1):013016, 2014.

[17] J.F. Freitas, E.J. Soares, and R.L. Thompson. Viscoplastic-viscoplastic displacement in a plane channel with interfacial tension effects. *Chem. Eng. Sci.*, 91:54–64, 2013.

[18] P.J. Fryer, G.K. Christian, and W. Liu. How hygiene happens: physics and chemistry of cleaning. *Int. J. Dairy Technol.*, 59(2):76–84, 2006.

[19] C. Gabard and J.P. Hulin. Miscible displacement of non-Newtonian fluids in a vertical tube. *Eur. Phys. J. E.*, 11(3):231–241, 2003.

[20] R. Glowinski and P. Le Tallec. Augmented Lagrangian and operator-splitting methods in nonlinear mechanics. *Phys. Fluids*, 19:084106, 2007.

[21] S. Hill et al. Channeling in packed columns. *Chem. Eng. Sci.*, 1(6):247–253, 1952.

[22] K.E. Holloway, P. Habdas, N. Semsarillar, K. Burfitt, and J.R. de Bruyn. Spreading and fingering in spin coating. *Phys. Rev. E*, 75(4, 2):046308, 2007.

[23] S. Hormozi, K. Wielage-Burchard, and I.A. Frigaard. Entry, start up and stability effects in visco-plastically lubricated pipe flows. *J. Fluid Mech.*, 673:432–467, 2011.

[24] P.D. Howell, S.L. Waters, and J.B. Grotberg. The propagation of a liquid bolus along a liquid-lined flexible tube. *J. Fluid Mech.*, 406:309–335, 2000.

[25] D. Huh, H. Fujioka, N. i. Tung, Y. C. Futai, R. Paine, J. B. Grotberg, and S. Takayama. Acoustically detectable cellular-level lung injury induced by fluid mechanical stresses in microfluidic airway systems. *Proc. Natl. Acad. Sci.*, 104(48):18886–18891, 2007.

[26] P.C. Huzyak and K.W. Koelling. The penetration of a long bubble through a viscoelastic fluid in a tube. *J. non-Newt. Fluid Mech.*, 71(1):73–88, 1997.

[27] L.W. Lake. *Enhanced oil recovery.* Prentice Hall, 1989.

[28] A. Lindner, P. Coussot, and D. Bonn. Viscous fingering in a yield stress fluid. *Phys. Rev. Lett.*, 85(2):314, 2000.

[29] A. Lindner, P. Coussot, and D. Bonn. Viscous fingering in a gel. In *Branching in Nature*, pages 433–438. Springer, 2001.

[30] A. Maleki, S. Hormozi, A. Roustaei, and I.A. Frigaard. Macro-size drop encapsulation. *J. Fluid Mech.*, 769:482–521, 2015.

[31] N. Maleki-Jirsaraei, A. Lindner, S. Rouhani, and D. Bonn. Saffman–Taylor instability in yield stress fluids. *J. Phys. Condens. Matter*, 17(14):S1219, 2005.

[32] S. l. Malhotra and M. M. Sharma. Impact of fluid elasticity on miscible viscous fingering. *Chem. Eng. Sci.*, 117:125–135, 2014.

[33] K.V. McCloud and J.V. Maher. Experimental perturbations to Saffman–Taylor flow. *Phys. Rep.*, 260(3):139–185, 1995.

[34] G.V.L. Moisés, M.F. Naccache, K. Alba, and I.A. Frigaard. Isodense displacement flow of viscoplastic fluids along a pipe. *J. non-Newt. Fluid Mech.*, 236:91–103, 2016.

[35] R. Mollaabbasi and S.M. Taghavi. Buoyant displacement flows in slightly non-uniform channels. *J. Fluid Mech.*, 795:876–913, 2016.

[36] S. Mora and M. Manna. Saffman–Taylor instability for generalized Newtonian fluids. *Phys. Rev. E*, 80(1):016308, 2009.

[37] J. Nase, D. Derks, and A. Lindner. Dynamic evolution of fingering patterns in a lifted Hele-Shaw cell. *Phys. Fluids*, 23(12):123101, 2011.

[38] E.B. Nelson and D. Guillot. *Well Cementing, 2nd Edition.* Schlumberger Educational Services, 2006.

[39] F.M. Orr and J.J. Taber. Use of carbon dioxide in enhanced oil recovery. *Science*, 224(4649):563–569, 1984.

[40] G. Papaioannou, J. Karapetsas, Y. Dimakopoulos, and J. Tsamopoulos. Injection of a viscoplastic material inside a tube or between two parallel disks: Conditions for wall detachment of the advancing front. *J. Rheol.*, 53(5):1155–1191, 2009.

[41] M.A. Parvez, N.S. Ong, Y.C. Lam, and S.B. Tor. Gas-assisted injection molding: the effects of process variables and gas channel geometry. *J. Mater. Process. Technol.*, 121(1):27–35, 2002.

[42] H. Pascal. Dynamics of moving interface in porous media for power law fluids with yield stress. *Int. J. Eng. Sci.*, 22(5):577–590, 1984.

[43] H. Pascal. Rheological behaviour effect of non-Newtonian fluids on dynamic of moving interface in porous media. *Int. J. Eng. Sci.*, 22(3):227–241, 1984.

[44] H. Pascal. Rheological effects of non-Newtonian behavior of displacing fluids on stability of a moving interface in radial oil displacement mechanism in porous media. *Int. J. Eng. Sci.*, 24(9):1465–1476, 1986.

[45] P. Petitjeans and T. Maxworthy. Miscible displacements in capillary tubes. part 1. experiments. *J. Fluid Mech.*, 326:37–56, 1996.

[46] A.J. Poslinski, P.R. Oehler, and V.K. Stokes. Isothermal gas-assisted displacement of viscoplastic liquids in tubes. *Polym. Eng. Sci.*, 35(11):877–892, 1995.

[47] G. Rousseaux, A. De Wit, and M. Martin. Viscous fingering in packed chromatographic columns: Linear stability analysis. *J. Chromatogr. A*, 1149(2):254–273, 2007.

[48] A. Roustaei. *Yield stress fluid flows in uneven geometries*: *applications to the oil and gas industry*. PhD thesis, University of British Columbia, 2016.

[49] K.C. Sahu, H. Ding, P. Valluri, and O.K. Matar. Pressure-driven miscible two-fluid channel flow with density gradients. *Phys. Fluids*, 21(4):043603, 2009.

[50] T. Séon, J.P. Hulin, D. Salin, B. Perrin, and E.J. Hinch. Buoyancy driven miscible front dynamics in tilted tubes. *Phys. Fluids*, 17(3):031702, 2005.

[51] P. A. P. Swain, G. Karapetsas, O.K. Matar, and K.C. Sahu. Numerical simulation of pressure-driven displacement of a viscoplastic material by a Newtonian fluid using the lattice Boltzmann method. *Eur. J. Mech. B-Fluid*, 49:197–207, 2015.

[52] S.M. Taghavi, K. Alba, and I.A. Frigaard. Buoyant miscible displacement flows at moderate viscosity ratios and low Atwood numbers in near-horizontal ducts. *Chem. Eng. Sc.*, 69:404–418, 2012.

[53] S.M. Taghavi, K. Alba, M. Moyers-Gonzalez, and I.A. Frigaard. Incomplete fluid-fluid displacement of yield stress fluids in near-horizontal pipes: experiments and theory. *J. non-Newt. Fluid Mech.*, 167-168:59–74, 2012.

[54] S.M. Taghavi, K. Alba, T. Séon, K. Wielage-Burchard, D.M. Martinez, and I.A. Frigaard. Miscible displacement flows in near-horizontal ducts at low Atwood number. *J. Fluid Mech.*, 696:175–214, 2012.

[55] S.M. Taghavi, T. Seon, D.M. Martinez, and I.A. Frigaard. Buoyancy-dominated displacement flows in near-horizontal channels: the viscous limit. *J. Fluid Mech.*, 639:1–35, 2009.

[56] S.M. Taghavi, T. Séon, D.M. Martinez, and I.A. Frigaard. Influence of an imposed flow on the stability of a gravity current in a near horizontal duct. *Phys. Fluids*, 22(3):031702, 2010.

[57] S.M. Taghavi, T. Séon, K. Wielage-Burchard, D.M. Martinez, and I.A. Frigaard. Stationary residual layers in buoyant Newtonian displacement flows. *Phys. Fluids*, 23(4):044105, 2011.

[58] G.I. Taylor. Cavitation of a viscous fluid in narrow passages. *J. Fluid Mech.*, 16(04):595–619, 1963.

[59] G. Vinay. *Modélisation du redémarrage des écoulements de bruts paraffiniques dans les conduites pétrolieres*. PhD thesis, École Nationale Supérieure des Mines de Paris, 2005.

[60] A.R. White and T. Ward. Constant pressure gas-driven displacement of a shear-thinning liquid in a partially filled radial Hele-Shaw cell: Thin films, bursting and instability. *J. non-Newt. Fluid Mech.*, 206:18–28, 2014.

[61] K. Wielage-Burchard and IA. Frigaard. Static wall layers in plane channel displacement flows. *J. non-Newt. Fluid Mech.*, 166(5):245–261, 2011.

[62] J. Wiklund, M. Stading, and C. Trägårdh. Monitoring liquid displacement of model and industrial fluids in pipes by in-line ultrasonic rheometry. *J. Food Eng.*, 99(3):330–337, 2010.

Chapitre 5

Pressure-driven displacement flows of yield stress fluids: Viscosity ratio effects

5.1 Résumé

Nous étudions par simulation numérique les écoulements à déplacement de deux fluides miscibles sur un canal 2D presque horizontal, commandée par pression et densité instable. Le fluide de déplacement est un fluide Newtonien un peu plus lourd que le fluide à seuil (Bingham) déplacé. L'écoulement à déplacement imposé est laminaire. Nous montrons que l'écoulement à déplacement est principalement géré par cinq nombres sans dimension et leurs combinaisons, y compris le nombre de Reynolds (Re), le nombre de Bingham (Bn), le nombre de Froude (Fr), le taux de viscosité (m) et l'angle d'inclinaison du canal (β). Dans cet article, nous nous concentrons principalement sur le rapport de viscosité et nous fournissons une compréhension détaillée des comportements d'écoulement via l'étude des effets de m sur les modèles d'écoulement, classifications de régimes basées sur les régimes d'écoulement déplacements «center-type»/«slump- type», «back flow»/«no-back flow», et enfin les effets de m à différents angles d'inclinaison.

5.2 Abstract

We numerically investigate pressure-driven, density-unstable displacement flows of two miscible fluids along a near-horizontal 2D channel. The displacing fluid is a Newtonian fluid, slightly heavier than the displaced yield stress (Bingham) fluid. The imposed displacement flow is laminar. We show that the displacement flow is mainly governed by five dimensionless numbers, and their combinations, including the Reynolds number (Re), the Bingham number (Bn), the densimetric Froude number (Fr), the viscosity ratio (m) and the channel inclination

angle (β). In this work, we primarily focus on the viscosity ratio, and provide a detailed understanding of the flow behaviours via studying the effects of m on displacement flow patterns, regime classifications based on slump-type and centre-type displacement flow regimes, leading and trailing displacement front features, and finally the effects of m at different inclination angles.

5.3 Introduction

Pressure-driven displacement flows wherein one fluid pushes another one towards the geometry exit frequently occur in many natural and industrial systems. These fascinating flows may emerge in various flow geometries, usually with density and viscosity contrasts between the fluids involved. These flows are studied from different perspectives, in particular, in terms of flow patterns and the overall displacement efficiency. Displacement flows find applications in oil and gas industries (34; 35; 28; 4), biomedical and biotechnological applications (24; 25; 8), food processing (21; 58; 18), cleaning of equipment (55; 6), displacement of magma in volcanoes (45) and numerous other applications (39; 36; 22; 53). In some of the aforementioned processes, due to the presence of a yield stress, the displaced fluid is difficult to remove by the displacing fluid. In this study, we consider miscible displacements of a yield stress fluid by a Newtonian fluid in a near-horizontal 2D channel, in the presence of density and viscosity ratios.

The rheological behaviours of displacing and displaced fluids have remarkable effects on the key displacement flow features, such as flow morphology, interfacial instabilities and displacement efficiency. In this context, Newtonian displacement flows have been studied from various points of view, numerically, analytically and experimentally, (29; 44; 43; 23; 3; 51) while their non-Newtonian counterparts have been less explored, due to complex characteristics of these fluids. A majority of non-Newtonian displacement studies have analyzed pattern formations in the Hele-Shaw geometry, while considering shear-thinning (56; 5), shear-thickening (33; 5), yield stress (9; 37), elasticity (30; 26) and elasto-visco-plastic properties (13; 14). There have been relatively fewer non-Newtonian research works in other flow geometries, perhaps with the exception of yield stress displacement flows in capillary tubes (10), capillary plane channels (17), 2D channels (46; 48), channels with uneven walls (42; 41), horizontal pipes (31), vertical tubes (19) and symmetric and asymmetric tubes (11).

The effects of various flow parameters have been studied on yield stress displacements. For example, the effects of a yield stress on the displacement flow efficiency of a near-horizontal 2D channel flow have been evaluated analytically (52). In terms of the effects of buoyancy, heavy-light displacements of yield stress fluids in near-horizontal and highly-inclined pipes have been studied (50; 1). Two distinct flow patterns have been identified: (1) a *slump*-type and (2) a *centre*-type displacement flow regime, which appear depending on the density contrast between the displacing and displaced fluids. The formation of these flow regimes has been confirmed via computational approaches (12).

Another critical feature in yield stress displacements is the presence of static residual layers of the displaced fluid during the displacement process. Contrary to purely viscous displacements, in which the residual layers are typically moving, the residual layers in yield stress displacements can be completely static (2; 57). This makes the removal of these layers even harder, in particular, from the interior sections of a flow geometry. Static residual layers may form when the yield stress value of the displacing fluid is less than that of the displaced fluid (2). The yield stress in the displaced fluid resists the imposed stresses during the displacement flow; accordingly, the displaced fluid layers can remain attached to the geometry walls. Quantifying the residual layer thickness of the displaced fluid on solid surfaces has been the subject of past and recent research studies. For example, Poslinski *et al.* (38) and Eslami *et al.* (13) have experimentally studied the displacement of a yield stress fluid by a Newtonian fluid in tubes and Hele-Shaw cells, respectively. They have found that the mean residual layer thickness for yield stress fluid flows is larger in comparison with their Newtonian counterparts. Mollaabbasi and Taghavi (32) have analytically studied the influence of a flow geometry non-uniformity on yield stress displacements in 2D channels. They have demonstrated that the static residual wall layer thickness increases (decreases) in diverging (converging) channels.

A viscosity ratio between the fluids involved in a displacement flow can affect the flow patterns and it can be also a source for interfacial instabilities (27; 23). Wielage-Burchard and Frigaard (57) have studied computationally the effects of the viscosity ratio of the displaced fluid to that of the displacing fluid (m) on static residual layer thicknesses in iso-dense displacements of a Bingham fluid. At low Reynolds number (e.g., $Re = 0.1$), they have found that the thickness of these layers is independent of m. However, at larger Reynolds numbers (e.g., $Re = 100$), the static residual layer thickness is a function of the viscosity ratio. Zare *et al.* (59) have considered density-stable displacements of a yield stress fluid by a Newtonian one in a vertical 2D channel. For a narrow range of viscosity ratios ($0.1 \leq m \leq 10$), they have shown that increasing m results in increasing the residual layer thickness. For zero yield stresses, Etrati *et al.* (15) have experimentally investigated the impacts of m on miscible displacements in an inclined pipe, showing that the displacement efficiency, back-flow behaviours and flow stabilities are strongly affected by m. Despite these efforts, there is no clear picture of the effects of m on different features of displacement flows. More specifically, understanding the effects of m on yield stress displacements requires a deeper analysis, as carried out in the current work.

The structure of this manuscript is as follows. Below in Section 5.4, the flow geometry and the governing equations are provided. The details of the computational methodology are explained in Section 5.5. Section 5.6 presents our main results. The paper ends with a brief summary in Section 5.7.

5.4 Problem setting

In the current study, the pressure-driven miscible displacement of a light yield stress fluid by a heavy Newtonian one along a 2D plane channel is considered. The flow geometry, the initial flow configuration, the schematic displacement flow configuration, and the notations used in this study are represented in Fig. 5.1. As illustrated, $\hat{x}$ represents the streamwise direction [1]. The mean imposed displacement velocity is $\hat{V}_0$ (laminar). The dimensional channel length is $\hat{L}$ and the dimensional channel height is $\hat{D}$. The flow geometry is oriented at an angle close to horizontal (β). The aspect ratio of the channel ($\frac{\hat{D}}{\hat{L}}$) is equal to 0.01. The fluids have different densities and viscosities. The ratio of the plastic viscosity of the displaced fluid ($\hat{\mu}_L$) to the viscosity of the displacing fluid (Newtonian fluid's viscosity, $\hat{\mu}_H$) is the viscosity ratio (m), as presented later below. The Newtonian fluid (fluid H in Fig. 5.1) is denser than the yield stress one (fluid L in Fig. 5.1). Fig.5.1b illustrates the flow configuration after the onset of the displacement flow, for which a *leading* front (with velocity $\hat{V}_f$) and a *trailing* front (with velocity $\hat{V}_b$) can be identified.

The two fluids are miscible and they are assumed to be incompressible. They are also assumed to have a small density difference. Based on these assumptions, to develop a computational model to describe the flow, a natural formulation includes a concentration-diffusion equation coupled to the motion equations (Navier-Stokes and continuity equations). In dimensionless form, the motion equations coupled to the concentration-diffusion equation can be written as (40; 47; 59)

$$[1+\phi At]Re\left[\frac{\partial}{\partial t}\mathbf{u}+\mathbf{u}.\nabla\mathbf{u}\right]=-\nabla p+\nabla.\boldsymbol{\tau}+\frac{\phi Re}{Fr^2}\mathbf{e}_g, \tag{5.1}$$

$$\nabla.\mathbf{u}=0, \tag{5.2}$$

$$\frac{\partial C}{\partial t}+\mathbf{u}\cdot\nabla C=\frac{1}{Pe}\nabla^2 C, \tag{5.3}$$

where $\mathbf{u}$, p and $\boldsymbol{\tau}$ are the velocity, the pressure and the deviatoric stress, respectively. We also have $\mathbf{e}_g$ = (cos β, -sin β). The change between heavy and light fluids is modelled using a scaler concentration, C, and the function $\phi(C) = 2C - 1$ changes linearly between -1 and 1. In order to make the governing equations dimensionless, $\hat{D}$ and $\hat{V}_0$ are employed as length and velocity scales, respectively. A mean static pressure gradient is initially subtracted from the momentum equation before scaling the reduced pressure using $(\hat{\mu}_H\hat{V}_0/\hat{D})$. The time and shear stresses are scaled with $(\hat{D}/\hat{V}_0)$ and $(\hat{\mu}_H\hat{V}_0/\hat{D})$, respectively.

1. In this paper, we adopt the convention of denoting dimensional quantities with the ˆ symbol and dimensionless quantities without.

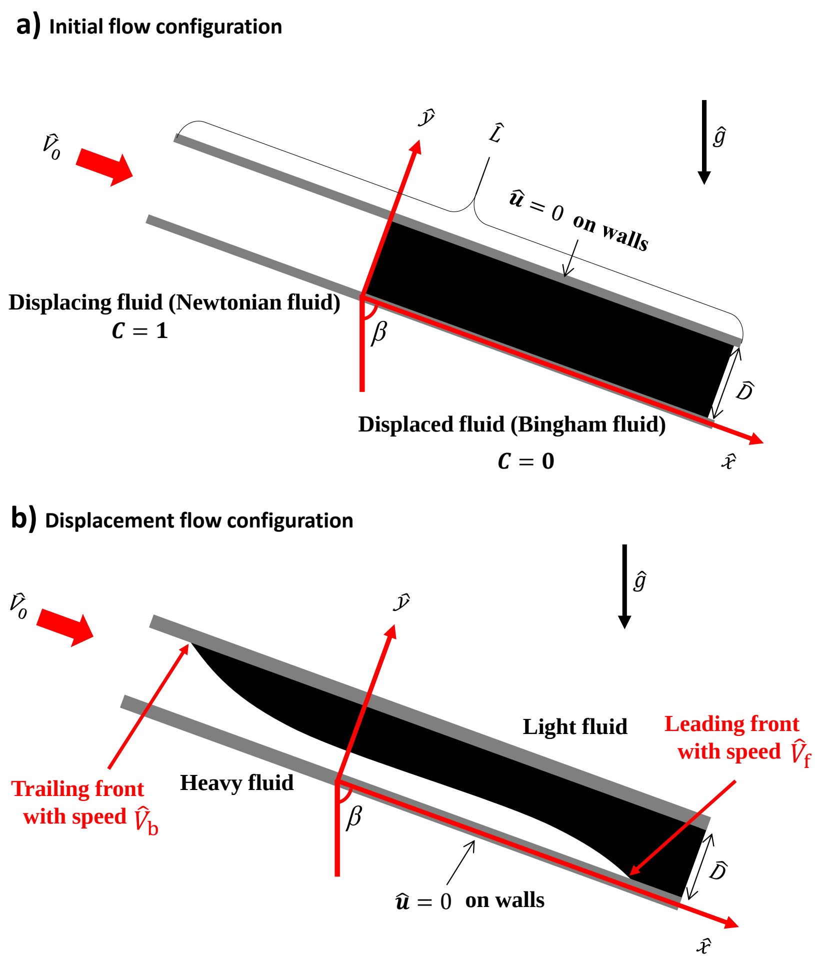

FIGURE 5.1 – Schematic of (a) the initial flow configuration and (b) the displacement flow configuration.

In general, there are seven dimensionless groups that influence our yield stress displacement flow, five of which appear in equations (5.1-5.3): the Péclet number ($Pe = \frac{\hat{V}_0\hat{D}}{\hat{D}_m}$), the Reynolds number ($Re = \frac{\hat{V}_0\hat{D}}{\hat{\nu}}$), the channel inclination angle (β), the densimetric Froude number ($Fr = \frac{\hat{V}_0}{\sqrt{At\hat{g}\hat{D}}}$) and the Atwood number ($At = (\hat{\rho}_H - \hat{\rho}_L)/(\hat{\rho}_H + \hat{\rho}_L)$). The two remaining dimensionless groups are related to the rheological parameters, explained further below. In these dimensionless groups, $\hat{D}_m$ is the molecular diffusivity, $\hat{g}$ the gravitational acceleration, $\hat{\nu} = \frac{\hat{\mu}_H}{((\hat{\rho}_L + \hat{\rho}_H)/2)}$ the kinematic viscosity, $\hat{\rho}_H$ the heavy fluid's density, and $\hat{\rho}_L$ the light fluid's density. In this work, we neglect the effects of Pe by considering that $Pe \gg 1$, implying that the fluids only mix to hydrodynamic effects (in other words, numerical diffusion dominates), and we neglect the effects of At by assuming that $At \ll 1$ (the Boussinesq approximation).

The constitutive law for the Newtonian fluid (displacing fluid) is

$$\tau_H(\boldsymbol{u}) = \dot{\gamma}(\boldsymbol{u}), \tag{5.4}$$

with $\dot{\gamma} = \nabla\mathbf{u} + (\nabla\mathbf{u})^T$. The dimensionless constitutive law for the Bingham fluid (displaced fluid) which includes a yield stress is defined by

$$\tau_L(\mathbf{u}) = \left[m + \frac{Bn}{\dot{\gamma}(\mathbf{u})}\right]\dot{\gamma}_{ij}(\mathbf{u}) \Leftrightarrow \tau_L(\mathbf{u}) > Bn, \tag{5.5}$$

$$\dot{\gamma}_{ij}(\mathbf{u}) = 0 \Leftrightarrow \tau_L(\mathbf{u}) \le Bn, \tag{5.6}$$

where $m = \dfrac{\hat{\mu}_L}{\hat{\mu}_H}$. Note that, to be consistent with the previous literature of similar displacement flows (46; 57; 59), m is conveniently defined as the ratio of the viscous part of the Bingham fluid's effective viscosity (i.e., plastic viscosity) to the Newtonian fluid's viscosity. Considering this definition allows us to computationally explore a wide range of m, for which both small and large values may represent realistic/practical situations. For instance, large values of m represent the displacement of a typical Bingham fluid via a low viscosity Newtonian fluid. On the other hand, small values of m represent a situation where a typical Bingham fluid (e.g., with a small or moderate plastic viscosity) is displaced by a highly viscous Newtonian fluid.

The last dimensionless number that appears in equations (5.5-5.6) is the Newtonian Bingham number ($Bn = \dfrac{\hat{\tau}_y\hat{D}}{\hat{\mu}_H\hat{V}_0}$, with τ_y being the yield stress). In the equations above, the strain rate tensor has components:

$$\dot{\gamma}_{ij}(\mathbf{u}) = \frac{\partial u_i}{\partial x_j} + \frac{\partial u_j}{\partial x_i}, \tag{5.7}$$

and the second invariants, $\dot{\gamma}(\mathbf{u})$ and $\tau_L(\mathbf{u})$, can be written as

$$\dot{\gamma}(\mathbf{u}) = \left[\frac{1}{2}\sum_{i,j=1}^{2}\left[\dot{\gamma}_{ij}(\mathbf{u})\right]^2\right]^{1/2},$$

$$\tau_L(\mathbf{u}) = \left[\frac{1}{2}\sum_{i,j=1}^{2}\left[\tau_{L,ij}(\mathbf{u})\right]^2\right]^{1/2}. \tag{5.8}$$

5.5 Computational approach

Our computational simulations cover a wide range of Bingham numbers ($Bn = 0 - 600$), viscosity ratio ($m = 0.003 - 600$), and also a specific range of channel inclinations ($\beta = 82, 88, 90°$). The equations are discretized using a mixed finite element/finite volume method. A classical augmented Lagrangian approach (20) is used to precisely capture unyielded fluid regions (in particular, to identify static residual layers attached to the channel walls).

The numerical algorithm is implemented using PELICANS (available at https://gforge.irsn.fr /gf/project/pelicans/), i.e., a C++ object oriented open source platform developed at IRSN, France. PELICANS is suitable for the solution of PDEs. More details about the numerical method used in this study or using the PELICANS platform for CFD simulations are available. (40; 57)

Regular rectangular meshes are used for all simulations while they are refined slightly towards the walls (y-direction). Typically, 1500 girds along the channel length and 42 grids along the channel width are used (i.e., 63,000 mesh cells). Note that the independency of the simulation results on the mesh density is investigated, leading to the optimum choice for the mesh density (1500×42=63,000) in terms of accuracy and computational costs. (12) For example, regarding the leading front velocity in a typical displacement flow, the difference between the results of 63,000 mesh cells and those of 71,400 mesh cells is less than 1%. In the computational domain, an imaginary gate valve located at $x = 0$ (at distance $L/4$ from the channel inlet) separates the initial interface between the fluids (see Fig. 5.1a). Our numerical code is benchmarked by comparing our results against those of (49) (for Newtonian displacements) as well as (57) and (46) (for Bingham fluid displacements). Additional details on the benchmarking of numerical code can be found in the recent work. (12)

5.6 Results and discussions

Before we proceed, it should be noted that a large number of parameters appear in displacement flows in practical situations: For example, these flows occur in 3D flow geometries, which can be also inclined at different inclination angles, from horizontal to vertical. In addition, the rheological behaviours are quite complex, which may include elastic, plastic, thixotropic, shear-thinning, and other effects. Here, we have considered a flow problem with a Newtonian fluid displacing a Bingham fluid in a 2D channel. Therefore, we have significantly simplified both the flow geometry and rheological features, in favour of providing a fundamental understanding about these flows by focusing on certain flow parameters.

In this section, we will present our main computational findings for a wide range of the dimensionless flow parameters, in particular by focusing on the effects of the viscosity ratio (m).

5.6.1 Effects of viscosity ratio on displacement flow patterns

Let us first discuss the general effects of a viscosity ratio on yield stress displacements, for example using the panorama of concentration colormaps (at a given time) in Fig. 5.2. These results are for fixed values of β, Fr and Re, for Newtonian displacements ($Bn = 0$) and yield stress displacements ($Bn = 100$). It can be seen that by increasing m, the displacement flow morphology changes. In particular, increasing m affects the front shapes and the residual wall layers, which in return modify the displacement flow efficiency. For all values of m, the displacement flow is nearly symmetric as the displacing finger advances approximately in the

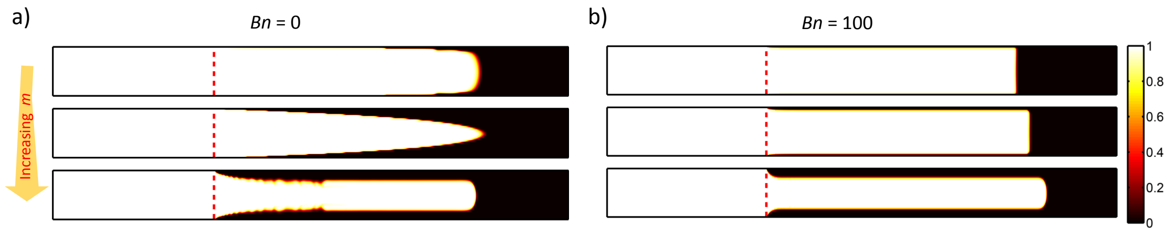

FIGURE 5.2 – Panorama of concentration colormaps at $\beta = 90°$, $Fr = 1000$ and $Re = 500$ for (a) $Bn = 0$ and (b) $Bn = 100$. The rows from top to bottom show $m = 0.01, 1, 100$. The domain size shown is 1×75. The last image, at the right hand side of (b), is the colorbar of the concentration values (here and elsewhere). The red broken lines display the position of the initial interface $x = 0$ (here and elsewhere).

middle of the channel. While the flow behaviours observed for $m = 1$ resemble those of a Newtonian plane Poiseuille flow, the flow pattern changes for $m = 100$, for which interfacial instabilities also appear due to the notable viscosity contrast. However, for $m = 100$ and $Bn = 100$ (last subfigure in Fig. 5.2b), the large yield stress ($Bn \gg 1$) can damp the interfacial waves observed for $m = 100$ and $Bn = 0$. The residual layers of the yield stress fluid seem to be static and their thicknesses appear to grow as m increases.

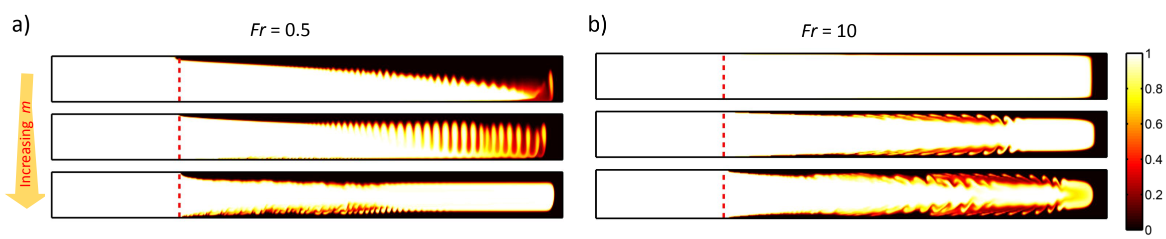

FIGURE 5.3 – Panorama of concentration colormaps at $\beta = 90°$, $Bn = 5$ and $Re = 300$ for (a) $Fr = 0.5$ and (b) $Fr = 10$. The rows from top to bottom show $m = 0.01, 1, 50$. The domain size shown is 1×100.

Fig. 5.3 shows the concentration colormaps for different Fr and m (with the other flow parameters fixed). As seen, the displacement flows are destabilized due to the density and viscosity contrasts, resembling Rayleigh-Taylor or Kelvin-Helmholtz-like instabilities. (46; 12) Fig. 5.3a presents three examples of unstable displacement flows at a small Froude number, $Fr = 0.5$, leading to three different flow patterns. As seen, m influences the flow patterns. For instance, at $m = 0.01$ there is an inertial tip at the displacing front, whereas the inertial tip is damped at $m = 50$. For smaller viscosity ratios ($m = 0.01$ and $m = 1$), the displacing fingers move near the lower channel wall, while the interfacial instabilities are visible in the form of *sinusoidal* shaped waves on the upper interface. The growths of these waves become significant at $m = 1$. For $m = 50$ it is interesting to note that, unlike the smaller viscosity ratios, the displacing finger is more towards the channel centre, while non-uniform, asymmetric waves are formed at the two sides of the displacing finger (i.e., the lower and upper sides of the interface). However, when the buoyancy forces are smaller (i.e., $Fr = 10$) as shown in Fig. 5.3b, the effects of m on the flow patterns are quite different. For $m = 0.01$, the flow is symmetric and resembles a plug-like profile, while for $m = 1$ and $m = 50$ unstable displacements appear. In these conditions, symmetric unstable waves form at the upper and lower displacing finger sides. Increasing the value of m leads to growing the instabilities and eventually the fluids mix at the interface. Eslami *et al.* (12) have numerically investigated similar flows finding that, for $m = 1$, the crucial parameter that controls the onset of these instabilities is Fr. They have mentioned that these instabilities do not form at higher values of Froude numbers (e.g., $Fr > 10$), independent of the yield stress value, while for smaller Fr their appearance depends on the yield stress value.

It can be seen from Fig. 5.3a that there are fascinating interfacial waves appearing on the upper interface of the displacing finger. Although these waves are mainly formed due to the existence of significant buoyancy effects (smaller Fr), the other governing dimensionless numbers also have notable effects on their appearance, albeit with to a lesser extent. In order to give a broader understanding of these waves, characterizing their wavelength versus Bn, m and Fr can be useful. To do so, the variation of the mean wavelength of the interfacial waves ($\bar{l}$) at long time versus Bn is plotted in Fig. 5.4. Note that $\bar{l}$ for all the cases is calculated based on the seven waves closest to the channel end, while excluding the frontal inertial tip. At fixed Re and Fr, Fig. 5.4a shows that $\bar{l}$ decreases with both Bn and m. However, at larger Re, Fig. 5.4b shows that Bn has an opposite effect on $\bar{l}$. This implies that the variation of $\bar{l}$ is not monotonic versus Bn and it depends on the other flow parameters. In addition, Fig. 5.4b shows that by increasing Fr, $\bar{l}$ slightly decreases (note that at almost $Fr > 10$ the flow becomes stable and the waves disappear). Our simulations also reveal that the wave amplitude is strongly controlled by all the dimensionless flow parameters, especially Fr and Bn (not shown for brevity). Indeed, these interfacial waves are quite complex, whereas our approach in analyzing them has been quite crude; therefore, to better understand the appearance of these waves, a detailed stability analysis may seem necessary.

5.6.2 Effects of viscosity ratio on slump-type and centre-type flow regimes

Fig. 5.5 shows the displacement concentration colormaps for fixed β, Re, Bn and Fr, and different m. The channel is strictly horizontal ($\beta = 90°$). In Fig. 5.5a, buoyancy forces ($Fr = 0.8$) clearly result in the formation of a slump-type displacement flow where the Newtonian displacing finger is close to the channel lower wall. However, even in this regime, there is still a thin yield stress fluid layer (with thickness h_l) adjacent to the lower wall. There is also a thick displaced layer (with thickness h_u) attached to the upper wall. These fluid layers seem to be static. The corresponding speed contours and velocity profiles are given in Fig. 5.5b and Fig. 5.5c, respectively. Fig. 5.5b confirms that the displacement flow is stable and the residual layers are smooth. In addition, the speed contours are zero within the yield stress fluid layers

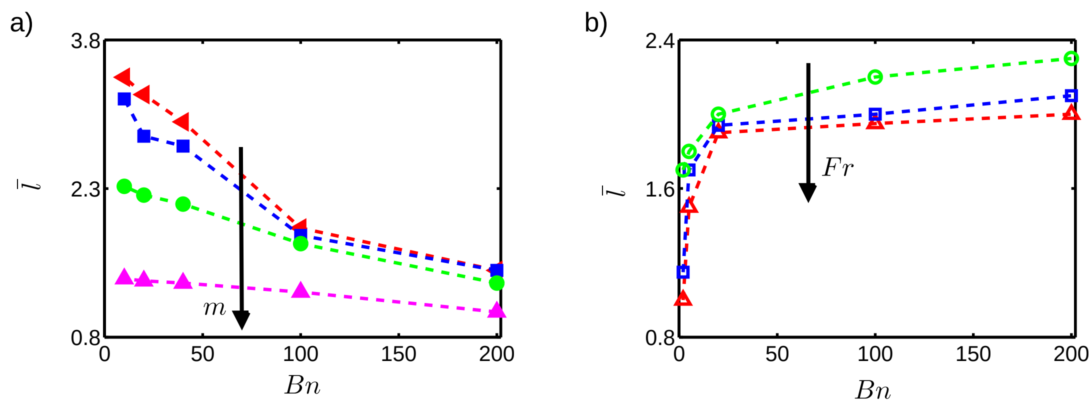

FIGURE 5.4 – The mean wavelength of the interfacial waves ($\bar{l}$) at $t = 36$ as a function of Bn. (a) At $Re = 200$ and $Fr = 0.2$ with the data corresponding to $m = 0.01$ (◂), $m = 0.1$ (■), $m = 1$ (●) and $m = 20$ (▲); (b) At $Re = 500$ and $m = 40$ with the data corresponding to $Fr = 0.1$ (○), $Fr = 0.2$ (□) and $Fr = 0.4$ (△).

adjacent to the upper wall and in the vicinity of the lower wall, confirming that they are fully static. The same interpretations can be made using the velocity vector fields.

Fig. 5.5d presents the displacement concentration colormaps for the same parameters as in Fig. 5.5a albeit for $m = 50$. The heavy fluid flows as a finger in the middle of the channel (i.e., a centre-type displacement). In this case, the ratio of the upper to lower static layer thicknesses approaches unity ($h_u/h_l \to 1$). Comparing Fig. 5.5a and Fig. 5.5d reveals the important effects of increasing m on the displacement flow patterns: while for $m = 1$ a slump-type regime is observed, for $m = 50$ a centre-type flow regime is found. This implies that for larger m, the buoyancy force is apparently less effective in pushing the displacing finger towards the lower wall. Fig. 5.5e and Fig. 5.5f show that the velocity field is nearly symmetry with respect to the channel centreline. While the high speed regions are towards the channel center, the fluid within the yield stress fluid layers (on the upper and lower walls) is static. For this flow, it seems as if the Newtonian displacing fluid is moving like a Poiseuille flow into a narrower channel for which the walls are made of the static yield stress fluid.

Let us classify our displacement flow results based on the appearance of the slump-type and centre-type flow regimes. To do so, we rely on Eslami *et al.* (12) who have introduced a criteria for such classification (for the case of $m = 1$), demonstrating that for $h_u/h_l > 1.6$ and $h_u/h_l \leq 1.6$, the slump-type and centre-type flow regimes appear, respectively. Fig. 5.6 plots these two regimes for different viscosity ratios in the plane of Bn and $\frac{Re}{Fr}$. This plane has been previously shown to be suitable to delineate slump-type/centre-type displacements. (50; 12) As can be seen, for all the subfigures, the flow regimes are reasonably segregated using Bn and $\frac{Re}{Fr}$ as the dimensionless groups. The results show that the transition between the slump-type and centre-type regimes is more or less independent of Bn. Moreover, for both $m = 0.01$ and

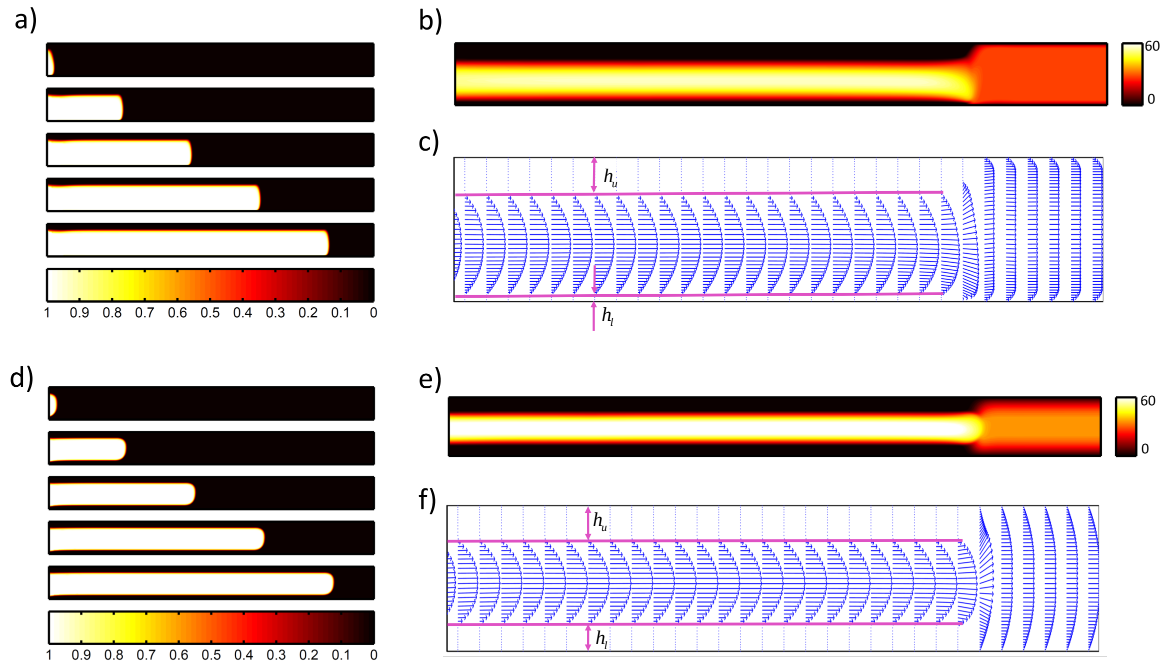

FIGURE 5.5 – Computational results for $\beta = 90°$, $Re = 500$, $Bn = 100$ and $Fr = 0.8$ at (a, b, c) $m = 1$ and at (d, e, f) $m = 50$; (a) & (d) Concentration colormaps at times $t = [2, 6.5, ..., 20]$; (b) & (e) Speed contours: $V = \sqrt{{V_x}^2 + {V_y}^2}$ at $t = 20$ (V_x denotes the stream-wise velocity component and V_y is the depthwise velocity component); (c) & (f) Velocity vectors and the interface heights at $t = 20$: h_u and h_l show the thickness of upper and lower static residual wall layers, respectively. The domain size shown is 1×50, starting from the gate valve position at $x = 0$. The bottom image in subfigures (a) & (d) is the colorbar of the concentration values (here and elsewhere).

$m = 1$, the datapoints are approximately separated on the two sides of the horizontal dashed line at $Re/Fr = 60$. The appearance of Re/Fr, as the relevant dimensionless group, highlights the role of a balance between buoyancy and viscous stresses in the critical transition. By increasing m, the transition still depends on Re/Fr but the critical transition value increases, i.e., for $m = 100$ and $m = 400$, we find $Re/Fr \approx 1200$ and $Re/Fr \approx 3000$, respectively.

Fig. 5.7 presents the variation of the critical values of Re/Fr (versus m) corresponding to the transition between slump-type and centre-type displacements. As seen, initially there is a plateau value for Re/Fr versus m but it eventually sharply increases. Our results indicate that for smaller viscosity ratios ($m \leqslant 1$), the variation in m does not seem to influence the appearance of slump-type/centre-type displacements. Nevertheless, increasing m beyond unity increases the critical value of Re/Fr and helps the formation of centre-type flows. This finding implies that the buoyancy force is apparently only effective in pushing the displacing finger towards the lower wall at smaller m.

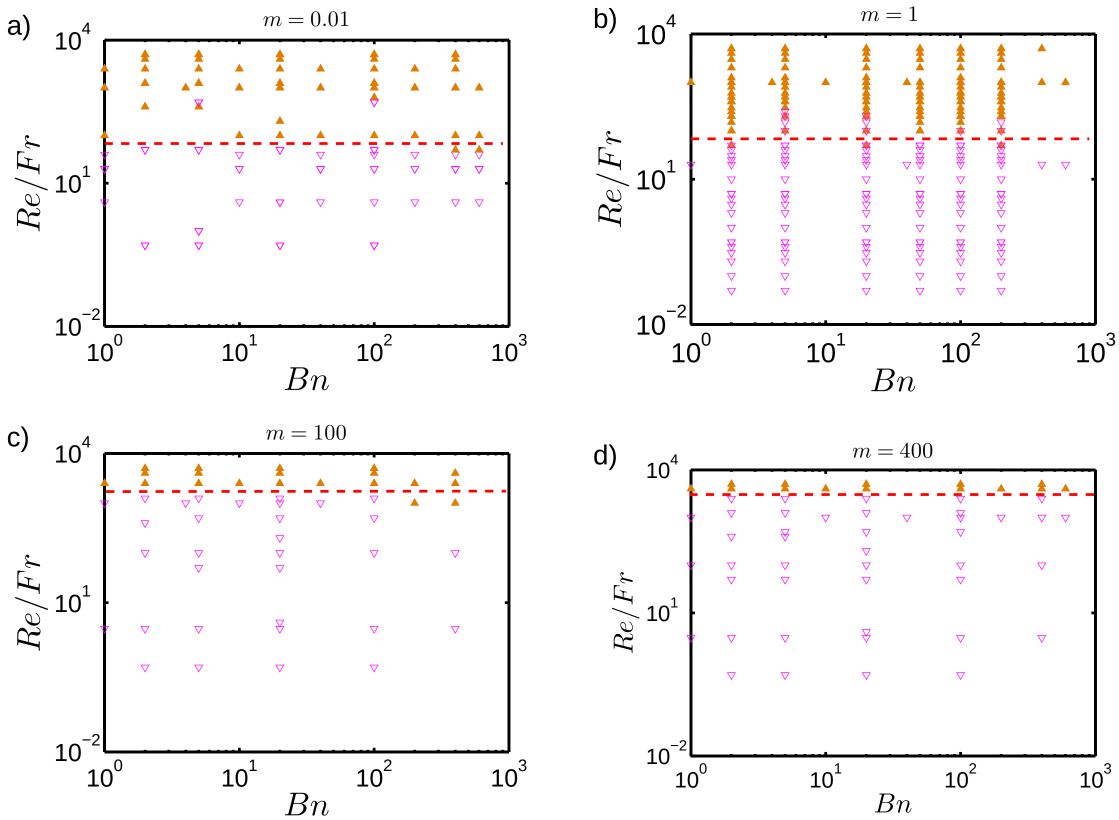

FIGURE 5.6 – Flow regime classification based on the class of the slump-type (▲) and centre-type (▽) regimes for different viscosity ratios. In each subfigure the horizontal dashed line represents (a) $Re/Fr = 60$, (b) $Re/Fr = 60$, (c) $Re/Fr = 1200$, and (d) $Re/Fr = 3000$.

5.6.3 Effects of viscosity ratio on leading front features

Here, we investigate the dimensionless front velocity of the advancing Newtonian displacing fluid into the yield stress displaced one (i.e., the leading front velocity, V_f) as a function of the governing dimensionless numbers. Since the aspect ratio of our channel is small, the front velocity may provide an indication of the overall displacement efficiency. If the front velocity is small (e.g., tending to unity), the displacement flow is efficient. The readers may consult (51) for details on the calculation of V_f.

The variation of V_f versus Bn is plotted in Fig. 5.8 for different m, at fixed values of Re and Fr. It can be seen that, first of all, increasing Bn generally results in decreasing V_f (59; 12); therefore, the displacement flow efficiency increases. This trend is in agreement with the finding of (57) for iso-desnity displacements, showing that increasing the yield stress of the displaced fluid affects the plug ahead of the Newtonian displacing finger, leading to a reduction in the thickness of the static residual wall layers, which in return decreases V_f. Fig. 5.8 also shows that V_f is strongly affected by changes in the value of m.

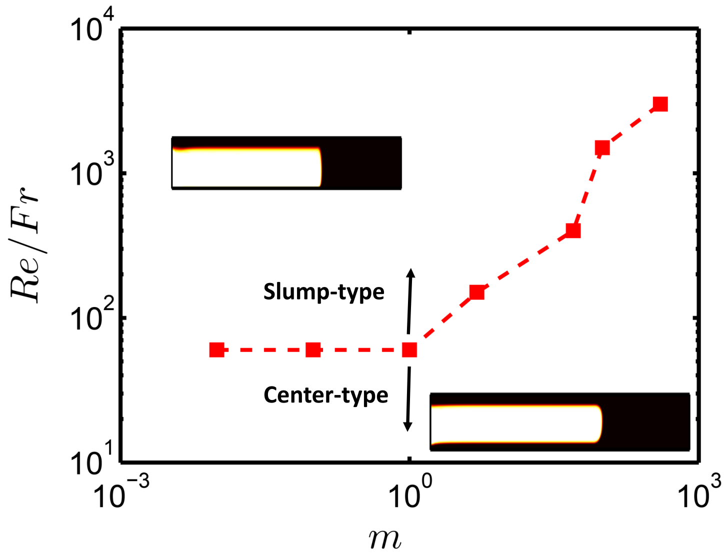

FIGURE 5.7 – The variation of the critical values of Re/Fr versus m for the transition between slump-type and centre-type displacements in a horizontal channel. Two illustrative snapshots corresponding to a slump-type flow and a centre-type flow are included.

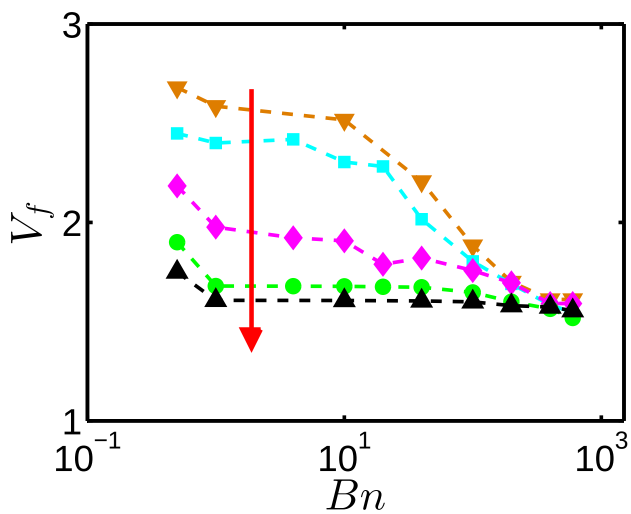

FIGURE 5.8 – The effect of Bn on the leading front velocity, V_f, for Re = 200 and Fr = 0.2. The channel is horizontal in all cases. The data correspond to m = 0.003 (▼), m = 0.01 (■), m = 1 (♦), m = 100 (●), m = 400 (▲). The value of m increases in the red arrow direction.

In order to further highlight the influence of the viscosity ratio on the displacement flow efficiency, Fig. 5.9 illustrates the variation of V_f versus m for different Bn and Fr. A comparison among the subfigures reveals that the effect of m on V_f is not monotonic with respect to Fr, such that m has an opposite impact on V_f at low and high values of Fr. For lower Fr

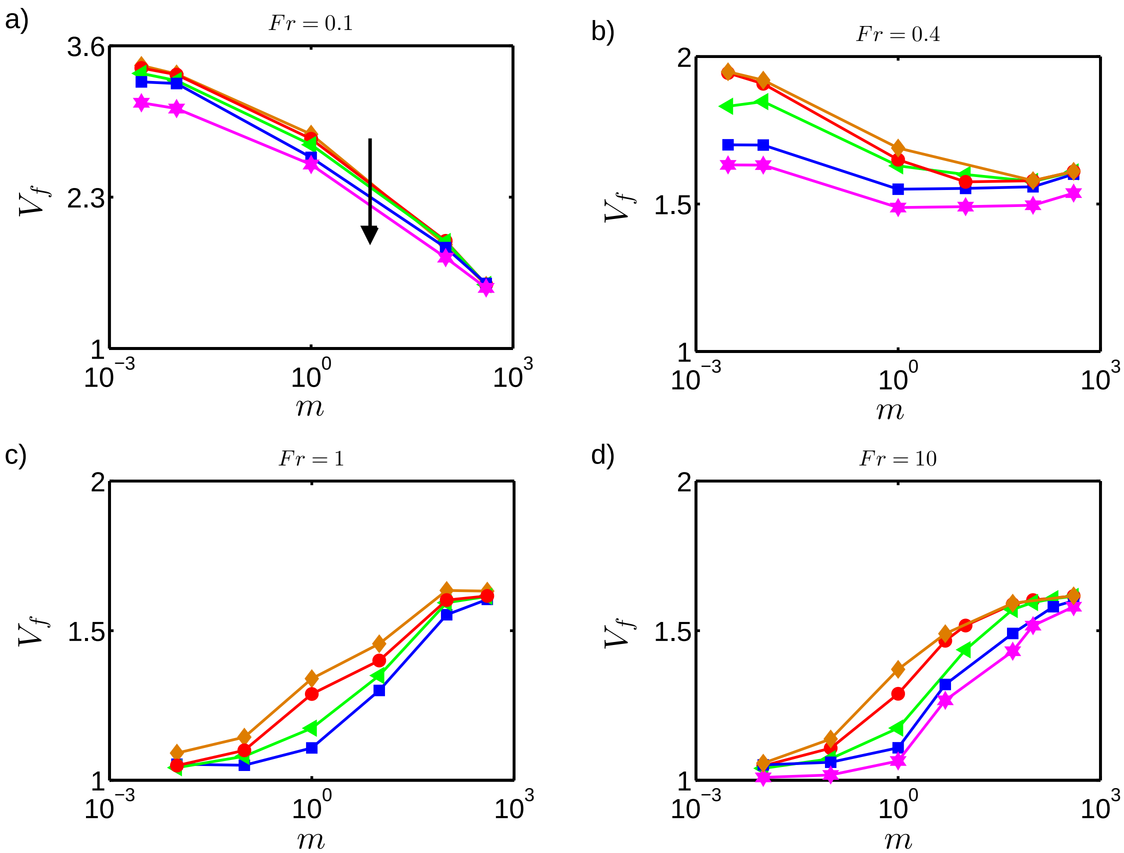

FIGURE 5.9 – Variation of V_f versus m at $Re = 500$ for (a) $Fr = 0.1$; (b) $Fr = 0.4$; (c) $Fr = 1$; and (d) $Fr = 10$. The data correspond to $Bn = 2$ (♦), $Bn = 5$ (●), $Bn = 20$ (◂), $Bn = 100$ (■) and $Bn = 400$ (★). The value of Bn increases in the black arrow direction.

(Fig. 5.9a and Fig. 5.9b), increasing m results in decreasing V_f but for higher Fr (Fig. 5.9c and Fig. 5.9d), the opposite occurs.

As mentioned above, the viscosity ratio (m) has a remarkable impact on the leading front velocity and consequently the displacement flow efficiency. In our work, we have defined m based on the ratio of the plastic viscosity of the displaced fluid ($\hat{\mu}_L$) to the viscosity of displacing fluid. Nevertheless, in a recent series of papers, Thompson & Soares and co-workers (54; 17; 7; 16) have shown that, when dealing with viscoplastic materials, a more reasonable way is to define an "effective viscosity ratio" (m^*) based on an "effective viscosity" by including the yield stress in the definition of the characteristic viscosity of the displaced fluid (i.e., $\frac{\hat{\tau}_y}{\hat{V}_0/\hat{D}} + \hat{\mu}_L$). Thus, our viscosity ratio (m) and that of Thompson (m^*) are simply related through $m^* = m + Bn$, which we use to describe the influence of the "effective viscosity ratio" on V_f. The effect of m^* on V_f is presented in Fig. 5.10 for different Fr. As seen, at small Fr, by increasing m^* the leading front velocity decreases whereas it increases by m^* at large $Fr = 10$. For all the results presented throughout the paper, the simple conversion between m and m^* (i.e., $m^* = m + Bn$)

can be used to analyze the influence of the effective viscosity ratio on our flows.

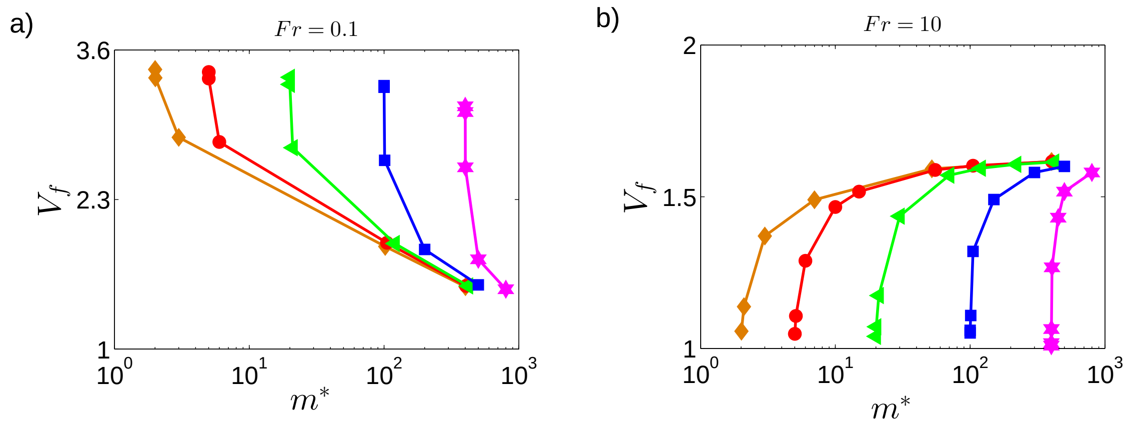

FIGURE 5.10 – Variation of V_f versus m^* at Re = 500 for (a) Fr = 0.1 and (b) Fr = 10. The data correspond to Bn = 2 (♦), Bn = 5 (•), Bn = 20 (◂), Bn = 100 (■) and Bn = 400 (★).

5.6.4 Effects of viscosity ratio on trailing front features

The main feature associated to the trailing front in displacement flows is the appearance of back-flow, which occurs when the trailing front moves against the mean flow direction, mainly due to buoyancy effects. The importance may become clear when noting that, in some industrial processes, the objective of a displacement process is to completely remove the displaced fluid by the displacing one; therefore, the appearance of a backward motion of the trailing front (in other words any buoyancy-driven back-flows) must be ideally avoided.

Fig. 5.11 portrays examples of our simulation results at fixed values of β = 90°, Re = 500, Bn = 2 and Fr = 0.4, for various m. Fig. 5.11a and Fig. 5.11b show a sequence of concentration colormaps for displacements with back-flows with m = 0.01 and m = 1, respectively. In these cases the trailing front moves against the mean imposed flow direction (i.e., a *back-flow regime*). Nevertheless, for m = 100 in Fig. 5.11c, the trailing front appears to be pinned on the top wall and, unlike the displacements at smaller m, the lighter displaced fluid does not move upstream (i.e., a *no-back-flow regime*). Since the backward motion of the trailing front is due to buoyancy, the existence of the no-back-flow regime at larger m implies that larger viscosity ratios reduce the relative strength of buoyancy in inducing the training front's backward motion. The behaviours of the trailing fronts can be observed in more detail in the spatio-temporal diagram of the depth-averaged concentration in Fig.s 5.11d, e & f. For example, at m = 100 in Fig. 5.11f, the trailing front does not move against the flow direction and it is pinned; consequently, the trailing front velocity is exactly zero during the displacement flow.

Although our focus in this paper is on the effect of m on displacement flows, it should be noted that the combination of Bn and Fr strongly affects the flow dynamics. For example, the main source of the back-flow regime is buoyancy, while the yield stress also has a notable role. To

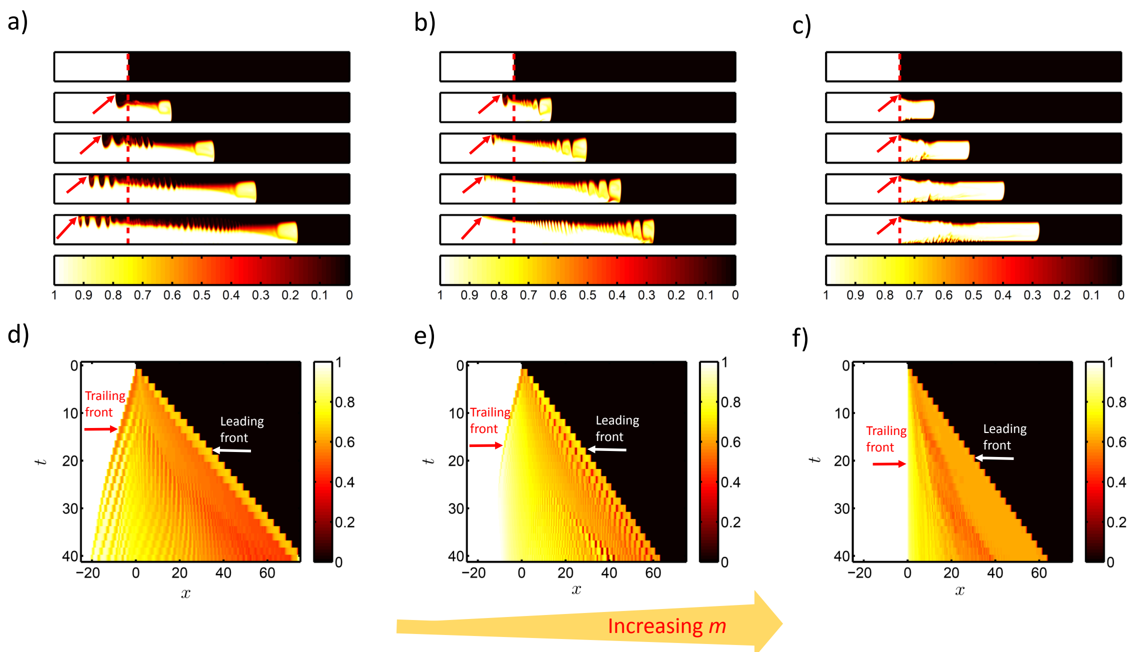

FIGURE 5.11 – Concentration colormaps at $t = [0, 7, ..., 28]$ at $\beta = 90°$, $Re = 500$, $Bn = 2$ and $Fr = 0.4$ for (a) $m = 0.01$ (a case with a back-flow), (b) $m = 1$ (a case with a back-flow) and (c) $m = 100$ (a case without a back-flow). (d), (e) & (f) Spatiotemporal diagrams of the depth-averaged concentration values for the same simulations as in (a), (b) and (c). The size of the domain shown is 1×100. The red/white arrow marks the trailing/leading front position.

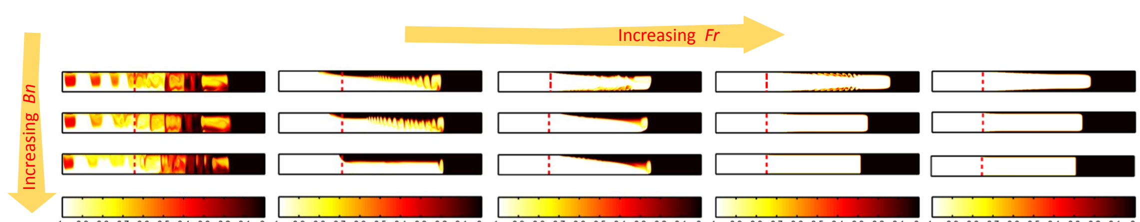

FIGURE 5.12 – Panorama of concentration colormaps at $\beta = 90°$, $m = 1$ and $Re = 500$. The rows from left to right show $Fr = 0.1, 0.4, 1, 10, 1000$. The rows from top to bottom display $Bn = 5, 20, 100$.

make this clear, Fig. 5.12 shows panoramas of the concentration colormaps at a given time, for fixed Re, β and m. As seen, for all Bn, by increasing Fr, a no-back-flow displacement occurs. At a given Froude number (e.g. $Fr = 0.4$), the movement of the trailing front against the mean flow direction decreases by increasing Bn. The motion completely stops at larger Bn (not shown). In addition to the appearance of the back-flow, by increasing Fr and Bn, the displacement flow morphology changes significantly. Stable displacements are observed at higher Fr, regardless of Bn. However, at smaller Fr, displacement flow patterns highly depends on Bn in a way that by increasing Bn the interfacial instabilities are damped.

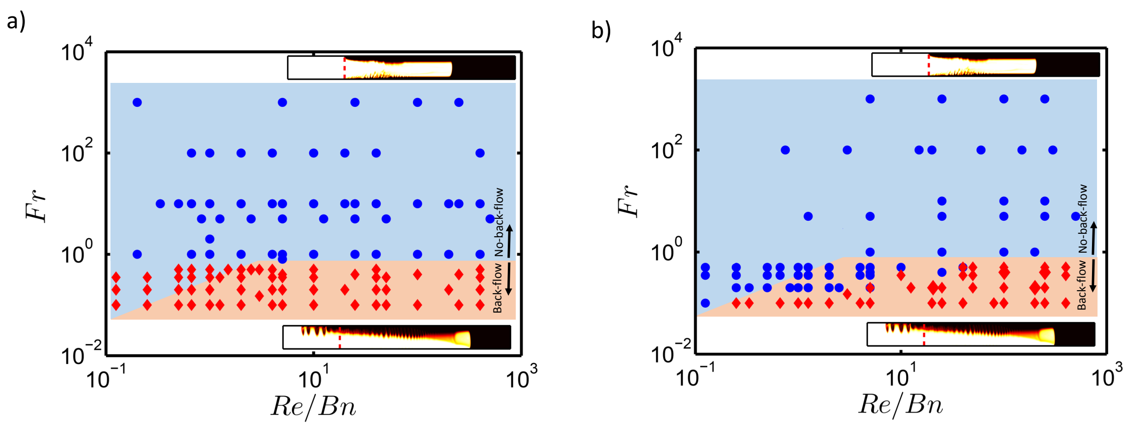

FIGURE 5.13 – Back-flow and no-back-flow regimes in the plane of Fr and Re/Bn for (a) $m = 0.01$ and (b) $m = 400$. The data corresponding to the no-back-flow regime are marked by (•) and the back-flow regime by (♦). The red and blue colored areas mark the back-flow and no-back-flow regimes $m = 1$. Two illustrative snapshots corresponding to a back-flow and a no-back-flow are included.

Let us quantify the formation of the back-flow and no-back-flow regimes for a large number of simulations, following the previous studies that have classified these regimes in Newtonian cases. (52; 51) The transition between the no-back-flow and back-flow regimes is governed by an interplay between buoyancy, inertia and yield stresses, which can be grouped into Fr and Re/Bn, (12) as depicted in Fig. 5.13a (for $m = 0.01$) and Fig. 5.13b (for $m = 400$). The simulations results for $m = 1$ are also superposed on both graphs. First of all, no-back-flow and back-flow displacements are segregated in this plane. For all m, no-back-flow displacements are in general observed at higher Fr. However, at smaller values of Fr, the flow regime seems to depend on both Re/Bn and Fr. In these conditions, back-flows are more frequent for $m = 0.01$ than for $m = 400$. Also, for $m = 400$, the minimum Froude number required for the transition to the back-flow regime decreases at smaller Re/Bn.

We end this section by reminding that, although previous relevant studies have concentrated on a narrow viscosity ratio range (typically $0.1 \leq m \leq 10$), our approach in exploring a wider viscosity ratio range ($0.003 \leq m \leq 600$) allows us to observe and analyze the flow dynamics at extreme values of m.

5.6.5 Effects of viscosity ratio in combination with different channel inclinations

Here, we present the effects of different viscosity ratios in combination with different channel inclination angles (β) on the displacement flow behaviours. Fig. 5.14 shows the displacement concentration colormaps for fixed Bn, Re and Fr. For a given viscosity ratio, by increasing the channel inclination, the displacement flow morphology changes notably. Let us first consider small viscosity ratios (i.e., $m = 0.01$ and $m = 1$). In these cases, instabilities appear at the interface and they generally grow by increasing β, implying that the buoyancy stress can locally overcome the yield stress when β increases, making the flow more unstable. In addition, in the strictly horizontal channel, an inertial front pattern is observed, which disappears at larger β where a plug-like front is instead formed. Furthermore, the backward motion of the trailing front can be enhanced by increasing β and the trailing front moves further backward, due to stronger buoyancy effects. For larger viscosity ratios (i.e., $m = 50$), non-uniform, asymmetric displacement flow patterns appear and they do not much vary with increasing the channel inclination.

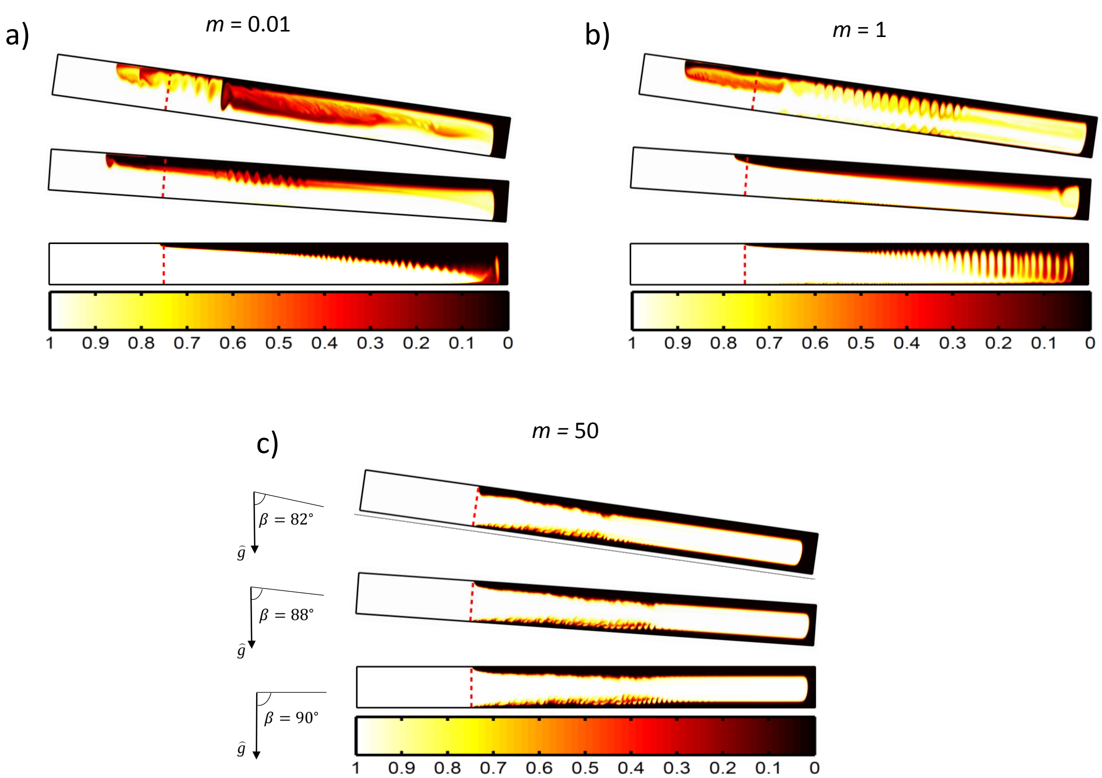

FIGURE 5.14 – Concentration colormaps at $Re = 300$, $Bn = 5$ and $Fr = 0.5$ for (a) $m = 0.01$, (b) $m = 1$ and (c) $m = 50$. The rows from top to bottom show $\beta = 82, 88, 90°$. The domain size shown is 1×100.

At a fixed viscosity ratio, the effects of the channel inclination angle on the trailing front behaviours can be further analyzed, as demonstrated in Fig. 5.15. The concentration colormaps for two displacement cases at $\beta = 88°$ and $\beta = 82°$ are presented in Fig. 5.15a and Fig. 5.15b, respectively. Although the trailing front moves backward in both cases, the type of the back-

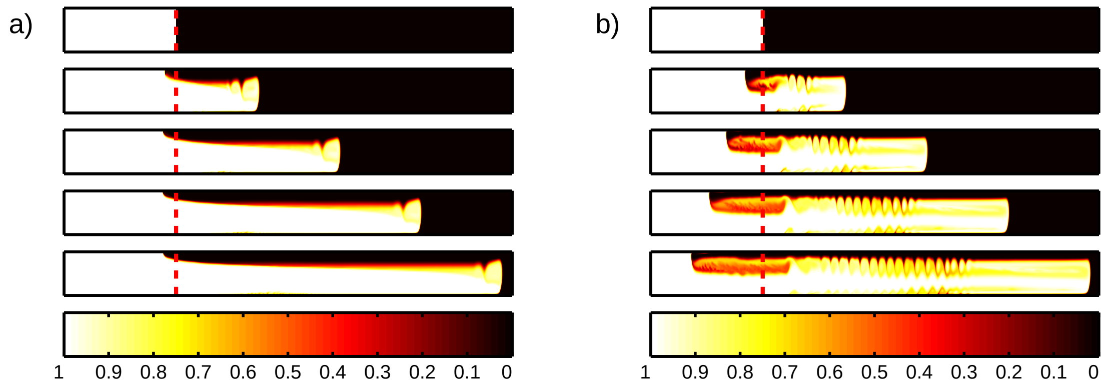

FIGURE 5.15 – Concentration colormaps at $t = [0, 7.5, ..., 30]$ at $Re = 300$, $Bn = 5$, $m = 1$ and $Fr = 0.5$ for (a) $\beta = 88°$ and (b) $\beta = 82°$, showing different types of back-flows. The size of the domain shown is 1×100.

flow is different: Fig. 5.15a corresponds to a *stationary interface flow* and Fig. 5.15b shows a *sustained back-flow*. (51) In the former, trailing front initially moves against the mean flow but eventually stops and becomes apparently pinned to the upper wall, so that the interface becomes nearly stationary. This is because the longitudinal buoyancy component that drives the trailing front motion progressively decreases (as the interface slope decreases), becoming relatively negligible when the interface becomes almost parallel to the channel wall. However, at $\beta = 82°$, the longitudinal buoyancy component is always present due the channel inclination and it is sufficiently strong to maintain a sustained back-flow motion.

5.7 Summary

We have computationally considered displacement flows of two miscible fluids along a 2D plane channel where the displacing fluid is denser than the displaced fluid. We have focused on the displacements of yield stress Bingham fluids by Newtonian fluids for a wide range of flow parameters. We have shown that different displacement flow behaviours can be characterized in the terms of five dimensionless numbers: the Bingham number (Bn), the viscosity ratio (m), the Reynolds number (Re), the densimetric Froude number (Fr) and the channel inclination (β).

We have focused our attention to the viscosity ratio, showing its remarkable effects on the flow. In particular, we have analyzed in detail the effects of m on the displacement flow patterns, the main flow regime (i.e., slump-type and centre-type flow regimes), the leading front features (e.g., the leading front velocity) and the trailing front features (back-flow/no-back-flow regimes). We have shown that the appearance of slump-type/centre-type displacements does not depend on m when it is small ($m \leqslant 1$), whereas higher values of m help the formation of centre-type flows. The viscosity ratio has an opposite impact on the leading front velocity at low and high values of Fr. Also, increasing m leads to the formation of no-back-flow regimes. We have also analyzed the effect of m in combination with different channel inclinations, finding that increasing β changes the displacement flow morphology, making the flow generally more unstable.

It is worth reminding about a limitation of the current work, i.e., the 2D flow geometry assumption in place of a more realistic 3D flow geometry. However, it should be also noted that our simulations have focused on near horizontal channel inclinations, for which the effects of mixing on the flow dynamics remain minor and, thus, 2D simulations can be still successful in providing essential understandings about the flow. As shown in the previous work (12), the general viscoplastic displacement flow aspects (e.g., static layers, slump-type and centre-type flow regimes, etc.) observed in 2D would also exist in 3D flow geometries. In addition, some of the important flow aspects, such as the onset of instabilities, can be understood using 2D plane channel flows.

We end this paper by providing a future perspective. First, although there has been a growing number of research works considering displacement flows in recent years, certain fundamental flow features require more attention. For instance, stability analyses of viscoplastic displacements have not been well developed in the literature. Second, since in natural and industrial applications, practical fluids exhibit many competing non-Newtonian behaviours simultaneously, a future direction can consider displacement flows with several exotic non-Newtonian effects (especially viscoelastic effects). Third, as most of the numerical and semi-analytical studies concerning displacement flows (including the current work) have considered 2D flow geometries, performing detailed displacement simulations in 3D flow geometries seems essential. Finally, a review paper on displacement flows covering Newtonian and non-Newtonian behaviours can help to provide a global understanding of these flows.

Acknowledgements

This research has been carried out at Université Laval, supported partially by the Canada Foundation for Innovation (Grant no.s GF112622, GQ113034 and GF517657) and the Discovery Grant of the Natural Sciences and Engineering Research Council of Canada (Grant no. CG10915). The research has been enabled in part by support provided by Calcul Québec. AR also acknowledges the support via the Iran National Science Foundation (Grant no. 97013654).

5.8 Bibliography

[1] K. Alba, S.M. Taghavi, J.R. de Bruyn, and I.A. Frigaard. Incomplete fluid-fluid displacement of yield-stress fluids. part 2: Highly inclined pipes. *J. non-Newt. Fluid Mech.*, 201:80–93, 2013.

[2] M. Allouche, I. Frigaard, and G. Sona. Static wall layers in the displacement of two visco-plastic fluids in a plane channel. *J. Fluid Mech.*, 424(1):243–277, 2000.

[3] A. Amiri, F. Larachi, and S.M. Taghavi. Buoyant miscible displacement flows in vertical pipe. *Phys. Fluids*, 28(10):102105, 2016.

[4] S.H. Bittleston, J. Ferguson, and I.A. Frigaard. Mud removal and cement placement during primary cementing of an oil well–Laminar non-Newtonian displacements in an eccentric annular Hele-Shaw cell. *J. Eng. Math.*, 43(2-4):229–253, 2002.

[5] R. Brandao, J.V. Fontana, and J.A. Miranda. Interfacial pattern formation in confined power-law fluids. *Phys. Rev. E*, 90(1):013013, 2014.

[6] D. Burfoot, K.E. Middleton, and J.T. Holah. Removal of biofilms and stubborn soil by pressure washing. *Trends Food Sci.Technol.*, 20:S45–S47, 2009.

[7] H.M. Caliman, E.J. Soares, and R.L. Thompson. An experimental investigation on the Newtonian-Newtonian and viscoplastic-Newtonian displacement in a capillary tube. *J. non-Newt. Fluid Mech.*, 247:207–220, 2017.

[8] N.G. Cogan and J.P Keener. Channel formation in gels. *SIAM J. Appl. Math.*, 65(6):1839–1854, 2005.

[9] P. Coussot. Saffman–Taylor instability in yield-stress fluids. *J. Fluid Mech.*, 380:363–376, 1999.

[10] D.A. de Sousa, E.J. Soares, R.S de Queiroz, and R.L. Thompson. Numerical investigation on gas-displacement of a shear-thinning liquid and a visco-plastic material in capillary tubes. *J. non-Newt. Fluid Mech.*, 144(2):149–159, 2007.

[11] Y. Dimakopoulos and J. Tsamopoulos. Transient displacement of a viscoplastic material by air in straight and suddenly constricted tubes. *J. non-Newt. Fluid Mech.*, 112(1):43–75, 2003.

[12] A. Eslami, I.A. Frigaard, and S.M. Taghavi. Viscoplastic fluid displacement flows in horizontal channels: Numerical simulations.
em J. non-Newt. Fluid Mech., 249:79–96, 2017.

[13] A. Eslami and S.M. Taghavi. Viscous fingering regimes in elasto-visco-plastic fluids. *J. non-Newt. Fluid Mech.*, 243:79–94, 2017.

[14] A. Eslami and S.M. Taghavi. Viscous fingering of yield stress fluids: The effects of wettability. *J. non-Newt. Fluid Mech.*, 264:25–47, 2019.

[15] A. Etrati, K. Alba, and I.A. Frigaard. Two-layer displacement flow of miscible fluids with viscosity ratio: Experiments. *Phys. Fluids*, 30(5):052103, 2018.

[16] J.F Freitas, E.J. Soares, and R.L. Thompson. Immiscible Newtonian displacement by a viscoplastic material in a capillary plane channel. *Rheol. Acta.*, 50(4):403–422, 2011.

[17] J.F. Freitas, E.J. Soares, and R.L. Thompson. Viscoplastic-viscoplastic displacement in a plane channel with interfacial tension effects. *Chem. Eng. Sci.*, 91:54–64, 2013.

[18] P.J. Fryer, G.K. Christian, and W. Liu. How hygiene happens: physics and chemistry of cleaning. *Int. J. Dairy Technol.*, 59(2):76–84, 2006.

[19] C. Gabard and J.P. Hulin. Miscible displacement of non-Newtonian fluids in a vertical tube. *Eur. Phys. J. E.*, 11(3):231–241, 2003.

[20] R. Glowinski and P. Le Tallec. Augmented Lagrangian and operator-splitting methods in nonlinear mechanics. *Phys. Fluids*, 19:084106, 2007.

[21] S. Hill et al. Channeling in packed columns. *Chem. Eng. Sci.*, 1(6):247–253, 1952.

[22] K.E. Holloway, P. Habdas, N. Semsarillar, K. Burfitt, and J.R. de Bruyn. Spreading and fingering in spin coating. *Phys. Rev. E*, 75(4, 2):046308, 2007.

[23] G.M. Homsy. Viscous fingering in porous media. *Annu. Rev. Fluid Mech.*, 19(1):271–311, 1987.

[24] P.D. Howell, S.L. Waters, and J.B. Grotberg. The propagation of a liquid bolus along a liquid-lined flexible tube. *J. Fluid Mech.*, 406:309–335, 2000.

[25] D. Huh, H. Fujioka, N. i. Tung, Y. C. Futai, R. Paine, J. B. Grotberg, and S. Takayama. Acoustically detectable cellular-level lung injury induced by fluid mechanical stresses in microfluidic airway systems. *Proc. Natl. Acad. Sci.*, 104(48):18886–18891, 2007.

[26] P.C. Huzyak and K.W. Koelling. The penetration of a long bubble through a viscoelastic fluid in a tube. *J. non-Newt. Fluid Mech.*, 71(1):73–88, 1997.

[27] E. Lajeunesse, J. Martin, N. Rakotomalala, and D. Salin. 3D instability of miscible displacements in a Hele-Shaw cell. *Phys. Rev. Lett.*, 79(26):5254, 1997.

[28] L.W. Lake. *Enhanced oil recovery.* Prentice Hall, 1989.

[29] T.F Lins and J.l Azaiez. Flow instabilities of time-dependent injection schemes in immiscible displacements. *Can. J. Chem. Eng.*, 94(11):2061–2071, 2016.

[30] Sl Malhotra and M M Sharma. Impact of fluid elasticity on miscible viscous fingering. *Chem. Eng. Sci.*, 117:125–135, 2014.

[31] G.V.L. Moisés, M.F. Naccache, K. Alba, and I.A. Frigaard. Isodense displacement flow of viscoplastic fluids along a pipe. *J. non-Newt. Fluid Mech.*, 236:91–103, 2016.

[32] R. Mollaabbasi and S.M. Taghavi. Buoyant displacement flows in slightly non-uniform channels. *J. Fluid Mech.*, 795:876–913, 2016.

[33] S. Mora and M. Manna. Saffman-Taylor instability for generalized Newtonian fluids. *Phys. Rev. E.*, 80(1):016308, 2009.

[34] E.B. Nelson and D. Guillot. *Well Cementing, 2nd Edition.* Schlumberger Educational Services, 2006.

[35] F.M. Orr and J.J. Taber. Use of carbon dioxide in enhanced oil recovery. *Science*, 224(4649):563–569, 1984.

[36] M.A. Parvez, N.S. Ong, Y.C. Lam, and S.B. Tor. Gas-assisted injection molding: the effects of process variables and gas channel geometry. *J. Mater. Process. Technol.*, 121(1):27–35, 2002.

[37] H. Pascal. Rheological behaviour effect of non-Newtonian fluids on dynamic of moving interface in porous media. *Int. J. Eng. Sci.*, 22(3):227–241, 1984.

[38] A.J. Poslinski, P.R. Oehler, and V.K. Stokes. Isothermal gas-assisted displacement of viscoplastic liquids in tubes. *Polym. Eng. Sci.*, 35(11):877–892, 1995.

[39] G. Rousseaux, A. De Wit, and M. Martin. Viscous fingering in packed chromatographic columns: Linear stability analysis. *J. Chromatogr. A*, 1149(2):254–273, 2007.

[40] A. Roustaei. *Yield stress fluid flows in uneven geometries: applications to the oil and gas industry.* PhD thesis, University of British Columbia, 2016.

[41] A. Roustaei and I.A. Frigaard. Residual drilling mud during conditioning of uneven boreholes in primary cementing. part 2: Steady laminar inertial flows. *J. non-Newt. Fluid Mech.*, 226:1–15, 2015.

[42] A. Roustaei, A. Gosselin, and I.A. Frigaard. Residual drilling mud during conditioning of uneven boreholes in primary cementing. part 1: Rheology and geometry effects in non-inertial flows. *J. non-Newt. Fluid Mech.*, 220:87–98, 2015.

[43] K.C. Sahu, H. Ding, P. Valluri, and O.K. Matar. Pressure-driven miscible two-fluid channel flow with density gradients. *Phys. Fluids*, 21(4):043603, 2009.

[44] T. Séon, J.P. Hulin, D. Salin, B. Perrin, and E.J. Hinch. Buoyancy driven miscible front dynamics in tilted tubes. *Phys. Fluids*, 17(3):031702, 2005.

[45] D. S. Stevenson and S. Blake. Modelling the dynamics and thermodynamics of volcanic degassing. *Bull. Volcanol.*, 60(4):307–317, 1998.

[46] P. A. P. Swain, G. Karapetsas, O.K. Matar, and K.C. Sahu. Numerical simulation of pressure-driven displacement of a viscoplastic material by a Newtonian fluid using the lattice Boltzmann method. *Eur. J. Mech. B-Fluid*, 49:197–207, 2015.

[47] S.M. Taghavi. *From displacement to mixing in a slightly inclined duct*. PhD thesis, University of British Columbia, 2011.

[48] S.M. Taghavi. A two-layer model for buoyant displacement flows in a channel with wall slip. *J. Fluid Mech.*, 852:602–640, 2018.

[49] S. M. Taghavi, K. Alba, and I.A. Frigaard. Buoyant miscible displacement flows at moderate viscosity ratios and low Atwood numbers in near-horizontal ducts. *Chem. Eng. Sci.*, 69:404–418, 2012.

[50] S. M. Taghavi, K. Alba, M. Moyers-Gonzalez, and I. A. Frigaard. Incomplete fluid-fluid displacement of yield stress fluids in near-horizontal pipes: experiments and theory. *J. non-Newt. Fluid Mech.*, 167-168:59–74, 2012.

[51] S. M. Taghavi, R. Mollaabbasi, and Y. St-Hilaire. Buoyant miscible displacement flows in rectangular channels. *J. Fluid Mech.*, 826:676–713, 2017.

[52] S. M. Taghavi, T. Seon, D. M. Martinez, and I. A. Frigaard. Buoyancy-dominated displacement flows in near-horizontal channels: the viscous limit. *J. Fluid Mech.*, 639:1–35, 2009.

[53] G.I. Taylor. Cavitation of a viscous fluid in narrow passages. *J. Fluid Mech.*, 16(04):595–619, 1963.

[54] R.L. Thompson and E.J. Soares. Viscoplastic dimensionless numbers. *J. non-Newt. Fluid Mech.*, 2016.

[55] G. Vinay. *Modélisation du redémarrage des écoulements de bruts paraffiniques dans les conduites pétrolieres*. PhD thesis, École Nationale Supérieure des Mines de Paris, 2005.

[56] A.R. White and T. Ward. Constant pressure gas-driven displacement of a shear-thinning liquid in a partially filled radial Hele-Shaw cell: Thin films, bursting and instability. *J. non-Newt. Fluid Mech.*, 206:18–28, 2014.

[57] K. Wielage-Burchard and I. A. Frigaard. Static wall layers in plane channel displacement flows. *J. non-Newt. Fluid Mech.*, 166(5):245–261, 2011.

[58] J. Wiklund, M. Stading, and C. Trägårdh. Monitoring liquid displacement of model and industrial fluids in pipes by in-line ultrasonic rheometry. *J. Food Eng.*, 99(3):330–337, 2010.

[59] M. Zare, A. Roustaei, and I.A. Frigaard. Buoyancy effects on micro-annulus formation: Density stable displacement of Newtonian–Bingham fluids. *J. non-Newt. Fluid Mech.*, 247:22–40, 2017.

Conclusions

I Summary and conclusions

In this Ph.D. thesis, we have addressed in detail two fundamental viscoplastic displacement flow problems. First, we have experimentally studied immiscible displacements of viscoplastic fluids by Newtonian fluids through Hele-Shaw cells. Second, we have numerically investigated miscible displacement flows of yield stress fluids by Newtonian fluids, along a long 2D plane channel. In this chapter, we summarize the key findings and contributions made to provide an understanding of these displacement flow problems. Then, we close the chapter with recommendations for future research directions in this area.

I.1 Viscoplastic displacement flows of two immiscible fluids: Experimental approach

The displacement flow problem is experimentally considered in $Chapters$ 1, 2 and 3, for which the impacts of various flow parameters on the viscous fingering instability are studied. A summary of the main findings is presented below:

• The effects of a complex rheology on the displacement of elasto-visco-plastic fluids:
We considered the viscous fingering instability for viscoplastic fluids in the Hele-Shaw cell, in which a less viscous fluid (i.e., air) displaced a more viscous fluid (i.e., Carbopol gel). The gel used exhibits yield stress, shear-thinning as well as elastic behaviors. The intricate nature of the problem, caused by a considerable number of dimensionless groups (i.e., the capillary number (Ca), the Bingham number (Bn), the Weissenberg number (Wi), the Weber number We, the aspect ratio (δ), and power-law index (n)) made the investigation of the flow challenging. Scrutinizing the morphological differences and the finger width variations, we identified three distinct flow regimes: the yield stress regime, the viscous regime and the elasto-inertial regime. We also provided a profound knowledge about these regimes and their transition boundaries. For the yield stress regime, we demonstrated that the finger width is independent of the finger tip velocity, while the width of finger decreases by increasing the velocity in the viscous regime. However, for the elasto-inertial regime, the variation of finger width is completely different so that after the initial increase the finger width seems to reach

more or less a plateau value. In addition, our study considered some secondary flow features, including the thickness of the residual wall layers, and finding a network structure regime. We indicated that the transition from the network structure regime is controlled by Bn and Ca.

• The influences of wettability on the removal of viscoplastic fluids:
Unlike most of the traditional studies in which the displaced fluid wets the wall, we studied the wetting displacement where a less viscous wetting fluid displaced a more viscous non-wetting fluid. We identified four displacement flow regimes, i.e., the capillary, the yield stress, the viscous, and the elasto-inertial regimes. The formation of each regime depends on the experimental parameters such as the gap thickness, the imposed velocity, the wettability condition and the Carbopol concentration. The capillary regime is a unique regime which appears at very low velocities. For this regime, the dynamic contact angle has a significant role as an interplay between interfacial tension and yield stress effects leads to its appearance. In this regime, the finger width is almost equal to the width of the Hele-Shaw cell. Our results demonstrated the remarkable impact of wettability on the flow patterns and the displacement flow efficiency. We also provided a comprehensive master curve, enabling a collapse of data for both wetting and non-wetting flows, using $(\frac{Ca}{Bn}\delta^{1+n})$. Finally, we indicated the influences of wettability on the characteristics of side branches.

• The impacts of flow geometry aspect ratio on the viscoplastic displacement flow:
We experimentally studied a two-phase interfacial flow wherein air pushes a yield stress fluid (i.e., Carbopol gel) in long, uniform horizontal channels of various rectangular cross-sections. Compared to traditional narrow channel cases (i.e., Hele-Shaw cells), the gap thickness in our rectangular channels was slightly increased to consider the effects of the cross-section aspect ratio and buoyancy, on the removal of the yield stress fluid and the induced flow patterns. We showed that the yield stress in conjunction with buoyancy effects influence the flow patterns. Here, in particular, we indicated that branched fingering patterns, reported in the literature for negligible buoyancy effects, are not formed. Finally, we analyzed the flow using the dimensionless air finger width, for various aspect ratios and buoyancy effects, and provided a comprehensive flow regime map. We found that even in the presence of gravity, a simple control parameter $(Ca\delta^{1+n})$ which leads to the collapse of all the finger width on the same master curve; although this finding is valid for cells with $\delta > 6$.

I.2 Miscible Newtonian-viscoplastic displacement flows: Numerical approach

The displacement flow problem has been numerically considered in *Chapters* 4 and 5. The main scientific conclusions and contributions are summarized below:

• The impacts of yield stress and buoyancy on the displacement flow features:
We computationally examined the displacement flows of a yield stress fluid by a Newtonian

one, along a horizontal 2D plane channel, in which the heavier fluid pushed the lighter fluid. We analyzed the details associated with various displacement flow features, especially the thicknesses of the residual wall layers as well as the locations where uniform static layers appear. First, we discussed the variation of static residual wall layers of the displaced fluid versus governing dimensionless numbers (i.e., the Reynolds number (Re), the Bingham number (Bn) and the densimetric Froude number (Fr)). We presented that for a wide ranges of Re and Fr, increasing Bn results in decreasing both the upper and lower static residual layers. Second, we introduced three classes of displacement flow regimes: the slump/center-type, the no-back/temporary-back-flow and the stable/unstable displacements. We observed that the appearance of the slump/center-type regime is independent of Bn and the transition from slump-type to center-type occurs at $Re/Fr \approx 60$. We showed that the transition between the no-back-flow and temporary-back-flow regimes slightly depends on Bn, whereas this transition is mainly controlled by Fr.

• The effects of viscosity ratio and geometry inclination on the removal of yield stress fluids from rectangular 2D plane channels:
We studied miscible viscoplastic displacement flows along a near-horizontal 2D plane channel, where the displacing fluid was denser than the displaced one. Our CFD simulations covered displacements of a Bingham fluid by a Newtonian fluid for a wide range of flow parameters. We studied the qualitative and quantitative aspects of the flow using the Bingham number (Bn), the viscosity ratio (m), the Reynolds number (Re), the densimetric Froude number (Fr) and the channel angle (β). We observed that the Rayleigh-Taylor and Kelvin-Helmholtz-like instabilities are more visible for relatively small Froud numbers, and that these instabilities can be damped by increasing the Bingham number. We focused our attention to the viscosity ratio, showing its remarkable effects on the flow features. In particular, we investigated the effects of m on the displacement flow patterns, the main flow regime (i.e., slump-type and center-type flow regimes), the leading front features (e.g., leading front velocity) and trailing front features (back-flow/no-back-flow regimes). We showed that the appearance of slump/center-type displacement is independent of m for the smaller values of viscosity ratios ($m \leqslant 1$), whereas higher values of m help the formation of center-type flows. Also, unlike the Bingham number, Re/Fr has a significant impact on the slump-type and center-type flow regimes. The viscosity ratio has an opposite impact on front velocity at low and high values of Fr. In addition, we mentioned that the appearance of the back-flow regime is influenced by m so that increasing m leads to the formation of no-back-flow regimes. The variation of the displacing front velocity has been quantified as a function of m, Bn and Fr. Finally, we studied the effect of the viscosity ratio in conjunction with different channel inclinations. We observed that increasing β changes the displacement flow morphology so that the flow becomes more unstable.

II Recommendations for future work

Based on the findings in this dissertation, the following perspectives could be considered for each chapter:

• In *Chapter* 1, we investigated experimentally the effect of a complex rheology for immiscible fluids; the following interesting areas could be proposed as the complementary works:

— Analyzing displacement flows for Bingham-capillary numbers higher than one.
— Impact of particle migrations on yield stress suspensions.
— Analyzing miscible flows instead of immiscible flows.
— Investigation of iso-density and heavy-light viscoplastic displacement flows.
— Studying the effect of the Hele-Shaw cell inclination.
— Investigation of the impact of elastic wall boundaries.

• *Chapter* 2 is an experimental study of the impacts of wettability on viscous fingering of viscoplastic fluids. Investigations of the following topics can bring novelty to the future works:

— Influences of solid wall surfaces and slip conditions.
— Impact of buoyancy force on wetting displacement flows.
— Effect of misciblity on wetting displacements.
— Adding surfactant to decrease the surface tension of Carbopol solutions and comparison of the results with miscible results.
— A detailed stability analysis of the wetting displacement flow for viscoplastic fluids.

• *Chapter* 3 studied the influence of flow geometry aspect ratio on viscous fingering of viscoplastic fluids through experimental approaches. To complete this work, the following topics are recommended:

— Monitoring the side view displacement flow especially at higher buoyancy effects.
— Finding the velocity field and the local velocity using the Particle Image Velocimetry (PIV) and Ultrasound Doppler Velocimetry (UDV) techniques.
— Effect of aspect ratio on the wetting displacement flow.
— Studying the viscoplastic displacement flow through non-uniform geometry, e.g., converging/diverging cell.

• In *Chapter* 4 considered numerical simulations of viscoplastic fluids in 2D plane channels, while analyzing the impact of buoyancy, inertia and yield stress on the miscible displacement flows. To complete this research, the following directions can be proposed:

— Immiscible displacement flows by considering a pressure drop at the interface of fluids.
— Developing 3D numerical simulations of pipe or channel flow displacements.
— Density stable (light-heavy) displacements of viscoplastic fluids.
— Viscoplastic displacement flows in slightly non-uniform channels.

• *Chapter* 5 extended *Chapter* 4 to consider the effects of the viscosity ratio and the channel inclination. The following suggestions can be made for future works:

— Displacement flows in vertical channels.
— Displacement flows with several non-Newtonian features at the same time.
— A detailed stability analysis of the flow via analytical approaches.